Liquid crystal drops in suspensions of colloidal plates

Universiteit Utrecht

Cover - Aqueous gibbsite suspension with Rayleigh-Taylor instabilities dripping from an upper nematic phase that displays birefringent patterns due to buckling distortions. The lower isotropic phase contains nematic tactoids with various sizes and director fields. See Chapter 4 and 8. (Two polarized light microscopy images combined with image editing software)
Cover design: Annemarie Verhoeff and Lia Verhoeff

Printed by Wöhrmann Print Service

ISBN 978-90-393-5498-8
Subject headings: Gibbsite/liquid crystals/colloids/nematic/columnar/tactoids/magnetic fields/interfaces.

Liquid crystal drops in suspensions of colloidal plates

Vloeibaar kristallijne druppels in suspensies van colloïdale plaatjes

(met een samenvatting in het Nederlands)

Proefschrift

ter verkrijging van de graad van doctor aan de
Universiteit Utrecht op gezag van de rector magnificus,
prof. dr. J.C. Stoof, ingevolge het besluit van het
college voor promoties in het openbaar te verdedigen
op maandag 24 januari 2011 des middags te 2.30 uur

door

Aletta Adriana Verhoeff

geboren op 17 mei 1983 te Utrecht

Promotoren: Prof. dr. H. N. W. Lekkerkerker

Prof. dr. ir. P. P. A. M. van der Schoot

Het in dit proefschrift beschreven onderzoek werd gefinancierd door de Koninklijke Nederlandse Akademie van Wetenschappen (KNAW).

Contents

1

General Introduction

1.1. Colloidal liquid crystals

It has been known for a considerable amount of time that suspensions of rod-like colloidal particles[1] above a certain concentration spontaneously align to form a uniaxial, nematic liquid-crystalline phase.[2] In the nematic phase, the particles possess orientational order along some preferred direction called the director, but lack positional ordering. First reports of the nematic phase date back to the 1920s, when Zocher observed the spontaneous orientational alignment of ribbon-like vanadium pentoxide particles (V_2O_5) with the aid of polarized light microscopy [5]. In the 1930s, the nematic phase was also found to occur in suspensions of rod-like tobacco mosaic virus (TMV) [6]. Inspired by these observations, Onsager showed theoretically that these fascinating examples of self-organization can be explained as resulting from the competition between the loss of orientational entropy and the gain of free volume, i.e., translational entropy [7]. At sufficiently high concentrations, the translational entropy gain dominates and the particles as a result of that favour nematic alignment. The theoretical considerations of Onsager have long since been confirmed by computer simulations [8, 9].

In 1950, Oster observed in addition to the nematic phase a smectic phase in suspensions of TMV in which the particles possess (quasi long-range) positional order in one dimension [10]. Theory and computer simulations demonstrated that also in this case the spontaneous ordering can be explained in terms of hard-core repulsive interactions only [11, 12]. Since, the field of liquid crystals in suspensions of rod-like particles has developed rapidly. On the one hand, dedicated systems were synthesized including akagenite (β-FeOOH) [13], boehmite (γ-AlOOH) [14], goethite (α-FeOOH, consisting of board-like particles) [15, 16], cadmium selenide semiconductor nanorods [17], gold nanorods [18] and very recently silica rods [19]. On the other hand, in addition to polarized light microscopy several other experimental techniques have given deeper insight in the properties of liquid crystal phases, of which we mention small angle x-ray and neutron scattering [20–22], atomic force microscopy [23], as well as nuclear magnetic resonance [24, 25]. In addition, extensive simulations have been done that mapped out the complete phase diagram in particular of suspensions of so-called hard rod-like particles, showing that apart from nematic and smectic phases also several crystal phases and a plastic phase form, depending on density and aspect ratio of the particles [26–28].

In 1938, Langmuir observed a nematic phase in suspensions of plate-like clay particles, which he referred to as California bentonite and that nowadays is known as hectorite [29]. Soon after, Onsager made plausible that the same competition of orientation

[1] Colloidal particles can be defined as particles that have dimensions roughly between a few nanometers and a few micrometers. If dispersed in a liquid medium, we speak of a suspension. For a first introduction to colloid science we refer to [1], for a more extensive treatment see [2].

[2] For classic introductions to liquid crystals we refer to [3, 4].

and packing entropy that is responsible for nematic alignment in suspension of rod-like particles, also stabilized the nematic phase in suspensions of plate-like particles [7]. Until recently and despite many attempts, the observations of Langmuir could not be reproduced, which hampered the development of the field for a long time. In the 1990s, computer simulations by Veerman and Frenkel confirmed that suspensions of plate-like particles should indeed form a nematic phase, and in addition a columnar phase in which the particles exhibit positional order in two dimensions [30]. In the last 10 years, these phases were indeed observed in a number of systems, starting with nickel hydroxide ($Ni(OH)_2$) [31] and gibbsite (γ-$Al(OH)_3$) [32–34], later followed by Na-fluorohectorite [35,36] and mixed-metal hydroxides [37]. Recently, stable nematic phases were finally also observed in suspensions of natural clay platelets, being nontronite [38] and beidellite [39].

Of all these systems, gibbsite is unique in that it is the only plate-like system that forms both a nematic and a columnar phase. It does so in suspensions of sterically stabilized gibbsite dispersed in apolar solvent [33], as well as in suspensions of charge stabilized gibbsite dispersed in water [34]. These two types of system not only differ in inter-particle interaction but also in their optical properties. We show in this thesis that whereas the birefringence of sterically stabilized gibbsite is determined by the positive intrinsic platelet birefringence, in aqueous gibbsite suspensions the negative birefringence prevails that arises due to the anisometric particle shape. A surprising feature of gibbsite platelets is that even a polydispersity of 25% in the platelet diameter does not preclude the formation of the columnar phase [33]. Moreover, we discovered that a bimodal distribution of the platelet aspect ratio enriches the phase behavior with the occurrence of a remarkable isotropic-nematic density inversion, as well as a three phase, nematic-isotropic-columnar phase coexistence. The unique birefringent properties and phase behaviour of gibbsite suspensions will be treated in the first part of this thesis.

1.2. Nematic tactoids

Along with the early observations of the nematic phase in suspensions of vanadium pentoxide particles, Zocher reported on the existence of elongated, spindle-shaped droplets consisting of nematic phase floating in the isotropic phase. He called the nematic droplets "Taktoide" in his native German (from the Greek $\tau\alpha\kappa\tau\acute{o}\varsigma$ meaning "ordered") and tactoids in English [5,40]. These peculiarly shaped droplets were recognised as precursors of the nematic phase. They were later also observed in suspensions of other rod-like particles that give rise to nematic phases, such as goethite [41], TMV [42] and boehmite [43], and more recently feline distemper (fd) virus [44], polymer-coated sepiolite clay [45] and F-actin [46]. From the birefringent patterns that these spindle-shaped droplets display when observed between crossed polarizers, it was deduced that

they have a bipolar director field with the director lines running from end to end and near the interface parallel to the interface. It was also found that larger droplets tend to be more spherical whereas smaller drops are more elongated.

Bernal and Fankuchen provided an explanation for the characteristic droplet shape based on the anisotropic interfacial tension, i.e., an interfacial tension that depends on the angle the director makes with the interface [42]. Further theoretical studies along these lines were performed by Chandrasekhar [47] and Virga [48, 49], who investigated spindle-shaped drops presuming the director field to be uniform and to prefer planar alignment at the interface. However, such an anisotropic interfacial tension alone cannot account for the observed volume dependence of the tactoid shape. A better explanation that does account for this is that the preferred droplet shape and director field arise from a competition between interfacial as well as elastic free energies associated with non-uniform director fields, as was first suggested by Dubois-Violette and Parodi [50]. Later, Williams showed that bipolar tactoids indeed optimize their shape by a balance between a minimal deformation of the director field and a minimal interfacial free energy [51]. Further studies based on this idea finally lead to complete phase diagrams of tactoid shapes and director fields in terms of tactoid size, interfacial tension, anchoring strength, and various elastic constants [52–54]. Not unimportantly, it was shown that information on the tactoid shape as a function of tactoid size may be used to determine ratios of elastic constants and the surface tension [46, 52, 55, 56].

In fact, a simple scaling analysis making use of the various contributions to the free energy of a tactoid already gives us useful insight on the relation of director field and tactoid size [52]. First, the free energy of the droplet is a function of its internal structure, i.e., the particle director field configuration, and scales as KR with K some average of the elastic constants and R the radius of the tactoid that is presumed more or less spherical. Second, the interfacial free energy of the tactoid depends on the anchoring of the particles with respect to interface. If the director field is uniform, then this anchoring free energy scales with wR^2, where w is the anchoring strength. This implies that at a characteristic length scale $\xi \equiv K/w$, also referred to as extrapolation length [57], a transition must occur from behaviour dominated by the interfacial anchoring if $R > \xi$, to behaviour dominated by bulk elasticity if $R < \xi$. As a consequence, a transition must take place from a bipolar droplet to a droplet with a uniform director field if the droplet is sufficiently small, a scenario recently confirmed by means of computer simulation [58]. In 2010, Puech and co-workers presented the first unambiguous observations of spindle-shaped droplets with a uniform director field in suspensions of carbon nanotubes [59]. However, they did not observe the director-field transition, possibly because the width of the distribution of drop sizes was not large enough. In this thesis we present the to our knowledge first unequivocal experimental evidence for the director-field transformation in nematic droplets.

Evidently, nematic droplets are extremely interesting as their inner structure and shape are the result of the direct competition between bulk and surface interactions. The fact that the nematic drops found in suspensions of rod-like particles can be very much elongated with aspect ratios as large as six [52], implies that the bare surface tension must be very low indeed. Note that this in itself is of considerable interest. It is because of the competition between the surface and elastic properties of nematic droplets, that an analysis of tactoid shapes and director fields provides a way to obtain values of important material parameters associated with these properties. Whereas tactoids in suspensions of rod-like particles have for this purpose been investigated extensively, both experimentally and theoretically, hardly any observations have been reported on suspensions of plate-like particles. Interestingly, whilst rod-like colloids prefer to align planar (parallel) with respect to the isotropic-nematic interface, plate-like particles prefer homeotropic (perpendicular) anchoring. As we shall see in this thesis, this gives rise to different tactoid shapes and director fields.

It is important to point out that in the field of *thermotropic* liquid crystals, so liquid crystals found in fluids of low-molecular weight compounds, nematic drops both with planar and homeotropic anchoring have been studied extensively. This is especially so after the field experienced a revival in the 1980s, when it was discovered that polymer dispersed liquid crystal (PDLC) materials could be used for a new class of electro-optical modulators [60]. Theoretical studies, for the most part restricted to spherical drops, showed that in the case of homeotropic anchoring the same scaling applies as for planar anchoring but that in this case tactoids larger than K/w have a radial director field whereas smaller ones again have a uniform director field [61–63]. In thermotropic liquid crystals, the length scale K/w is usually very small, i.e., in the sub-micrometer range [63], which implies that interesting phenomena associated with the director field transition occur at length scales where direct observation of the tactoids is practically impossible.

However, recent work on the isotropic-nematic interface in gibbsite suspensions showed that the length scale K/w in this system is in the order of tens of micrometers [64]. For that reason, we chose gibbsite to study tactoids in the interesting size region around the extrapolation length. As already mentioned, gibbsite platelets can be stabilized sterically to be dispersed in apolar solvent as well as charge stabilized for dispersion in polar solvents. Although the values for the elastic constant K, the anchoring strength w and surface tension γ in both types of system are of the same order of magnitude, it is the ratio of various combinations of these parameters that determines the droplet characteristics. For instance, the ratio K/w determines whether elasticity or interfacial anchoring prevails whereas the ratio of w/γ distinguishes between strong and weak anchoring of the director field to the interface. We find that these ratios are significantly

different for sterically stabilized and charged gibbsite, which enlarges the experimental window (Chapter 4). Because gibbsite platelets exhibit perpendicular alignment in a magnetic field, this allows us to manipulate the shape and director field of tactoids with an externally applied magnetic field. Here, the magnetic field acts as an additional tool to determine important material parameters such as the splay elastic constant, the interfacial tension and the anchoring strength (Chapter 5 and 6).

We not only studied tactoid shapes and director fields but also dynamical processes including the coalescence (Chapter 7) and breakup of nematic droplets and threads (Chapter 8). There, in addition to the parameters K, w and γ, the (anisotropic) viscosities both of the isotropic mother phase as well as of the droplets freely floating in it play an important role.

1.3. Columnar droplets

As already mentioned, gibbsite is a unique system because it forms in addition to the nematic phase also a columnar phase. Moreover, the specific gibbsite system that exhibits a three phase equilibrium allows direct observation of droplets of the columnar phase in the isotropic phase (Chapter 9). These droplets have a flat, disk-like shape and consist of short, hexagonally arranged stacks of platelets. This tendency of platelets to form stacks has been observed for a long time in suspensions of platelets of kaolinite [65], and also in computer simulations [30]. It is interesting to compare these observations with the observations of Maeda and Maeda on the nucleation of the smectic phase in suspensions of akagenite rods, which is accompanied by large single particle layers [66] for which computer simulations provided a basic understanding [67,68]. We also studied the formation of the columnar phase from a kinetically arrested glassy state. Here again, it seems that stacks of platelets play a crucial role (Chapter 10).

1.4. Outline of this thesis

This thesis is organized in four parts.

In **Part 1** we deal with some general aspects of liquid crystalline phases in suspensions of gibbsite platelets to provide a basic framework for the research described in the remainder of the thesis. We begin with a brief review of birefringence and polarized light microscopy applied to liquid crystalline phases in gibbsite suspensions (Chapter 2). Furthermore, we investigate the intrinsic and form birefringence of the nematic phase in gibbsite suspensions as a function of solvent refractive index, and show that if the refractive index of the solvent is close to that of gibbsite, the intrinsic birefringence of the platelets dominates. On the other hand, if the refractive index is considerably different, form birefringence due to the anisometric particle shape prevails over the intrinsic birefringence. Chapter 3 is devoted to a gibbsite system that plays an important

role throughout the thesis. The bimodal distribution of the platelet aspect ratio in this system leads to remarkable phase behavior, including an isotropic-nematic density inversion and a three phase coexistence.

In **Part 2** we focus on the static properties of nematic droplets or tactoids. We start in Chapter 4 with an investigation of the shape and director field of these tactoids in polar and apolar solvent. From a detailed analysis of the tactoid properties as a function of size we obtain values for the ratio of the splay elastic constant K_1 and the anchoring strength w, as well as the ratio of the anchoring strength w and the isotropic-nematic interfacial tension γ. This is followed by a study of the deformation of tactoids in an externally applied magnetic field, where we observe significant deformation of tactoid shapes and director fields. First with a simple model (Chapter 5), and subsequently with a more extensive model (Chapter 6), we do not only account for the observed tactoid shapes and director configurations but are also able to determine the splay elastic constant K_1, the isotropic-nematic interfacial tension γ, and the surface anchoring strength w of the platelets.

Subsequently, in **Part 3** we explore dynamic phenomena of tactoids. In Chapter 7 the coalescence of tactoids with the isotropic-nematic interface and the coalescence of two tactoids is investigated. Broadly speaking, small tactoids behave like isotropic molecular fluids, while the behavior of larger tactoids shows remarkable resemblance to immiscible drops that translate through a liquid-liquid interface. The buoyancy driven coalescence of two tactoids appears to proceed as in the case of isotropic fluids. In Chapter 8 we show that droplet pinch-off and breakup of a nematic thread are strongly influenced by the liquid crystalline order present in the thread. Depending on the values of K_1/w and w/γ different scenarios are observed.

Finally, in **Part 4** the formation of the columnar phase is studied, first by an investigation of droplets of the columnar phase (Chapter 9), followed by a study of the devitrification of the glassy state, where after an extended period of time (months to years) the columnar phase nucleates in a dynamically arrested gibbsite suspension (Chapter 10).

Part 1

Suspensions of Colloidal Platelets

2

Birefringence of liquid crystal phases and droplets in suspensions of colloidal gibbsite

Abstract

In this chapter we discuss the birefringence of colloidal liquid crystals and briefly review the principles of polarized light microscopy applied to the investigation of liquid crystals. Subsequently, we study the birefringence of the nematic phase in colloidal gibbsite suspensions as a function of solvent refractive index. We find that for solvents with a refractive index close to the particle refractive index, the intrinsic birefringence of the platelets dominates, resulting in positive birefringence. On the other hand, if the solvent has a considerably different refractive index, birefringence due to the anisometric particle shape prevails over the intrinsic birefringence, resulting in negative birefringence.

2.1. Introduction

In this thesis we study the liquid crystal phases and droplets formed in suspensions of plate-like gibbsite colloids. In section 2.2 of this chapter we describe the preparation of the colloidal gibbsite particles that are subject of investigation. In the studied liquid crystal phases and droplets the gibbsite platelets possess orientational order (in the nematic phase), and also positional order (in the columnar phase), and due to this ordering the systems display birefringence.

Birefringence, an effect that occurs in optically anisotropic materials, is a fascinating phenomenon. The most well-known example is probably the double refracting iceland spar crystal, which was already studied by Christiaan Huygens and Isaac Newton in the 17^{th} century [69]. Due to the two different refractive indices ($n_o = 1.658$ and $n_e = 1.486$) of the transparent calcite rhomb, light that enters the crystal is, depending on the polarisation direction, refracted into an ordinary and an extraordinary ray, resulting in a double image visible through the crystal [69]. Birefringence has also proven a useful material property for many applications, especially in a variety of optical devices, but also in pathology [70] and medical diagnostics [71]. Moreover, it is the key property for the investigation of minerals and liquid crystals with polarized light microscopy [69,72].

Colloidal liquid crystalline phases display birefringence due to the anisometric particle shape, referred to as form or shape birefringence [73]. This property was for example used by Wilkins and Oster to study the alignment of the on itself isotropic tobacco mosaic virus rods [74]. In the case of liquid crystalline phases in suspensions of colloidal gibbsite, the particles themselves are also optically anisotropic, in other words exhibit intrinsic birefringence, leading to interesting effects. In section 2.3 of this chapter we will discuss the theoretical background of intrinsic and form birefringence and show that in the case of gibbsite platelets we have the rather unique situation that depending on the suspending medium, either the one or the other dominates. Polarized light microscopy is the tool of choice to investigate liquid crystalline phases and droplets, which we present in section 2.4 of this chapter. We describe first of all the principles of polarized microscopy. Also, we briefly indicate the microscope used, the sample preparation, and the use of an external magnetic field. Finally, in section 2.5 we describe results obtained with gibbsite liquid crystals aligned in a magnetic field, anchored at the wall and a planar interface, and confined to droplets, and discuss what these experiments learn us about the optical properties of gibbsite liquid crystals.

2.2. Preparation of colloidal gibbsite

Colloidal gibbsite (γ-$Al(OH)_3$) platelets were synthesized by hydrothermal treatment of aluminum alkoxides in acidic environment, a procedure developed in our laboratory [75]. To that end, an acidic aqueous solution containing hydrochloric acid (HCl

0.09 M, 37%, Merck), aluminium sec-butoxide (0.08 M, 95%, Fluka Chemika) and aluminium iso-propoxide (0.08 M, 98+%, Acros Organics) was prepared and mechanically stirred for 10 days. Subsequently, the mixture was heated in a glass reaction vessel in a water bath at 85 °C for 72 h. Then, the colloidal dispersion was centrifuged at 1000g (overnight, 15-20 h) in order to remove the smallest particles and decrease the polydispersity. The resulting dispersion was dialyzed against demineralized water in tubes of regenerated cellulose (Visking, MWCO 12 000-14 000) until the conductivity dropped to 20 μS cm^{-1}. The obtained particles were characterized with transmission electron microscopy (Tecnai 10, FEI Company), see Figure 2.1(a). The hexagonal platelets typically have a diameter of around 200 nm and a thickness of 8 nm.

Subsequently, the obtained particles were treated either to enhance the stability in aqueous dispersions, or to enable dispersion in apolar solvents. For enhanced stability in aqueous dispersions, 0.5 w/w % aluminum chlorohydrate (Locron P, Hoechst AG, Germany) was added to the dispersion. The enhanced stability is associated with the presence of aluminum polycations (Al_{13} Keggin ions, $[Al_{13}O_4(OH)_{24}(H_2O)_{12}]^{7+}$) that form at pH $\approx$ 4 [76] and adsorb on the surface of the gibbsite particles. This gives rise to a steep repulsive particle interaction which prevents the platelets from aggregating [77]. After three days, the dispersion was centrifuged to remove excess aluminum chlorohydrate and the particles were subsequently redispersed in a 10^{-2} M NaCl solution. To enable dispersion of the gibbsite platelets in apolar solvents the particles were sterically stabilized with a amino-modified poly-iso-butylene (SAP 230 TP, Infineum, UK), by following two different procedures.

The first procedure involves a gradual substitution of the solvent upon addition of the stabilizing polymer, as described in [32]. The particles obtained through this method were dispersed in 2-bromotoluene (Acros, 99%). Following an alternative method, the gibbsite platelets were freeze-dried in the presence of poly-iso-butylene in 1-propanol (Acros, 99%) [78, 79]. The thus stabilized particles were dispersed in toluene (J.T. Baker, 99.5%).

Finally, the dispersions were concentrated with centrifugation and subsequent redispersion to reach the desired particle concentration.

2.3. Birefringence

At sufficiently high concentration, suspensions of gibbsite particles form nematic and columnar liquid crystal phases with orientational ordering and one-dimensional positional ordering, respectively. As a result, these phases are birefringent, and as is shown in Figure 2.1(b) and (c) light is transmitted if they are placed between crossed polarizers. The isotropic phase is dark, but can be made birefringent by gently moving the sample so that the platelets align in the resulting flow.

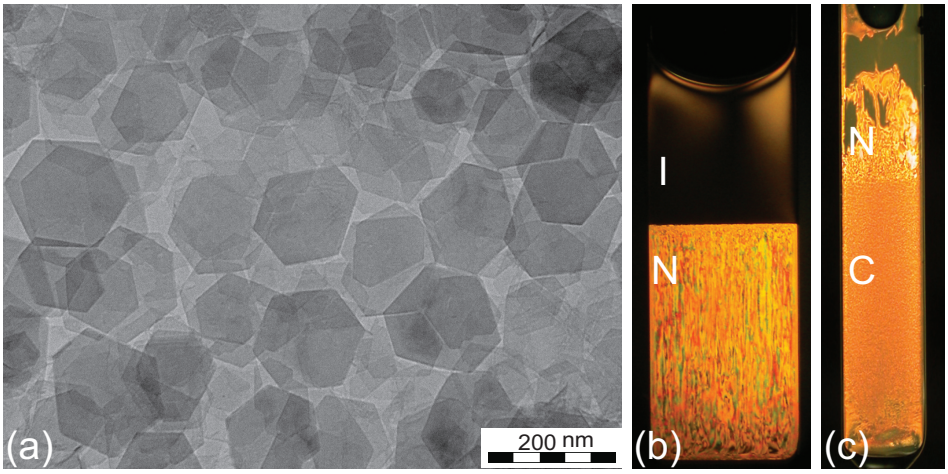

Figure 2.1. (a) Transmission electron micrograph of colloidal gibbsite platelets. (b) Isotropic-nematic and (c) nematic-columnar phase separated gibbsite suspensions between crossed-polarizers. The birefringence visible in the isotropic phase of sample (b) is flow birefringence caused by gentle movement.

Birefringent materials have two or more refractive indices. Here, we will focus on uniaxial materials, with two refractive indices. If linearly polarized light enters such a material, it is refracted into two components with orthogonal vibration directions, the ordinary ray (o-ray) with the polarisation perpendicular and the extraordinary ray (e-ray) parallel to the axis of anisotropy. The birefringence is defined as $\Delta n \equiv n_e$ - n_o, with the n_e and n_o the refractive indices for the e-ray and the o-ray. For uniaxial materials n_e and n_o correspond to n_2 and n_1 respectively. Because of the different refractive indices for these rays, they travel with a different velocity through the material, giving rise to a phase difference δ:

$$\delta = \frac{2\pi}{\lambda}(n_2 - n_1)t \tag{2.1}$$

with λ the wavelength of the incident light and t the path length through the material [80]. The value $\mid (n_2 - n_1) \mid t$ is referred to as retardation or optical path difference (OPD) [69]. When the refracted light arrives at the second polarizer (also, analyzer) that is at a 90° angle with respect to the first one, only the component with the vibration direction parallel to the polarizer will pass through. The resulting intensity is given by:

$$I = E^2 \sin^2 2\theta \sin^2 \frac{\delta}{2} \tag{2.2}$$

with E the amplitude of the electro-magnetic vector and θ the angle between the polarisation of the incident light and n_1 [80]. We will find a minimum intensity behind the analyzer if $\theta = 0, \pi/2, \pi, \ldots$ and relative maxima for $\theta = \pi/4, 3\pi/4, 5\pi/4, \ldots$ with values of:

$$I_{max} = E^2 \sin^2 \frac{\delta}{2}. \tag{2.3}$$

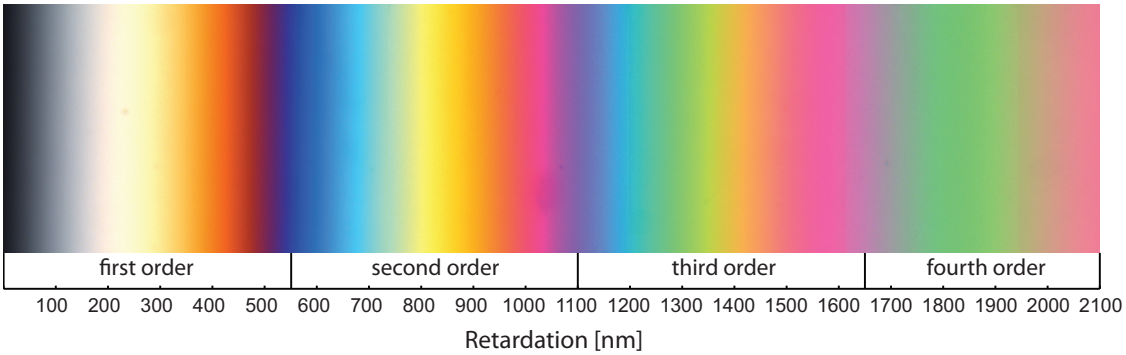

Figure 2.2. Newton's color scale, here visualized with a Babinet compensator, represents the retardation color sequence as a function of retardation.

Due to the wavelength dependence of δ, the use of white light leads to beautiful interference (or retardation) colors, as part of the wavelengths will interfere constructively and others destructively. These colors occur in a specific sequence, known as Newton's color scale and are often presented as a function of retardation in the form of a Michel-Levy chart. Figure 2.2 shows the color sequence visualized with a Babinet compensator, a tunable retardation plate that is composed of two opposed quartz wedges [72].

One can distinguish two types of birefringence: intrinsic and form birefringence. Intrinsic birefringence is caused by the anisotropy of the crystal lattice and therefore a fixed material parameter. Gibbsite (γ-Al(OH)$_3$) has a monoclinic crystal lattice with the following refractive indices: natural gibbsite $\alpha \simeq 1.56$-1.58, $\beta \simeq 1.56$-1.58, and $\gamma \simeq 1.58$-1.60. For synthetically prepared gibbsite $\alpha = \beta = 1.577$ and $\gamma = 1.595$ has been reported [81]. The optic axial plane (where the refractive index does not depend on the polarization direction of the incident light) is perpendicular to the (010) plane, and the extinction angle has an angle of -21° with the z-axis [81].

For colloidal gibbsite, which consists of hexagonal platelets, this implies that the largest refractive index, or slow axis, has an angle of -21° with respect to the particle director (see Figure 2.1). However, in the nematic phase, although the platelets have a net average orientation of the particle director, in the particle plane all orientations are allowed. The resulting intrinsic birefringence is therefore effectively parallel to the director, with $\Delta n_i \approx (\gamma - \alpha)\cos[21°] = 0.016$. Following [15, 82] the birefringence of a suspension due to the intrinsic particle birefringence is given by

$$\Delta n_{intr} = \Delta n_i \phi S_2 \tag{2.4}$$

with ϕ the particle volume fraction and S_2 the nematic order parameter.

On the other hand, form (or shape) birefringence arises if anisometric molecules or particles are dispersed in an ordered arrangement in a liquid with a different refractive index. It depends on the particle shape and the solvent refractive index and can therefore be manipulated.

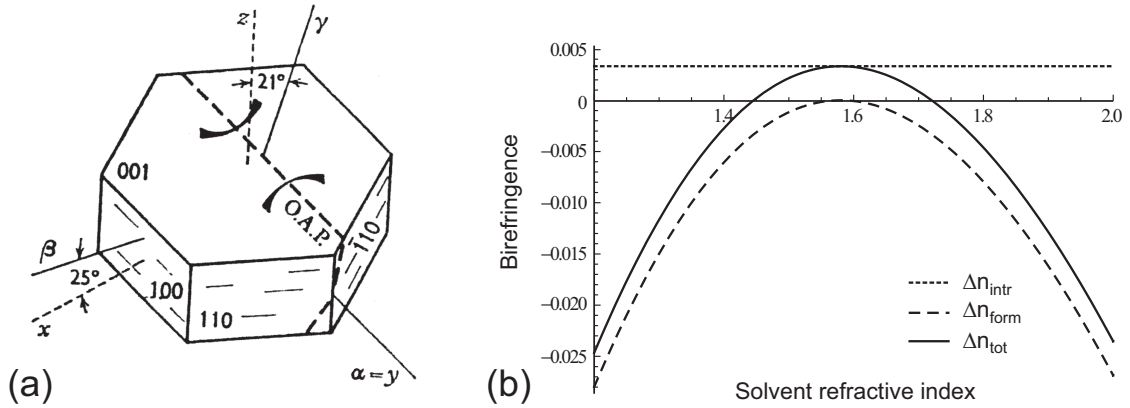

Figure 2.3. (a) Crystallographic and optical axes of gibbsite; reprinted from [81] with permission of The Geological Society London. (b) Intrinsic, form and total birefringence of a nematic phase of colloidal gibbsite as a function of solvent refractive index for $\phi = 0.26$, $S_2 = 0.8$, $L_a = 0.03$ and $L_b = 0.94$.

Wiener [73] showed that an assembly of thin parallel plates in a medium with a different refractive index behaves like a negative uniaxial crystal. Bragg and Pippard [83] extended his work to ellipsoids and obtained for the form birefringence of an assembly of particles with refractive index n_p in a solvent with n_s:

$$\Delta n_{form} = n_a - n_b = \phi(n_p - n_s)\frac{9k}{(3+k)^2}(L_b - L_a) \tag{2.5}$$

with ϕ the particle volume fraction, $k = (1-\phi)(n_2^2/n_1^2 - 1)$, and L_a and L_b depolarizing factors that depend on the particle symmetry. To obtain a reasonable estimate for the form birefringence of gibbsite where the particles possess intrinsic birefringence as well, we can use this equation with an average of the three refractive indices, $n_p = 1.58$. Although this is not exact, according to Twersky [84] it should introduce little error because the refractive indices are close. In their derivation Bragg and Pippard considered an assembly with perfectly aligned particles (orientational order parameter $S_2 = 1$), which is obviously not true for the gibbsite nematic phase. To account for this, we multiply by S_2 [15, 82], analogous to Equation 2.4. Previous experiments on the alignment of the gibbsite nematic phase in a magnetic field established typically $S_2 \approx 0.8$ [85].

In Figure 2.3(b) we plot the intrinsic and form birefringence as a function of solvent refractive index n_s, for a volume fraction ϕ of 0.26. The depolarizing factors can be calculated by considering the particles as ellipsoids [86], resulting in $L_a = 0.03$ and $L_b = 0.94$ for a bare platelet with an aspect ratio of 25. Δn_{tot} is obtained by simply taking the sum of the two contributions. We find that the birefringence of a gibbsite nematic phase is negative for most solvents, except if the refractive index is close to that of gibbsite itself.

2.4. Polarized light microscopy

The tool of choice to study birefringent specimens is the polarized light microscope, in fact just a bright-field microscope equipped with an adjustable polarizer and analyzer, strain-free optics and a slot to insert a compensator or retardation plate. This filter is used to determine the orientation of the liquid crystalline phase and consists of birefringent material (either a thin slice of a birefringent mineral or an aligned birefringent polymer between glass plates) with a known birefringence and orientation. It is placed in the light path between the polarizer and analyzer at an angle of 45° for maximum effect, and it adds a fixed retardation to all the wave fronts in the optical path. Depending on the respective orientation of the slow axes of the liquid crystal and the retardation plate, the retardation is added (parallel orientation) or subtracted (perpendicular orientation). Throughout this thesis we use a full wave retardation plate with an optical path difference of 530 nm, with a typical magenta tint.

The nematic phase we find in gibbsite suspensions typically has a retardation of about 150 nm for a sample thickness of 100 μm, which corresponds to a greyish retardation color, see Figure 2.2. This implies that if the slow axis of the nematic phase coincides with that of the retardation plate, the OPD is added and the retardation is shifted to 680 nm with a blue retardation color. Similarly, if the slow axes of the nematic phase and the retardation plate are perpendicular, the resulting OPD is 380 nm, corresponding to an orange retardation color.

In order to interpret the polarized light micrographs in the remainder of this thesis one has to realize the following. If light passes through crossed polarizers, we are dealing with an ordered phase, the orientation of which is not parallel to one of the polarizers. More precise information on this orientation can be determined with the retardation plate as described above. Conversely, if no light is coming through the crossed polarizers there are three possibilities. We are dealing with:

- an unordered (isotropic) phase; the phase is always dark, independent of the orientation of the polarizers.
- an ordered phase oriented with the director parallel to one of the polarizers; birefringence will appear if the polarizers are rotated.
- an ordered phase with the director perpendicular to the focal plane (in other words, the platelets are lying flat in the focal plane); dark irrespective of the polarizer orientation, but birefringence will appear if the sample is tilted with respect to the focal plane.

The polarized light microscope used throughout this thesis is a Nikon LV100Pol microscope, equipped with a full wave retardation plate ($\lambda = 530$ nm), a 2× Nikon CFI Plan UW objective, and 10× and 20× Nikon CFI Plan Fluor ELWD objectives. The microscope was in a tilted position with the focal plane along gravity in order to

allow investigation of the samples in upright position. Images were captured with a MicroPublisher 5 megapixel ccd camera (MP5, QImaging). In the remainder of this thesis we will use this camera, unless explicitly stated otherwise.

2.4.1. Magnetic field

To investigate the influence of a magnetic field a home-built polarization microscope setup was used, assembled from the head of a Zeiss Axiolab microscope, equipped with crossed polarizers, and a 2× Edmund Optics objective. The magnetic field was generated with a Bruker BE25v Electromagnet, equipped with large flat pole shoes producing a very homogeneous magnetic field in the sample volume. Field strengths ranged from $B = 0$ - 1.8 T and were monitored with a LakeShore 421 Gaussmeter. The samples could be rotated along their vertical axis with adjustable velocity (usually $\approx$ 0.25 Hz).

2.4.2. Sample preparation

Samples were prepared in flat optical capillaries (VitroCom, NJ, USA), with internal dimensions of $0.1 \times 2 \times 40$ mm^3 for the experiments in magnetic field and at the isotropic-nematic interface and $0.2 \times 4 \times 40$ mm^3 for study of tactoids, and flame-sealed to avoid evaporation of the solvent. The samples were homogenized and left to phase separate, which evolved via the formation, sedimentation and subsequent coalescence of tactoids.

2.5. Intrinsic versus form birefringence in nematic phases of colloidal gibbsite

2.5.1. Nematic phase aligned in a magnetic field

Colloidal gibbsite platelets have an anisotropic magnetic susceptibility, which implies that an external magnetic field gives rise to an induced magnetic moment in the particles. Previous studies on sterically stabilized gibbsite suspensions [64, 87] established that the magnetic anisotropy of these platelets is negative ($\Delta\chi$ = -10^{-22} J/T^2), and therefore the platelets tend to align with their director perpendicular to an externally applied magnetic field. This implies that the director orientation is restricted to the plane perpendicular to the magnetic field direction. If instead of a static field a rotating field is used, the platelets will align in a single direction, with the director perpendicular to the rotation plane. Rotation of the sample in a static field has the same effect, and it has been shown that one can obtain a single domain nematic phase with a well-defined orientation [87].

We will now use this method, schematically depicted in Figure 2.4(a) to study the birefringence of the nematic phase of colloidal gibbsite suspended in toluene, which has

a refractive index of $n_s = 1.4969$ and compare this to the gibbsite nematic phase in water with $n_s = 1.333$.

Figure 2.4(b) and (c) show the two isotropic-nematic phase separated gibbsite suspensions after rotation at 0.25 Hz for one hour in a magnetic field with a field strength of 1.8 T. The left hand sample is a suspension in toluene with an overall volume fraction $\phi = 0.22$, while the sample at the right hand side is a dispersion of gibbsite in an aqueous salt solution (10^{-2} M NaCl) at $\phi = 0.25$. There is a distinct difference in the retardation colors of the samples, in the isotropic phase and even more clearly in the nematic phase. With the retardation plate in the horizontal direction (Figure 2.4(b)) the retardation color of the sample in toluene corresponds to first order orange, implying a subtraction of the optical path difference with roughly 140 nm (see Figure 2.2). On the other hand, the aqueous sample displays a second order blue tint, corresponding to an addition of the optical path difference with about 210 nm. If we rotate the retardation plate to the vertical direction, the retardation colors are reversed and we find +140 nm for the sample in toluene and -210 nm for aqueous gibbsite.

These values of the retardation correspond to a Δn for toluene of $1.4 \cdot 10^{-3}$ and $\Delta n = -2.1 \cdot 10^{-3}$ for aqueous gibbsite. By combining Equation 2.4 and 2.5 in the previous section, we find $\Delta n = 2 \cdot 10^{-3}$ for gibbsite dispersed in toluene, in line with our result. For aqueous gibbsite we find $\Delta n = -8 \cdot 10^{-3}$, which is somewhat lower than the experimental value, but still in reasonable agreement taking into account the approximations with regard to the order parameter and the volume fraction of the nematic phase.

From these results we deduce that for gibbsite dispersed in toluene the birefringence is positive, corresponding to the intrinsic birefringence of the platelets. On the other hand, for aqueous gibbsite, with a much larger difference between the refractive index of particle and solvent, the birefringence is negative, implying that form birefringence is dominant over the intrinsic particle birefringence.

2.5.2. Anchoring at a planar wall and the isotropic-nematic interface

An alternative way to determine the birefringence is to examine the alignment of the nematic phase along the capillary wall and the isotropic-nematic interface. For entropic reasons, colloidal platelets exhibit homeotropic anchoring, which means that they tend to align with the director perpendicular to the isotropic-nematic interface as well as to hard walls [64, 88], as illustrated in Figure 2.5(a).

Figure 2.5(b) shows the alignment near the isotropic-nematic interface and the capillary wall in the suspension in toluene. The bulk nematic phase appears with the same color as the isotropic phase, the typical magenta color of the retardation plate, which implies that it does not exhibit birefringence. Thus the platelets must be oriented with

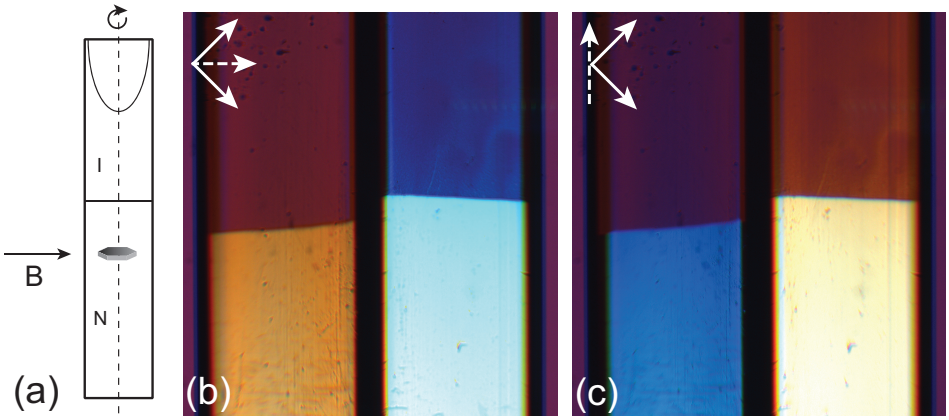

Figure 2.4. (a) Rotation of the sample around its vertical axis in a magnetic field aligns the platelets with the director in the vertical direction. (b-c) Isotropic-nematic phase separated suspension of sterically stabilized gibbsite (left) and charge stabilized gibbsite (right) after one hour rotation in a magnetic field with a strength of 1.8 T. Solid arrows indicate the polarizers, dashed arrow the orientation of the retardation plate. Scale: the capillaries have a width of 2 mm.

their director pointing into the focal plane, indeed homeotropically aligned to the capillary walls. Near the isotropic-nematic interface the nematic phase appears orange, which corresponds to a subtraction of the retardation with respect to the retardation plate (see Figure 2.2). On the other hand, a blue retardation color can be observed near the capillary wall, corresponding to an addition of the optical path difference. From these observations we can again conclude that the slow axis is parallel to the platelet director and that intrinsic birefringence is dominant.

If we now compare this to the aqueous suspension shown in Figure 2.5(c), we observe that the retardation colors are exactly reversed: blue at the isotropic-nematic interface and orange near the capillary wall. This implies that the slow axis is now perpendicular to the platelet director and that form birefringence prevails over the intrinsic birefringence.

The result we obtain here is the same as from the experiment in magnetic field, implying that particle stabilization does not affect the anchoring preference and is indeed a result of the particle shape. This is in contrast to *thermotropic* liquid crystals, where the preferred orientation of the director with respect to the isotropic-nematic interface or a solid wall is dictated by chemical interaction rather than molecular shape [57]. However, the absolute magnitude of the anchoring strength does depend on particle stabilization and solvent, as we will see in Chapter 4.

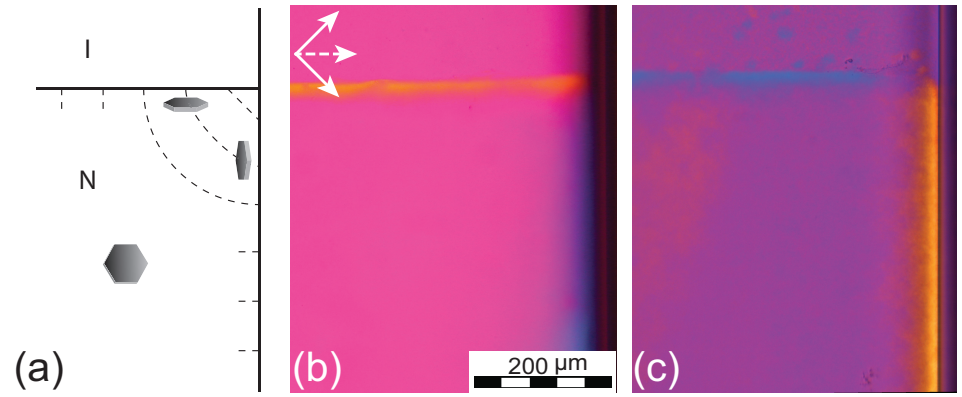

Figure 2.5. Alignment of the nematic phase at the isotropic-nematic interface and the capillary walls; schematically depicted in (a) and observed with polarized light microscopy in a system of gibbsite dispersed (b) in toluene and (c) in water.

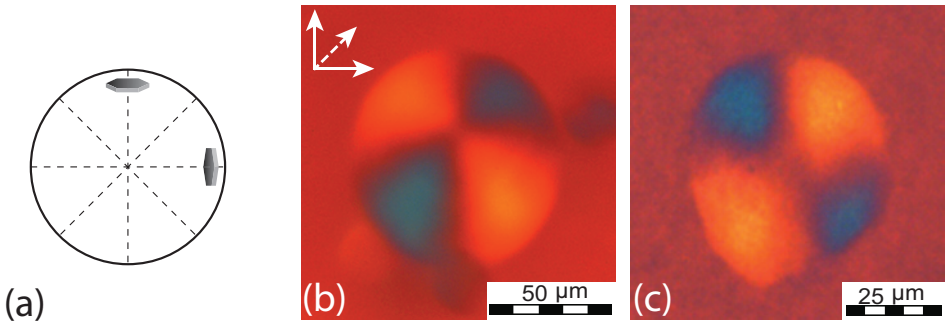

Figure 2.6. Tactoid with radial director field and hedgehog defect; (a) schematically depicted, and observed with polarized light microscopy in a gibbsite suspension (b) in bromotoluene and (c) in water.

2.5.3. Nematic phase confined to droplets

Finally, a third method to study the birefringence of the nematic phase is to investigate the nematic phase confined to micrometer-sized droplets. The properties of such droplets, or tactoids, are determined by a competition between surface anchoring and bulk elastic free energy, the balance of which depends on the droplet size. This will be discussed in detail in Chapter 4. For large tactoid sizes this competition leads to a spherical droplet shape and a radial director field with a point defect in the center, a so-called hedgehog, as depicted schematically in Figure 2.6(a).

Figure 2.6(b) and (c) displays two of such tactoids, one in a suspension in 2-bromotoluene and the other in an aqueous gibbsite suspension. The refractive index of bromotoluene is very close to that of gibbsite ($n = 1.556$ and $n \approx 1.58$ respectively), so that the gibbsite platelets are almost index matched. We observe the characteristic birefringence pattern of a radial tactoid, consisting of four parts with the opposite quarters

the same retardation color. The retardation colors of the tactoids in the two solvents are reversed: the quarters that are blue in the one are yellow/orange in the other and vice versa. This confirms again the inversion of the birefringence observed above, resulting in positive birefringence for gibbsite dispersed in bromotoluene and negative birefringence in aqueous suspensions.

2.6. Conclusions

Polarized light microscopy is a powerful tool to study liquid crystals, even more so if combined with the aligning power of an externally applied magnetic field.

Furthermore, we have demonstrated that it is possible to tune the birefringence of the nematic phase in suspensions of gibbsite platelets by varying the solvent refractive index. In solvents with a refractive index close to that of the gibbsite platelets (toluene and bromotoluene) the positive intrinsic birefringence of the particles determines the birefringence of the nematic phase, whereas in the case of water, where the refractive index is considerably lower, form birefringence prevails over the intrinsic birefringence.

Acknowledgements

Rogier Brand is thanked for his experimental work on the birefringence of gibbsite. We also acknowledge the work of Bonny Kuipers in constructing the polarized light microscope setup in magnetic field. Maurice Mourad is thanked for his help with the PIB coating.

3

Liquid crystal phase transitions in systems of colloidal platelets with bimodal shape distribution

Abstract

We have studied a system of polydisperse, charged colloidal gibbsite platelets with a bimodal distribution in the particle aspect ratio. We observe a density inversion of the coexisting isotropic and nematic phases as well as a three-phase equilibrium involving a lower density nematic phase, an isotropic phase of intermediate density and a higher density columnar phase. To relate these phenomena to the bimodality of the shape distribution, we have calculated the liquid crystal phase behavior of binary mixtures of thick and thin hard platelets for various thickness ratio. The predictions are based on the Onsager-Parsons theory for the isotropic-nematic (I-N) transition combined with a modified Lennard-Jones-Devonshire cell theory for the columnar (C) state. For sufficiently large thickness ratios, the phase diagram features an I-N density inversion and three phase I-N-C equilibrium, in agreement with experiment. The density inversion can be attributed to a marked shape fractionation among the coexisting phases with the thick species accumulating in the isotropic phase. At high concentrations, the theory predicts a coexistence between two columnar phases with distinctly different concentrations. In experiment, however, the demixing transition is pre-empted by a transition to a kinetically arrested, glassy state with structural features resembling a columnar phase.

3.1. Introduction

The phase behavior of bidisperse colloidal systems incorporates many intriguing phenomena such as the formation of stable superstructures and phase equilibria involving multiple phases. For example, mixtures of spheres with a diameter ratio of around 0.5 are known to form AB_2 and AB_{13} binary crystals, as first observed in natural opals [89, 90] and reproduced in suspensions of latex particles [91, 92] and colloidal hard spheres [93–95]. Mixtures of long and short rod-like colloids show a demixing of the nematic phase which leads to a coexistence of two nematic phases with different compositions including a triphasic isotropic-nematic-nematic equilibrium, as observed experimentally [96, 97] and confirmed by theory [98]. A similar behavior has been observed recently in binary mixtures of thin and thick hard rods with equal length [99], as originally predicted with an Onsager-Parsons description [100].

In contrast to rods, the phase behavior of plate-shaped colloids has only been explored over the last decade [31–33, 35, 38, 101]. A remarkably feature of some of these systems is that the formation of a partially crystalline columnar phase is not suppressed by the considerable spread in particle size [33], as is the case with crystalline and smectic order in polydisperse systems of spheres [102] and rods [103]. Moreover, a large spread in the plate thickness may give rise to a so-called isotropic-nematic *density inversion*, in which the isotropic phase becomes denser than the coexisting nematic. This phenomenon originates from a pronounced fractionation in the thickness of the particles amongst the coexisting phases with the thick species accumulating in the isotropic and the thin ones in the nematic phase. Although the nematic phase has a higher particle concentration than the isotropic, its mass density falls below that of the isotropic phase due to a high fraction of thin platelets with a lower particle mass. This phenomenon has been observed in a polydisperse system of *sterically* stabilized gibbsite platelets [104] and analyzed by a simple theory based on Onsager's second virial theory extended to binary mixtures [105]. A similar density inversion can be predicted from fundamental measure theory based on the Zwanzig model for binary hard platelets [106].

In this chapter we report our findings on a system of *charged* gibbsite platelets, which forms a remarkable three-phase equilibrium, involving a low-density nematic phase, an isotropic phase of intermediate density and a dense columnar phase. A size analysis using atomic force microscopy (AFM) reveals that the distribution of the aspect ratio, defined as the plate thickness-to-diameter ratio, is characterized by a distinct bimodal shape. In an analogous fashion to the sterically stabilized system [104], the charged plate system exhibits a density inversion of the isotropic and nematic phases induced by a strong fractionation effect with respect to aspect ratio. The fractionation scenario is corroborated by the size distributions measured in the coexisting phases, which

demonstrate that the isotropic phase is rich in thick platelets, while the corresponding nematic phase consists mainly of thin platelets corresponding to a small aspect ratio.

A theoretical underpinning of the observed effects is provided by calculating the phase diagram of a binary mixture of thin and thick platelets for various thickness ratio. This is done by combining the Onsager-Parsons theory for the isotropic to nematic transition with a modified Lennard-Jones-Devonshire cell theory for the columnar state [107]. For a sufficiently large ratio of the particle thickness, the I-N density inversion and three phase isotropic-nematic-columnar coexistence can both be satisfactorily reproduced. Moreover, at high particle concentrations, our theory predicts a demixing of the columnar phase into a fraction containing predominantly thin species and a 'mixed' fraction with equal portions of thin and thick platelets. This demixing could not be observed in the experimental system, due to the formation of a dynamically arrested glassy state at high particle concentrations.

3.2. Materials and Methods

Gibbsite platelets were synthesized by hydrothermal treatment of aluminium alkoxides as described in Chapter 2, including surface treatment with aluminium chlorohydrate to increase particle stability.

The gibbsite platelets were analyzed with transmission electron microscopy (TEM) using a Tecnai 10 microscope (FEI Company), and atomic force microscopy (AFM) utilizing a multimode scanning probe microscope (Digital Instruments). AFM measurements were performed in tapping mode with a standard TESP silicon tip. Samples were prepared by dilution of the gibbsite dispersion with a 1:1 water-ethanol mixture. The diluted suspension was subsequently spread onto carbon-coated copper grids (TEM measurements) or freshly cleaved mica (AFM measurements). To obtain the distributions of the particle dimensions, the diameter, thickness and aspect ratio of 200 to 270 particles were measured.

The gibbsite platelets had a well-defined hexagonal shape (see the micrographs in Figure 3.1(a) and (b)), with an average diameter (that is: corner-to-corner distance) of 207 nm with a standard deviation in the average σ_D of 35% and an average thickness of 8.2 nm with a σ_L of 46%. The diameter of the platelets had a rather broad, symmetrical distribution, while the thickness was strongly peaked with a long tail towards the thicker particles (see Figure 3.1(c)). The aspect ratio, however, was bimodal, with a relatively narrow distribution of thick species and a much wider spread of thin ones.

The gibbsite dispersion was concentrated via centrifugation and redispersion with 10^{-2} M NaCl to the concentration where phase separation was just hindered by kinetic arrest. Samples of decreasing concentration were prepared upon dilution and stored in 50 $\times$ 4 $\times$ 0.2 mm sized glass capillaries (VitroCom), which were flame-sealed and

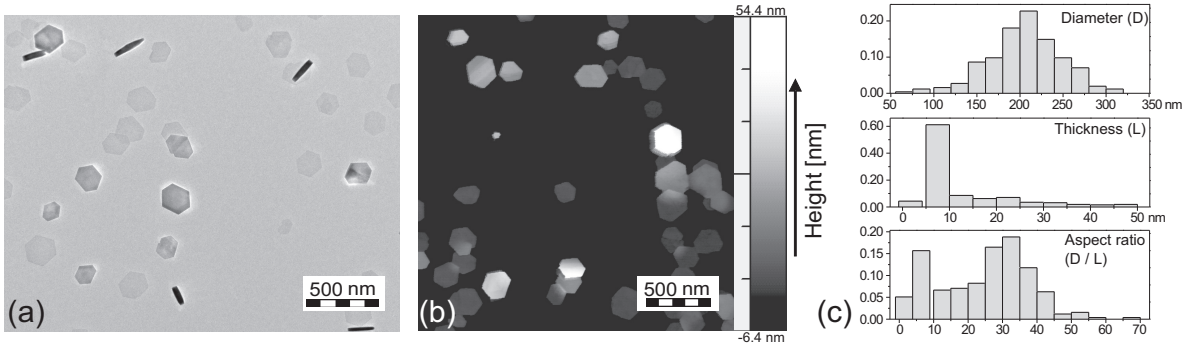

Figure 3.1. (a) Transmission electron micrograph and (b) Atomic force micrograph of the gibbsite platelets. (c) Histograms of the diameter, thickness, and inverse aspect ratio D/L of the platelets, determined with atomic force microscopy.

subsequently glued to avoid evaporation of the solvent. The suspensions were left in upright position to phase separate and equilibrate at room temperature for two weeks.

The phase behavior of the system was studied on a macroscopic scale with a home-built polarization setup, consisting of two crossed polarizing filters that could be illuminated by a 150 W lamp in combination with a condenser lens and a ground glass diffuser for homogeneous illumination. The samples were photographed with a Nikon Coolpix 995 digital camera. The samples were examined in more detail with polarized light microscopy as described in Chapter 2. Bragg reflections were observed with the polarizing microscope while the sample was illuminated with a cold light source (Dolan Jenner, Model 190).

3.3. Phase behavior experiments

In Figure 3.2(a) we show a concentration series of the charge stabilized gibbsite platelets. Upon increasing the particle concentration, the system enters the isotropic-nematic biphasic regime, with a nematic phase at the bottom and an isotropic phase at the top of the capillary, separated by a sharp interface. Further increasing the particle concentration leads to the onset of a density inversion, where the isotropic starts to become denser than the nematic phase. Around the inversion point, the I-N interface shows a regular pattern of fingers reminiscent of a Rayleigh-Taylor instability (see the second capillary of Figure 3.2(a) and an enlarged view in (b)) [108]. At higher concentrations the inverted state is reached with a nematic top and an isotropic bottom phase, separated by a sharp interface. Upon subsequent densification, the system enters a triphasic region, where the isotropic phase is located between a nematic upper phase and a columnar bottom phase, all separated by sharp interfaces. The columnar bottom phase is also characterized by bright Bragg reflections (see Figure 3.2(c)), which originate from the two dimensional hexagonal arrangement of the columnar stacks of

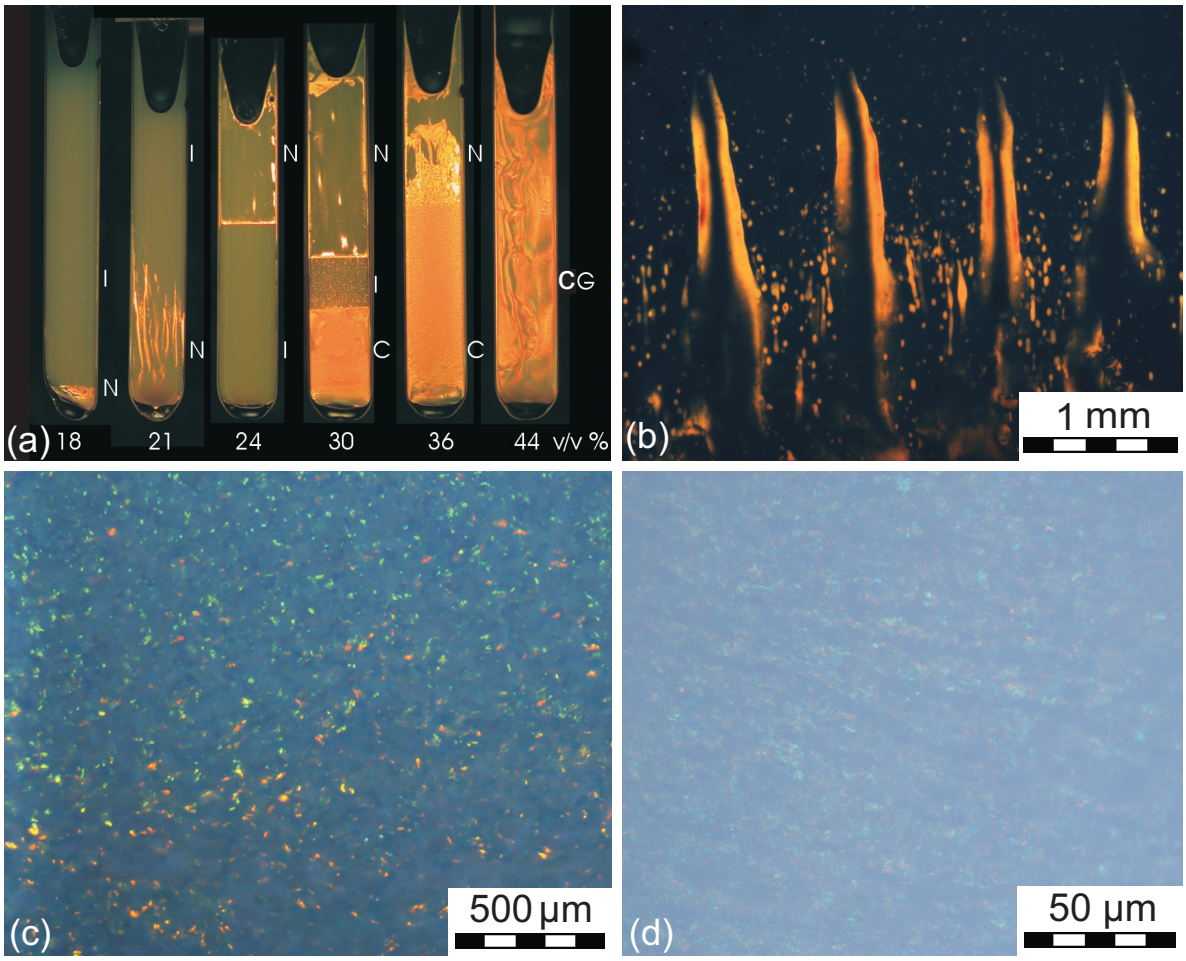

Figure 3.2. (a) Concentration series of suspensions of charged gibbsite platelets. A sequence of phase equilibria is observed, ranging from biphasic isotropic-nematic (I-N), inverted biphasic isotropic-nematic (I-N), triphasic isotropic-nematic-columnar (I-N-C), biphasic nematic-columnar (N-C) to a columnar glass (CG). (b) Regular fingering pattern in an isotropic-nematic sample at a density of 20 v/v %, close to the inversion point. (c) Bragg reflections in the columnar phase, and (d) dynamically arrested columnar glass.

platelets. The color associated with the Bragg reflections ranges from green to red, which corresponds to an average inter-columnar distance of about $\sim$ 250 nm. When the particle concentration is further increased, the isotropic phase disappears, leaving an upper nematic phase in coexistence with a lower columnar phase. Finally, at very high concentrations, an arrested state is reached which no longer undergoes macroscopic phase separation. Birefringent patterns are clearly visible and persist over a long time. These correspond to 'frozen-in' regions of particle alignment caused by the shear forces during the filling of the capillary. After a period of three months, the sample also shows Bragg reflections originating from tiny grains with a domain size of about 2 - 5 µm, as

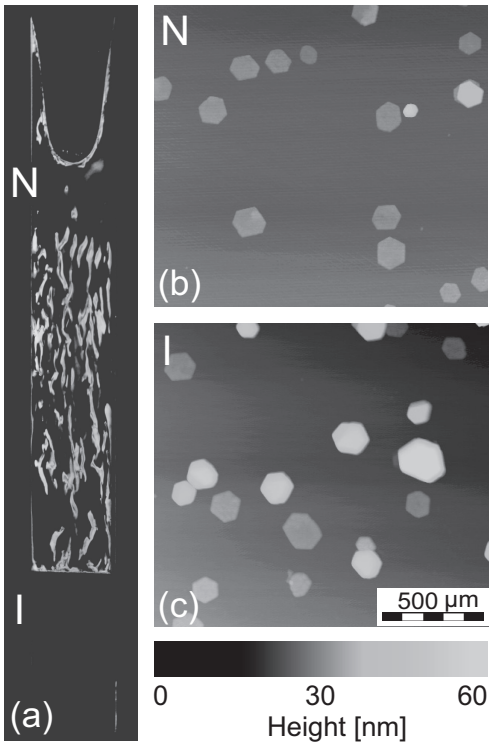

Figure 3.3. (a) Image of a Gibbsite suspension with isotropic-nematic density inversion, taken between crossed polarizers. AFM images of gibbsite platelets sampled from the nematic (b) and isotropic phase (c).

depicted in Figure 3.2(d). This indicates local nucleation of the hexagonal columnar phase. We will further discuss this interesting observation in Chapter 10.

The capillary containing the inverted isotropic-nematic phase equilibrium was further investigated by splitting the capillary and analyzing the two coexisting phases separately with AFM. In Figure 3.3 we depict the sample between crossed polarizers together with AFM images of the gibbsite platelets in both phases. The measured diameter, thickness and (inverse) aspect ratio distributions of the platelets in the isotropic and nematic phase are presented in Figure 3.4. Although the diameter distribution is virtually the same in both phases, the thickness distributions are significantly different, with the isotropic phase markedly enriched in thick platelets. The most distinct difference can be inferred from the histograms showing the (inverse) aspect ratio distribution in both phases. From this it is evident that the nematic phase is characterized by a unimodal distribution of thin platelets (large D/L), whereas the isotropic phase possesses a bimodal shape distribution with a significant fraction of thick species (small D/L).

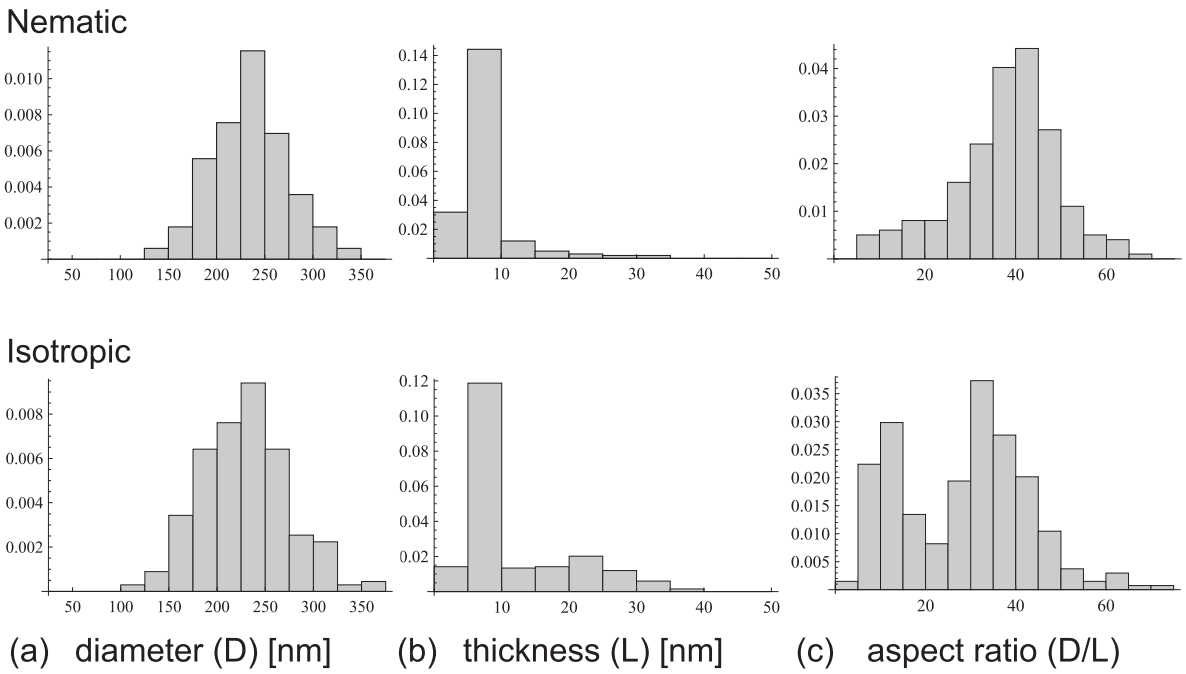

Figure 3.4. Histograms of the platelet diameter (a), thickness (b) and aspect ratio (c) sampled from the nematic and isotropic phase of a sample with isotropic-nematic density inversion (see Figure 3.3), determined with AFM.

3.4. Onsager-Parsons theory for the isotropic-nematic transition

A simple theory is now employed to describe the main features of the experimental system. For the present system of charged platelets, a theory would be required based on a hard-core model supplemented with a suitable electrostatic potential. Unfortunately, the effective (screened) pair potential between two uniformly charged platelets resulting from the Poisson-Boltzmann theory is not known in analytical form [109] and multipole expansions - aimed at providing an analytical approximation valid at large plate separations - are questionable at high particle densities (in particular in the nematic and columnar phases). Headway can be made by restricting the plate orientations to the three Cartesian axes. Within the so-called Zwanzig approximation, a tractable density functional theory can be formulated which allows one to scrutinize the effect of charge on the structure and phase behavior of colloidal platelets [110]. Alternatively, interaction site models, based on a discretization of the surface charge into Yukawa sites compacted onto a circular disk-shaped array, can be analyzed with integral equation theory to elucidate the pair correlation functions of charged platelets at low to moderate densities [111].

The scope of this chapter is to keep the theory as tractable as possible while maintaining the essential physics of the problem. Therefore, we will build on the simple but

physically plausible idea that the main effect of the double layers is to alter the effective shape of the platelets, such that the effective thickness by which the platelets interact is enhanced. The use of an effective hard particle is merited by the fact that the electric double layers surrounding the platelets are rather tight [1].

Let us consider a binary mixture of $N = N_1 + N_2$ hard cylinders with two different lengths, L_1 and L_2, and common diameter $D = D_1 = D_2$ in a macroscopic volume V. For the plate-like cylinders we consider here, the aspect ratio L_i/D $(i = 1, 2)$ is much smaller than unity. Henceforth, we shall assign the label '2' to the thickest particles. The overall concentration of the system is expressed in dimensionless form via $c = ND^3/V$. Following [105], the Onsager-Parsons Helmholtz free energy of such a mixture at a given c and mole fraction $x_i = N_i/N$ is given by:

$$\begin{aligned}\frac{\beta F}{N} &= (\ln \tilde{\mathcal{V}} c - 1) + \sum_{i=1,2} x_i \{\ln x_i + \langle \ln 4\pi f_i \rangle_i\} \\ &\quad + \frac{cG_P(\phi)}{2} \sum_i \sum_j x_i x_j \langle\langle \tilde{V}_{\rm excl}^{ij}(\gamma) \rangle\rangle_{ij} \end{aligned} \tag{3.1}$$

where $\beta^{-1} = k_B T$ is the thermal energy and $\tilde{\mathcal{V}} = \prod_i \mathcal{V}_i^{x_i}/D^3$ with $\mathcal{V}_i$ the thermal volume of species i (including rotational contributions). The brackets $\langle(\cdot)\rangle_i = \int d\Omega f_i(\Omega)(\cdot)$ denote an orientational average according to some unknown orientational distribution function f_i, normalized via $\int d\Omega f_i(\Omega) = 1$. Several entropic contributions can be distinguished in Eq. (3.1). The first three are *exact* and denote the ideal translational, mixing, and orientational entropy, respectively. The last term represents the excess translational or packing entropy which accounts for the particle-particle interactions at the approximate level of pair-interactions. The key quantity here is the excluded volume $V_{\rm excl}^{ij}$ between two plate-like cylinders of type i and j at fixed interparticle angle γ [7]:

$$\begin{aligned}\tilde{V}_{\rm excl}^{ij}(\gamma) &= \frac{V_{\rm excl}^{ij}(\gamma)}{D^3} = \frac{\pi}{2}|\sin\gamma| + \left(\frac{L_i}{D} + \frac{L_j}{D}\right) \\ &\quad \times \left(\frac{\pi}{4} + E(\sin\gamma) + \frac{\pi}{4}\cos\gamma\right) + 2\frac{L_i L_j}{D^2}|\sin\gamma| \end{aligned} \tag{3.2}$$

with $E(x)$ the complete elliptic integral of the second kind. Although the structure of Eq. (3.1) is similar to the classic Onsager second-virial free energy, higher order virial terms are incorporated approximately through a density rescaling according to Parsons' recipe [112–114] as extended to mixtures (see [115] for a recent review of the use of the Onsager-Parsons free energy to describe mixtures of hard particles). This involves a rescaled density cG_P where the factor $G_P = (1 - 3\phi/4)/(1 - \phi)^2$ depends on the total plate volume fraction $\phi = c\sum_i x_i(\pi L_i/4D)$. Note that G_P approaches unity in the

[1] The Debye screening length in a 10^{-2} M sodium chloride solution is 3 nm.

low-density limit $\phi \to 0$ in which case the original second-virial theory is recovered, as required.

One must then specify the orientational averaging. By definition, all orientations are equally probable in the isotropic (I) phase and $f_i = 1/4\pi$. The orientational contributions then simply become

$$\langle \ln 4\pi f_i \rangle_i \equiv 0, \qquad \text{(I)} \tag{3.3}$$

Using the isotropic averages $\langle\langle \sin\gamma \rangle\rangle = \pi/4$, $\langle\langle E(\sin\gamma)\rangle\rangle = \pi^2/8$ and $\langle\langle \cos\gamma\rangle\rangle = 1/2$ we obtain for the excluded volume contribution:

$$\langle\langle \tilde{V}^{ij}_{\text{excl}}(\gamma)\rangle\rangle = \frac{\pi^2}{8} + \left(\frac{L_i}{D} + \frac{L_j}{D}\right)\left(\frac{3\pi}{8} + \frac{\pi^2}{8}\right) + \frac{L_i L_j}{D^2}\frac{\pi}{2} \tag{3.4}$$

In the nematic (N) phase, the particles are expected to be oriented along a common nematic director. For strongly ordered states it is expedient to adopt a Gaussian trial function to describe the orientational probability density [116]. For a uniaxial nematic phase, the Gaussian trial function takes on the following form:

$$f_i(\theta) \equiv \begin{cases} \frac{\alpha_i}{4\pi}\exp[-\frac{1}{2}\alpha_i\theta^2] & \text{if} \quad 0 \le \theta \le \frac{\pi}{2} \\ \\ \frac{\alpha_i}{4\pi}\exp[-\frac{1}{2}\alpha_i(\pi-\theta)^2] & \text{if} \quad \frac{\pi}{2} \le \theta \le \pi \end{cases} \tag{3.5}$$

with θ the polar angle between the plate normal and the nematic director and $\alpha_i \gg 1$ a variational parameter. With the use of the Gaussian trial function, the orientational averages in the free energy can be rendered analytically tractable by performing asymptotic expansions for large α_i and retaining the leading order terms. The result for the orientational entropy is

$$\langle \ln 4\pi f_i \rangle_i \sim \ln \alpha_i - 1 \qquad \text{(N)} \tag{3.6}$$

For small angles γ the orientationally averaged excluded volume can be expanded as follows:

$$\begin{aligned} \langle\langle \tilde{V}^{ij}_{\text{excl}}(\gamma)\rangle\rangle_{ij} \;&=\; \pi\left(\frac{L_i}{D} + \frac{L_j}{D}\right) + \left(\frac{\pi}{2} + \frac{2L_iL_j}{D^2}\right)\langle\langle\gamma\rangle\rangle_{ij} \\ &\quad + \mathcal{O}\langle\langle\gamma^2\rangle\rangle_{ij} \end{aligned} \tag{3.7}$$

Within the Gaussian approximation the double orientational average of γ is given by [117]

$$\langle\langle\gamma\rangle\rangle_{ij} \sim \left(\frac{\pi}{2}\right)^{1/2}\left(\frac{1}{\alpha_i} + \frac{1}{\alpha_j}\right)^{1/2} \tag{3.8}$$

up to leading order in α_i, while $\langle\langle\gamma^2\rangle\rangle_{ij} \sim \mathcal{O}(\alpha^{-1}_{i/j})$ generates the next-leading order terms which we will neglect here. If we further assume the plate aspect ratio to be sufficiently small so that all contributions of order L_iL_j/D^2 are of negligible importance,

the resulting double orientationally averaged excluded volume in the nematic phase can be approximated as:

$$\langle\langle \tilde{V}_{\rm excl}^{ij}(\gamma)\rangle\rangle_{ij} \sim \pi\left(\frac{L_i}{D}+\frac{L_j}{D}\right)+\left(\frac{\pi}{2}\right)^{3/2}\left(\frac{1}{\alpha_i}+\frac{1}{\alpha_j}\right)^{1/2} \tag{3.9}$$

which has the important advantage that the Gaussian variational parameters are now fully *decoupled* from the thickness. Inserting this result together with Eq. (3.6) into the free energy and minimizing with respect to α_i yields a simple quadratic concentration dependence for the equilibrium value of α_i:

$$\alpha_i \sim \frac{4}{\pi}(cG_P)^2, \qquad i=1,2 \tag{3.10}$$

which is the same result as for the monodisperse case [118]. Since there are no explicit minimization equations for α_i to be solved, the nematic free energy for the mixtures is entirely algebraic. Phase equilibria between isotropic and nematic states are found in the usual numerical way by imposing equality of chemical potentials μ_i of each component i and pressure P. These quantities are obtained from the free energy using the standard thermodynamic derivatives, $P=-(\partial F/\partial V)_{NVT}$ and $\mu_i=(\partial F/\partial N_i)_{N_jVT}$.

3.5. Cell theory for the columnar phase

To describe the thermodynamical properties of a columnar phase we use an extended cell theory as proposed in [107]. In this approach, the structure of a columnar phase is envisioned in terms of columns ordered along a perfect lattice in two lateral dimensions with a strictly one-dimensional fluid behavior of the constituents in the remaining direction along the columns. As for the latter, the canonical partition function of a binary mixture of *parallel* platelets with thicknesses L_1 and L_2 (and equal diameter D) with their centre-of-mass moving along the plate normal on a line of length ℓ is formally given by:

$$Q_{\rm fluid}(N_1,N_2,\ell,T)=\frac{\left[\ell-(N_1L_1+N_2L_2)\right]^N}{\Lambda_1^{N_1}\Lambda_2^{N_2}N_1!N_2!} \tag{3.11}$$

with Λ_i the thermal de Broglie wavelength of the respective particle species. Next, we allow the platelets to rotate slightly about their centre-of-mass. At high packing fractions, the rotational freedom of each platelet is assumed to be asymptotically small and the configurational integral above may be approximated as follows

$$\begin{aligned} Q_{\rm fluid}(N_1,N_2,\ell,T) &\approx \frac{Q_1^{\rm or}Q_2^{\rm or}}{(\mathcal{V}_1^1)^{N_1}(\mathcal{V}_2^1)^{N_2}N_1!N_2!} \\ &\times \left[\ell-\left(N_1\langle L_1^{\rm eff}\rangle_1+N_2\langle L_2^{\rm eff}\rangle_2\right)\right]^N \end{aligned} \tag{3.12}$$

where $\mathcal{V}_i^1$ represents the 1D thermal volume of species i including contributions arising from the (3D) rotational momenta of the platelet. Furthermore, $Q_i^{\rm or}=\exp[-N_i\langle\ln 4\pi f_i\rangle_i]$ is an orientational partition function depending on the orientational probability density

distribution f_i of platelets of type i. In the *mean-field* description implied by Eq. (3.12) there is no coupling between the orientational degrees of freedom of the platelets. The rotation of the platelets becomes manifest in an *effective entropic thickness*, defined as

$$\langle L_i^{\rm eff}\rangle_i = L_i \left\{ 1 + \frac{1}{2}\frac{D}{L_i}\int d(\cos\theta)|\theta| f_i(\theta) + \cdots \right\} \tag{3.13}$$

up to leading order in the polar angle θ which describes the deviation of the plate normal from the direction of the column. The prefactor of '1/2' in Eq. (3.13) has been included to correct in part for the azimuthal rotational freedom and captures the effect that the excluded length between two platelets at fixed polar angles becomes minimal when the azimuthal orientations are the same. The free energy of the 1D fluid then follows from $\beta F = -\ln Q$:

$$\begin{aligned} \frac{\beta F_{\rm fluid}}{N} &\sim (\ln \tilde{\mathcal{V}}\rho_0 - 1) + \sum_{i=1,2} x_i \left\{ \ln x_i + \langle \ln 4\pi f_i\rangle_i \right\} \\ &\quad - \ln\left[1 - \rho_0 \sum_i x_i q_i \langle \tilde{L}_i^{\rm eff}\rangle_i \right] \end{aligned} \tag{3.14}$$

where $\tilde{\mathcal{V}}^1 = \prod_i (\mathcal{V}^1)^{x_i}/L_0$. Furthermore, $\rho_0 = NL_0/\ell$ (with L_0 some reference thickness), $q_i = L_i/L_0$ and $\tilde{L}_i^{\rm eff} = L_i^{\rm eff}/L_i$. The equilibrium forms for the distributions $f_i(\theta)$ are found by a formal minimization of the free energy while constraining them to be normalized. The corresponding stationarity condition is

$$\frac{\delta}{\delta f_i}\left(\frac{\beta F_{\rm fluid}}{N} - \lambda_i \int d(\cos\theta) f_i(\theta) \right) = 0 \tag{3.15}$$

with λ_i a Lagrange multiplier. The solutions can be obtained in closed form and turn out to be of simple exponential form:

$$f_i(\theta) = \frac{\xi_i^2}{4\pi}\exp[-\xi_i|\theta|] \tag{3.16}$$

with

$$\xi_i = \left(\frac{3}{2}\frac{D}{L_i}\right)\frac{\rho_0 q_i}{1 - \rho_0(x_1 q_1 + x_2 q_2)} \tag{3.17}$$

The orientational averaging is now easily carried out and the expressions for the orientational entropy and entropic thickness are given by

$$\begin{aligned} \langle \ln 4\pi f_i\rangle_i &= 2\ln\xi_i - 2 \\ \langle \tilde{L}_i^{\rm eff}\rangle_i &= 1 + \left(\frac{D}{L_i}\right)\frac{1}{\xi_i} \end{aligned} \tag{3.18}$$

We now turn to the free energy associated with the positional order along the lateral directions of the columnar liquid crystal. A formal way to proceed is to map the system onto an ensemble of N disks ordered on a 2D lattice. Near close packing, the

configurational integral of the system is well approximated by the Lennard-Jones and Devonshire cell model [119, 120] so that we may write

$$\begin{aligned} Q_{\text{cell}}(N) &= \Lambda^{-2N} \int d\mathbf{r}^N \exp[-\beta U(\mathbf{r}^N)] \\ &\approx \left(\Lambda^{-2} \int d^2\mathbf{r} \exp\left[-\frac{\beta}{2} u_{\text{cell}}^{\text{nn}}(\mathbf{r}) \right] \right)^N \end{aligned} \tag{3.19}$$

and recall that $N = N_1 + N_2$. Within the framework of the cell model, particles are considered to be localized in 'cells' centred on the sites of a fully occupied lattice (of some prescribed symmetry). Each particle experiences a potential energy $u_{\text{cell}}^{\text{nn}}(\mathbf{r})$ generated by its nearest neighbors. In the simplest version, the theory presupposes that each cell contains one particle moving *independently* from its neighbors. For hard interactions, the second phase space integral is simply the cell *free area* available to each particle. If we assume the nearest neighbors to form a perfect hexagonal cage, the free area is given by $A_{\text{free}} = \sqrt{3}(\Delta_c - D)^2/2$ with Δ_c the nearest neighbor distance. The configurational integral then becomes

$$Q_{\text{cell}}(N) \approx \left(\Lambda^{-2} A_{\text{free}} \right)^N \sim \left(1 - \bar{\Delta}_c^{-1} \right)^{2N}, \tag{3.20}$$

in terms of the dimensionless lateral spacing $\bar{\Delta}_c = \Delta_c/D$. Applying the condition of single-occupancy (i.e., one array of platelets per column) we can use $\bar{\Delta}_c$ to relate the *overall* particle volume fraction $\phi_0 = (\pi/4)NL_0D^2/V$ to the overall linear density ρ_0 via

$$\phi_0^* \bar{\Delta}_c^2 = \rho_0 \tag{3.21}$$

where $\phi_0^* = \phi_0/\phi_{\text{cp}}$ is a reduced variable in terms of $\phi_{\text{cp}} = \pi/(2\sqrt{3}) \approx 0.907$ the volume fraction at close packing. The total free energy of the columnar state is now obtained by combining the fluid and cell contributions

$$\frac{\beta F}{N} \sim (\ln \tilde{\mathcal{V}} c - 1) + \sum_i x_i \left\{ \ln x_i + 2 \ln \left(\frac{3}{2} \frac{D}{L_i} \frac{\phi_0^* q_i}{\bar{\Delta}_c^{-2} - \phi^*} \right) \right\} - \ln \left(\frac{1 - \phi^* \bar{\Delta}_c^2}{3} \right) - 2 \ln(1 - \bar{\Delta}_c^{-1}) \tag{3.22}$$

with $\tilde{\mathcal{V}}$ the 3D thermal volume [cf. Eq. (3.1)] and

$$\phi^* = \phi_0^*(x_1 q_1 + x_2 q_2) \tag{3.23}$$

is the *total* reduced packing fraction of the system. The final step is to minimize the total free energy with respect to $\bar{\Delta}_c$. The stationarity condition $\partial F/\partial \bar{\Delta}_c = 0$ yields a third-order polynomial whose physical solution reads:

$$\bar{\Delta}_c = \frac{-3^{1/3} 4\phi^* + 2^{1/3} K^{2/3}}{6^{2/3} \phi^* K^{1/3}} \tag{3.24}$$

with

$$K = 27(\phi^*)^2 + [3(\phi^*)^3(32 + 243\phi^*)]^{1/2} \tag{3.25}$$

which is the same result as one would get for the monodisperse case since the lateral spacing does not depend explicitly on the composition of the mixture (but only implicitly via Eq. (3.23)). A more manageable expression for $\bar{\Delta}_c$ can be obtained by performing a Taylor expansion around the close packing limit, using $(1-\phi^*)$ as a smallness parameter:

$$\bar{\Delta}_c = 1 + \frac{1}{5}(1-\phi^*) + \frac{12}{125}(1-\phi^*)^2 + \frac{178}{3125}(1-\phi^*)^3 + \cdots \tag{3.26}$$

This cubic expression provides and excellent description of the exact result with a discrepancy of less than 0.1 % throughout the entire range of relevant densities ($0.5 < \phi^* < 1$). As in the case of Onsager-Parsons free energy of the nematic state, our treatment is entirely algebraic and no explicit minimization conditions need to be solved numerically along with the coexistence conditions. The latter can be established in the usual way from the pressure and chemical potentials associated with Eq. (3.22).

We now have all the ingredients needed for the calculation of the phase diagram, which are constructed for mixtures of platelets with distinctly different anisotropies. More precisely, we will consider binary systems consisting of thin platelets (which exhibit the full isotropic-nematic-columnar ($\mathrm{I}-\mathrm{N}-\mathrm{C}$) phase sequence in its pure state), mixed with thick ones (which only have an isotropic-columnar ($\mathrm{I}-\mathrm{C}$) transition) [2]. To best match the experimental systems we shall fix the aspect ratio of the thick species to $D/L = 5$ and vary that of the thin species within the interval $10 < D/L < 15$. Taking into account the electrostatic screening effect induced by the electric double layers, these numbers provide reasonable estimates for the *effective* aspect ratios associated with the two peaks in the histograms of the "real" aspect ratio of the system shown in Figure 3.1(c).

3.6. Results and discussion

With the theoretical approach described in the previous sections, the phase behavior of the polydisperse charged plate system can be reproduced qualitatively. Representative examples of the theoretical predictions of the phase diagram are shown in Figure 3.5 and Figure 3.6. In both cases there is a marked triple $\mathrm{I}-\mathrm{N}-\mathrm{C}$ equilibrium extending over a considerable range of overall compositions. Since the relative proportion of thick and thin platelets is fixed in the experimental system, we can draw a dilution line in Figure 3.5 which samples a sequence of phase equilibria observed in the experiments. These range from a biphasic isotropic-nematic, through a triphasic isotropic-nematic-columnar, to a nematic-columnar biphasic equilibrium found at high concentrations.

A density inversion occurs upon traversing the isotropic-nematic coexistence region, as illustrated in Figure 3.7. As alluded to earlier, this observation stems from the

[2] The quantitative merits of the present theory can be tested against computer simulation results for a *monodisperse* system of platelets. This will be the subject of a forthcoming publication.

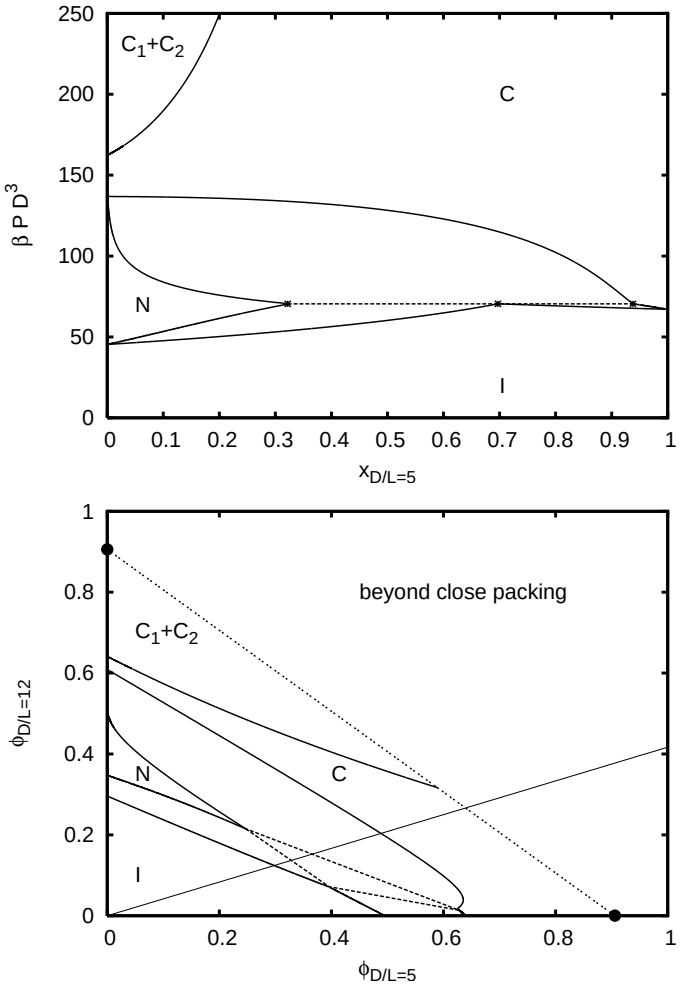

FIGURE 3.5. Phase diagram of a binary mixture of platelets with $D/L_1 = 12$ and $D/L_2 = 5$ ($L_2/L_1 = 2.4$) in the pressure-composition plane (top) and the density-density plane (bottom). Triphasic equilibria are indicated by dashed lines which form a triangle in the density-density representation. The thin continuous line running from the origin represents an equimolar dilution line ($x_1 = x_2 = 0.5$). The line connecting filled circles denotes the bound of the unphysical region beyond close packing.

pronounced fractionation amongst the coexisting phases with a high proportion of thin species concentrated in the nematic phase [105]. This behavior becomes manifest in the pressure-composition representations of the phase diagram where the mole fraction of thick species is systematically larger in the isotropic phase, in agreement with the histograms depicted in Figure 3.4. We note that, experimentally, the density inversion appears to be driven by a fractionation in shape (i.e., aspect ratio) rather than the plate thickness alone.

In the region of the density inversion, the interface shows a regular pattern of fingers with a spacing of about 1 mm. Such a pattern is reminiscent of the Rayleigh-Taylor

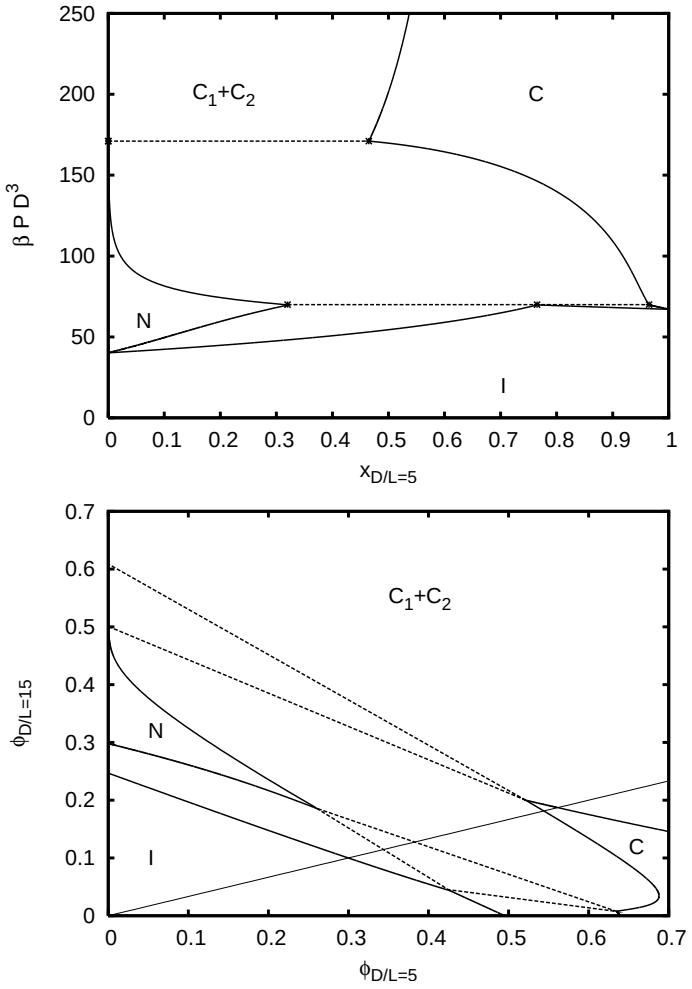

FIGURE 3.6. As Figure 3.5 for the binary mixture with $D/L_1 = 15$ and $D/L_2 = 5$ ($L_2/L_1 = 3$).

instability [4, 108], which occurs when the density in the upper phase is higher than in the lower phase. Since the density difference between both phases is very small near the inversion point, small density gradients induced by gravity may already give rise to such an instability. The observation of a pattern with a wavelength of about 1 mm is in agreement with the fact that the wavelength of the fastest growing mode should be larger than the critical wavelength. The latter is given by $2\pi\sqrt{\gamma/\Delta\rho g}$ with γ the interfacial tension, $\Delta\rho$ the density difference, and g the gravitational acceleration [4]. Guided by the work on sterically stabilized systems the interfacial tension is estimated to be of order $\gamma = 10^{-7}$ to 10^{-8} N/m. This is in line with theoretical predictions for the interfacial tension of charged platelets based on the approximate Zwanzig model [110]. If we further estimate a density difference $\Delta\rho$ of about 0.1 % the critical wavelength is found to be indeed less than 1 mm.

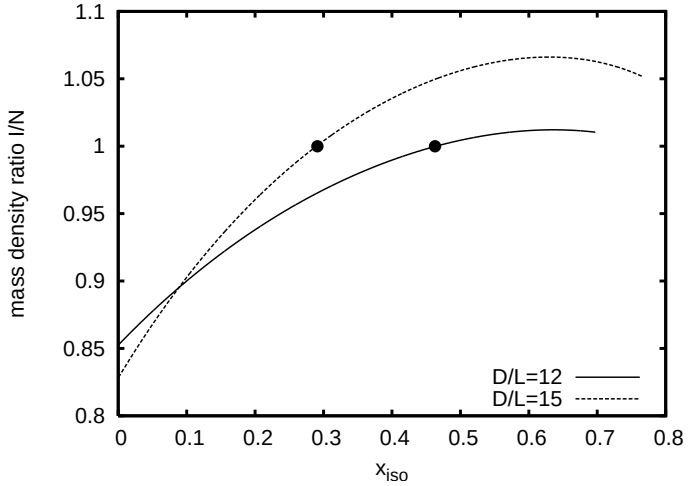

FIGURE 3.7. Mass density ratio $\sum_i x_i^{(I)}\phi_i^{(I)} / \sum_i x_i^{(N)}\phi_i^{(N)}$ of the isotropic phase relative to the coexisting nematic phase as a function of the composition of the isotropic $x_{iso} = x_2^{(I)}$. The filled circles indicate the inversion point of equal mass density. Ratios larger than unity correspond to the inverted state where the isotropic phase is denser than the coexisting nematic.

The fact that the formation of a columnar phase is not impeded by the considerable size polydispersity (particularly in the particle diameter) stands in contrast with the earlier studied sterically-stabilized gibbsite system with similar polydispersity, where density inversion was observed, but no columnar phase could be found, even at very high particle concentrations [104]. A possible explanation could lie in the electric double layers surrounding the platelets. Due to electrostatic screening, both the plate diameter and thickness attain an effective value which is roughly equivalent to the bare value plus the Debye screening length. Consequently, the *effective* aspect ratio the platelets 'feel' in solution is larger than the bare one, which may facilitate the formation of the columnar phase.

A remarkable feature of the theoretical phase diagram is that a demixing of the columnar phase is predicted if the overall concentration exceeds a certain value. At sufficiently high pressures, the columnar phase phase separates into an essentially pure fraction C_1 of thin platelets ($x_2 = 0$), and a bidisperse fraction C_2, both with a different overall packing fraction and associated inter-columnar spacing. The C_1 branch of the binodal is located on the vertical axis and meets the other branch at a critical point located at $x_2 \sim 0$. A detailed inspection of the free energy reveals that the same demixing scenario occurs at smaller thickness ratios with the critical pressure increasing rapidly for smaller ratios. If the thickness ratio is increased, the critical pressure shifts to lower values until the C_1-C_2 region eventually meets the $N - C$ region at a triple pressure. At this point a $N - C_1 - C_2$ triple equilibrium occurs which is seen to span a

wide composition range (see Figure 3.6). The coexistence of two columnar phases could not be realized experimentally presumably because the demixing process is suppressed by the glassy dynamics prevalent at these high particle concentrations.

3.7. Conclusions

In this chapter, we have explored the rich phase behavior of suspensions of charged platelets with a bimodal distribution in the aspect ratio with a combined experimental and theoretical effort. The isotropic-nematic phase separation is found to be accompanied by a large degree of shape fractionation, with the thick species strongly accumulating in the isotropic phase. The fractionation effect has a significant influence on the relative mass densities of the coexisting isotropic and nematic phases and leads to a *density inversion* where the top and bottom coexisting phases are seen to switch in a test tube as the overall plate concentration is gradually increased. Moreover, a distinct three-phase equilibrium involving an isotropic, nematic, and columnar phase is observed. We propose a simple, tractable theory based on the Onsager-Parsons free energy combined with a simple cell approach for the columnar state. By mapping the polydisperse, bimodal distribution onto a simple binary mixture of hard platelets of different thickness but common diameter, phase diagrams can be determined for various thickness ratios which bear out the fractionation scenario, density inversion and triphasic equilibrium, in agreement with the experimental observations. At high pressures (which would correspond to concentrated samples), the theoretical phase diagram features an additional demixing of the mixture which gives rise to a coexistence between two columnar phase with distinctly different compositions and structure. For the larger thickness ratios, a triphasic nematic-columnar-columnar equilibrium is predicted. Experimentally, the high concentration regime is characterized by a dynamically arrested, metastable glassy state with local columnar order.

Acknowledgements

This work was done in collaboration with Rik Wensink and George Jackson. David van der Beek is thanked for particle synthesis. We also thank Mark Vis for the AFM measurements. His work was supported by a Schlumberger grant.

Part 2

Static properties of nematic tactoids

4

Tactoids of plate-like particles: size, shape, director field

Abstract

We studied, by means of polarized light microscopy, the shape and director field of nematic tactoids as a function of their size in dispersions of colloidal gibbsite platelets in polar and apolar solvents. Due to the homeotropic anchoring of the platelets to the interface, we found large tactoids to be spherical with a radial director field whereas small tactoids turn out to have an oblate shape and a homogeneous director field, in accordance with theoretical predictions. The transition from a radial to a homogeneous director field seems to proceed via two different routes depending in our case on the solvent. In one route, the what presumably is a hedgehog point defect in the center of the tactoid transforms into a ring defect with a radius that presumably goes to infinity with decreasing drop size. In the other route, the hedgehog defect is displaced from the center to the edge of the tactoid, where it becomes virtual again going to infinity with decreasing drop size. Furthermore, quantitative analysis of the tactoid properties provides us with useful information on the ratio of the splay elastic constant and the anchoring strength and the ratio of the anchoring strength and the surface tension.

4.1. Introduction

If an isotropic suspension of highly anisometric colloidal particles is brought under conditions where it coexists with a nematic liquid-crystalline phase, nematic droplets form. These droplets, or tactoids, have a non-trivial shape and intricate internal structure, i.e., a spatial distribution of the local preferred orientation of the particles, the director. Both the director-field configuration and the shape of tactoids are governed by the competition between the surface tension, anchoring strength and bulk elastic properties of the nematic. Which of these properties prevails varies with tactoid size. This implies that the size dependence of the tactoid structure provides insight into these properties.

Tactoids formed in suspensions of rod-like colloidal particles have been studied for some time. The first observations by Zocher [5] on tactoids in vanadium pentoxide sols date back to the 1920s. After that, tactoids were studied in suspensions of tobacco mosaic virus [42], aluminum hydroxide (boehmite) [43] and more recently fd virus [44], vanadium pentoxide [55, 56], f-actin [46] and carbon nanotubes [59]. In these studies, director-field configurations were probed by means of polarized light microscopy, which revealed elongated (spindle-shaped) droplets with a bipolar director field. The bipolar director field is characterized by two surface point defects called boojums. The origin of this director field can be contributed to the preferred parallel (planar) anchoring of the particles to the isotropic-nematic interface [51–53, 55, 56].

As already advertised, tactoid shape and director field are determined by a balance of the surface anchoring and bulk elastic free energies. A simple scaling analysis proves useful here. whereas the anchoring free energy of a drop of radius R scales as the surface area, R^2, times the anchoring strength, w, the bulk elastic free energy scales as the relevant elastic constant, K, times the tactoid volume, R^3, times the square of one over the radius of curvature of the director field, $1/R^2$. This implies that for a more or less spherical drop there must be a cross-over size $R \approx K/w$, above which the surface anchoring predominates.

For planar anchoring conditions this leads to the aforementioned bipolar director-field configuration. For tactoids smaller than this critical size the elastic free energy dominates, imposing a uniform director field on the drop [52, 53, 59, 63]. On the other hand, perpendicular (or homeotropic) anchoring to the isotropic-nematic interface gives rise to spherical tactoids with a radial director field emanating from a hedgehog point defect located in their center [60, 63, 121]. This point defect could in fact also be a small ring-shaped disclination line [122, 123]. Obviously, the scaling argument holds irrespective of the anchoring conditions, so a crossover to a uniform director field has to be expected in the case of homeotropic anchoring as well if the tactoids are sufficiently small, that is, if $R \approx K/w$.

Although the transition of a deformed to a uniform director field with decreasing tactoid size has been predicted a long time ago, and was also confirmed by means of computer simulations [58, 124], until very recently, there had not been any convincing experimental evidence for it. The main reason presumably is that the length scale K/w (known as the "extrapolation" length [57]) can be very small, in particular in thermotropic liquid crystals where the transition is expected to take place in the sub-micron range [125]. Apart from the fact that it is difficult to prepare in a controllable way such small droplets, it is also problematic to analyze them properly with polarized light microscopy.

Still, about a year ago Gupta and co-workers succeeded in preparing sub-micron sized liquid-crystalline droplets confined in polymeric shells, allowing them to study their structure to sizes down to 0.7 μm [126]. Remarkably, they found that upon decreasing the shell size, the liquid crystal structure progresses from a bipolar director field (associated with a planar anchoring) via a pre-radial to a radial director field (typical of homeotropic anchoring). So, these authors did not observe a crossover to a uniform director field and argued that previously ignored saddle-splay and splay-bend elastic energies are responsible for this, and that no transition to a uniform ordering for sufficiently small drops is to be expected if the saddle-splay constant is sufficiently large compared to the splay constant. Actually, according to their own analysis, the order of the transition should in that case be reversed with sufficiently large drops becoming uniform. This was not observed, however, so the issue remains somewhat contentious also because it requires negative free energies of elastic deformation [126].

More recently, Haseloh and collaborators studied the internal structure of liquid-crystal based colloidal particles in the micrometer range, where the anchoring could be controlled by different types of dispersion polymerization [127]. They did find a transition from a radial to an axial director field upon decreasing the droplet size to around 1 μm. Unfortunately, they could not unequivocally confirm the existence of the uniform director field because of difficulties associated with the characterization of tactoids smaller than 1 μm. Indeed, due to Brownian motion these particle move around uncontrollably, leaving only a characteristic blinking if observed under the polarized light microscope. This blinking would indeed be indicative of a uniform director field.

In the various colloidal rod systems studied over the years, the transition to a uniform director field was never observed either, presumably because, apparently, the ratio K/w corresponds to tactoid sizes less than ten times the rod length [52]. Still, very recently Puech and co-workers were able to observe highly elongated tactoids with a uniform director field in aqueous dispersions of carbon nanotubes [59]. For this particular system, the extrapolation length was deduced to be in excess of 35 μm, so this system would in principle be a good candidate to observe the crossover. Unfortunately, droplet sizes observed remained below this critical value [59].

In suspensions of colloidal platelets, a value for the extrapolation length K/w of 70 μm has been reported, determined from the director-field configuration of a nematic phase near the interface between coexisting isotropic-nematic phases and a vertical solid wall [64]. This means that such a system is an excellent candidate to study the transition from a uniform to a non-uniform director field, as this transition should occur for tactoid sizes well within the experimentally accessible range provided large enough drops are present in the dispersion. In this chapter, we are indeed able to confirm this expectation, and report on the size dependence of the shape and director field of tactoids observed in suspensions of colloidal gibbsite platelets.

We study both sterically stabilized gibbsite in an apolar solvent (bromotoluene), and charged gibbsite particles in a polar solvent (water). These two systems, although based upon the same colloidal particles, give rise to different elastic and surface properties of the respective nematic phases. The first question we attempt to answer is whether it is possible to observe tactoids with a uniform director field, and, if so, what the shape of these droplets is. Plate-like particles for entropy reasons prefer homeotropic anchoring, and in that case a flat (oblate or lens-shaped) droplet shape appears to be optimal shape for tactoids smaller than $R \approx K/w$. This is in line with what could be expected from the familiar Wulff construction if the anchoring strength is sufficiently large relative to the surface tension [47, 49, 128, 129].

Secondly, an interesting question we address is how precisely the transition from a radial to a uniform director field proceeds with tactoid size. On theoretical and experimental grounds [61, 63, 127, 130, 131], one could imagine two plausible scenarios, illustrated in Figure 4.1:

1. The hedgehog point defect in the tactoid's center transforms into a ring defect, with a radius that increases to infinity with decreasing droplet size. This route involves both the splay and the bend elastic deformations of the director field.
2. The hedgehog point defect displaces itself from the center of the tactoid to its edge, where it becomes virtual and moves further away with decreasing droplet size. This route would involve a splay elastic deformation and suboptimal anchoring of the director field to the interface.

Of course, these scenarios represent a highly idealized and maybe somewhat naive picture of what is actually going on, and combinations of these two routes are conceivable as well. Which route turns out to be most favorable presumably depends on the values of splay and bend elastic constants relative to the anchoring strength. We may therefore expect a different kind of behavior in the sterically stabilized and charged gibbsite systems, based on what we know to be the case for systems of rod-like particles where these parameters are known to be sensitive to how particles are stabilized against demixing [132, 133].

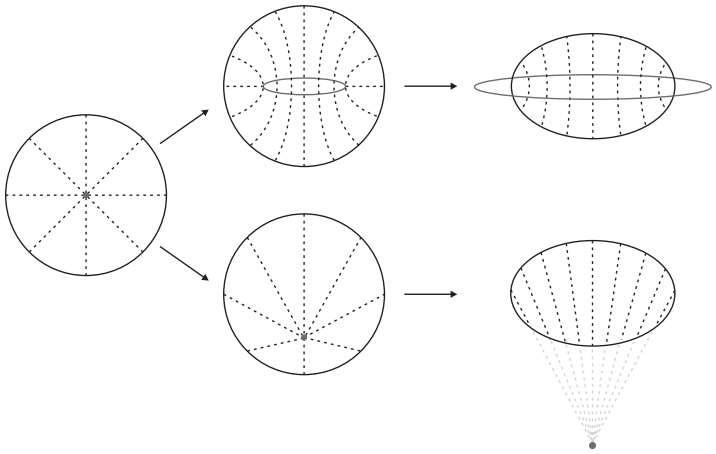

Figure 4.1. Sketch of possible transition pathways from a radial to a uniform director field upon decreasing tactoid size.

The remainder of this chapter is organized as follows. Section II deals with the experimental details and analysis of microscopy images. Then, in section III we present the various observed tactoidal shapes and director fields as a function of tactoid size, both in aqueous gibbsite suspensions and sterically stabilized gibbsite dispersed in bromotoluene. In section IV we perform a quantitative analysis of the structural properties of the tactoids, extract from our results values for the ratio of the anchoring strength and surface tension and that of the splay elastic constant and the anchoring strength. Section V contains the discussion of our findings and we finish in section VI with a concluding summary.

4.2. Experimental Methods

4.2.1. Particle synthesis and characterization

Two different gibbsite systems were used to study tactoid properties in the polar solvent water and the apolar solvent bromotoluene. For aqueous gibbsite, we used the gibbsite system described in Chapter 3, including surface treatment with aluminum chlorohydrate to enhance the particle stability. The stabilized particles were dispersed in a 10^{-2} M NaCl solution.

For the experiments in bromotoluene, colloidal gibbsite ($Al(OH)_3$) platelets were synthesized via the procedure described in Chapter 2, subsequently coated with modified poly-iso-butylene (Shell, SAP 230) following the procedure of Van der Kooij and coworkers [32] and then dispersed in 2-bromotoluene.

Both systems were characterized with transmission electron microscopy (TEM, Tecnai 10, Philips), which resulted in a particle diameter of 207 nm ($\pm$35%) for the platelets to be studied in polar solvent, and 220 nm ($\pm$22%) for the gibbsite in apolar solvent.

4.2.2. Sample preparation

The suspensions were concentrated by centrifugation and re-dispersed to a concentration where phase separation occurs and the isotropic and nematic phases coexist, which we found to be at 24 v/v% for the charged gibbsite and 21 v/v% for the sterically stabilized gibbsite. A second sample of the charged stabilized gibbsite was prepared at a higher concentration (30 v/v%) where the isotropic, nematic and columnar phases coexist. The tactoids in these two samples showed no significant differences. Samples of the homogenized suspensions were prepared in flat glass capillaries (VitroCom) with internal dimensions of $0.2 \times 4 \times 40$ mm^3. The capillaries were flame-sealed and glued to prevent evaporation of the solvent and were subsequently kept in vertical position.

4.2.3. Polarized light microscopy

The tactoid shape and director fields were examined with polarized light microscope as described in Chapter 2. As we have shown in Chapter 2, Gibbsite has a positive intrinsic birefringence, which means that the slow axis is parallel to the main axis of the platelets. However, in the nematic phase there is an additional contribution from the form birefringence, which is due to the elongated particle shape and is negative because both solvent refractive indices are smaller than the refractive index of gibbsite (n=1.57). The resulting birefringence is positive when the refractive difference with the solvent is relatively small, and negative when this difference is large. Effectively, this results in a positive birefringence for the gibbsite system in bromotoluene (n=1.55) and a negative birefringence for the system in water (n=1.33).

4.2.4. Image analysis

Analysis of the microscopy images of the charged gibbsite was performed with a computer program created in IDL 7.1 [134]. The program was developed to sample tactoids automatically and extract the relevant properties (size, shape, director field, color) with a combination of an edge detection [135, 136] and an ellipse detection [137] algorithm. Tactoids that were obviously deformed by hydrodynamic interaction with other tactoids or coalescence events are either not detected or were removed manually. The micrographs of the sterically stabilized system were measured manually with the microscopy analysis software iTEM [138].

4.3. Results

Soon after homogenization of both types of gibbsite suspension, many tactoids appeared in the isotropic phase, which, dependent on the sample, either rose ("creamed") or sedimented and coalesced to form the nematic phase. In the sterically stabilized gibbsite system, the isotropic phase is, as usual, the phase with the lowest density, in contrast to the aqueous gibbsite system where the nematic phase has the lowest density. This density inversion is caused by a fractionation effect due to a bimodal

distribution of the platelet aspect ratios in this particular gibbsite system, which we discussed in Chapter 3. Because this fractionation results in a monomodal distribution in the nematic phase, we do not expect this to influence significantly the results.

In the initial stages, the phase separation is quite a chaotic process and most tactoids seem to have non-equilibrium shapes due to coalescence events and the presence of flow fields in the dispersion. Therefore, we probed the properties of the tactoids only after the macroscopic isotropic-nematic interface has been formed and the tactoids remaining in the isotropic phase are far enough apart that their shape is not distorted by hydrodynamic interactions between them, which is typically after a few days to weeks. Figure 4.2 presents a typical polarized light image showing tactoids of various sizes and different director fields (a) just below the isotropic-nematic interface in the aqueous gibbsite system and (b) just above the isotropic-nematic interface in the sterically stabilized system.

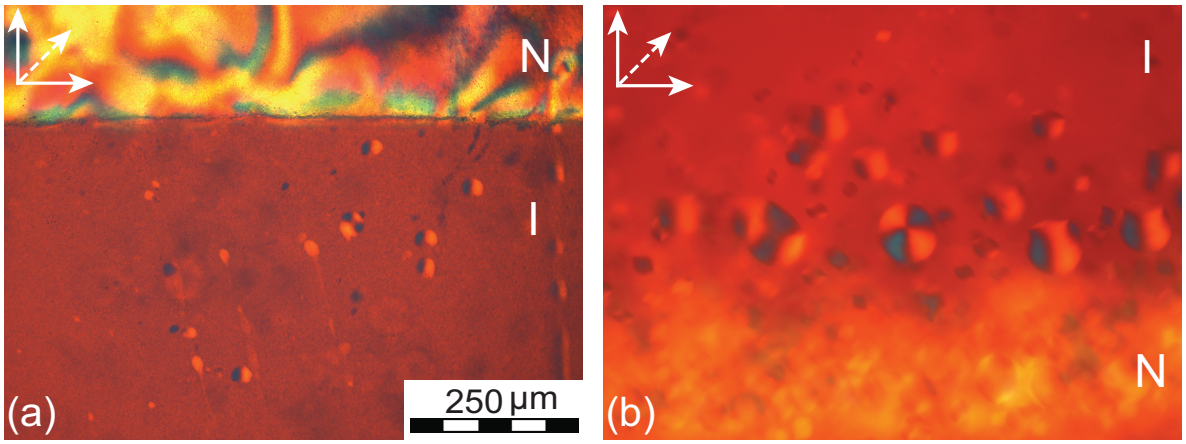

Figure 4.2. Nematic tactoids in the isotropic phase; (a) just below the IN-interface in an aqueous gibbsite system and (b) just above the IN-interface in a sterically stabilized gibbsite suspension. Polarizers are indicated with arrows, and the retardation plate is indicated with a dashed arrow.

4.3.1. Charge stabilized gibbsite

Starting with the aqueous gibbsite suspensions, we observe that the largest tactoids are spherical with a dark cross (also called a Maltese cross [72]) parallel to the polarizers, which rotates with the polarizers, indicating alignment of the particles parallel to these as well as the presence of rotational symmetry (Figure 4.3(a-b)). With the retardation plate inserted (Figure 4.3(c)), two opposite quarters appear as blue, whereas the other quarters are orange. The blue color corresponds to an addition of the optical path difference (largest refractive index parallel to the retardation plate), whereas orange corresponds to a subtraction (largest refractive index perpendicular to the retardation plate).

Because in aqueous gibbsite suspensions the birefringence is negative, this implies that the platelets are aligned with their director perpendicular to the interface and, in other words, exhibit homeotropic anchoring. Combining all this information we deduce that large tactoids in the aqueous gibbsite system have a radial director field with a hedgehog point defect near their center, see Figure 4.3(d). For the tactoid shown in the micrographs presented in that figure, the point defect is located somewhat off-center and as we observed this tactoid to move upward with time; this means that it is offset in the direction of the rear with respect to the translation direction. As we shall see, we also observe a similar phenomenon for tactoids with different director field structures. We attribute this to the influence of the flow fields caused by the sedimenting and creaming of the droplets in respectively the charge- and sterically stabilized systems. We return to this below.

Tactoids of smaller size in aqueous suspensions of colloidal gibbsite can have various appearances. Two representatives of droplets somewhat smaller than the ones that have a radial director fields, are shown in Figure 4.3(e-h) and (i-l). Focusing on the first one, which is only occasionally observed and shown in (e-h), one might surmise that this tactoid must have a hole through the center or even exhibit a toroidal shape, but this would seem energetically very unfavorable. A more plausible explanation of the extinction pattern is that in Figure 4.3(e) and (g) the director lines in the central part point into the image, in which orientation the nematic phase is not birefringent. This would correspond to an axial director field with a ring disclination, as drawn in Figure 4.3(h), which in 4.3(e) and (g) we observe in top view. In 4.3(f) the axial part is parallel to the polarizer and therefore also not birefringent. Below, we will observe this kind of director-field configuration in side view for the sterically stabilized gibbsite system, where it is more common.

More frequently observed is the distorted oblate-shaped tactoid displayed in Figure 4.3(i-l). These tactoids have an asymmetric radial director field emanating from a point (or a small ring) defect at the edge of the tactoid. Because the dark bands in Figure 4.3(j) are slightly curved, there might be some bend deformation present as well, consistent with the director field drawn in Figure 4.3(l). The tactoids in this system are creaming, and the defect is always located at their lower edge, in other words, at the rear end with respect to the translation direction. Occasionally, we find that if such a tactoid collides with another one, it rotates and the top view can be observed, revealing a circular radial pattern. In that orientation, it becomes indistinguishable from a spherical tactoid with a radial director field. The anchoring with the interface in this peculiar configuration is clearly suboptimal, to be discussed further in the next section.

The smallest tactoids in the aqueous gibbsite system as depicted in Figure 4.3(m-p) clearly have a different appearance. They have an ellipsoidal shape with rounded edges

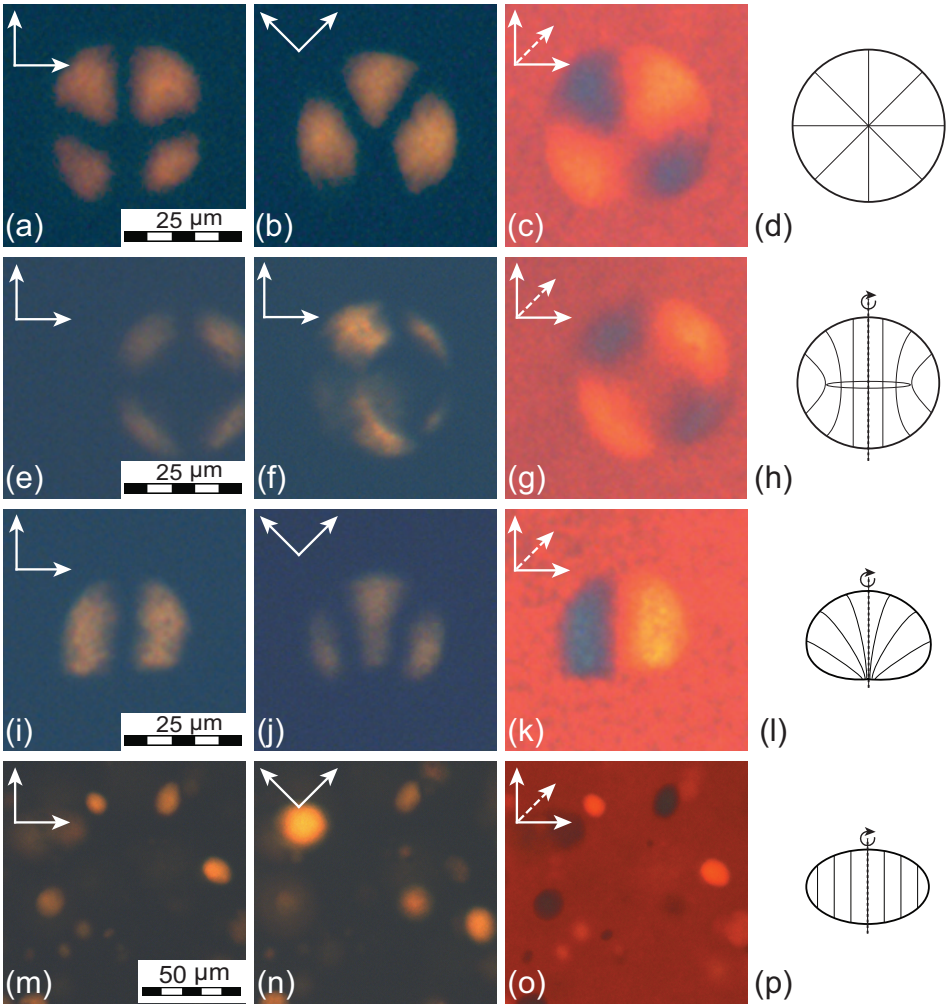

Figure 4.3. Nematic tactoids in aqueous gibbsite system imaged with polarized light microscopy, and a sketch of the director field configurations in the final row. Polarizers are indicated with solid arrows and the retardation plate is indicated with a dashed arrow. Large tactoids (a-d) are spherical with 3D splay director field and a point defect in the center. Tactoids of intermediate size are either spherical with an axial director field and ring disclination (e-h), or oblate-shaped with an asymmetric radial director field (i-l). The smallest tactoids (m-p) have an oblate shape and uniform director field.

and are either entirely birefringent or non-birefringent, depending on the orientation of the polarizers. This can only mean that the director field is uniform. Moreover, the aspect ratio of the droplets is independent of their size, which is another indication that these tactoids must have a uniform director field [52]. From the image taken with the retardation plate (Figure 4.3(o)), we conclude that the director must be oriented perpendicular to the major droplet axis, which is to be expected because in that configuration a larger fraction of the platelets has the preferred homeotropic alignment with the interface. This then also implies that for symmetry reasons these tactoids must

have an oblate shape. The fact that we never observe a circular shape, which is the appearance of an oblate viewed from the top, is explained by the fact that the tactoid is not birefringent in top view. As we will see in the next section, the aspect ratio of this oblate-shaped tactoid contains interesting information, because it solely depends on the ratio of the anchoring energy and the interfacial tension between the isotropic and nematic phases.

4.3.2. Sterically stabilized gibbsite

We now turn to the various tactoid shapes and director fields that we find in suspensions of sterically stabilized gibbsite, a system with similar behavior to that of the charged-stabilized gibbsite but also with marked differences. We start again with the largest tactoids, a typical example of which is shown in Figure 4.4(a-d). The Maltese cross can be observed again, and like in the previous case of aqueous gibbsite, the tactoids are spherical with a radial director field and a hedgehog defect in the center (Figure 4.4(d)). Note that the retardation colors are reversed (Figure 4.4(c)) as a result of the positive birefringence of colloidal gibbsite in bromotoluene.

Figure 4.4(e-h) shows a typical tactoid of intermediate size in the sterically stabilized gibbsite system. The tactoid still has a spherical shape but the Maltese cross, typical for the radial director field of the large tactoids, has now opened (Figure 4.4(f)). Together with the image of the polarizers in horizontal-vertical orientation and with retardation filter (Figure 4.4(e) and (g)) we conclude that the intermediate tactoid has an axial director field with a ring disclination positioned off-center, near the upper part of the tactoid. In the sterically stabilized system, the tactoids slowly sediment toward the macroscopic isotropic-nematic interface, which means that this ring disclination is located away from the translation direction, similar to what we observed in the aqueous gibbsite system.

Small tactoids in this system, shown in Figure 4.4(i-l), appear rather different from the small tactoids that we found in aqueous gibbsite. They seem more lens-shaped and clearly have a non-uniform director field. When the polarizers are parallel to the droplet axes, a non-birefringent cross is observed parallel to the polarizers. Rotation of the polarizers with 45 degrees makes the droplet (almost) completely birefringent, and this birefringence is much more intense. Furthermore, the image taken with a retardation plate (Figure 4.4(k)) reveals that the director is again perpendicular to the tactoid interface, implying homeotropic anchoring.

From these observations, we deduce an axial director field as drawn in Figure 4.4(l). The director pattern is not exactly symmetric with respect to the equator, the lower part is somewhat larger. We will return to this in the discussion. We have not observed a tactoid with a uniform director field in this system but this might be simply because

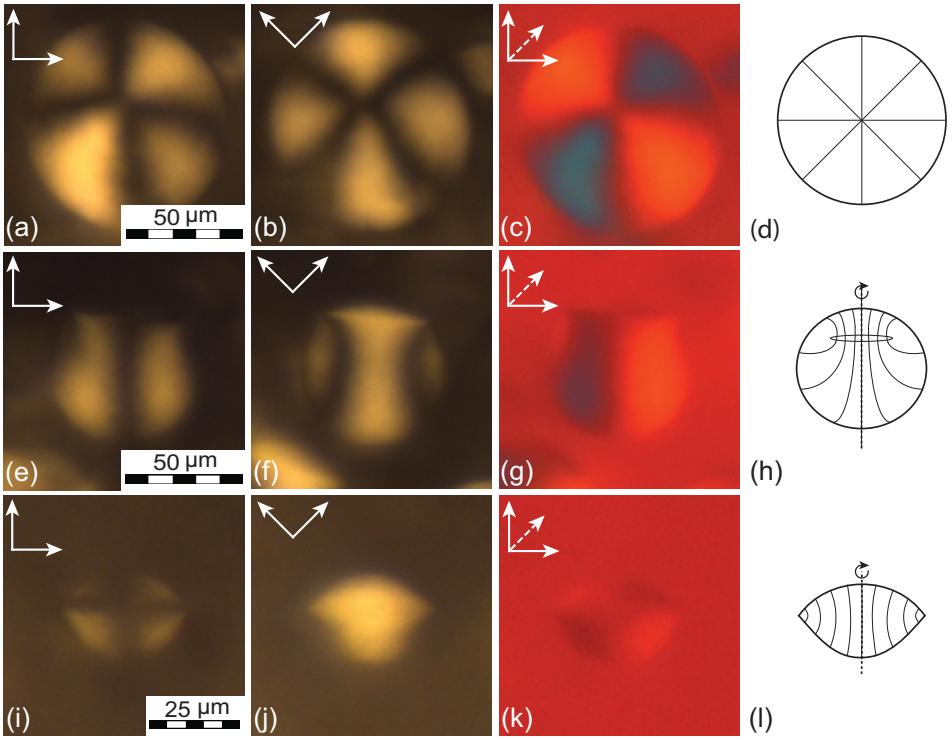

Figure 4.4. Nematic tactoids in a suspension of sterically stabilized gibbsite imaged with polarized light microscopy, and a sketch of the director field configurations in the final row. Polarizers are indicated with solid arrows and the retardation plate is indicated with a dashed arrow. Large tactoids (a-d) are spherical with a 3D splay director field and a point defect in the center. Tactoids of intermediate size (e-h) are spherical with an axial director field and out-of-center ring defect. The smallest tactoids (i-l) are lens shaped with an axial director field.

we have not been able to analyze tactoids smaller than 10 µm due to the poor contrast as a consequence of the small birefringence in this system.

If we consider all of the observed tactoid shapes and director fields, then we envisage two pathways for the transition from a radial to a uniform director field:

1. Via the opening of the point defect into a ring disclination. Upon decreasing tactoid size this ring defect increases in diameter. As it becomes larger the tactoid shape adapts by flattening the droplet so that the anchoring conditions are met. This ultimately leads to the observed lens-shaped tactoids with axial director field, where the ring defect runs along the equator. Finally, we expect the ring defect to become virtual, leading to a uniform tactoid where the radius of the virtual defect is large compared to the size of the drop;
2. Via the displacement of the central point defect. With decreasing tactoid size the point defect moves toward the edge of the tactoid. This may induce a flattening in the droplet shape due to suboptimal anchoring, and to the introduction of a

bend deformation of the director field to counteract this further. For yet smaller tactoid sizes the defect becomes virtual yet the characteristic radial director field approximately survives in the drop. In the limit where the virtual defect is infinitely far removed from the drop the director field becomes truly uniform.

The first transition pathway was mainly observed in the sterically stabilized system, although a ring disclination was also observed occasionally in aqueous gibbsite suspensions. The second pathway was mainly observed in aqueous gibbsite suspensions; although the defects in the sterically stabilized gibbsite were sometimes also out of the tactoid center but never at the tactoid edge. We will come back to these asymmetric defects in the discussion below.

4.4. Analysis

Now that we have identified the various director fields and tactoid shapes present in suspensions of colloidal gibbsite, we proceed to analyze these tactoids quantitatively in order to obtain useful material properties from the observations. To begin with, and as already alluded to previously, the cross-over tactoid size from a uniform to a radial director field is set by the so-called extrapolation length $\xi \equiv K_1/w$, i.e., the ratio of the splay elastic constant, K_1, and the anchoring strength, w. So, by finding the crossover size, we can establish a value of this length scale.

Before doing that, it is useful to recall how this follows from a simple free-energy analysis, presuming for simplicity that the drops are spherical, even though that this is not quite the case. If the interfacial energy σ has the familiar Rapini-Papoular form, then $\sigma = \gamma + w \sin^2\theta$ with γ the bare surface tension and θ the angle between the surface normal and the director field at the surface [139].[1] A straightforward calculation now shows that the anchoring energy associated with a uniform director field then equals $\frac{8}{3}\pi w R^2$, with R the tactoid radius, whilst the elastic deformation energy of the radial director field is $8\pi K_1 R$ [50]. The free energy associated with the surface tension is the same for both configurations, so the radial director field is adopted if the anchoring energy of the uniform director field exceeds the elastic energy of the radial field, which happens if $R > 3\xi$. So, using this inequality we can deduce the value of ξ if we know R.

Of course, from the experiments we know that the tactoids with a uniform director field are not quite spherical but oblate. A slightly better estimate may be obtained by invoking the Wulff construction that gives the optimal shape for a homogeneous configuration [48, 128, 140]. Indeed, we do find a lower free energy than that for the sphere and, as a consequence, a slightly higher bound than $R > 3\xi$ for the radial field

[1] The interfacial free energy of coexisting isotropic and nematic phases in dispersions of rod-like particles seems to follow the Rapini-Papoular form, as was recently determined by an inverse Wulff construction for tactoids of carbon nanotubes [59].

to take over from the uniform one (Chapter 6). However, the difference is so small that our estimate presuming a spherical shape remains excellent for the smallish aspect ratios found here.

To find the crossover radius from the experiments, we present a histogram of all of the observed tactoid shapes and director fields as a function of size in Figure 4.5 for both systems of charge- and sterically stabilized gibbsite. Interestingly, in the charged gibbsite system, the size ranges of the uniform and radial tactoids both overlap with the size range of the intermediate tactoids but they hardly overlap each other. This allows for a fairly accurate determination of the cross-over tactoid size. What we have to keep in mind, though, is that the intermediate tactoid with the defect at the edge has a radial appearance in top view, so that occasionally an intermediate tactoid might have been identified as a radial tactoid.

We therefore determined the cross-over tactoid size from radial to uniform from the largest uniform tactoid, which has a size $2R = 36$ μm, resulting in a value for the ratio $K_1/w = 6$ μm. Although for the sterically stabilized gibbsite system we cannot accurately determine K_1/w, because we have not been able to observe tactoids with a uniform director field, the lack of this observation provides us with an upper bound for K_1/w, being $K_1/w < 2$ μm. These rather different values seem to point to quite different surface and elastic properties of nematic phases of the two types of system. Note that in both systems we do see for a range of sizes coexistence of the different tactoid shapes and director field structures, which means that in this crossover regime the free energy difference between the different structures must be small, as is to be expected.

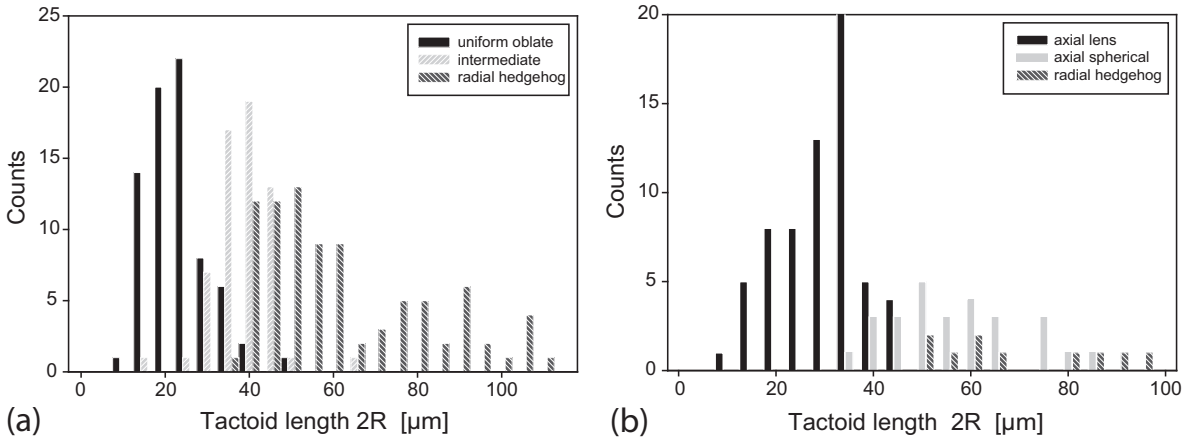

Figure 4.5. Histograms of the observed tactoid shapes and director fields as a function of size in (a) an aqueous suspension of charged gibbsite and (b) a suspension of sterically stabilized gibbsite in bromotoluene.

The shape of the uniform tactoids in the aqueous gibbsite system provides us with additional information. First, we measured the color of these tactoids as a function of

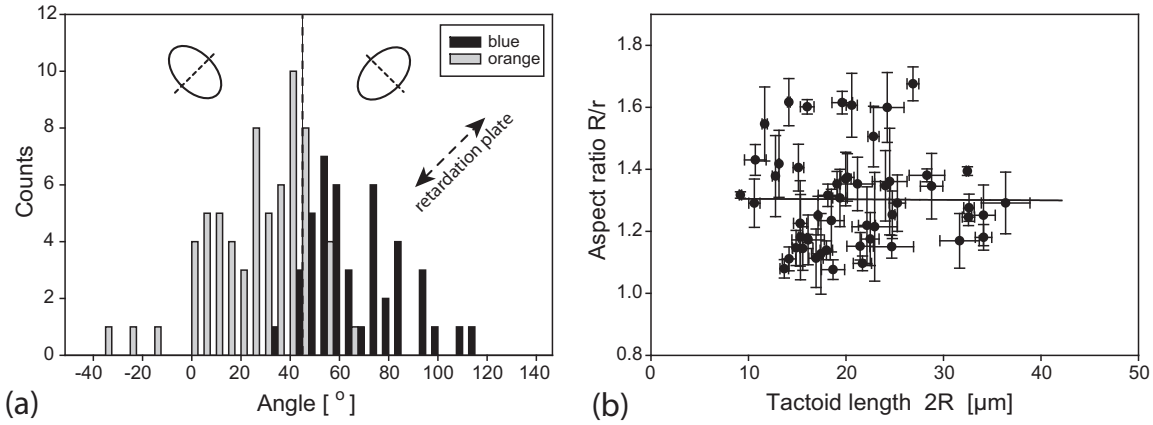

FIGURE 4.6. (a) Interference color of uniform tactoids in the aqueous gibbsite system as a function of the angle of the tactoid symmetry axis with respect to the retardation plate. See also the main text. (b) Aspect ratio R/r as a function of length of small uniform tactoids in the aqueous gibbsite system. The line represents a least squares fit of a horizontal line at R/r=1.3 ± 0.07.

the angle of their symmetry axis with respect to the retardation plate. Recall that if the nematic director is parallel to the retardation plate, the tactoid will appear blue, whereas in the perpendicular orientation it will appear orange. The histogram in Figure 4.6(a) clearly shows that the droplets with their symmetry axis parallel (-45 - 45°) to the retardation plate mostly appear orange, whereas the tactoids in perpendicular orientation (45 - 135°) are blue. This means that the nematic phase indeed has its director parallel to symmetry axis of the droplet, as to be expected for the case of homeotropic anchoring.

As we already mentioned, the aspect ratio of the uniform tactoids contains information on the anchoring strength. From the Wulff construction [128, 140] it follows that the ratio, R/r, of the long and short axes of the oblate shapes is determined only by the ratio of the anchoring strength and the surface tension w/γ [47–49]:

$$R/r = \begin{cases} (w/\gamma) + 1 & \text{if} \quad 0 < w/\gamma < 1 \\ 2\sqrt{w/\gamma} & \text{if} \quad w/\gamma > 1 \end{cases} \tag{4.1}$$

These two equations reflect the transition from an oblate droplet for values of $0 < w/\gamma < 1$, to a lens shape with a sharp rim for $w/\gamma > 1$.

In Figure 4.6(b) the aspect ratio of the tactoids is plotted as a function of tactoid size, showing a cloud of data points without correlation. So, the aspect ratio is independent of the tactoid size, as should be the case for tactoids with a uniform director field. The horizontal line is obtained from a least-squares fit resulting in an average value for $R/r = 1.3$ (± 0.07). From this we find that $w/\gamma = 0.3$. The huge spread in the

aspect ratio is indicative of an (ultra)low interfacial tension, but is here also partially caused by the fact that with polarization microscopy, which is based on transmission, we measure a 2D projection of a 3D object in different orientations. Therefore, the average aspect ratio found by the fit is probably too low, although we are aided by the fact that the tactoids are practically invisible (not birefringent) if viewed from the top, and, on the other hand, have the largest contrast when viewed from the side. Hence, a better estimate for the aspect ratio would be 1.6, which provides us with a value of $w/\gamma = 0.6$. This is in line with what could be expected given the oblate shape of these tactoids.

For the sterically stabilized gibbsite, the aspect ratios of the lens-shaped tactoids that we measured as a function of size is depicted in Figure 4.7. In contrast to the aqueous gibbsite, where the aspect ratio of uniform tactoids was a constant of size, there is a clear trend of a decreasing aspect ratio with increasing tactoid size. This is to be expected, of course, because in this case the drops are not quite uniform but have an axial director field, and because the largest drops that have a radial director field are spherical.

Although there is no prediction available giving the relationship between the aspect ratio and the tactoid size in the case of an axial director field, we can still obtain a lower bound for w/γ from the largest aspect ratio observed. The aspect ratio of uniform tactoids in this system (which, again, we have not found in our experimental setup) should be larger than the largest aspect ratio found for tactoids with an axial director field. This means that the aspect ratio of uniform tactoids should be larger than 2.2, which via equation 4.1 provides us with a lower bound for $w/\gamma > 1$. Again, we see that the properties of dispersions of gibbsite are fairly sensitive to the mode of colloidal stabilization, even if they seem to behave as hard particles.

4.5. Discussion

An observation in our view worthy of some discussion concerns the shapes and director fields of the intermediate tactoids, and in particular their asymmetric nature. We know from the literature that transitions of the director structure can involve exotic structures such as those observed by Volovik and Lavrentovich, who established that the transition from a radial to a bipolar director field upon changing the boundary conditions also involves asymmetric hedgehog defects and disclination rings [141]. We focus in particular on the oblate tactoid with a point (or small ring) defect off center, i.e., at or near the symmetry axis of the drop but away from its center of mass.

Let us first for simplicity presume that this drop is more or less spherical and consider the second route from a radial director field to a uniform field we put forward in the introduction. The change of the free energy of a radial nematic drop that occurs if we displace the point defect from the center of the drop to the boundary and ultimately

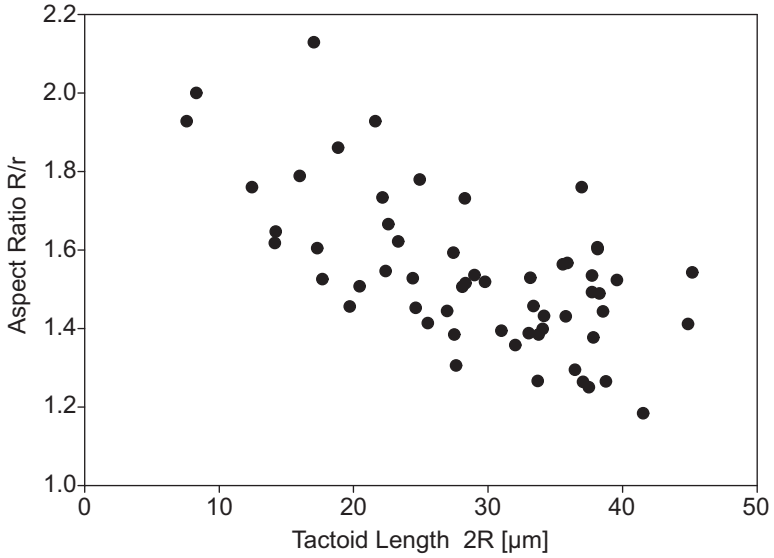

Figure 4.7. Aspect ratio R/r of the small, lens-shaped tactoids in suspensions of sterically stabilized colloidal gibbsite.

place it infinitely far away from the drop is straightforward to calculate within the usual macroscopic description if we presume that the (virtual) director field remains radial in the process. Not surprisingly, we find that the elastic free energy of the drop is lowered by displacing the defect away from the center until it has half of its original value if at the boundary of the drop. However, displacing the core of the defect goes at the expense of the introduction of an anchoring free energy, which is zero if it resides in the center of the drop. If the defect moves outside the droplet, then the anchoring cost increases further albeit the elastic energy decreases further until it vanishes completely at infinity. In that case, the director field inside the drop has effectively become uniform.

Our calculations show that no configuration in which the hedgehog defect is not in the center nor at infinity can be a free-energy minimum, see also Figure 4.8. So, in order to go from the radial field to the uniform field a free energy maximum has to be overcome associated with a configuration where the defect is close to the surface of the tactoid. The argument remains valid for non-spherical drops as well, because the more realistic lens shape associated with the uniform field has a lower free energy than the sphere considered before, making a defect even more unfavorable. This is confirmed by a calculation, in which we fixed a defect on the surface of the drop, and optimized the shape of the drop presuming the deviation from the spherical shape remains small. We find that the configuration with a surface defect never has the lowest free energy of the three for a given tactoid size and anchoring strength w/γ. So, we conclude that the boundary hedgehog must be an unstable configuration, at least for pure splay fields. We speculate that its occurrence must be caused by the effects of the flow field around the creaming tactoid, as discussed in section 4.3.1.

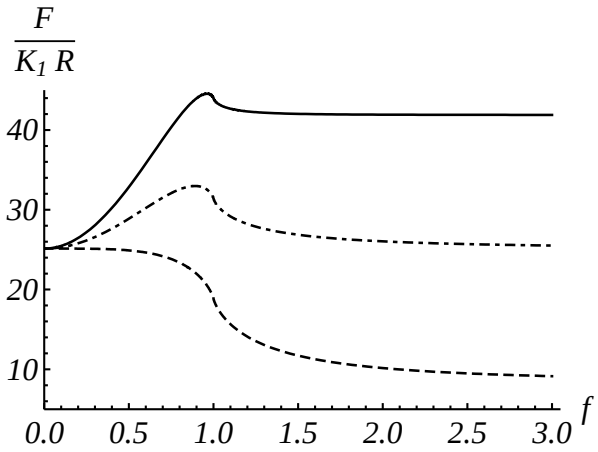

Figure 4.8. Free energy, F, of a spherical drop with a point defect with radial director field as a function of the location of the defect. F has been made dimensionless by dividing it by $K_1 R$, where K_1 is the splay elastic constant and R is the tactoid radius. The defect is located a distance fR from the drop center, such that for $f = 0$ it is in the center, for $f = 1$ it is on the boundary, and for $f \to \infty$ it lies at infinity, giving a uniform director field in the drop. Shown are the free energies for $Rw/K_1 = 1$ (dashed), 3 (dotted-dashed) and 5 (solid). For $Rw/K_1 = 3$ the configurations with central defect and the uniform director field have the same free energy.

In fact, it is well known that flow fields can considerably distort the director field in tactoids [142]. The fact that the defect is consistently located at the rear of the tactoid is a strong indication that this effect plays an important role here, too. Also, the shape of the intermediate tactoid in Figure 4.3(i-l) strongly resembles the shape of a sedimenting drop of an isotropic fluid in another isotropic fluid, where an initially oblate-shaped droplet develops to an asymmetric oblate, very similar to what we observe, at Bond numbers of 10-20 (Bo, defined as the ratio of gravitational and surface forces) and a viscosity ratio of around 1 [143]. If we estimate the Bond number for tactoids with this director field in our system, then we obtain values in that range.[2]

The other intermediate director field structure, the one with a ring disclination is also interesting from theoretical point of view. Such a ring disclination is in fact unstable unless very small [144, 145], the reason being that it is under tension. In our case, it might be stabilized due to the confinement by the droplet and the interaction of the director field with the surface. In fact, this director-field configuration has been observed

[2]The Bond number is defined as $Bo \equiv \Delta\rho g R^2/\gamma$, with $\Delta\rho$ the isotropic-nematic density difference, g the gravitational acceleration, R the droplet radius, and γ the isotropic-nematic interfacial tension. For tactoids with the asymmetric hedgehog defect we find that, depending on the tactoid size, Bo varies from 5 to 15.

Table 4.1. Values for K_1/w and w/γ as obtained from analysis of tactoid shape and director field as a function of size.

	charged gibbsite	sterically stabilized gibbsite
K_1/w [10^{-6} m]	6	2 [a]
w/γ	0.6	1.1 [b]

[a] upper bound
[b] lower bound

before as an intermediate in the transition from a radial to uniform director structure in thermotropic liquid crystals of E7 confined to spherical cavities of decreasing size [61].

The values for K_1/w and w/γ that we obtained from the analysis of the tactoid properties are summarized in Table 4.1. K_1/w is significantly smaller in sterically stabilized than in charge-stabilized gibbsite, whereas the surface anchoring of the director field in our aqueous gibbsite dispersions is considerably weaker than that of the sterically stabilized gibbsite dispersions. We will discuss these remarkable differences further in the discussion of Chapter 6.

Finally, the question arises why the transition from radial to uniform director field follows different pathways in the two systems studied here. We put forward that this might be due to differences on the one hand in the anchoring strength and on the other hand in the relative magnitudes of the splay and bend elastic constants. This is because for the intermediate tactoid with the defect on or near the tactoid edge the anchoring conditions are only partially met, hence it is understandably more present in the aqueous gibbsite system where anchoring is weak. Also, the intermediate structure with the ring disclination involves a stronger bend deformation than the asymmetric defect structure does that is more splay deformed. This suggests that for the sterically stabilized gibbsite, where this ring disclination is mostly observed, the bend elastic constant might be relatively smaller. Obviously, without any quantitative measurements of the various elastic constants, this remains pure speculation and further study is needed.

4.6. Conclusion

We have studied the shape and director field of nematic tactoids as a function of size in suspensions of charged gibbsite in water and sterically stabilized gibbsite in bromotoluene. The properties of the tactoids are determined by a competition of interfacial and elastic free energies, which due to homeotropic anchoring of the platelets leads to an oblate shape with a uniform director field for small tactoids, whereas large tactoids

are spherical with a radial director field. In our studies we observed various intermediate tactoid structures, from which we deduce two different pathways for the transition from a radial to a uniform director field.

The route found mostly in sterically stabilized gibbsite proceeds via the opening of the central point defect to a ring defect of increasing size with decreasing tactoid size, leading to a lens shaped tactoid with axial director field where the ring defect runs along the equator, and eventually to a uniform director field when the defect is much larger than the tactoid. In the other pathway, mainly observed in the aqueous gibbsite dispersion, the central point defect moves to the edge of the tactoid, accompanied by a flattening of the droplet shape, until for even smaller tactoid size the defect becomes virtual, resulting in an oblate tactoid with a (for all intents and purposes) uniform director field.

From a quantitative analysis of the shape and director field of our tactoids, we have been able to extract values for ratio of the splay elastic constant and the anchoring strength and for the dimensionless anchoring strength showing that aqueous gibbsite exhibits weak and sterically stabilized gibbsite strong anchoring of the platelets to the isotropic-nematic interface. The observed differences in transition pathways for charged and sterically stabilized gibbsite can be attributed to this difference in anchoring strength and possibly also partially to different magnitudes of the splay and bend elastic constants.

Acknowledgements

Ronald Otten is thanked for calculations on the stability of the different tactoid configurations. Emile Bakelaar is acknowledged for developing the program to analyze the tactoid properties, as well as for his work on the analysis.

5

Tactoids of sterically stabilized gibbsite in a magnetic field

Abstract

We investigated by means of polarization microscopy the influence of a magnetic field on the shape and director field of nematic droplets in dispersions of sterically stabilized colloidal gibbsite platelets with a negative diamagnetic anisotropy. Our findings provide the first experimental evidence for the existence of the split-core defect structure predicted ten years ago by Mkaddem and Gartland [Phys. Rev. E **62** (2000), 6694]. The split-core structure is a metastable director-field configuration that can be stabilized by a sufficiently strong externally applied magnetic field but only if the diamagnetic anisotropy of the particles is negative. To interpret the experimental observations we put forward a simple theory in which we presume strong anchoring and a spherocylindrical droplet shape. This model allows us to extract values for the interfacial tension and the splay elastic constant from the experimental data.

5.1. Introduction

Tactoids are nematic droplets formed in the early stages of the emergence of a nematic liquid-crystalline phase in suspensions of sufficiently anisometric colloidal particles. They are an interesting object of study because their shape and director-field configuration are determined by a competition between elastic and interfacial forces, the balance of which is a function of their size [51, 60, 63]. In the previous chapter we showed that from an analysis of the tactoid properties as a function of size one can obtain values for the dimensionless anchoring strength and the ratio of the splay elastic constant and the anchoring strength.

Traditionally, magnetic fields have played an important role in the investigation of liquid crystals and the probing of their bulk and surface properties [57]. An important example is the Frederiks transition, where a thin layer of a well-aligned nematic between parallel plates undergoes a sudden change in the director field at a critical magnetic field strength. This method allows, e.g., for the experimental determination of the Frank elastic constants of nematic compounds. It is now widely applied, and started with the work of Frederiks on thermotropic liquid crystals of rod-like molecules in the 20's [146] and was first applied in the 80's by Meyer et al. to lyotropic liquid crystals [147]. Recently Van der Beek and co-workers applied this method to lyotropic liquid crystals of plate-like gibbsite particles [87].

Bipolar tactoids in colloidal dispersions of rod-like colloidal particles have been shown to orient and stretch under the influence of a magnetic field but do not exhibit a Frederiks transition [55]. This observation can be understood by applying standard elasticity theory and by realizing that the drops are freely suspended in solution. The measurements can in fact be described quantitatively if ratios of the bend and splay elastic constants of $K_3/K_1 \sim 10-100$ are inserted and a surface tension γ of order 10^{-6} N/m is invoked. The remarkably large values of K_3/K_1 found were in [53] attributed to the neglect of the saddle-splay surface elastic constant K_{24}.

Interestingly, about ten years ago, Mkaddem and Gartland [123] investigated defects in radial tactoids within Landau-de Gennes theory and, apart from the familiar radial hedgehog and the (small) ring disclination, reported on the existence of what they termed the split-core defect structure. This configuration, in essence a radial point defect extended to a straight disclination line defect, was found to be metastable. However, the authors suggested that it could be stabilized in a magnetic field, provided the particles have a negative magnetic anisotropy.

In this chapter, we study with the aid of polarized light microscopy tactoids of sterically stabilized plate-like particles with a radial director field in a magnetic field. We find that tactoids in dispersions of gibbsite platelets, which have a negative magnetic anisotropy, do indeed exhibit this remarkable defect structure at sufficiently high

magnetic-field strengths. The associated Frederiks-like transition is caused by a tension characteristic of a disclination line, a tension that has to be overcome by the action of the magnetic field.

Moreover, we observe that this change of director field structure is accompanied by a deformation of the tactoid shape. We put forward a simple model for this transformation. Our model allows us to determine experimentally the splay elastic constant from the critical magnetic field strength at which the director field starts to change, and the interfacial tension from the degree of deformation of the tactoid at higher magnetic field strengths.

5.2. Materials and methods

We used the sterically stabilized gibbsite system dispersed in bromotoluene that was studied in Chapter 4.

The dispersion was concentrated so as to be in the biphasic (isotropic-nematic coexistence) regime (overall volume fraction $\phi = 21$ v/v%). The sample was homogenized and left to phase separate, which evolved via the formation, sedimentation and subsequent coalescence of tactoids. Samples were studied in flat optical capillaries (Vitro-Com, NJ, USA), with internal dimensions of $0.2 \times 4 \times 40$ mm^3, and flame-sealed to avoid evaporation of the solvent.

The samples were studied in a magnetic field with the polarized light microscope setup described in Chapter 2. Images were taken with a Nikon Coolpix 995 CCD camera.

5.3. Results

Figure 5.1 shows a typical large tactoid of the sterically stabilized colloidal gibbsite platelets with homeotropic anchoring. From the fact that there is rotational symmetry (figure 5.1(a) and (b)) and from the observed interference colours (figure 5.1(c)), the director field shown in figure 5.1(d) can be deduced. (Note: the director is perpendicular to the long side of the platelets.) The tactoid has a radial director field with a point defect of topological charge +1 (a so-called hedgehog defect) in its center.

When a tactoid with such a director field is placed in a magnetic field, from a certain critical field strength on the dark cross inside the tactoid transforms into a dark band, as depicted in Figure 5.2. The fact that the dark band is aligned along the magnetic field direction, itself inclined at 45° relative to the polarizers, implies that in that region we must be viewing the gibbsite platelets face-on. In this configuration, the particles do not exhibit any birefringence. Such a configuration makes sense, of course, once we realize that the negative magnetic diamagnetic susceptibility tends to align the platelets perpendicular to the magnetic field direction. With this in mind, we can now interpret

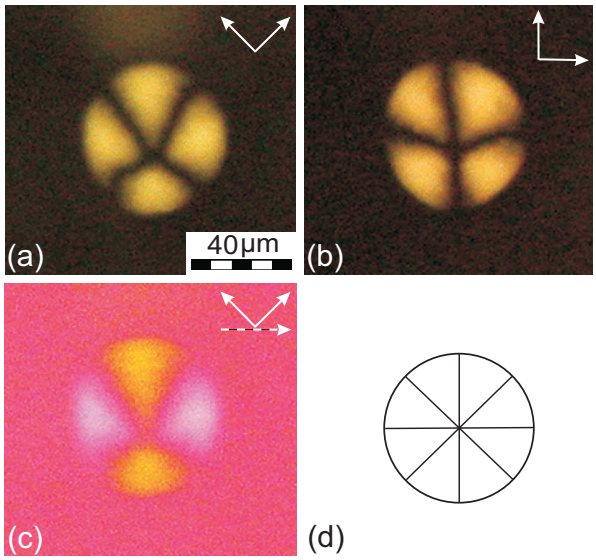

Figure 5.1. Tactoid of sterically stabilized plate-like gibbsite particles with a radial director field and a point defect (hedgehog) in its center. (a) Polarization microscopy image, with the white arrows indicating the polarizers. (b) The same tactoid with the polarizers rotated for 45 degrees. The black cross, where the particles are oriented along the polarizers, rotates with the polarizers, indicating a rotationally symmetric director field. (c) The same as (a), now with retardation plate, the dashed arrow indicating the direction of the slow axis. In the blue parts the director is parallel and in the yellow parts perpendicular to the slow axis of the retardation plate. (d) Deduced director field of the tactoid.

the transformation of extinction patterns in terms of a transformation of the point defect into a disclination line, ending in what must be the two halves of a point defect, in the direction of the magnetic field, as illustrated in figure 5.4.

This implies that from this line defect the director-field lines must run radially to the droplet's interface, resulting in a 2D radial director field in the middle part of the droplet, while the director field on both sides of this structure remains radial in 3D. So, the emergence of the dark horizontal band in the direction of the magnetic field must indeed be due to the alignment of the platelets perpendicular to the magnetic field: looking directly at the core of the disclination line the director field points into the focal plane and in this orientation the particles do not display any birefringence.

When the magnetic field is increased even more, the tactoid is elongated with its long axis in the direction of the magnetic field. Upon decreasing the magnetic field the tactoid relaxes back to its original configuration within a few minutes, so the process is reversible. Figure 5.3 shows the degree of deformation as a function of magnetic field strength of two different tactoids in terms of the ratio of the length L' and the diameter D.

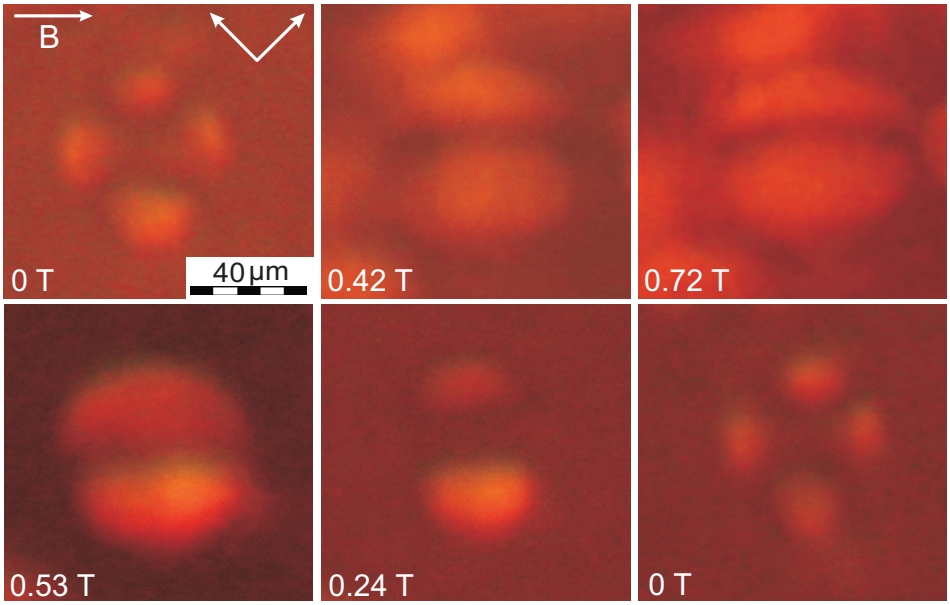

Figure 5.2. Deformation of a tactoid of sterically stabilized gibbsite platelets in a magnetic field of increasing strength (upper figures). The point defect is stretched to a line defect, and the tactoid becomes elongated in the magnetic field direction. When the field is decreased (lower figures) the tactoid relaxes back to its original configuration.

It is of some interest to point out that the observed director-field structure corresponds to that associated with the so-called split-core defect, the existence of which in nematic drops was predicted ten years ago by Mkaddem and Gartland albeit only as a metastable state [123]. These authors also suggested, however, that the split-core defect could be stabilized by the application of a magnetic field, but only if the nematogens have a negative diamagnetic susceptibility. This corresponds exactly to the situation that we have investigated. So, our measurements confirm that the spit-core defect structure, which as far as we are aware has never been observed before, can indeed be made stable in a magnetic field, in agreement with theoretical prediction.

5.4. Theoretical model

We now describe a simple model that can explain the director field transition and the accompanying elongation of a tactoid for a sufficiently strong magnetic field. We presuppose a particular shape and internal structure of the elongated droplet that permits a straightforward calculation of the magnitude of the deformation of the director field and the computation of the overall surface area. The approach we follow is first to write down an appropriate free energy given the model description and to subsequently minimize this free energy with respect to a variational parameter that describes the

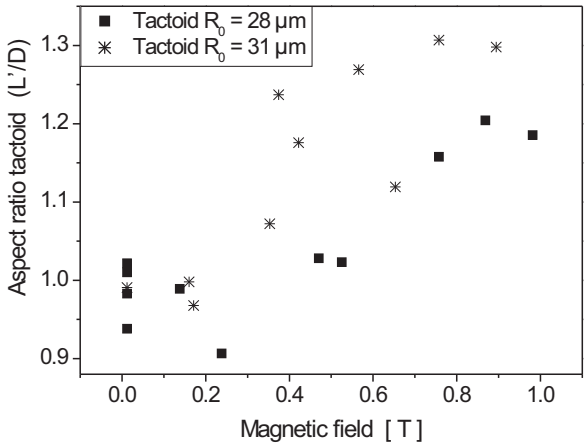

FIGURE 5.3. Aspect ratio L'/D of two different sized tactoids of sterically stabilized plate-like gibbsite particles as a function of magnetic field strength.

elongated shape of the tactoid. The application of this model to the experimental data then enables us to extract values for the splay elastic constant and the surface tension.

In the spherical nematic droplet, the platelets are presumed to exhibit perfect parallel alignment to the surface throughout the entire tactoid, so we assume strong-anchoring conditions to hold. This expresses itself in a radial director field characterized by a hedgehog point defect at the center of the drop. For a sufficiently strong magnetic field, its influence on the orientation of the particles becomes significant. This field biases a certain orientation of the platelets, determined by the sign of the diamagnetic susceptibility anisotropy $\Delta\chi_a$. For negative $\Delta\chi_a$, as is the case for our colloidal gibbsite platelets [85,87], the particles tend to align their director perpendicular to the magnetic field. In the spherical droplet with radially symmetric director field, the orientation of the particles does minimize the surface energy but not their magnetic energy. Therefore, by way of compromise a non-spherical shape, elongated in the direction of the magnetic field, allows more particles to align with the magnetic field and yet remain their homeotropic alignment to the surface.

In our model we presume the droplet shape to by described by a cylinder of length L and radius R with two hemispherical end caps, see figure 5.4. In addition, we suppose the director field in the end caps to be of the same type as in the spherical tactoid, i.e., radial in three dimensions, and in the cylindrical part to be radial in two dimensions with the cylinder axis as the axis of symmetry. This implies that the point defect in the spherical configuration is stretched to a line (or disclination) defect of topological charge +1. Associated with the formation of the line defect from the point defect is an increase of the elastic free energy of the director field. Furthermore, the surface area increases with the elongation, giving rise to an additional surface free energy cost. These two effects are compensated for by the free energy gain on account of an increase of the number of particles aligning with the magnetic field.

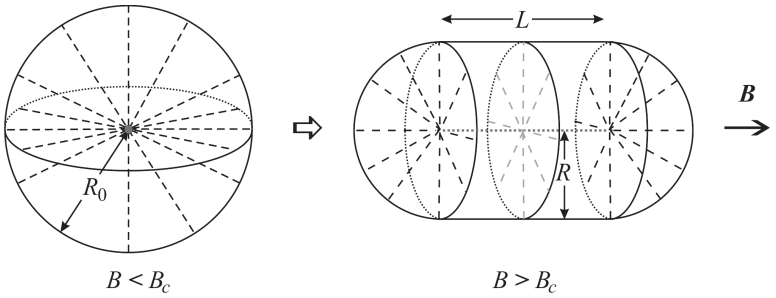

Figure 5.4. Left: for a magnetic field B smaller than a critical field B_c, the droplet is spherical with radius R_0: the director field (dashed lines) is radial in 3D (pure splay) with a point defect (central dot). Right: for a magnetic field larger than B_c, the tactoid adopts an elongated shape that we model by a cylinder of length L and radius R with hemispherical end caps. In the cylinder, the field is radial in 2D with a defect line on the axis and in the caps the field is radial in 3D, originating from the ends of the defect line.

The free energy we set up comprises three contributions: magnetic, elastic, and surface energy. The magnetic energy $F_{\rm mag}$ obeys [57]:

$$F_{mag} = -\frac{\rho\Delta\chi_a}{2}\int \mathrm{d}\boldsymbol{r}(\boldsymbol{n}\cdot\boldsymbol{B})^2 = \Sigma R^3,$$

with $\boldsymbol{n}$ the director field, $\boldsymbol{B}$ the uniform magnetic field with magnitude B, ρ the particle number density, and $\Sigma \equiv -\frac{2}{9}\pi\rho\Delta\chi_a B^2$. This contribution comes from the end caps, since the director field is perpendicular to the magnetic field in the cylinder.

The elastic energy $F_{\rm el}$ associated with the distortion of the director field has contributions from the hemi-spherical end caps and from the cylindrical mid section. The contribution of the cylindrical part can in turn be divided into a part from the bulk and a part from the core containing the defect line on the cylinder axis. This gives an elastic free energy proportional to $f_{\rm core}La^2$, with $f_{\rm core}$ the energy density of the core of the defect and a the core diameter of the defect line. We absorb this contribution into the bulk free energy of the cylindrical portion of the drop by introducing an effective defect core diameter b that we expect to be of the order of the diameter of the platelets.

A radial director field in the cylinder portion and in the end caps implies that it is irrotational in the entire droplet. This makes the deformation of the field a pure splay one, giving an elastic deformation energy of the form [148]: $F_{\rm el} = \frac{K_1}{2}\int \mathrm{d}\boldsymbol{r}(\nabla\cdot\boldsymbol{n})^2$, where K_1 is the splay elastic constant. We conclude that the elastic energy of our model tactoid must obey

$$F_{\rm el} = K_1 L\pi \ln\left(\frac{R}{b}\right) + 8\pi K_1 R. \tag{5.1}$$

The surface energy $F_{\rm surf}$ is proportional to the surface area of the elongated droplet, so

$$F_{\rm surf} = \gamma(2\pi RL + 4\pi R^2),$$

with γ the surface tension.

From the total free energy $F \equiv F_{\rm mag} + F_{\rm el} + F_{\rm surf}$ we subtract the reference free energy of a spherical droplet of the same volume. Invoking volume conservation enables us to express the shape in terms of a single parameter, i.e., the radius R of the cylinder, which allows for the minimization of F to be performed by differentiation with respect to R. The equation for the optimal shape we find reads

$$3\xi r^2 + \frac{4K_1'\pi}{3}\left(\left(-\frac{2}{r^3}-1\right)\ln\left(\frac{r}{b_0}\right)+\frac{1}{r^3}-1\right) + 8\pi K_1' + \frac{8\pi}{3}\left(r-\frac{1}{r^2}\right) = 0, \tag{5.2}$$

where $\xi \equiv \Sigma R_0/\gamma$, $K_1' \equiv K_1/\gamma R_0$, $r \equiv R/R_0$, and $b_0 \equiv b/R_0$, with R_0 the radius of the spherical tactoid. If the optimal value of R is larger than R_0, then by construction $R \equiv R_0$ because the model allows for negative values of the length of the cylindrical part of the drop.

The critical value of the magnetic field strength, B_c, where the director-field transition occurs can be obtained from equation (5.2) by insisting that $r = R/R_0 = 1$, giving

$$B_c^2 = \frac{6K_1}{\rho\Delta\chi_a R_0^2}\left(\ln b_0 + 2\right). \tag{5.3}$$

This critical magnetic field is independent of the surface tension γ because at the onset of the transition the droplet is not deformed yet. This allows us to determine K_1 from equation (5.3), which can then be used to find γ by fitting equation (5.2) to the experimental data of the tactoid size for different magnetic fields.

5.5. Analysis

The model described above enables us to extract material parameters of the liquid crystal from the deformation of the tactoid in the magnetic field. First of all, from the critical magnetic field, where the deformation starts, we obtain the splay elastic constant K_1. From figure 5.3 we observe for the tactoid with $R_0 = 28$ μm a critical field strength $B_c = 0.3$ - 0.4 T and for the tactoid with $R_0 = 31$ μm a critical field strength $B_c = 0.2$ - 0.3 T.

Using equation (5.3), with $\Delta\chi$ is -10^{-22} J/T^2, $\rho = 4 \cdot 10^{20}$ and $b_0 = 10^{-2}$ (where we assume that the size of the defect is of the order of the platelet diameter) we find $K_1 = 1.4$ - $2.6 \cdot 10^{-13}$ N for the 28 μm tactoid and 0.9 - $2 \cdot 10^{-13}$ N for the 31 μm tactoid. From the deformation of the shape above the critical field strength the interfacial tension γ can be determined. Figure 5.5(a) depicts a fit of the deformation of the 28 μm tactoid with equation (5.2), using $\gamma = 5 \cdot 10^{-7}$ N/m. The dashed lines, representing theoretical results for $\gamma = 3$ and $7 \cdot 10^{-7}$ N m^{-1}, show that the shape is strongly dependent on the interfacial tension where a lower interfacial tension results

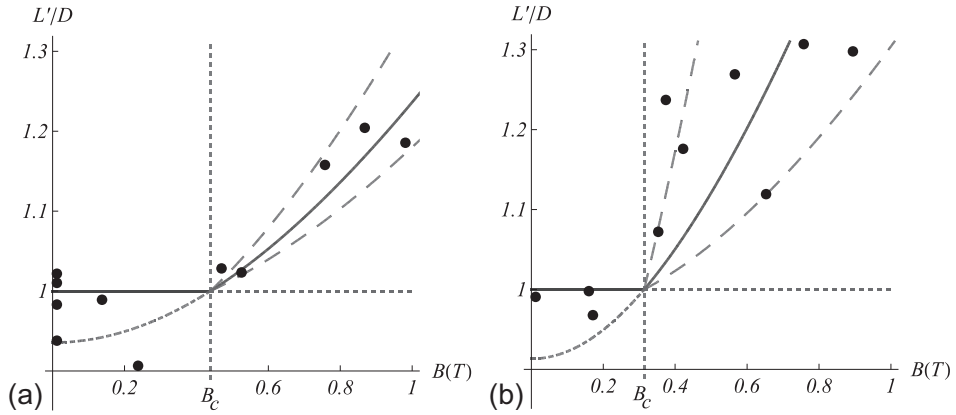

Figure 5.5. Aspect ratio in terms of L'/D of tactoids of sterically stabilized plate-like gibbsite particles as a function of magnetic field strength. The points depict the experimental data and the solid lines the fit to our theoretical model. The dashed-dot line for $B < B_c$ and $L'/D < 1$ represent the non-physical solution of equation (5.2). (a) Fit of the deformation data of the 28 μm tactoid, using $K_1 = 3 \cdot 10^{-13}$ N, and $\gamma = 5 \cdot 10^{-7}$ N/m (solid line), and $\gamma = 3$ and 7 $\cdot\ 10^{-7}$ N/m (dashed lines). (b) The same results for the 31 μm tactoid with $K_1 = 2 \cdot 10^{-13}$ N and $\gamma = 2 \cdot 10^{-7}$ N/m (solid line), and 0.2 and $5 \cdot 10^{-7}$ N/m (dashed lines). The steepest lines correspond to the smallest γ.

in a stronger deformation, and the value we find for γ therefore robust. A similar fit for the 31 μm tactoid, depicted in figure 5.5(b), gives an interfacial tension of $2 \cdot 10^{-7}$ N/m, with the dashed lines representing 0.2 and $5 \cdot 10^{-7}$ N/m.

5.6. Discussion

The value we find for the splay elastic constant $K_1 = 0.9$ - $2.6 \cdot 10^{-13}$ N should be compared to the value for the bend elastic constant K_3 measured by Van der Beek, $K_3 = 7 \pm 1 \cdot 10^{-14}$ N [87]. We see that K_1 is 1.5 to 3 times larger than K_3, in agreement with theoretical predictions by Osipov and Hess [149] and recent computer simulations by O'Brien et al [150].

As expected for these large particles the interfacial tension is low [57], though recent capillary rise experiments resulted in an even lower value for the interfacial tension of $\gamma = 3 \cdot 10^{-9}$ N/m [64]. In order to understand this rather significant difference it should be noted that in our analysis of the elastic free energy we ignored the so-called saddle-splay deformation of the field [148], which is non-zero for a three-dimensional radial director field. This means that the second term of equation (5.1), originating from the elastic deformation in the end caps, actually contains a renormalized elastic constant $K_1 - K_{24}$, with K_{24} the unknown saddle-splay deformation constant.

Still, even invoking a renormalized splay elastic constant cannot quite account for the discrepancy because the corresponding third term of equation (5.2) is relatively small

compared to the first and second term with $b_0 \sim 10^{-2}$. So the shape is determined primarily by a balance between the magnetic contribution and the term associated with the director field deformation in the cylinder.

A moot point, apart from the quite idealized shape description of the tactoids, is that we presume strong anchoring of the platelets, which may be too strong an assumption both in the cylinder and the end caps. In the end caps, this assumption implies that there are relatively many particles that show (almost) perpendicular alignment with the magnetic field, which is expensive energetically. In the cylinder, complete anchoring is imposed by choosing a cylindrical tactoid shape, whereas a shape with non-zero curvature of the tactoid surface along the direction of the magnetic field, e.g., an ellipsoid, is probably a more realistic model of a tactoid.

If we presume imperfect anchoring, the critical magnetic field strength becomes a function of the anchoring strength [151, 152], w. Also, this would lead to a reduction in the deformation of the droplets with increasing magnetic field strength, because the droplet can adjust its director field without actually deforming its shape. This implies that the observed deformation is smaller than the one would expect based on perfect anchoring, and therefore that an estimate for this interfacial tension γ based on it must produce a value that is larger than the actual value.

We will explore this effect in the next chapter, where we develop a theoretical model that includes imperfect anchoring and a more realistic droplet shape in the form of an ellipsoid.

5.7. Conclusions

Tactoids of plate-like colloidal particles characterized by a radial director field and a hedgehog point defect in the center exhibit a very interesting deformation behavior when exposed to an externally applied magnetic field. This includes a symmetry change of the director field as well as a shape deformation. The hedgehog point defect develops into a split-core defect in a sufficiently strong field. The split-core defect develops only provided the diamagnetic susceptibility anisotropy is negative – a prediction made ten years ago by Mkaddem and Gartland [123] that we have been able to confirm.

By studying the deformation of these tactoids in a magnetic field we have been able to determine both the splay elastic constant and the interfacial tension in a single experiment by applying a theory that balances surface, elastic, and magnetic forces.

Our approximate theoretical model explains why a minimal (critical) magnetic field strength is required in order to deform the tactoid. The splay elastic constant $K_1 = 0.9$ - $2.6 \cdot 10^{-13}$ N obtained from this critical magnetic field strength is 1.5 to 3 times larger than the previously measured bend elastic constant K_3, and in reasonable agreement with theory and simulations.

The value of $\gamma = 2 \text{ - } 5 \cdot 10^{-7}$ N/m we found for the interfacial tension is significantly larger than found previously for the same system from capillary rise experiments. We attribute this to effects of imperfect surface anchoring neglected in the theory.

Acknowledgements

We would like to acknowledge Ronald Otten for his work on the theoretical model. We also thank Bonny Kuipers for constructing the magnetic polarized light microscopy setup.

6

Tactoids of plate-like particles in a magnetic field

Abstract

We extend the investigation of the effect of a magnetic field on the shape and director field of nematic droplets in dispersions of sterically stabilized gibbsite described in Chapter 5 to charge-stabilized colloidal gibbsite platelets. Depending on the magnetic field strength and tactoid size, we observe several interesting structures, with different shapes and director fields both with and without defects. To account for our observations, we present a calculation of the stability regions of different shapes and director-field structures as a function of tactoid size, anchoring conditions, surface tension, elastic constants and magnetic field strength. By fitting the experimental data to the theoretically predicted structures, we are able to extract values for the splay elastic constant, interfacial tension and anchoring strength. We also reanalyze the results obtained in the previous chapter in terms of the present model. Remarkably, we find significant differences between the two systems studied: for sterically stabilized gibbsite in bromotoluene the anchoring strength is one order of magnitude larger than that of aqueous gibbsite, with the latter exhibiting weak and the former strong anchoring of the director field to the interface. The splay elastic constants that we obtain are in agreement with earlier experiments, simulations and theory, while the interfacial tension and anchoring strength are considerably larger than what was found in earlier experiments.

6.1. Introduction

The isotropic-to-nematic phase transition in dispersions of anisometric colloidal particles is accompanied by the formation of metastable nematic droplets or "tactoids" that eventually coalesce to become a nematic phase on macroscopic scales [153]. The shape and director field of a tactoid are determined by an interplay between its bulk elastic and interfacial free energy [52, 55]. As we have shown in Chapter 4 the balance of these two free energy contributions depends on the tactoid size.

Depending on the size relative to a persistence length, $\xi \equiv K/w$, defined as the ratio between an average Frank elastic constant, K, and the anchoring strength, w, large droplets are spherical with a radial director field and small droplets tend to be flat and oblate shaped because the surface anchoring for plates is preferentially homeotropic.

In the previous chapter, we showed that large tactoids with a radial director field formed in suspensions of sterically stabilised *plate-like* gibbsite particles in bromotoluene respond to an increasing magnetic field not by a continuous deformation but by a sudden rearrangement of the director field if the field strength exceeds a critical value, a phenomenon reminiscent of a Frederiks transition. This is a unique feature of tactoids of plates, because free floating tactoids of *elongated* particles do *not* exhibit a Frederiks transition in a magnetic field: rather they reorient and at sufficiently high field strength become slightly stretched along the field direction [55].

The difference in the behaviour of rod- and plate-like colloidal particles is due to different anchoring conditions to the interface between co-existing isotropic and nematic phases. While colloidal rods favour parallel anchoring to the interface, colloidal plates prefer homeotropic anchoring, resulting in spherical tactoids with a radial director field and a hedgehog defect in the centre of the droplet. Not surprisingly, the spherical symmetry of these tactoids leads to fundamentally different behaviour in an external field. For instance, radial tactoids of particles with a positive magnetic anisotropy should transform to an axial field with ring defect according to theoretical calculations [50, 152] and Monte Carlo simulations [154]. In the previous chapter we have shown that radial tactoids of particles with a negative magnetic anisotropy develop a split-core defect at sufficiently strong magnetic field.

Here, we extend the work on tactoids of sterically stabilized gibbsite platelets in an apolar solvent (bromotoluene) described in the previous chapter to charge-stabilized ones in the polar solvent water. As we shall see, the sterically and charge-stabilized gibbsite systems represent fundamentally different systems governed by a strong versus a weak surface anchoring of the director field. In the former the formation of the split-core defect is associated with an elongation of the tactoids, whilst for the latter this is not so. A macroscopic model accounting for the Frank elastic energy, magnetic energy and surface and anchoring energies rationalizes our findings, and allows us to

extract from our measurements the splay-elastic constant and the ratio of the anchoring strength and surface tension.

Analysis of the data from our earlier experiments on tactoids of sterically stabilized gibbsite in terms of the present model produces values for the splay elastic constant and surface tension that are in agreement with those obtained from the much cruder model described in the previous chapter. This reconfirms our earlier conclusion that the isotropic-nematic surface tension obtained from the tactoid shape differs considerably from that found from capillary rise experiments [64]. We have no explanation for this discrepancy.

6.2. Materials and Methods

We used the charge stabilized gibbsite system dispersed in 10^{-2} M NaCl described in chapter 3.

The gibbsite dispersion was concentrated by centrifugation and subsequent redispersion to attain a concentration in the range where the isotropic and nematic phases coexist, which was 21 v/v% for the sterically stabilized gibbsite and 24 v/v% for the charged gibbsite. The particle number density in the nematic phase, ρ, was estimated to be around $4 \cdot 10^{20}/\mathrm{m}^3$. Samples of the homogenized dispersions were prepared in flat glass capillaries (VitroCom, NJ, USA), with internal dimensions of 200 μm $\times$ 4 mm $\times$ 4 cm. The capillaries were filled by capillary action and subsequently flame-sealed, and glued to avoid evaporation of the solvent. In a few hours tactoids appeared and coalesced to form the nematic phase. Measurements were performed near the end of the phase separation process, typically after a few days to weeks, to minimize the effect of flow fields on the tactoid shape and director field.

Magnetic field experiments were performed as described in Chapter 2. Previous optical and small angle x-ray scattering experiments on suspensions of *sterically stabilized* gibbsite in toluene resulted in a diamagnetic susceptibility anisotropy $\Delta\chi$ of -10^{-22} $\mathrm{J/T^2}$ [85]. This means that the platelets prefer alignment with the director perpendicular to the magnetic field. We expect that the charge-stabilized gibbsite system used here will have approximately the same value, because the platelets are of comparable size.

Tactoid shape and director field were observed directly in the magnetic field with the polarized light microscopy setup described in Chapter 2.

6.3. Experimental results

A typical polarized light micrograph of tactoids in an aqueous suspension of our gibbsite platelets is given in Figure 6.1, showing a group of tactoids of different size and director-field configuration. From groups like the one shown in the figure, we

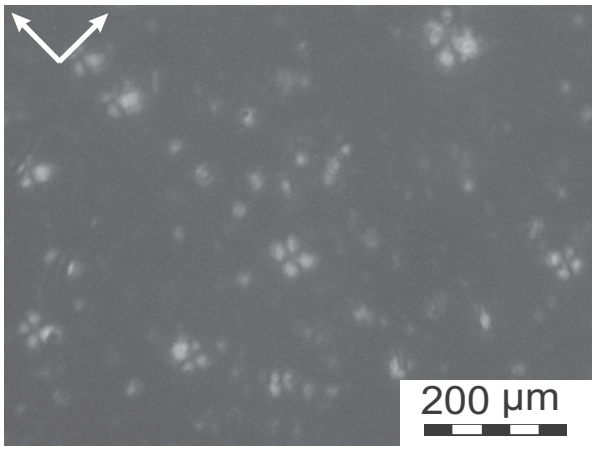

Figure 6.1. Polarization light micrograph showing nematic tactoids of various sizes and director-field configurations in an aqueous suspension of charge-stabilized gibbsite platelets. Arrows indicate the orientation of the polarizers.

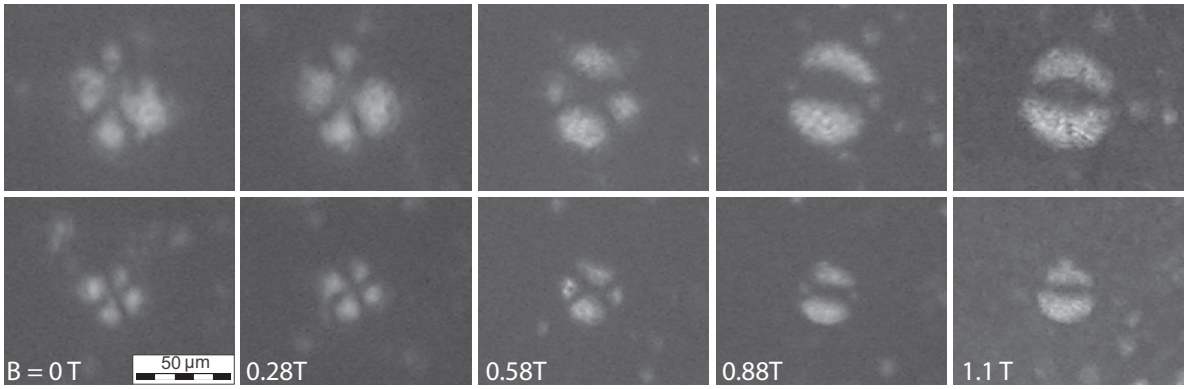

Figure 6.2. Polarization microscopic images, showing tactoids of approximately 30 µm (top row) and 19 µm (bottom row) radius in a dispersion of charge-stabilized gibbsite platelets in water for a series of increasing magnetic field strengths indicated. The orientations of the polarizers and the magnetic field are indicated by arrows in the upper-left corner, and the magnetic field with the horizontal arrow in the lower-left corner. The extinction pattern changes fairly abruptly with increasing field strength. As discussed in the main text, we attribute this to the transformation of a radial director field characterized by a point defect at low magnetic field strength to a so-called split-core line defect that increases in length with increasing magnetic field strength.

investigated the response of representative droplets of different size to the application of a magnetic field.

Figure 6.2 shows how two large tactoids with a radius of ≈ 19 and 30 µm are perturbed by an externally applied magnetic field. At zero field, the tactoids are spherical

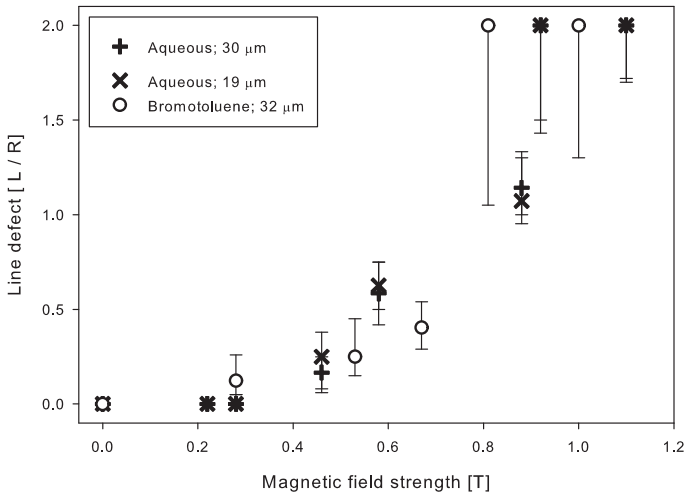

Figure 6.3. Length of the line defect as a function of magnetic field strength, for tactoids of charge-stabilized gibbsite in water (crosses and pluses) and sterically stabilized gibbsite in bromotoluene (circles). Indicated in the box are the (initial) radii of the tactoids. The length of the split-core defect, deduced from the length of the extinction band along the magnetic field shown in Figure 2, is scaled in the aqueous system to the tactoid radius and in bromotoluene with half the tactoid length in the direction of the line defect. See the main text for an explanation of how the line-defect length was exactly measured. We note here that tactoids in bromotoluene do not remain spherical but elongate in the field direction.

and the extinction pattern corresponds to that of a 3D radial director field emanating from a hedgehog point defect in the center of the tactoid (Chapter 4), see also the schematic representation of Figure 6.6(e). This follows from the observation that the diagonal extinction cross, associated with the region where the platelets are aligned parallel to the polarizers, co-rotates with the polarizers.

However, if the magnetic field strength is larger than some critical value that according to our observations seems to depend on the radius of the tactoid, the dark diagonal cross transforms into a horizontal band. As we have pointed out in the previous chapter, this corresponds to a split-core defect structure, with a 2D radial director field in the middle part of the tactoid, while the director field on both sides of this structure remains radial in 3D.

Upon a further increase of the magnetic field, the length of the line defect increases until its length spans the entire tactoid width. For the two tactoids of different radii of Figure 2, this happens at a field strength of about 1 T. The length of the line defect relative to the radius of the tactoid is shown in Figure 6.3, as a function of the magnetic field strength. In contrast to thermotropic liquid crystals where line defects

can actually be observed, in this system the line-defect length has to be deduced from the extinction pattern, which is not trivial. We have determined the length of line defect by extending the diagonal extinction bands shown in Figure 6.2 until they cross the horizontal extinction band along the magnetic field, and then measured the distance between these crossing points. The indicated error bars were determined from the distance of these points to the ends of the horizontal dark band. Although the size of these tactoids differs by a factor of 1.6, the transition from a radial to a split-core type director field seems to take place in the same admittedly somewhat broad range of about 0.3 to 0.6 T. On the other hand, the director-field structures observed at 1.1 T, where for both drops the defect lines seem to traverse the entire drop, are slightly different. The dark horizontal band of the largest tactoid of the two seems slightly wider in the middle, while it is much more uniform in the smaller tactoid. This might indicate that the director field of the largest tactoid is not a purely 2D splay field but may exhibit a slight bend deformation as well.

Experiments described in the previous chapter showed that tactoids of sterically stabilized gibbsite in the apolar solvent bromotoluene display a similar transformation with increasing magnetic field observed in the aqueous system. For comparison, we have plotted in Figure 6.3 the length of the split-core defect in tactoids of sterically stabilized gibbsite as a function of magnetic field strength, in this case scaled with the half the length of the droplet in the direction of the line defect.

It is important to stress that there is a significant difference between the behavior of tactoids in the two types of solvent. For the sterically stabilized gibbsite platelets in bromotoluene, the formation of the split-core defect is accompanied by an elongation of the droplet in the field direction. See also Figure 6.6(g) for a schematic representation. This elongation starts at a slightly higher magnetic field strength than the "stretching" of the point defect into the line defect that we believe to be the split-core defect. In the previous chapter the tactoid elongation was explained by presuming a rigid anchoring of the director field to the interface of the tactoids. The fact that tactoids of the present system of charge-stabilized gibbsite in water remain spherical, despite the emergence of a growing split-core defect with increasing field strength, implies that in this case the anchoring of the director field to the interface must be much weaker. We return to this important issue in our discussion below.

Interestingly, very small tactoids we find to behave rather differently from the larger ones, and in fact do not exhibit the typical Maltese cross extinction pattern typical of a radial director field. This is shown in Figure 6.4, presenting a micrograph series of tactoids up to about 40 μm in diameter in a magnetic field of increasing strength. A retardation plate was used here indicated by the dashed arrow, pointing along the magnetic field direction. At zero field (not shown), these tactoids have different but otherwise uniform colors (orange and blue tints). This means that the tactoids have a

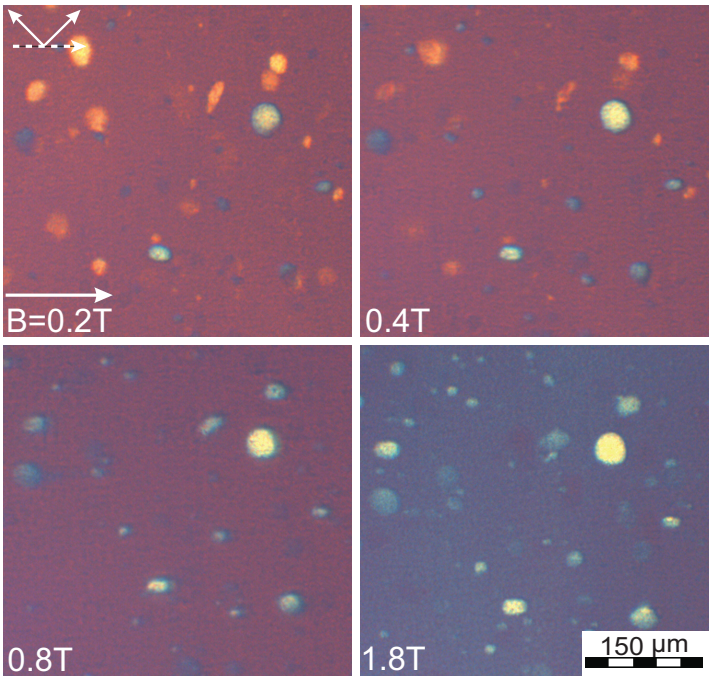

Figure 6.4. Polarization microscopic images showing tactoids of charge-stabilized gibbsite in water with a uniform director field in a magnetic field. Indicated are the orientations of the polarizers (arrows at right angles in the top left-hand corner), retardation plate (dashed arrow), and the magnetic field direction (horizontal arrow). Different colors represent different director orientations, as explained in the main text. The isotropic background aligns in the magnetic field and the tactoids rotate with increasing field strength to orient their director perpendicular to the field direction.

uniform director field and different orientations with respect to the retardation plate. For orange ones the nematic director is oriented parallel and for the blue ones perpendicular to the retardation plate. With increasing magnetic field strength, several changes can be observed.

First, the color of the isotropic background shifts from the magenta-red of the retardation plate to a blue tint. This indicates that the isotropic background phase aligns in the magnetic field and forms a para-nematic phase with the director perpendicular to the retardation plate and the field direction. Second, the color of some of the tactoids turns from orange into blue, indicating that the nematic director rotates from an orientation parallel to the field to that perpendicular to it. Some of the orange-colored tactoids seem to (almost) disappear from view, which plausibly is due to their alignment perpendicular to the focal plane in which case they do not exhibit any birefringence. Blue tactoids display a color shift towards green/yellow, plausibly caused by a slight rotation of the director to a more vertical orientation and possibly also an increase of the nematic order parameter. Note that tactoids also appear blue if the orientation is

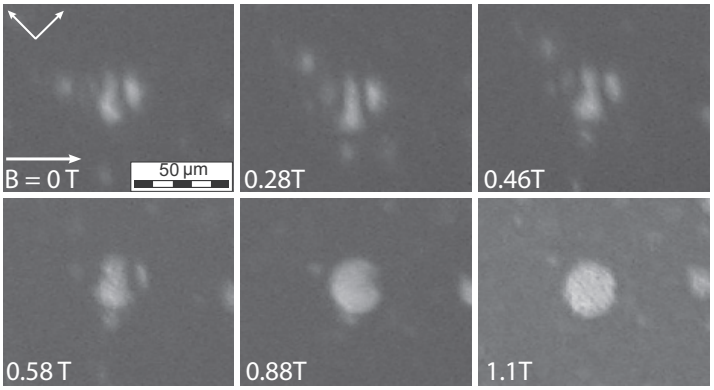

Figure 6.5. Polarization micrograph of an intermediate-sized tactoid with increasing magnetic field strength. Arrows in the upper-left corner indicate the orientation of the polarizers, and the magnetic field direction is indicated by the horizontal arrow. At zero field, the extinction pattern is consistent with an axial director field and a ring defect close to the top of the droplet, where we note that gravitational force points downwards along the vertical. See also figure 7(c). The central part of the tactoid, where the director is more or less uniform and oriented along the vertical direction, becomes larger with increasing field strength until the entire tactoid has a uniform director field.

not completely perpendicular to the retardation plate. Finally, some of the tactoids seem to become slightly elongated in the field direction.

As we shall show in the next section, these observations can be rationalized from the standard continuum theory of nematics. Before we turn to that, we end this section with a brief discussion of how different director fields transform themselves from one to the other.

To this end, we present in Figure 6.5 a tactoid with a director-field structure in between the radial and uniform director fields typical of large and small tactoids, respectively. As we explained in Chapter 4, the transition from a radial tactoid to that with a uniform director field we imagine to be able proceed via two different routes. Plausibly, this may happen either via the continuous displacement of the point defect from the center of the drop to a position outside it where it becomes virtual and eventually move to infinity, or via a transition of the point defect to a ring defect with increasing radius that also becomes virtual if it leaves the droplet.

The director field of the particular tactoid studied here is depicted schematically in Figure 6.6(c) and represents the route where the point defect opens up to become a ring defect with a radius that increases as the drop size decreases. Note that the tactoid sediments towards the nematic phase and that presumably due to the flow fields this ring defect we always find to be on the rear of the drop with respect to the direction of translation [142]. If a magnetic field is applied to this tactoid, the size of the birefringent

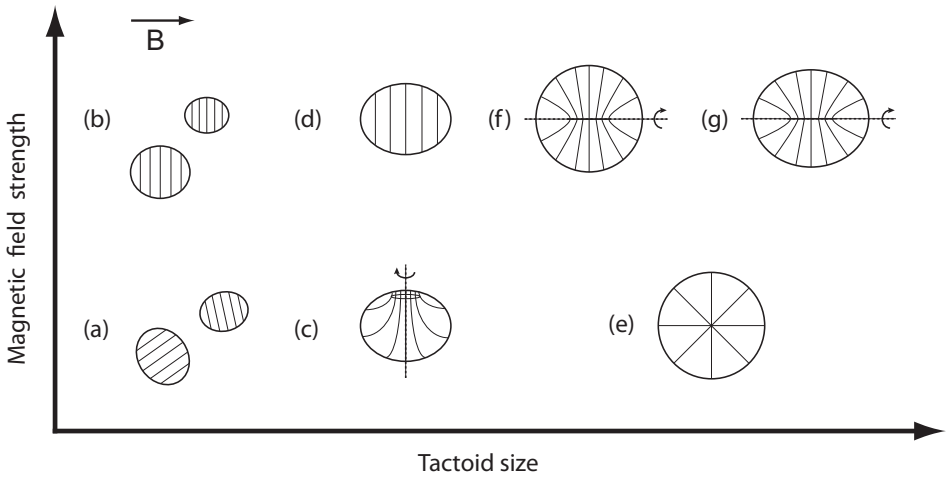

Figure 6.6. Schematic overview of tactoid shapes and director-field configurations observed in dispersions of gibbsite in water (a-f) and in bromotoluene (e-g), as a function of the tactoid size and the magnetic field strength. The arrow indicates the direction of the magnetic field. Note that the main body axis of the platelets (the surface normal) points in the mean along the director. See also figure 8.

part in the center of the tactoid increases with increasing magnetic field strength, which implies that the radius of the ring defect must increase accordingly. This continues until the director field becomes uniformly oriented at a right angle to the magnetic field at a magnetic field strength of 1.1 T. So, the transformation from a non-uniform to a uniform director field with increasing magnetic field strength seems to proceed in a similar way to that in the absence of an external field with decreasing tactoid size.

To summarize our findings, we refer to the overview of the observed director-field structures in Figure 6.6. Different transitions or crossovers can be distinguished as a function of tactoid size, magnetic field strength and solvent type. With increasing magnetic field we find for: (1) small tactoids with uniform director field (a) a reorientation to have their directors positioned perpendicularly to the magnetic field (b); (2) intermediate sized tactoids with a ring defect (c) a transformation to a uniform director field (d); (3) large radial tactoids with a hedgehog defect (e) a transformation to a split-core defect with the drops remaining spherical in a polar solvent (f), or adopting an ellipsoidal shape in an apolar solvent (g).

In the next section we put forward an approximate theory that explains our observations. As we shall see, the theory in fact enables us to extract from the experiments useful physical parameters of the system in hand.

6.4. Theory

It appears that the director field of nematic tactoids in dispersions of gibbsite particles is not fixed but responds to both their size and the strength of the magnetic field. In addition, tactoids of sterically stabilized gibbsite in bromotoluene become elongated in a sufficiently strong magnetic field, whilst those in dispersions of charge-stabilized gibbsite in water remain spherical. In order to rationalize these observations, summarized in Figure 6.6, we present a macroscopic theory based on a competition between the elastic, surface and magnetic properties of drops of a nematic phase freely floating in an isotropic phase.

Our free energy $F = F_E + F_S + F_M$ of a nematic drop of given volume V consists of three contributions:

1) The Oseen-Frank free energy of a deformed director field $\overrightarrow{n}(\overrightarrow{r})$ that in the one-constant approximation reads

$$F_E = \frac{1}{2}K \int d^3\overrightarrow{r} \left[(\overrightarrow{\nabla} \cdot \overrightarrow{n})^2 + (\overrightarrow{\nabla} \times \overrightarrow{n})^2 \right], \tag{6.1}$$

where K is some average of the elastic constants. In our calculations we shall presume only pure splay deformations, in which case $K = K_1$, i.e., the splay elastic constant. The integration over the spatial co-ordinate $\overrightarrow{r}$ is implied to be taken over the entire volume V of the drop;

2) For the interfacial energy we presume a form of the Rapini-Papoular type [139],

$$F_S = \int d^2\overrightarrow{r} \left[\gamma + w - w(\overrightarrow{q} \cdot \overrightarrow{n})^2 \right], \tag{6.2}$$

where the integration is now implied over the entire surface of the drop. Here, γ is the bare surface tension of the drop, w an anchoring free energy per unit area, $\overrightarrow{q} = \overrightarrow{q}(\overrightarrow{r})$ the surface normal and $\overrightarrow{n}$ the director field at the interface. Platelets for entropic reasons prefer homeotropic alignment [64], so $w > 0$;

(3) The magnetic energy of a nematic drop obeys [57]

$$F_M = -\frac{1}{2}\rho\Delta\chi \int d^3\overrightarrow{r} (\overrightarrow{n} \cdot \overrightarrow{B})^2, \tag{6.3}$$

where ρ is the particle number density, $\Delta\chi$ the diamagnetic susceptibility anisotropy, and $\overrightarrow{B}$ the magnetic field vector. Our gibbsite platelets have a negative magnetic susceptibility, so $\Delta\chi < 0$ [85, 87].

In principle, we would need to minimize the free energy with respect to the director field and shape of the interface, given the fixed volume of the drop and given that the norm of the director is by definition equal to unity. This produces a constrained free boundary value problem that is very hard to solve, even numerically. So, we choose to simplify the problem by presuming the director field either to be uniform or to consist of a pure splay type. For a uniform field we apply the well-known Wulff construction [128]

to find the optimal shape. For the pure splay field we presume a line defect of given length to be in the center of the drop that in turn we presume to be of prolate shape, i.e., to be an ellipsoid of revolution. The director field over the entire length of the disclination line is presumed to be a 2D radial splay field, whilst in the remainder of the drop we presume a 3D splay field emanating from the split-core defect at the ends of the disclination line. We optimize both the length of the line defect and the aspect ratio of the drop. This we do perturbatively for aspect ratios near unity, i.e., for drops that are not very elongated, in line with our observations. Stability diagrams are calculated by comparing free energies of various types of drop, schematically presented in Figure 6.7.

In the following only an outline of the main results of our model are presented. A detailed account of our calculations, which are quite non-trivial, shall be given elsewhere [155]. We summarize our results in stability diagrams in Figure 6.9 that show the optimal tactoid shape and director field as a function of the three for the problem relevant dimensionless groups associated with the tactoid size, the anchoring strength of the director field the tactoid's surface, and the magnetic field strength. These dimensionless groups are $\Re \equiv R\gamma/K_1$, where R is the radius of the equivalent spherical drop, $\omega \equiv w/\gamma$ a dimensionless anchoring strength, and $\beta^2 \equiv -\rho\Delta\chi B^2 K_1/\gamma^2$, with B the strength of the magnetic field. There is also a fourth dimensionless group, $\aleph \equiv b\gamma/K_1$, associated with the core of the line defect the radius of which is presumed to be of order b. As b must be a microscopic length in lyotropic nematics [156, 157], i.e., on the scale of the diameter of the platelets, its magnitude can only be estimated (Chapter 5). Fortunately, $\aleph$ enters our equations only logarithmically so our results depend only very weakly on its value.

Before discussing our phase diagrams in more detail, it is useful to consider explicitly the driving forces for the transitions between the different tactoid shapes and director-field configurations presented in the previous section, and shown schematically in Figure 6.7. We can distinguish between droplets with perfect and imperfect planar alignment of the platelets to the surface, corresponding to perfect and imperfect homeotropic anchoring, see Figure 6.7. Clearly, a drop with a uniform director field has an imperfect anchoring. In this case, there is no deformation of the director field but also the magnetic energy is minimal because the drop is able to orient and align itself in the magnetic field. The alignment of the director field is perpendicular to the magnetic field on account of the negative diamagnetic susceptibility of the particles.

We conclude that for a drop with a uniform field the only free-energy cost is that associated with the imperfect surface anchoring, which incidentally can be minimized further by deforming the shape of the drop. Because of the preferred homeotropic surface anchoring the tactoids tend to become oblate-shaped and flatter the larger the dimensionless anchoring strength $\omega \equiv w/\gamma > 0$, the sole parameter that dictates the

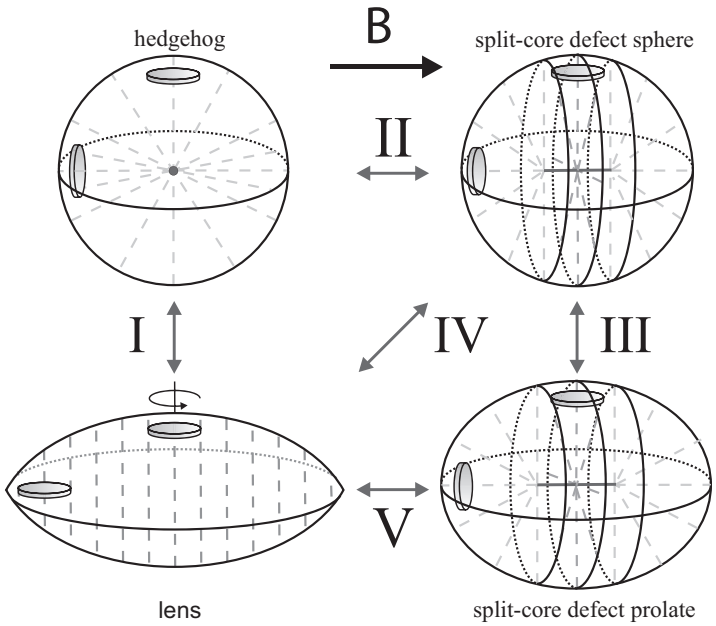

Figure 6.7. Schematic representation of the main droplet shapes and director fields, indicated by dashed lines, consistent with our observations. The competition between homeotropic surface anchoring, surface tension, elastic deformation and the magnetic field B gives rise to transitions between at least four types of tactoid, indicated by the Roman numerals I-V. The radial director field of the spherical tactoid with a hedgehog defect (top left) has perfect anchoring and minimal surface tension but has a suboptimal magnetic energy. Replacing the point defect by split-core line defect (top right) lowers the magnetic energy but increases the anchoring energy. Elongating the split-core droplet lowers the magnetic and anchoring energy at the expense of the surface energy. The lowest magnetic energy has a tactoid with a uniform field (bottom left). Its shape minimises the sum of the anchoring and surface energies, for homeotropic anchoring producing a lens-shaped object. The disks are not drawn to scale and serve to indicate the platelet orientations in the various drops.

shape of a drop with a uniform director field. Invoking the Wulff construction [128], we find that for $\omega \geq 1$ the oblate in fact transforms to a lens with a sharp rim. Interestingly, the difference in free energy between the exact Wulff shape and a lens constructed from two cut spheres and optimized with respect to the cutting angle is minute (less than 0.5 %) for all values of ω, so we for simplicity used this lens shape for constructing our stability diagrams.

For spherical tactoids, perfect or "strong" anchoring conditions are fulfilled by a three-dimensional radial director field that radiates outward from a hedgehog point defect in the center of the drop, see Figure 6.7. For this configuration, anchoring is ideal but the

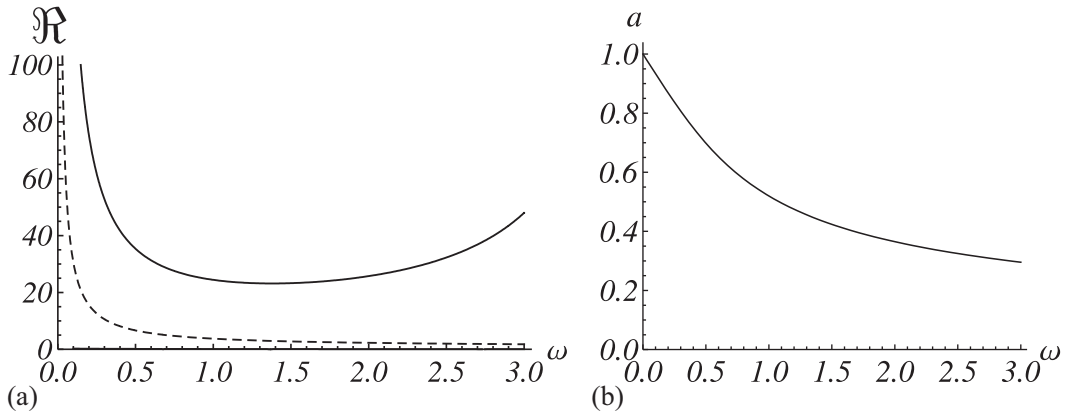

Figure 6.8. (a) The critical value of the dimensionless tactoid size $\Re \equiv R\gamma/K_1$ for the transition from a uniform to a radial director field as a function of the dimensionless anchoring strength $\omega \equiv w/\gamma$. Indicated by the dashed line is the critical value at zero magnetic field with $\beta^2 \equiv -\rho\Delta\chi B^2 K_1/\gamma^2 = 0$, and the solid line shows the limit for a very strong magnetic field where the defect is stretched through the entire tactoid ($L/R = 2$), which is the vertical asymptote (dotted line) in the phase diagram in Figure 6.10. (b) The aspect ratio a of the lens shape, i.e., the ratio of its thickness to its diameter, is determined completely by ω, and for the values in the phase diagram, i.e., $\omega \in (0.25, 2)$, it ranges from 0.84 to 0.36.

director field is distorted and the orientation of a part of the particles is suboptimal relative to the magnetic field that, again, prefers to align them perpendicular to it. The hedgehog director-field configuration wins out over the uniform one if the product $\Re \times \omega = Rw/K_1$ is large enough by an amount that is set by the dimensionless group $\beta^2 \equiv -\rho\Delta\chi B^2 K_1/\gamma^2$. In zero magnetic field this happens if $\Re\omega > 3$ for spherical drops and a slightly higher value for the transition from the lens to a spherical hedgehog, see Figure 6.8. This implies that if we observe the transition for a given tactoid size and if we establish the value of the elastic constant independently, this inequality produces a lower bound for w. We return to this in the discussion.

It follows that the hedgehog configuration is not favorable for a sufficiently small tactoid [60, 63]. For a strong enough magnetic field it cannot be maintained either, because then the magnetic energy penalty becomes prohibitively large. To allow more particles to comply with the preference imposed by the magnetic field, the drop can either adopt a uniform director field at the expense of imperfect anchoring or "stretch" the point defect to a line defect of topological charge +1 in the direction of the magnetic field. See Figure 6.7. In this split-core defect structure discussed in the preceding sections, perfect surface anchoring cannot be maintained albeit that it can be reduced by elongating the drop. This obviously can only happen at the expense of a surface energy. In comparison with the hedgehog configuration the split-core configuration

has a lower magnetic energy penalty, which may even become zero if the defect line runs through the entire tactoid but it does have a higher elastic deformation energy, a non-zero anchoring penalty and potentially a higher surface energy.

In our numerical calculations summarized in Figure 6.9, we set the value of the dimensionless anchoring strength equal to $\omega = 0.25, 0.5, 1$ and 2, where we note that a value around $\omega = 0.5$ was deduced from capillary-rise experiments for sterically stabilized gibbsite platelets in toluene [64]. In the limit of $\omega \to 0$ the free-energy cost of increasing of the surface area is infinite, implying that the tactoids remain spherical. The stability diagrams presented in Figure 6.9 show that, as expected, a sufficiently small tactoid has a homogeneous director field for any magnetic field strength because of the predominance of the Frank elastic energy. Larger tactoids adopt a hedgehog configuration for weak magnetic fields and a line defect that runs through the entire drop for very large magnetic fields, on account of the predominance of the anchoring energy. As advertised, the cross-over size in the absence and presence of a strong magnetic field can provide information on the anchoring strength and its dependence on ω is shown in Figure 6.8.

How the transition between a uniform and a hedgehog configuration proceeds we do not know for certain but it may involve either a hedgehog defect or a small ring defect that moves in from outside of the drop, where it is virtual. Indeed, we have in the previous section seen configurations with a defect that is close to the tactoid's surface. However, if we model a 3D radial director field emanating from a point defect that is off center, then it turns out that this configuration is always energetically more expensive than the central hedgehog or the lens with a uniform field (Chapter 4). Therefore, we conclude that the tactoid with boundary defect must be a metastable configuration and because of its relatively high free energy is absent in our phase diagram. We speculate that the observed configuration is stabilized by the flow field caused by the sedimentation [142].

The second transition we find in the diagrams is that of spherical drops with a central hedgehog to those with a split core. This transition happens for a sufficiently strong magnetic field and allows more particles to adopt the magnetically preferred orientation. The critical magnetic field strength B_c associated with this Frederiks-type of transition obeys

$$B_c^2 = \frac{4K_1}{\rho\Delta\chi R^2}\left(\log\left(\frac{b}{R}\right) + 2\right), \tag{6.4}$$

where b is the diameter of the core of the line defect that we expect to be of the order of the plate diameter. This expression differs by a factor of two thirds from our earlier, more approximate theory based on the presumption of perfect anchoring requiring the drop to stretch with increasing length of the split-core defect (Chapter 5). Eq. (6.4)

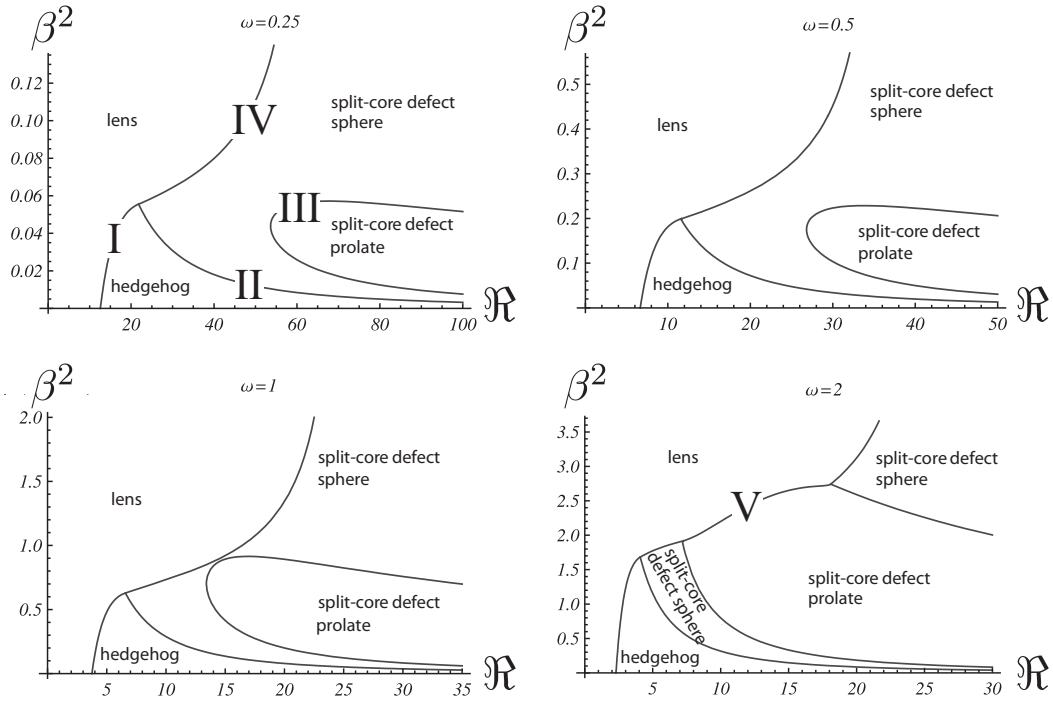

Figure 6.9. Phase diagram with a lens-shaped tactoid with uniform field, a spherical hedgehog, a spherical and prolate tactoid, both with split-core defect, for $\omega = 0.25$ (top left), $\omega = 0.5$ (top right), $\omega = 1$ (bottom left) and $\omega = 2$ (bottom right). The axes indicate dimensionless measures $\beta^2 \equiv -\rho\Delta\chi B^2 K_1/\gamma^2$ of the magnetic field strength B and $\Re \equiv R\gamma/K_1$ of the size of the tactoids, see the main text. The radius R of the spherical drops defines the volume of the tactoids, which for a given R is equal for all configurations. The Roman numerals correspond to the transitions as indicated in Figure 6.7. The transitions I, II, III and IV occur in every diagram, and transition V only occurs for $\omega = 2$.

is independent of ω because at the onset of the transition from hedgehog to split-core defect, the anchoring is still perfectly homeotropic. Given that we now allow for imperfect anchoring, the length of the defect increases with the magnetic field strength without stretching the drop. For very strong fields the line defect stretches throughout the entire tactoid to eliminate the magnetic energy cost altogether.

We find that for all four values of ω of Figure 6.9, there is a region of sizes and magnetic field strengths where tactoids are not spherical or lens-shaped, but elongated. These elongated tactoids have a split-core defect along their main axis, and their region of stability is larger for larger values of ω. The reason for this is that the ellipsoid has a lower anchoring energy than the equivalent sphere with line defect. For increasing magnetic field strength a sufficiently large spherical drop with a split-core defect stretches to an ellipsoid. This transition takes place at a magnetic field strength that we denote

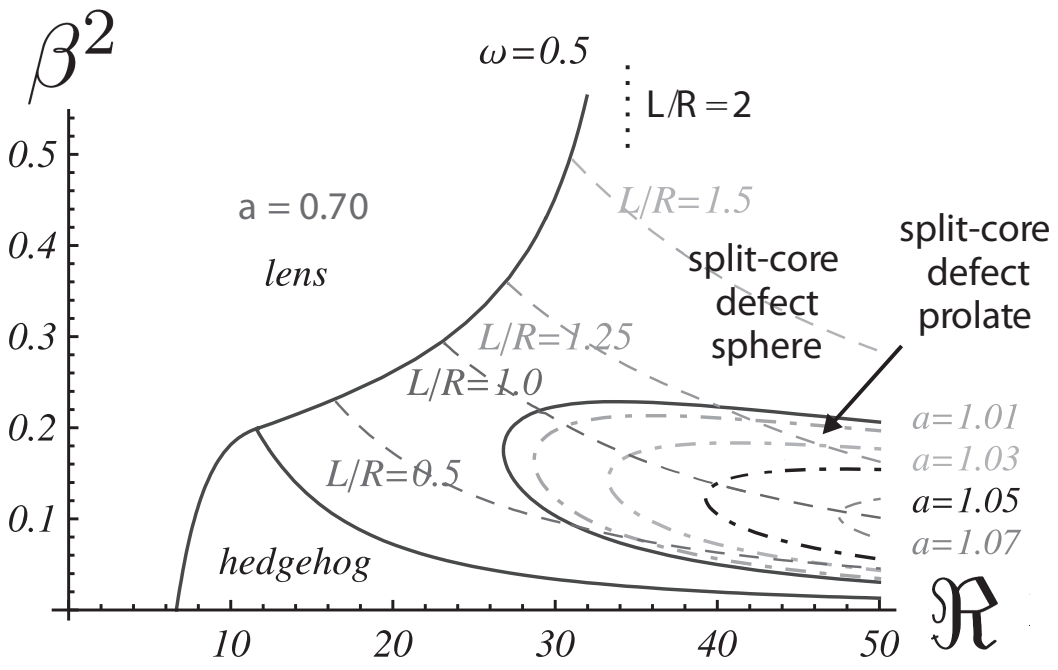

FIGURE 6.10. The phase diagram from Figure 6.9 for $\omega = 0.5$ with the structural details of the line-defect length and the aspect ratio. The dashed lines indicate a constant defect length L, relative to the sphere radius R. The dotted line shows the limit of $L/R = 2$, i.e., a split-core defect through the entire tactoid. The dash-dotted lines in the ellipsoid region have a constant aspect ratio a, where $a = 1$ at the transition from sphere to ellipsoid. The exact shape of the lens depends only on ω and its aspect ratio is 0.70 for $\omega = 0.5$.

by B_*, and is a very complicated expression that we present in a separate publication [155]. At this critical point the length of the defect line is about half the radius of the drop, $L \approx 0.5R$. The length of the line defect increases with increasing magnetic field strength, see Figure 6.10. The length of the line defect in the elongated drop is larger than that in equivalent spherical tactoid, as follows from the slight downward deflection of the lines of constant L/R in the ellipsoid region.

Interestingly, the aspect ratio of the drops at some point decreases again with increasing magnetic field strength, i.e., depends non monotonically on the magnetic field strength. For high enough fields the drops become spherical again, see also Figure 6.10. This is caused by the change in the line-defect length that affects the balance between the magnetic and anchoring energy. For large enough anchoring energies, elongated tactoid structures push out spherical hedgehog and split-core tactoids from the phase diagram. The maximum value of the aspect ratio observed is dictated by ω, allowing us to estimate this quantity from experiments.

In the following sections we apply the theory to our experimental data on charge-stabilized gibbsite in water. We also re-evaluate our previous findings on sterically

stabilized gibbsite in bromotoluene. These two cases correspond to very different values of ω, and are examples of weak and strong anchoring.

6.5. Fitting procedure

If we compare the experimentally observed shape and director-field transitions with those of the theory developed in the previous section, we find that all of the ones shown in Figure 6.6 are found in the predicted phase diagrams, except for the transitional structures associated with the point or ring defect near the surface of the tactoid. We believe on theoretical grounds that this configuration is not stable in a quiescent tactoid and may be caused by the flow field resulting from the sedimentation process, because those that we find have them always located on the far side of the moving drop. It is well established that flow fields influence director-field structures in nematic drops [142].

In fact, we are able to directly apply the theoretical model described in the previous section to the experimental data, and extract material parameters relating to our liquid crystal droplets. Of particular use here are the degree of tactoid elongation and length of the split-core defect, obtained as a function of the magnetic field strength and the size of the drops. Because of the numerous ways in which the parameters can be determined, we first give an outline of the approach that we have taken, and present the resulting curve fits and parameter values in the next section. Readers not interested in the technicalities of our fitting procedures may wish to directly jump to that section.

The two types of system investigated, i.e., the sterically stabilized gibbsite in the apolar solvent bromotoluene and the charged-stabilized gibbsite in the polar solvent water, turn out to provide us with examples of two limiting cases in terms of the dimensionless anchoring strength $\omega \equiv w/\gamma$. The drops found in the aqueous gibbsite dispersions exhibit no discernable deviation from the spherical shape, implying a high surface tension relative to the anchoring energy, so $\omega \to 0$. So, in this limit the model is independent of the surface tension γ and this necessitates a slight modification of the state diagrams such as plotted in Figure 6.9, where on both the horizontal and vertical axes we replace γ by w, so with the dimensionless groups $-\rho\Delta\chi B^2 K_1/w^2 \equiv \beta^2/\omega^2$ and $Rw/K_1 = \Re\omega$ on the axes. For the drops found in dispersions of sterically stabilized gibbsite, the energetic penalty for an increase in the surface area is not that large because they do become visibly elongated at high field strengths albeit not hugely so, implying $\omega \approx 1$.

There are a number of ways to determine the value of the parameters K_1, γ, and w from fitting the model to the experimental data. The data of both the length of the split-core defect and the tactoid elongation are a function of the magnetic field strength, which means that for the curve fits we have to traverse the phase diagrams vertically for a chosen scaled drop size $\Re \equiv R\gamma/K_1$ (for the sterically stabilized system) or $\Re\omega$ (for the charge-stabilized system) that has the best match with the data points of the

line-defect length or tactoid aspect ratio. The quality of this match is then determined by choosing the value of the dimension-bearing quantities $B^2/\beta^2 = \gamma^2/(-\rho\Delta\chi K_1)$ or $\omega^2 B^2/\beta^2 = w^2/(-\rho\Delta\chi K_1)$ depending on the type of system; and the curve fitting amounts to finding a compromise between the best fit to the critical magnetic field strengths where the aspect ratio (B_*) or split-core defect (B_c) starts to grow, and the best fit to the data beyond those critical field strengths. These two choices then produce a value for γ/K_1 and one for γ^2/K_1 for the sterically stabilized system and for w/K_1 and w^2/K_1 for the charge-stabilized gibbsite, from which both individual parameter values can be deduced.

The fact that in this way we find two slightly different values for B_c despite the fact that B_c in Eq. (6.4) is independent of ω, is caused by the choice of $\aleph = b\gamma/K_1$, associated with the core of the line defect. We take it as a constant, which is not exactly true for the different values of γ and K_1 in both fits, but the logarithmic dependence makes the difference in B_c quite small. We also remark that even though in both systems we did observe a line defect running throughout the entire tactoid at very high field strengths, as shown in Figure 6.3, we omit these last few data points from our curve-fitting procedure. The reason is that including these points would make the general fit to the other points very poor indeed, e.g., with a critical magnetic field strength that vanishes almost completely and, more worryingly, give the fitted curve the wrong curvature. On the other hand, and in support of this choice, it is also true that the experimental points at high magnetic field strength have a large degree of uncertainty because the contrast strongly diminishes as the "isotropic" (or rather, paranematic) background also aligns in the magnetic field. By way of consistency check, we use the analytic Eq. (6.4) for B_c in combination with the experimental data of Figure 6.3 to derive a value for K_1 that we compare with the values found from our curve fitting procedure.

For the curve fitting to the tactoid elongation data that we have obtained for the sterically stabilized system, there is an additional constraint that we require a minimum value of ω for the observed aspect ratios to occur in the phase diagram. This value turns out to be higher than expected from previous experiments in gibbsite platelets [64], which, in fact, is an important observation that we return to later. A value of $\omega = 1.5$ turns out not to suffice, but $\omega = 2$ does and gives a good fit, so we choose to take this value, which agrees with density functional simulations on hard rectangular platelets [106]. Here, it must be noted that a value that is, say, 10 % smaller or larger presumably also allows for an acceptable fit.

Finally, as already alluded to in the previous section, the emergence of a radial hedgehog director field in the absence of a magnetic field produces a lower bound for the anchoring strength, because this happens according to our theory only if $w > 3K_1/R$. Strictly speaking this is true only for the transition from a spherical drop with a uniform

field to a radial field; a slightly sharper, i.e., higher, lower bound can be found if we allow for the equilibrium lens shape, shown in Figure 6.8. For convenience we use the simple, but very accurate result that follows from the spherical drops, so then the choice for ω and $\Re$ then requires that $\Re\omega > 3$. The values for ω, γ and w that follow from these choices and lower bound mentioned above should then all be internally consistent. Because we have observed uniform tactoids in the aqueous gibbsite system, we have yet another check for the obtained values for K_1 and w, because we can independently determine the ratio of K_1/w from the tactoid size where the cross-over from a uniform to a radial director field takes place.

Results of our curve-fitting efforts are discussed next.

6.6. Analysis

6.6.1. Sterically stabilized gibbsite in bromotoluene

Let us first deal with the droplets consisting of the sterically stabilized platelets in bromotoluene, where we rely on the same data for the tactoid elongation as in the previous chapter, where we presumed perfect homeotropic surface anchoring. Hence, we reanalyze these data in the light of our more accurate model described in this work, allowing us to assess the effect of imperfect anchoring on the value of the obtained surface tension, γ.

We begin with a curve fit of our model to the measured length of the split-core defect (Figure 6.3) of a tactoid with an initial radius of 32 μm in this system. As we noticed in the previous section, we omit the data points at high magnetic field strength. The value of $\Re$ that produces the best fit to the critical magnetic field strength turns out to be $\Re = 100$, which is rather large, as we will see later. We obtain lower and upper bounds for the interfacial tension γ and the elastic constant K_1, of $\gamma = 2.1 \cdot 10^{-7}$ N/m and $\gamma = 2.8 \cdot 10^{-7}$ N/m, and $K_1 = 0.4 \cdot 10^{-13}$ N and $K_1 = 0.6 \cdot 10^{-13}$ N respectively, with $B_c = 0.16$ T and $B_c = 0.18$ T, see Figure 6.11. From Eq. (6.4) we can obtain another value for K_1 by determining B_c from the data for the defect length in Figure 6.3. We determine $B_c = 0.18 \pm 0.2$ T, which results in a value for $K_1 = 1.1 \pm 0.5 \cdot 10^{-13}$ N. These values agree reassuringly well, implying that we believe them to be robust.

Next, we attempt to confirm the previous analysis by a curve fit of our model this time to the aspect ratio of two elongated tactoids with an initial radius of 28 and 31 μm respectively, again for the system of sterically stabilized gibbsite. In order to obtain the correct aspect ratio of $a \approx 1.3$ for the tactoids, we have to take $\omega = 2$ as described above. The value of $\Re$ that produces the best fit to the critical magnetic field strength is smaller than in our curve fitting to the length of the split-core line defect, because the critical field strength B_c needed to elongate a tactoid is larger. For the tactoid of 28 μm we take $\Re = 25$, and the condition that $\Re\omega > 3$ is then also satisfied. See Figure 6.12. From the fit we find $B_* = 0.47$ T and a value of $\gamma = 0.9 \cdot 10^{-7}$ N/m with a lower

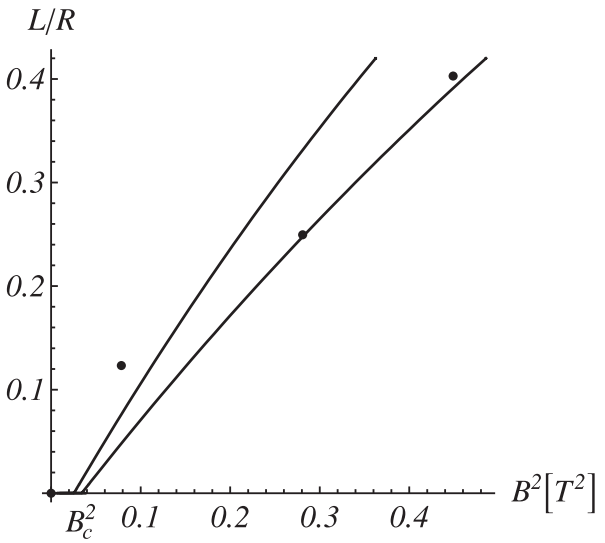

FIGURE 6.11. Ratio of the length of the split-core defect and the radius of the drop, L/R, as a function of the square of the magnetic field strength B^2 for a tactoid in a suspension of sterically stabilized gibbsite in bromotoluene. Tactoid radius: $R = 32$ μm. Experimental data: points, theoretical fits to the data: drawn lines. In order to get good agreement for both the critical magnetic field strength and the ratio L/R, we derive a lower and upper bound for $B^2/\beta^2 = \gamma^2/(-\rho\Delta\chi K_1)$. We find $B^2/\beta^2 = 25$ T^2 (left drawn curve) and $B^2/\beta^2 = 35$ T^2 (right drawn curve), respectively. See also the main text.

and upper bound of $\gamma = 0.6 \cdot 10^{-7}$ N/m and $\gamma = 1.2 \cdot 10^{-7}$ N/m. The same fit gives $K_1 = 1.0 \cdot 10^{-13}$ N, with bounds $K_1 = 0.7 \cdot 10^{-13}$ N and $K_1 = 1.3 \cdot 10^{-13}$ N. For the drop with a radius of 31 μm we take $\Re = 23$ and the best fit then produces $B_* = 0.30$ T and values of γ and K_1 of $\gamma = 0.4 \cdot 10^{-7}$ N/m with a lower and upper bound of $\gamma = 0.2 \cdot 10^{-7}$ N/m and $\gamma = 0.7 \cdot 10^{-7}$ N/m, and $K_1 = 0.5 \cdot 10^{-13}$ N, with bounds $K_1 = 0.3 \cdot 10^{-13}$ N and $K_1 = 1.0 \cdot 10^{-13}$ N. Again, these values are quite consistent with those obtained for the smaller drop.

Comparison of the found values for B_c (the critical field strength at which the line defect starts to grow) and B_* (the critical field strength at which the tactoid elongation starts) shows that $B_c < B_*$, in agreement with what was found in the theoretical model: upon an increase of the magnetic field first the point defect stretches to a line defect and subsequently at higher magnetic field strength the tactoid is elongated in the field direction. The theory also predicts that the tactoid should become spherical again at even higher magnetic field strength but this was not confirmed in our experiments. It must be noted, though, that at high magnetic field strength a precise measurement of the tactoid properties becomes increasingly difficult, due to alignment of the isotropic background.

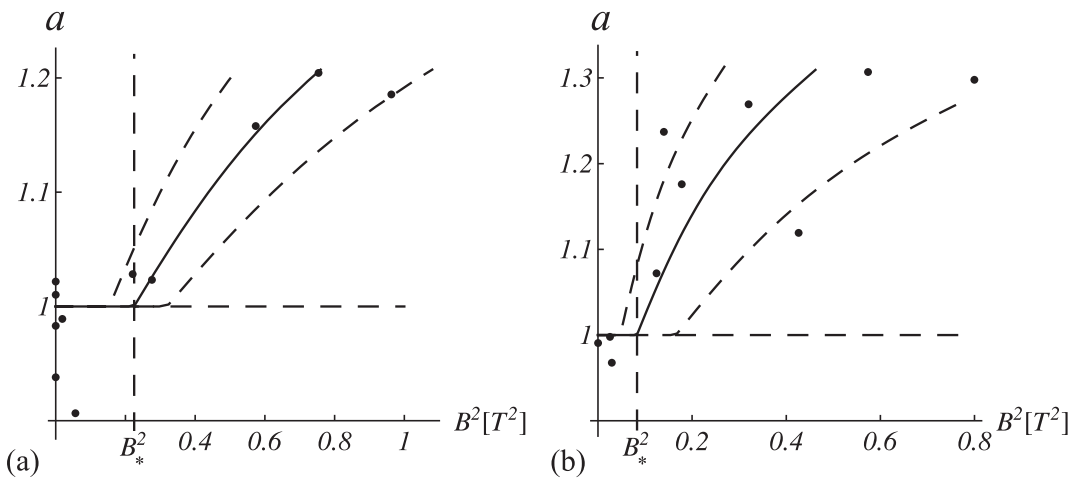

FIGURE 6.12. The aspect ratio a of two tactoids in the sterically stabilized gibbsite dispersion as a function of the square of the magnetic field strength B^2, where both the critical magnetic field strength B_* and the values of a are fitted. The points represent experimental data and the solid lines are fits to our model. For both fits $\omega = 2$ has been taken to reach the desired aspect ratios. The fit gives a value for $B^2/\beta^2 = \gamma^2/(-\rho\Delta\chi K_1)$ and the dashed lines indicate a lower and upper bound (see the main text). (a) Tactoid with $R = 28$ μm with $B^2/\beta^2 = 1.9$ T^2, giving $\gamma = 0.9 \cdot 10^{-7}$ N/m and $K_1 = 1.0 \cdot 10^{-13}$ N. (b) Tactoid with $R = 31$ μm with $B^2/\beta^2 = 0.7$ T^2 (solid line), giving $\gamma = 0.4 \cdot 10^{-7}$ N/m and $K_1 = 0.5 \cdot 10^{-13}$ N.

All the obtained values for γ and K_1 are summarized in Table 6.1, which also shows the values from the cited earlier work, obtained with a model that assumed complete anchoring described in the previous chapter. If we compare the values for γ obtained from the tactoid elongation with both models, it is clear that significantly lower values are obtained when incomplete anchoring is taken into account, $(0.4 - 0.9) \cdot 10^{-7}$ N/m versus $(2-5)\cdot 10^{-7}$ N/m, in agreement with the expectation put forward in the previous chapter. However, the value we obtained with the new model by the fitting of the length of the line defect as a function of magnetic field strength is somewhat larger, namely $2.5 \pm 0.4 \cdot 10^{-7}$ N/m, which results in an average value for the interfacial tension of sterically gibbsite in bromotoluene of $\gamma = 1.3 \cdot 10^{-7}$ N/m. So, all of the values of the surface tension we extract from the tactoid experiments are much larger than the value of $\gamma = 3 \cdot 10^{-9}$ N/m obtained from capillary-rise experiments, in the comparable system of sterically stabilized gibbsite in toluene as opposed to bromotoluene [64]. We come back on some of the drawbacks of our tactoid model below, although we do not believe these drawbacks can actually explain this discrepancy. The values for the elastic splay constant K_1 of both the fits to the line-defect length and the aspect ratio and B_c produce an average of $0.8 \pm 0.3 \cdot 10^{-13}$ N, which is somewhat smaller than the values that we established in our previous work of $K_1 = 0.9 - 2.6 \cdot 10^{-13}$ N, yet still consistent.

Table 6.1. Results of the fitting procedure for sterically stabilized gibbsite in bromotoluene. The first three columns of the table give values for K_1 from Eq. (6.4) for B_c and average values for K_1 and γ that follow from the upper and lower bound fits of the model to the relative split-core-defect length L/R, as depicted in Figure 6.11. The next two columns give the best fit values for for K_1 and γ that follow from the fits of the model to the elongation of the tactoid, i.e., the aspect ratio a, as depicted in Figure 6.12. The last column presents results obtained with the old model involving complete anchoring ($\omega \to \infty$).

	$\omega = 2$					$\omega \to \infty$
	line defect			elongation		elongation
	K_1 [10^{-13}N]	K_1 [10^{-13}N]	γ [10^{-7}N/m]	K_1 [10^{-13}N]	γ [10^{-7}N/m]	γ [10^{-7}N/m]
	B_c	fit L/R		fit a		fit a
$R = 32$ μm	1.1 ± 0.5	0.5 ± 0.1	2.5 ± 0.4	-	-	-
$R = 28$ μm	-	-	-	1.0 ± 0.3	0.9 ± 0.3	5 ± 2
$R = 31$ μm	-	-	-	0.5 ± 0.5 [a]	0.4 ± 0.3	3 ± 2

[a] This rather large value of the error is a consequence of the fact that the upper and lower bounds are asymmetrically deviating from the best fit, thus the lower bound is in fact not zero, but $0.3 \cdot 10^{-13}$ N.

6.6.2. Charge-stabilized gibbsite in water

Now we turn to the spherical tactoids in dispersions of charge-stabilized gibbsite in water, tactoids that do not deform even for the highest magnetic field strengths tested. As explained in the previous section, the fitting procedure for the length of the split-core defect in the charge-stabilized system is equal to that in the sterically stabilized system, apart from the fact that γ is now replaced by w. We have to find the value of $\Re\omega$ that gives the best agreement with the critical magnetic field strength B_c, where we again disregard the points at very high field strengths where $L/R \approx 2$. The fits give a lower and upper bound for $\omega^2 B^2/\beta^2 = w^2/(-\rho\Delta\chi K_1)$.

We use the measured length of the split-core defect of two tactoids of radius 30 and 19 μm, respectively, as depicted in Figure 6.3. For the drop with $R = 30$ μm we take the value $\Re\omega = 10$, and the fits with the best curvature and the best fit to the data give a lower and upper bound for w of $w = 4.8 \cdot 10^{-8}$ N/m and $w = 6.0 \cdot 10^{-8}$ N/m, and K_1 between $1.4 \cdot 10^{-13}$ N and $1.8 \cdot 10^{-13}$ N, where the critical magnetic field strengths vary between $B_c = 0.34$ T and $B_c = 0.38$ T, see Figure 6.13. If we use Eq. (6.4) with the data in Figure 6.3 we find $B_c = 0.34 \pm 0.2$ T, which results in a value for $K_1 = 3.5 \pm 0.4 \cdot 10^{-13}$ N. For the smaller drop with $R = 19$ μm we take the proportional value $\Re\omega = 6.3$, and we find from the best fit to the data bounds of w of $w = 2.2 \cdot 10^{-8}$

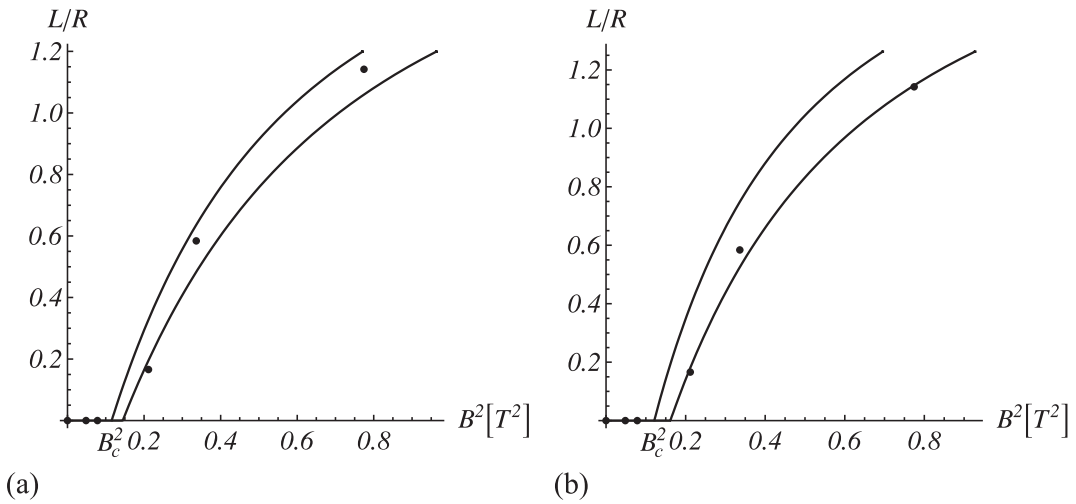

Figure 6.13. Ratio of the length of the split-core defect relative to the tactoid radius, L/R, as a function of the square of the magnetic field strength B^2 for the case of charge-stabilized gibbsite in water. Experimental data: points, the left and right drawn curves: theoretical curves, optimised with respect to the critical magnetic field strength B_c and to the experimental values of L/R at larger field strengths. (a) Tactoid of $R = 30$ μm with $\omega^2 B^2/\beta^2 = 0.4$ T^2 and $B_c = 0.34$ T (left drawn curve) and $\omega^2 B^2/\beta^2 = 0.5$ T^2 and $B_c = 0.38$ T (right drawn curve). (b) Tactoid of $R = 19$ μm with $\omega^2 B^2/\beta^2 = 0.18$ T^2 and $\omega^2 B^2/\beta^2 = 0.24$ T^2, giving $B_c = 0.35$ T and $B_c = 0.40$ T, respectively. See also the main text.

N/m and $w = 2.9 \cdot 10^{-8}$ N/m, and K_1 between $6.5 \cdot 10^{-14}$ N and $8.7 \cdot 10^{-14}$ N, and B_c between 0.35 T and 0.40 T. From Eq. (6.4) and Figure 6.3 we find $B_c = 0.32 \pm 0.2$ T and $K_1 = 1.4 \pm 0.2 \cdot 10^{-13}$ N. These values for K_1 are again reasonably consistent with each other.

The values for the elastic constant K_1 and the anchoring strength w in aqueous gibbsite that we obtained from the fits of the theoretical model to the experimental data are summarized in Table 6.2. If we average the obtained values we find for K_1 a value of $2 \pm 1 \cdot 10^{-13}$ N, and for w a value of $4 \pm 2 \cdot 10^{-8}$ N/m. It is, we repeat, not possible to extract a value for γ in aqueous gibbsite suspensions because the tactoids remain spherical, at least to within the measurement error. What we can say, though, is that ω must be at least smaller than 1, and γ therefore larger than $4 \cdot 10^{-8}$ N/m, because if this would not have been the case, it would have lead to a tactoid elongation of 10%, which should have been perceptible in the experiments.

6.7. Discussion

We now compare our findings for the two gibbsite systems with results we obtained in Chapter 4 from the investigation of tactoid properties as a function of tactoid size

Table 6.2. Values for the splay elastic constant K_1 and the anchoring strength w of the charge-stabilized gibbsite, obtained by fitting our theory to the experimental data for droplets of radius 30 and 19 μm. Values for K_1 are obtained individually from the critical magnetic field strength, B_c, and together with values for w from fit to the magnetic-field dependence of the dimensionless length of the line defect L/R in Figure 6.13, i.e., from the choice of $\Re$ as well as from the curvature fits. The values from the fits of L/R are averaged over the values obtained from the upper and lower bound fits. See also the main text.

	K_1 [10^{-13} N]		w [10^{-8} N/m]
	B_c	fit L/R	fit L/R
Tactoid $R = 30$ μm	3.5 ± 0.4	1.6 ± 0.2	5.4 ± 0.6
Tactoid $R = 19$ μm	1.4 ± 0.2	0.8 ± 0.1	2.5 ± 0.4

Table 6.3. Values for K_1/w, γ and ω as obtained from analysis of tactoid shape and director field as a function of size in Chapter 4 compared to values obtained from the deformation of tactoids in an externally applied magnetic field. The value for γ of aqueous gibbsite was determined by combining results of the two methods.

		tactoid shape and director field	tactoid deformation in a magnetic field
K_1/w [10^{-6} m]	charged	6	5
	steric	2 [a]	0.3
ω	charged	0.6	$\ll 1$
	steric	1.1 [b]	2
γ [10^{-7} N/m]	charged	0.7	
	steric	-	1.3

[a] upper bound
[b] lower bound

in both gibbsite systems, as summarized in Table 6.3. We can conclude that the values for K_1/w we obtained via the two methods are in good agreement for both sterically stabilized and charged gibbsite. The value for the dimensionless anchoring strength $\omega = 0.6$ that we found for aqueous gibbsite from the aspect ratio of the uniform tactoids is larger than the estimate close to zero obtained from the deformation behavior by magnetic field. The latter is based on the observation that the tactoids remained spherical even at high magnetic field strengths. However, if we closely examine the

calculated phase diagram for $\omega = 0.5$, close to what we find from the tactoid properties, a tactoid elongation of only 3 to 5 % is expected, which we could have easily missed in our observations. So, the apparent discrepancy does not seem to be a real one. Note that the value we find for ω for sterically stabilized gibbsite is in good agreement with the lower bound we found from the aspect ratio of axial tactoids. Furthermore, now that we have obtained a value for the anchoring strength w of aqueous gibbsite, we are also able to determine the isotropic-nematic interfacial tension γ, for this system. Using the value for dimensionless anchoring strength $\omega = 0.6$ that we determined in Chapter 4, we obtain a surface tension of $\gamma = 7 \cdot 10^{-8}$ N/m.

It is also interesting to compare the two gibbsite systems. It is clear that the surface anchoring of the director field in our aqueous gibbsite dispersions is considerably weaker ($\omega = 0.6$) than that of the sterically stabilized gibbsite dispersions ($\omega = 2$). Contrary to that, the values we find for K_1, $0.8 \pm 0.3 \cdot 10^{-13}$ N for sterically stabilized gibbsite and $2 \pm 1 \cdot 10^{-13}$ N for aqueous gibbsite, are rather close. Both are in good agreement with computer simulations [150]. Furthermore, they are about a factor of 2 larger than was found previously by Van der Beek et al. [87] for the bend elastic constant K_3 in the comparable system of sterically stabilized gibbsite in toluene, which agrees qualitatively with theoretical predictions [149].

Theoretically, these differences in the behavior of our two types of system are hard to rationalize. The reason is that both should and seem to behave more or less as hard-platelet systems. Indeed, with an ionic strength of 10^{-2} M, the Debye screening length of the charge-stabilized gibbsite dispersion is about 3 nm, whereas the thickness of the stabilizing polymer layer of the sterically gibbsite platelets is about 4 nm [33]. A naive rescaling of the charged platelet dimensions that effectively includes the impact of the Debye length and the stabilizing brush height, respectively, would clearly not sufficiently explain the differences. Clearly, a deeper theoretical (or simulational) investigation of the influence of the electrostatic interaction on the liquid-crystalline properties of plate-like systems would be very helpful.

Interestingly, the interfacial tensions that we find for the co-existing isotropic and nematic phases in dispersions of charge- and sterically stabilized gibbsite are two orders of magnitude larger than the one found previously for a comparable system from capillary rise experiments [64]. The origin of this large difference is unclear, but it might partly be due to the different stages in which the respective experiments are carried out. Our tactoid experiments were carried out when the phase separation process is not quite finished, while the capillary rise experiments require a fully equilibrated sample where all tactoids have sedimented and the different domains in the nematic phase have annealed. Such an equilibrated sample might very well have a higher order parameter. While elastic constants are generally accepted to be proportional to the square of the scalar order parameter of the nematic, the anchoring strength is linear in this order

parameter [57]. This implies that a higher order parameter would lead to a larger value for the extrapolation length. Moreover, during the equilibration a sedimentation equilibrium might have started to develop, which would change the concentrations in the co-existing phases, and as a consequence also change the elastic and surface properties of the nematic.

We end this section by a brief discussion of the caveats of the theoretical model that we advance in this chapter. For instance, we assume that all the model parameters, including the splay elastic constant K_1, the anchoring strength w and the surface tension γ are independent of the magnetic field strength. However, with increasing magnetic field strength the order parameter S of the nematic phase increases, which plausibly will also affect K_1 and w. While elastic constants are generally accepted to be proportional to the square of the nematic order parameter, S^2, the anchoring strength is linear in this order parameter [57]. Because both the elastic constant and the anchoring strength counterbalance the deformation by the magnetic field, an underestimation of K_1 could lead to a too high value for the anchoring strength and interfacial tension. Furthermore, the anchoring strength might also depend on the magnetic field strength due to alignment of the isotropic phase in the field. However, correction for the latter would lead to an even higher value for the anchoring strength in zero field.

A contribution that is missing in our free energy analysis is bend deformation, which might be present at high magnetic field where the line defect spans the entire tactoid. Although difficult to infer from the polarized light microscopy experiments, the curvature in the dark horizontal band (Figure 6.2) might point in that direction. Indeed, for plate-like particles, the bend elastic constant is thought to be smaller than the splay constant [150], so some elastic energy can be gained. An appropriate bend deformation also makes the anchoring less unfavorable, producing an additional reduction of the free energy. At this point, it is difficult to judge in what way that this should influence the results of our curve fitting.

In any event, it seems quite unlikely that these caveats could be responsible for a difference of almost two orders of magnitude between the interfacial tension that we find here and that obtained from capillary rise experiments. This is supported by the fact that the values for K_1/w and ω obtained from the tactoid properties as a function of size and from the deformation in magnetic field are in very good agreement. The origin of this discrepancy remains a mystery.

6.8. Conclusion

We find that nematic tactoids that form in dispersions of plate-like colloids exhibit an interesting response to an externally applied magnetic field due to the homeotropic surface anchoring of the platelets. As the director-field configuration is a function of the tactoid size, we have been able to observe a number of transitions between

different kinds of director-field structure and droplet shape with increasing magnetic field strength. Perhaps the most remarkable observation is that large tactoids that tend to be spherical and have a radial director field emanating from a hedgehog point defect in their center develop a split-core defect in a sufficiently strong field.

We focused our experiments on two types of system: charged gibbsite dispersed in water and sterically stabilized gibbsite in bromotoluene. We found these systems to behave very differently: in a magnetic field the latter not only develops the the split-core defect structure, but the droplets also become elongated in the field direction. This is not so for the former, these remain spherical. The difference in behaviour of the two types of dispersion is caused by the relative magnitude of the anchoring strength and the surface tension, which for the former is small and for the latter large.

We have been able to account for the observed transitions by invoking a macroscopic description that balances elastic, surface and magnetic free energies and predicts the structure of the tactoids as a function of their size, the splay elastic constant, surface tension and anchoring strength, and the magnetic field strength. Our idealized theory allowed us to extract values for the splay elastic constant (K_1), interfacial tension (γ) and anchoring strength (w) from our observations. Not surprisingly, we found remarkable differences between the sterically stabilized gibbsite in bromotoluene and the aqueous gibbsite system.

The anchoring strength is much larger in the sterically stabilized system, with a dimensionless anchoring strength ω of about 2, whilst that of the charge-stabilized system is about 0.6, implying that they represent the strong and weak anchoring limit respectively. The values for the splay elastic constant K_1 for the two systems are actually quite close, varying by no more than a factor of two. The value for the surface tension γ that we find here for the sterically stabilized gibbsite is still larger by two orders of magnitude than was found previously from capillary rise experiments [64], a discrepancy for which we have no explanation.

Acknowledgements

Ronald Otten is acknowledged for his work on the theory and analysis. We thank Bonny Kuipers for constructing the polarized light microscopy setup in magnetic field.

Part 3

Dynamics of nematic tactoids

7

Coalescence of tactoids with the isotropic-nematic interface and buoyancy-driven coalescence of two tactoids

Abstract

We studied the coalescence of nematic tactoids with the macroscopic isotropic-nematic interface as a function of tactoid size in colloidal gibbsite suspensions. We found that for coalescence of small drops with a uniform director field drainage of the fluid film between the drop and the interface is the time determining step, as is the case in isotropic fluids. For larger tactoids with an asymmetric director field gravitational forces turn out to be dominant so they do not exhibit a long drainage time, but instead behave as a deformable immiscible drop that passes through a liquid-liquid interface. We also studied the buoyancy driven interaction between tactoids with an asymmetric radial director field as a function of Bond number, i.e., the ratio of gravitational and interfacial forces. If a small drop is followed by a larger drop, the latter is coated by the smaller drop, an effect that becomes more pronounced with increasing Bond number, similar to what is observed in isotropic fluids.

7.1. Introduction

Drop coalescence is a phenomenon that is observed in everyday life and that is also important in many industrial processes, especially those that involve mixing, emulsification, liquid-liquid extraction, and foam stability. The process has been studied for a long time, starting with Reynolds [158] and Thomson and Newall [159] in the 19th century. Extensive investigations were undertaken in the second half of the last century, and a review of this work can be found in the somewhat dated but still useful overview of Jeffreys and Davies [160].

From these studies it becomes clear that one can distinguish three consecutive stages in the coalescence of a drop with its bulk phase. The first is drainage of the liquid film that forms between the drop and the bulk phase as the drop approaches the interface. Depending on the density difference of the fluids involved, the interfacial tension, and their relative viscosity this can involve large distortions of both the drop and the interface [161–163]. Subsequently, this continuous film breaks and a connection is formed between the drop and the bulk phase. This film rupture is induced by Van der Waals interactions or capillary waves [160,164]. In the final stage the drop material is extruded into the bulk phase, either completely or partially with subsequent coalescence cascade of small daughter drops [160, 165, 166].

For molecular fluids like water, coalescence (apart from the drainage stage) occurs very fast and is difficult to follow experimentally. In many experiments therefore high viscosity fluids such as glycerin and golden syrup are studied, in which coalescence is considerably slower [161, 167, 168]. Recently, another route was chosen, namely by lowering the interfacial tension. Colloid-polymer mixtures have an ultra-low interfacial tension, which slows down the coalescence process so that all three stages of the coalescence process can be studied in great detail with confocal microscopy [164].

If either the drop or the surrounding fluid possesses liquid crystalline order, additional effects play a role, giving rise to interesting novel features in the coalescence process. For instance, for water drops in a nematic matrix coalescence is significantly hindered with the droplets even forming large ordered structures, due to a combination of short range repulsion and long range attraction resulting from the anisotropic elasticity of the nematic matrix [169]. For the opposite case, emulsions of liquid crystal droplets in water, coalescence of droplets with a radial director field is suppressed due to the formation of a ring defect that for topological reasons has to be introduced in the neck between two merging droplets. The formation of this ring defect gives rise to an energy barrier of $\sim KR$, with K the elastic constant and R the droplet radius [144].

Here, we study coalescence of nematic tactoids with the isotropic-nematic interface in aqueous gibbsite dispersions. The density difference $\Delta\rho$ between the isotropic and nematic phase is small, about 5 kg/m^3, and the viscosity of the isotropic phase η= 1

Pa s is rather high. These system properties result in sedimentation rates in the range $10^{-9}-10^{-8}$ m/s and hence in Reynolds numbers $Re \equiv \rho v_{sed} R/\eta$, with ρ the mass density and v_{sed} the drop sedimentation velocity, in the range of $10^{-11} - 10^{-10}$, implying that viscous dissipation is far dominant over inertia. Furthermore, as we have established in the previous chapters, the isotropic-nematic interfacial tension $\gamma = 0.7 \cdot 10^{-7}$ N/m in this system is very low. As a consequence, not only the approach to the interface, but also the subsequent coalescence of the drops is sufficiently slow to be observed with real-time imaging of polarized light microscopy.

We investigate the coalescence process as a function of droplet size and as a function of director field, as these two are coupled (see Chapter 4). Different drop sizes result in different sedimentation velocities, which also changes the ratio of gravitational and surface tension forces. This ratio is set by the Bond number $Bo \equiv \Delta\rho g R^2/\gamma$, with g the gravitational acceleration. In practice, we deduce the Bond number from the sedimentation velocity of the tactoids. Invoking Stokes, the sedimentation velocity v_{sed} (ignoring prefactors pertaining to the circulation of fluid inside the drop) is roughly equal to $2g\Delta\rho R^2/9\eta$, which gives us $Bo = 9v_{sed}\eta/2\gamma$. In the present experiments, Bo varies from 0.1 to 2, which in combination with the different director field configurations leads to remarkable differences in coalescence behavior.

In the second part of this chapter, we study the buoyancy driven coalescence of two nematic tactoids in aqueous gibbsite dispersions, which proceeds via the same three stages. We use a sample with nematic-isotropic coexistence where the density difference between the two phases is considerably larger, resulting in Bond numbers $Bo > 1$. As a consequence the droplets deform considerably before and during coalescence. Coalescence seems to proceed along similar lines as in isotropic fluids at comparable Bo numbers.

7.2. Experimental

We used gibbsite platelets with a bimodal aspect ratio dispersed in 10^{-2}M NaCl, and we refer for details to Chapter 3. Coalescence of nematic droplets with the isotropic-nematic interface was studied in samples with coexisting nematic-isotropic-columnar phases at an overall volume fraction of 30 v/v%. Buoyancy driven tactoid coalescence was studied in nematic-isotropic samples at a volume fraction of 24 v/v%. Polarized light microscopy was performed as described in Chapter 2. In both systems, the nematic phase has a lower mass density than the isotropic phase, which results in the nematic droplets rising to the bulk nematic phase. This density inversion is a result of the bimodal distribution of the platelet aspect ratio as we have shown in Chapter 3.

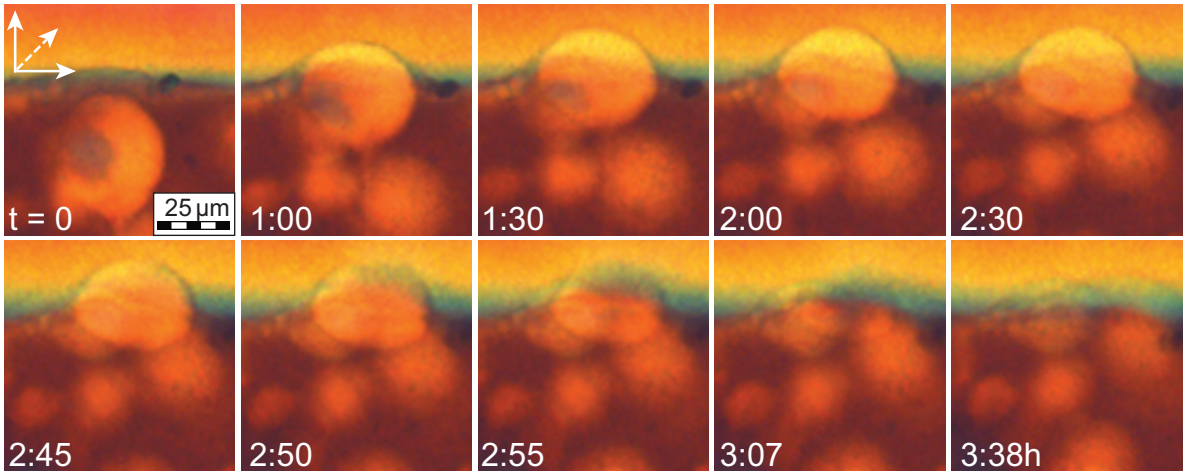

Figure 7.1. Coalescence of a small tactoid (R = 20 µm) with a uniform director field with the bulk nematic phase. At small separations the interface starts to deform and the drop slows down. After a drainage time of about two hours, the film ruptures and the drop coalesces with the bulk nematic phase.

7.3. Coalescence of tactoids with the isotropic-nematic interface

As we have seen in Chapter 4, the tactoid shape and director field depends on the tactoid size through a balance of interfacial anchoring energy and bulk elastic energy. In small droplets of radius $R < 3K/w$, with K the elastic constant and w the anchoring strength, the elastic free energy is dominant, leading to an oblate shaped drop with a uniform director field. Larger tactoids are more spherical with a (distorted) radial director field, resulting from a preferential homeotropic anchoring. We study the coalescence of nematic tactoids of various sizes with the isotropic-nematic interface during the last stages of the nematic-isotropic-columnar phase separation. Under these conditions the nematic phase still contains several defects and the isotropic-nematic interface has regions where the platelets have an unfavourable orientation with respect to the interface. The latter is not surprising taking into account that in aqueous gibbsite systems the anchoring of the platelets to the interface is relatively weak (see Chapters 4-6).

7.3.1. Small tactoids with uniform director field

The small tactoids (R = 10 - 20 µm) with a uniform director field rise to the nematic phase at a very low velocity v_{sed} of $1 - 5 \cdot 10^{-9}$ m/s, implying values for the Bond number Bo in the range 0.1 - 0.4. A representative example is shown in Figure 7.1. When the tactoids approach the interface to a distance of a few µm, the interface starts to deform. This continues until the droplet comes to an apparent rest at the interface with a very thin fluid film between the tactoid and the interface of roughly 2 µm, which is equivalent to only a few particle diameters. The droplet is somewhat flattened and,

remarkably, slightly more than half of the droplet protrudes into the bulk nematic. The latter observation implies that the density in the tactoid is somewhat lower than in the bulk nematic phase. This could be the result of fractionation and/or sedimentation effects.

In the following 'resting time' of half an hour to two hours that seems to be independent of the orientation of the director field inside the tactoid relative to the orientation in the bulk nematic phase at the interface, there seems to be not much happening until the film breaks and the actual coalescence with the bulk nematic phase starts. During this resting time, the thin fluid film between the drop and the interface is squeezed out, until the film is thin enough that film rupture can occur. The film rupture is here presumably caused by thermal fluctuations of the interface [164]. The thermal roughness of the interface is set by $L_T = \sqrt{k_B T/\gamma} = 0.24$ μm, with k_B the Boltzmann constant and T the absolute temperature. From the work of Aarts and Lekkerkerker [164], we find that for an interfacial tension of $1 \cdot 10^{-7}$ N/m the waiting time for a fluctuation of 1 μm is about 100 seconds.

Although there is no analytical expression for the drainage time of the fluid film between a drop and a deformable interface, we can obtain a rough estimate from the drainage rate for a solid sphere approaching a deformable interface [162, 170]. For a film to thin from h_0 to h takes

$$t = \frac{3}{16\pi}\frac{\eta A^2}{F}\left(\frac{1}{h^2} - \frac{1}{h_0^2}\right) \tag{7.1}$$

seconds, with $F = \frac{4}{3}\pi R^3 \Delta\rho g$, the force due to the weight of the sphere plus the hydrostatic pressure acting over its surface and A the area of film enclosed between the drop and the interface. With $\eta \approx 1$ Pa s, $R = 15$ μm, $\Delta\rho \approx 5$ kg/m ^{3}, and $A \approx 4 \cdot 10^{-10}$ m^2 we find from Equation 7.1 that for the fluid film to thin from 2 to 1 μm takes around 10^4 s. If the rigid sphere is replaced by a drop, fluid circulation in the drop will speed up the drainage [171], but nevertheless it seems reasonable that drainage of the fluid film indeed is responsible for the observed resting time of a few hours.

If after a while a connection between the drop and the bulk nematic is formed, then the radius of this neck grows with approximately $1.5 \cdot 10^{-8}$ m/s leading to complete coalescence with the bulk phase in twenty to fifty minutes. Although there is no explicit model prediction for the growth of this neck, a dimensional analysis learns that it must be set by the capillary velocity γ/η, as it is driven by capillary forces and slowed down by viscous forces [172]. We find for the neck growth $\approx 0.2\gamma/\eta$, which is in reasonable agreement with values obtained by Aarts and Lekkerkerker for coalescence in colloid-polymer mixtures [164].

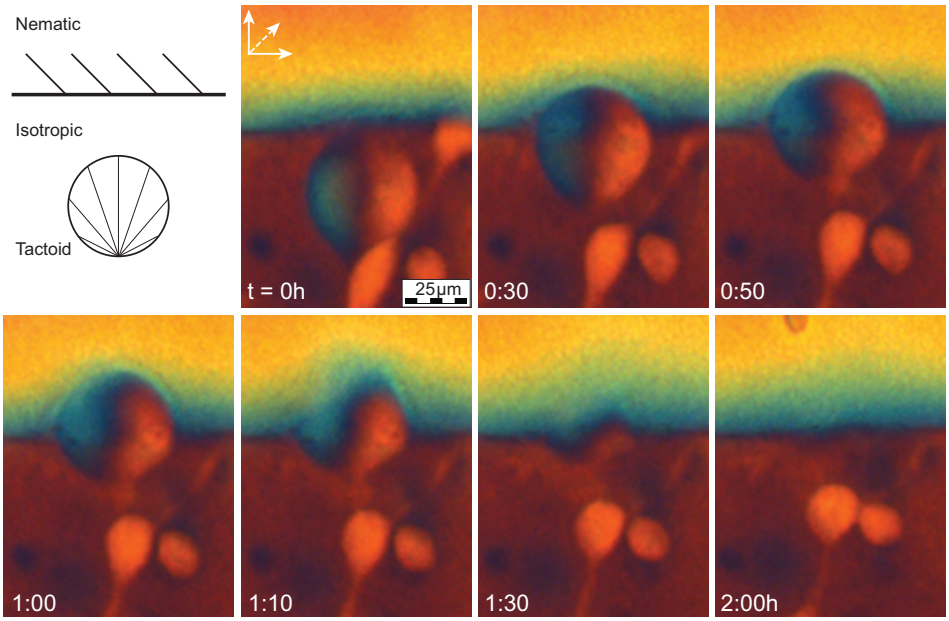

Figure 7.2. Sketch of tactoid with asymmetric radial director field approaching the interface (top left). The drop with radius $R = 27$ µm and Bond number $Bo = 0.8$ coalesces with the bulk nematic phase without a long drainage time. Film rupture occurs at the position where the orientation of the director field inside the drop is similar to the orientation in the bulk nematic phase, followed by an asymmetric neck growth.

7.3.2. Intermediate tactoids

Larger tactoids ($R \approx 27$ µm) have an asymmetric director field with a surface point defect, located at their rear end with respect to the translation direction, as schematically depicted in Figure 7.2(a). These droplets rise to the isotropic-nematic interface with a v_{sed} of about $1 \cdot 10^{-8}$ m/s, which corresponds to a Bond number $Bo = 0.8$. As the tactoid approaches the interface, the interface is pushed forward and the tactoid is somewhat flattened. In contrast to small droplets there is no long drainage time: as soon as the droplet is slightly more than halfway above the interface, the liquid film breaks. Interestingly, this film rupture takes place slightly off-center at a position where the orientation of director field inside the droplet is parallel to the orientation in the nematic phase. The subsequent neck growth is asymmetric where the part with a similar director field orientation has already coalesced while on the other side of the tactoid, where the orientation is perpendicular to the orientation in the nematic phase, the interface is still intact. Complete coalescence of the drop from the point of film rupture takes almost one hour.

A possible explanation for the absence of an extended drainage time may be found from the density difference between the tactoid and the nematic phase together with the Bond number, being now of the order of 1 because of the larger size of the drop. As

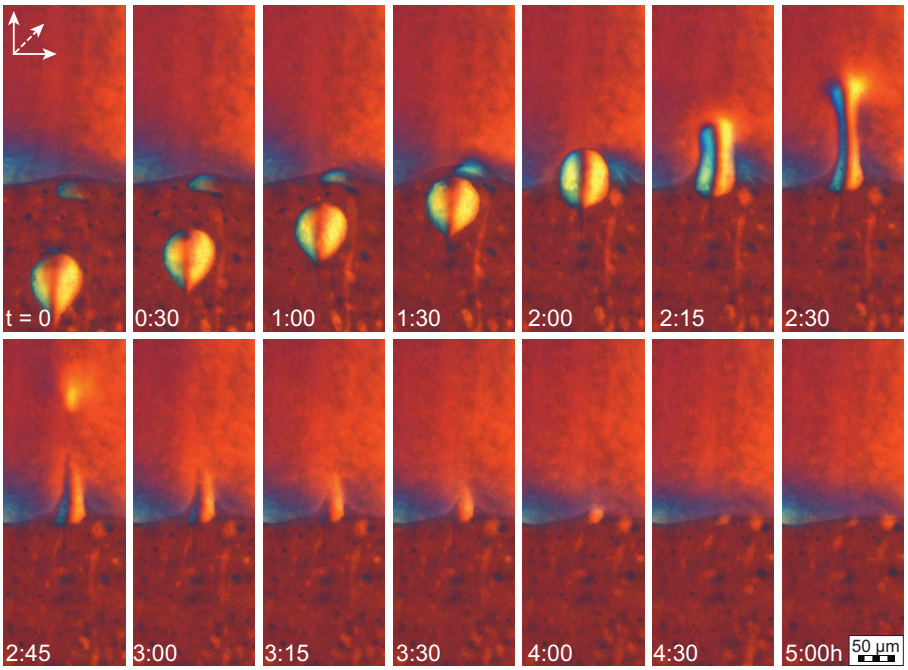

Figure 7.3. Large tactoid ($R = 40$ µm) with asymmetric radial director field coalesces with the bulk nematic phase. The tactoid remains intact while entering the nematic phase, becomes elongated in the z-direction, breaks up and finally coalesces.

a consequence, we might be dealing with a transition from the drainage to the tailing mode in the terminology of Geller, Lee and Leal [173]. Analogous to the transport of a rigid sphere through a liquid-liquid interface, for $Bo < 1$ drainage of the liquid film determines the sedimentation velocity at and through the interface, while for $Bo > 1$ gravitational forces are dominant. We are probably in the cross-over regime that occurs for Bond numbers around 1, where both capillary and gravitational forces determine the process [174].

7.3.3. Large tactoids

The largest tactoids studied here have a radius R of 30 - 45 µm and corresponding values for the Bond number in the range of 1 - 2. These tactoids also have an asymmetric radial director field with the point defect near the edge, nevertheless the coalescence process proceeds differently from that in the previous case. Figure 7.3 shows a typical example for $Bo \approx 1.6$. As the drop approaches the interface, the interface is pushed forward but now the drop enters the nematic phase without actually coalescing with it and preserving its director field. Moreover, the drop stretches in the vertical direction inside the homeotropically aligned nematic phase, resulting in an elongated drop with a

so-called escaped radial director field.[1] The escape direction of the director field points downwards. As this cylinder is stretched further, it breaks into two parts, leaving one drop at the interface and the other one moving deeper into the bulk nematic phase until finally both drops coalesce with the bulk phase. The upper drop in some cases rises up to 300 μm before it actually coalesces.

At first sight, the observed drop shape inside the nematic phase resembles the penetration of a drop into the bulk after coalescence as observed by Anilkumar, Lee and Wang [175], where the interfacial energy is transformed into kinetic energy pushing the drop into the bulk phase. However, in the present case we have a very low γ, which would result in a penetration depth of only a few μm. The observed elongated droplet shapes in fact show remarkable resemblance to the deformation of an (isotropic) immiscible drop or bubble that passes through a fluid-fluid interface at low Reynolds number [176]. Manga and Stone showed, both experimentally and theoretically, that if such a drop translates from a higher to a lower viscosity fluid, the droplet is extended vertically, provided $Bo > 1$. One could imagine that in the case of a drop with a radial director field inside a uniform nematic phase a wall defect is created between the drop and the uniformly aligned bulk nematic phase, which forms a barrier for coalescence and causes the remarkable resemblance to the translation of an immiscible drop through an interface.

7.4. Buoyancy driven coalescence of two tactoids

We now study the coalescence of two rising tactoids in nematic-isotropic phase separating sample, where a larger (faster) drop follows a smaller (slower) drop. For these experiments we use a sample at a volume fraction where the isotropic and nematic phase coexist. The density difference is considerably larger compared to the samples in the previous section, leading to larger sedimentation velocities of about $1 \cdot 10^{-7}$ m/s. The resulting Bond numbers are larger than one, implying that the buoyancy forces are larger than the restoring interfacial forces, resulting in strong shape deformations. Shown in Figure 7.4 are two tactoids of comparable, but slightly different size with $R = 19$ and 18 μm, rising in line to the bulk nematic phase. We estimate that the Bond number $Bo = 8$ based on the properties of the trailing drop. Both drops have an asymmetric radial director field with the point defect at the trailing edge. The trailing drop is larger and catches up with the smaller leading drop. Due to the flow fields induced by both tactoids, the smaller leading drop deforms into an oblate shape, while the larger trailing drop deforms into a prolate shape. Both drops maintain their asymmetric radial director field.

[1] An escaped radial director field is a 2D radial director field with the director escaping along the 3rd dimension. See also Chapter 8.

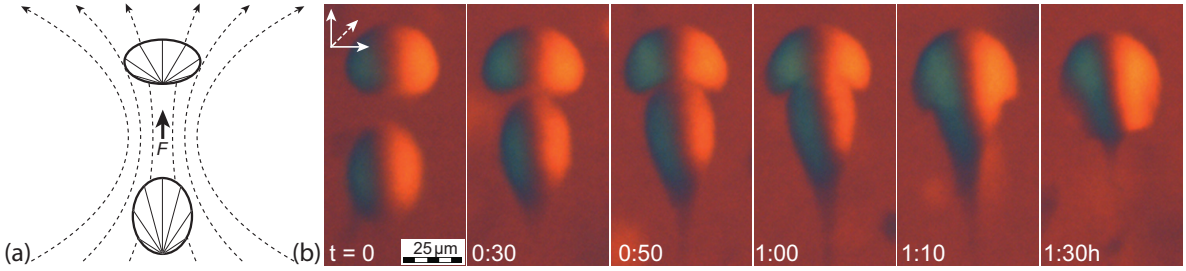

Figure 7.4. Buoyancy driven coalescence of two tactoids with asymmetric radial director field. (a) Sketch of the streamlines that are responsible for the deformation of the drops produced by the moving drops that are represented by the point force F, inspired by [176]. See also the main text. (b) Interaction between a smaller tactoid and a larger trailing one. The field of view follows the leading drop, which has a rising speed of 10^{-7} m/s. $Bo = 8$ (based on the trailing drop).

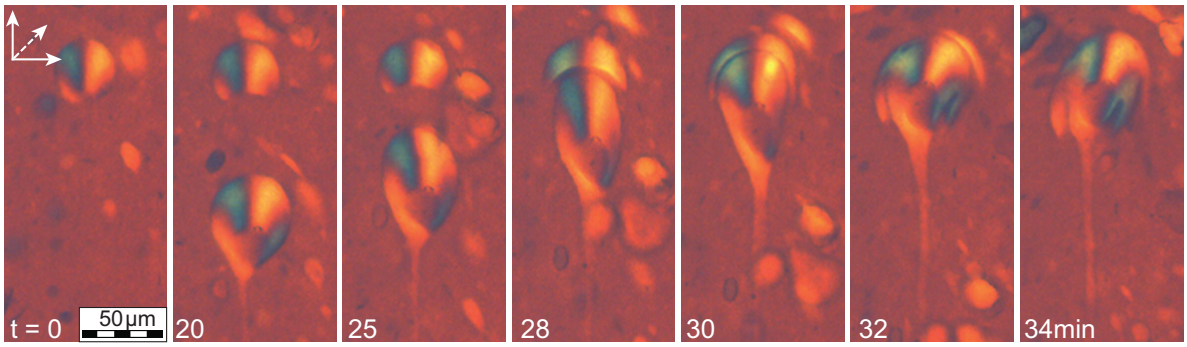

Figure 7.5. Buoyancy driven interaction of a smaller tactoid followed by a larger one. The field of view follows the leading drop, which has a rising speed of 10^{-7} m/s. $Bo = 16$ (based on the trailing drop). At t = 0 the leading drop is still spherical, but as the trailing drop gets close, it is coated by the leading drop. The trailing drop has a long tail, which is typical for high Bo.

This shape deformation can be understood if we consider both moving drops in a simplified manner as a point force F that impacts the neighbouring drop, as sketched in Figure 7.4(a). Note that in this simplified picture we only draw the streamlines produced by the moving drops that are represented by the point force. The trailing drop becomes elongated due to the viscous stresses associated with the convergence of streamlines in the flow produced by the leading drop, and on the other hand, the leading drop is flattened due to the viscous stresses associated with the divergence of streamlines in the flow produced by the trailing drop [177]. Due to this flow field, the elongated trailing drop even develops a tail and loses some material. Manga and Stone showed that for large Bond numbers, $Bo \gg 1$, when a large drop follows a small drop, the smaller drop eventually coats the larger drop, an effect that becomes more

pronounced with increasing Bo [177]. In Figure 7.4 we observe that at the point where the drops come very close (at t = 50 minutes), the leading drop indeed coats the trailing drop.

The effect is indeed much more pronounced at higher Bond numbers, as is shown in Figure 7.5. The trailing drop here is considerably larger than the leading drop (R = 28 and R = 18 μm) and has an estimated Bond number Bo = 16. We observe that the complete upper half of the trailing drop is coated by the leading drop, before they actually begin to coalesce. Also, the trailing drop has a longer tail, roughly twice the tactoid radius, which is typical for high Bond numbers [143].

Terentjev [144] argued that for two radial tactoids to coalesce there is an energy barrier KR, arising from the ring defect that needs to be formed in order to remove one of the two defects of the coalescing drops. In our case this would produce a considerable energy barrier of $\approx 10^3 k_B T$. However, although both tactoids have a (albeit distorted) radial director field with a point defect, there seems to be no barrier for coalescence because the process proceeds in a fashion similar to coalescence of isotropic Newtonian drops for comparable Bond numbers. However, if we consider the director field configuration of the two coalescing tactoids this is perhaps not so surprising. Both tactoids initially have an asymmetric radial director field with the defect located near or at the trailing tactoid edge. As the drops approach each other head-to-tail, they deform in such a way that the parts that have to coalesce have similar orientations, which can be deduced from the retardation colors in Figure 7.4 and 7.5. In fact, when we closely examine the director field in the 'coat' just before the film between the two drops breaks, we find that the point defect has moved outside the tactoid and has become a virtual defect located roughly in the center of the trailing drop. In this configuration, the anchoring with the interface is most favorable. This also implies that there is no need to form an additional defect upon coalescence, which explains the fact that the droplets do not seem to experience an energy barrier. Probably, if these drops would coalesce in head-to-head configuration they would experience a free energy barrier.

7.5. Conclusion

We have studied coalescence phenomena of drops with nematic liquid crystalline order in suspensions of colloidal plates as a function of drop size and director field. For small drops with homogeneous director field the coalescence with a bulk interface broadly resembles phenomena observed in molecular liquids albeit that the time scales are much longer. On the other hand, for larger droplets, which have an inhomogeneous director field and for which the Bond number is order unity or larger, new phenomena are observed. Remarkably, there is a close resemblance to the phenomena described by Manga and Stone [176] for the low Reynolds number motion of deformable drops of an immiscible liquid through a fluid-fluid interface. Probably the combination of the fact

that the nematic drop has a higher density than the bulk nematic phase and the fact that there is a wall defect between the tactoid with radial director field and the uniform bulk nematic phase are responsible for this behavior. The buoyancy driven interaction between two tactoids leads to tactoid shapes that closely resemble the buoyancy driven shape deformations of isotropic viscous droplets. In equilibrium, the shape of tactoids is governed by a competition between the surface tension, anchoring strength and bulk elastic properties of the nematic. Here, it seems that hydrodynamic interactions between tactoids lead to similar deformation as in isotropic fluids.

8

Droplet snap-off and breakup of nematic threads

Abstract

In this chapter, the droplet snap-off and breakup of pending and free floating nematic liquid crystalline threads is studied in suspensions of charged gibbsite in water and sterically stabilized gibbsite in bromotoluene. We found that the snap-off of a drop from a pending nematic liquid crystalline thread strongly depends on the anchoring of the platelets to the interface. If anchoring is weak, which is the case for aqueous gibbsite, the thread has a uniform director field and the droplet snap-off is determined by the viscous properties of the liquid crystal as well as by thermal fluctuations. On the other hand, in sterically stabilized gibbsite, where anchoring is strong, the neck has an escaped radial director field, and the neck thinning is retarded close to breakup due to an energy barrier involved in the separation of the droplet from the thread. Moreover, we observe in aqueous gibbsite that the breakup of free floating nematic threads proceeds in a symmetric or asymmetric manner, depending on the thread length.

8.1. Introduction

The breakup of liquid threads into droplets is a familiar phenomenon in everyday life and has been widely studied for a long time [178, 179]. One of the main reasons for study is that the stability and control of a liquid thread is a crucial factor in a variety of applications, such as diesel engine technology, ink-jet printing [180], and the manufacturing of electronic and optoelectronic devices [181]. Also, the subject is of scientific interest because of the universal behaviour close to the pinch-off event, where the geometry of the thinning neck as a function of time can be described by universal scaling functions, independent of initial conditions [179]. In general, breakup of a liquid thread is driven by the interfacial tension and counteracted by either viscosity or inertia of the liquid [178].

Recently, it was shown by simulations and theory that the formation and breakup of so-called nano-jets follows a fundamentally different mechanism [182, 183]. When the jet diameter approaches the molecular scale, thermal fluctuations start playing a role and dominate the breakup process. Experimental evidence for this mechanism was obtained from colloid-polymer mixtures, that phase separate into a colloid-rich phase and a polymer-rich phase with an ultra low interfacial tension [184]. The thermal roughness, defined as $L_T = \sqrt{k_B T/\gamma}$ with k_B the Boltzmann constant, T the absolute temperature and γ the interfacial tension, is of the order of micrometers in such systems and can be observed with confocal microscopy [185].

While Newtonian fluids have been studied extensively, also Non-Newtonian fluids have attracted quite some attention. In the latter, the breakup process cannot be described by universal scaling functions and is less well understood. For example, the breakup of viscoelastic fluids under certain conditions involves beeds-on-a-string structures [186], and the elastic stress built up during breakup of filaments of worm-like micelles can cause the falling drop to stall before pinch-off [187].

Another special case of breakup is when the fluid thread possesses liquid crystalline order. This is especially important for the production of liquid-crystalline polymer composites [188–190], but also for the formation of micro and nano-fibres by electro-spinning of elongated particles, such as long rod-like viruses [191]. Another example is the breakup of liquid crystalline threads in a microfluidic device that is used to produce liquid crystalline droplets [192]. Theoretical calculations by Cheong and Rey showed that the texture of nematic liquid crystalline fibres strongly influences the breakup, and in most cases will stabilize the thread [193]. Furthermore, simulations of the breakup of a nematic thread with homeotropic anchoring revealed that the breakup in this case requires a morphological transition with accompanying free energy barrier [194]. Recent simulations on capillary breakup in axial nematic fibres with planar anchoring, performed by Zhou and coworkers [195] showed that both the interfacial anchoring and

the bulk elasticity dampen the growth of capillary waves, by raising the threshold wavelength and suppressing the growth rate of unstable modes. However, they argue that these effects are only quantitative, and the nematic fibres break up in essentially the same way as Newtonian ones.

In this chapter, we investigate the breakup of a nematic thread in suspensions of colloidal gibbsite platelets, where several of the aforementioned effects come together, leading to new and interesting behaviour. Apart from the nematic liquid crystalline order, these systems have a very low interfacial tension so that thermal fluctuations could possible play a role as well. Two different gibbsite suspensions are studied, namely charge-stabilized gibbsite in water and sterically stabilized gibbsite in bromotoluene. We show that anisotropy of the liquid crystal indeed significantly influences the breakup and pinch-off process, and also that the differences between the two systems in terms of the splay elastic constant and anchoring strength (as described in Chapter 4-6) gives rise to quantitatively, but also qualitatively different behaviour. In particular the neck geometry, the occurrence of satellite drops and the breakup time scales appear to depend on the nematic structure of the thread.

8.2. Experimental

Two gibbsite systems are used in this study, namely charged gibbsite in aqueous dispersion and sterically stabilized gibbsite dispersed in bromotoluene. The experimental details of these gibbsite systems are described in Chapter 3 and 2, respectively.

The aqueous system consists of gibbsite platelets with a bimodal distribution of the aspect ratio. As we have seen in Chapter 3, this system exhibits a remarkable three phase equilibrium, with a bottom columnar phase, a top nematic phase and an isotropic phase sandwiched between the two. When such a three phase sample is left in upright position over a long period of time (months to years), a sedimentation equilibrium develops, resulting in a four phase coexistence as an isotropic phase appears on top of the nematic phase (see Figure 8.1(a)). This is accompanied by a density gradient in the nematic phase. The lower part of the nematic phase, which was originally homeotropically aligned in the relatively thin (200 μm) capillary, buckles under the pressure of the suspension above it, forming beautiful stripe patterns shown in Figure 8.1(b) similar to patterns that evolve when a homeotropically aligned nematic gel buckles upon cooling [196]. Furthermore, near the lower isotropic-nematic interface the mass-density eventually becomes larger than in the isotropic phase below, and Rayleigh-Taylor instabilities appear from which nematic droplets start dripping.

The sterically stabilized gibbsite system on the other hand, has a monomodal platelet distribution, and forms the usual isotropic-nematic phase coexistence with the nematic phase the bottom phase. The sample is contained in a rectangular Hellma cell of 2 mm path length (Hellma, Müllheim, Germany) closed with a stopper. This stopper

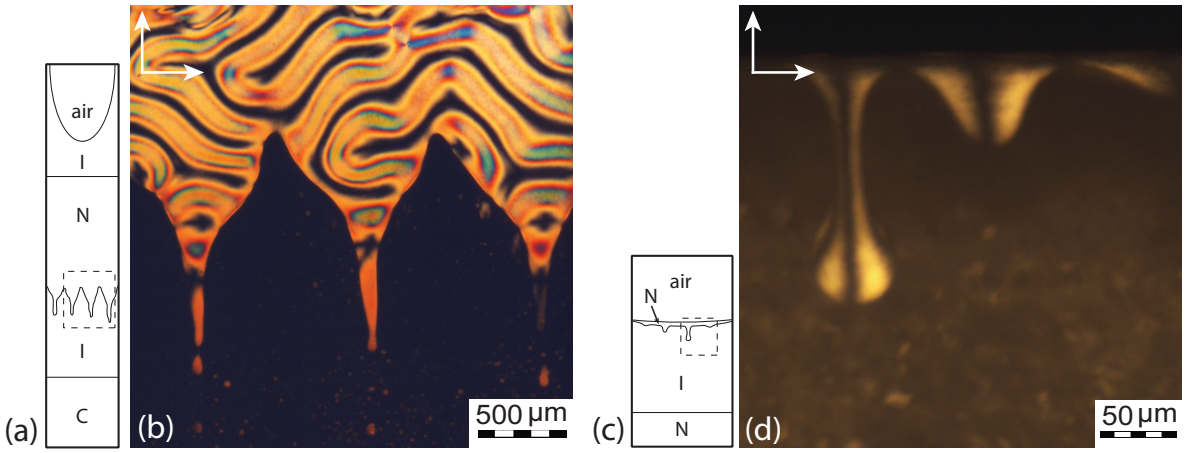

Figure 8.1. Rayleigh Taylor instabilities develop over time in both systems. (a) The initial three phase sample (NIC) of bimodal aqueous gibbsite develops in half a year to a four phase (INIC) coexistence, with Rayleigh instabilities at the lower nematic-isotropic interface. The dashed box indicates the area pictured in (b). (c) The solvent of the sterically stabilized gibbsite sample is allowed to evaporate slowly, giving rise to Rayleigh-Taylor instabilities of nematic phase at the air-suspension interface. The dashed box indicates the area pictured in (d)(not to scale). Arrows indicate the orientation of the polarizers.

does not close the cell air-tight and the solvent evaporates slowly, leading to a higher particle concentration near the air-suspension interface. After a few weeks, a thin layer of nematic phase starts to form in the top-layer, heavier than the isotropic phase, and Rayleigh-Taylor instabilities appear with nematic droplets snapping off and sedimenting towards the nematic phase.

Both systems are studied with polarized light microscopy as described in Chapter 2. Image analysis of the aqueous gibbsite samples was performed with IDL-based routines [134, 197]. The sterically stabilized system was analyzed manually with the microscopy software iTEM [138].

8.3. Droplet snap-off Rayleigh-Taylor instability

The formation of Rayleigh-Taylor instabilities and the subsequent snap-off of nematic droplets is extremely slow in both systems. For one drop to snap off takes hours in the sterically stabilized system to even days in aqueous gibbsite. This is not surprising, taking into account the material properties of the systems (see Table 8.1): The density difference $\Delta\rho$, the driving force for the growth of a Rayleigh-Taylor instability, is small. Moreover, for the subsequent droplet snap-off, the interfacial tension γ, the driving force, is very small, and the viscosity of the nematic phase η, the counteracting force, is large.

Table 8.1. Relevant system properties and scaling lengths for the two gibbsite suspensions, see also the main text.

	charge stabilized gibbsite	sterically stabilized gibbsite
γ [10^{-7} N/m]	0.7	1.3
η [Pa · s] [a]	10	0.1
$\Delta\rho$ [kg/m^3] [b]	1.3	2.7
ω [$\equiv w/\gamma$]	0.5	2
K_1/w [μm]	>10	0.3
L_T [μm]	0.24	0.18
L_c [μm]	74	70
L_η [m]	10^6	10^2

[a] Average viscosity of the nematic phase, estimated on the basis of rheological measurements by [75, 198].

[b] Estimated from the sedimentation velocity of the droplet after snap-off.

As we have seen in the previous chapters (Chapters 4 - 6), the two systems represent different regimes with regard to anchoring of the platelets to the isotropic-nematic interface. Both prefer homeotropic alignment, but the aqueous gibbsite sample represents the weak anchoring regime with a dimensionless anchoring strength $\omega = 0.6$, while the sterically stabilized system with $\omega = 2$ exhibits rather strong anchoring. In the present case, this leads to a different director configuration during the breakup process. In order to investigate how these different director field structures influence the breakup of the nematic thread, we will now analyse and compare the breakup process for both systems, first qualitatively, in terms of neck geometry, breakup position and the occurrence of satellite drops, and also quantitatively when we measure the minimal neck thickness as a function of time.

8.3.1. Aqueous gibbsite

In the aqueous gibbsite (Figure 8.1(a-b)) both the thinning neck and the pending drop are, depending on the orientation of the polarizers, either completely birefringent or completely non-birefringent, which implies that they have a uniform director field. The use of a retardation plate (Fig. 8.2) reveals that the particle director points in the horizontal direction, as schematically depicted in Figure 8.2. The fact that even the drop, with a size of 60 × 100 μm, has a uniform director field is surprising, because for the ratio of the splay elastic constant K_1 and the anchoring strength w that was determined for this system in Chapters 4 - 6, droplets of this size are expected and have been observed to have a radial director field (see Chapter 4). However, this

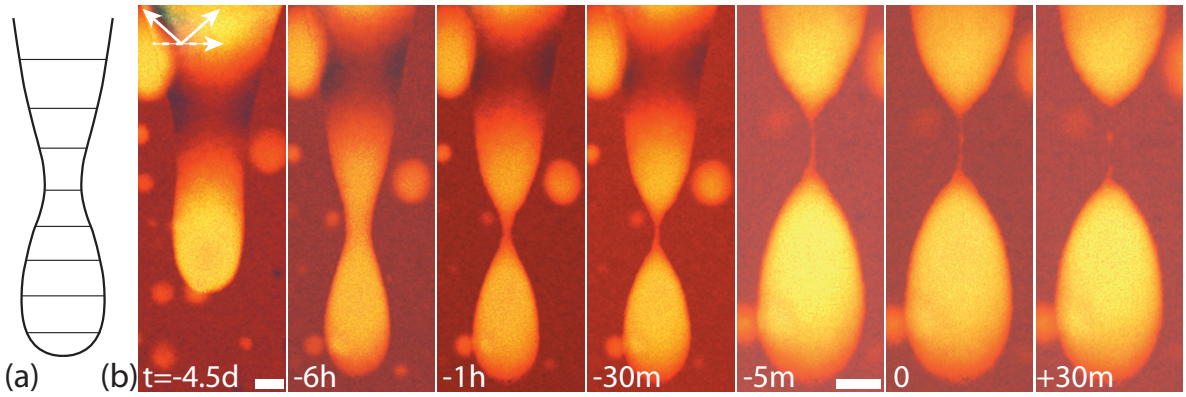

Figure 8.2. Droplet snap-off in aqueous gibbsite system. (a) Uniform director field in both the thinning neck and the pending drop. (b) Time series of a droplet pinch-off event in aqueous gibbsite. Time is set to zero at pinch-off. Solid arrows indicate the orientation of the polarizers and the dashed arrow that of the retardation plate. The scale bar denotes 25 μm.

value for K_1/w was determined from tactoid properties during the phase separation process, whereas this capillary has been standing for over a year. In the meantime a sedimentation equilibrium has developed, which is evidenced by the appearance of an isotropic phase on top of the nematic phase and a gradient in the scattering intensity that is visible on a macroscopic scale. The concentration in the lower part of the nematic phase is therefore probably higher than in a freshly phase separated sample, also because the mass density has now become larger than that of the isotropic phase below. As elastic constants are proportional to the square of the concentration and the anchoring strength has a linear dependence, a higher concentration would indeed lead to a larger value for K_1/w [57]. From the size of the falling droplet we can determine that K_1/w in this case must be larger than 10 μm (see Chapter 4).

Neck and drop geometry – The thinning neck has a symmetric shape with the drop elongated in the z-direction. A symmetric neck with elongated drop is typical for breakup under influence of thermal noise, although in that case the neck should be more cone-shaped [182, 197]. Also, the isotropic-nematic interface appears rather smooth, until the thinning neck becomes the order of micrometers, the thermal length scale in this system, while the symmetric shape develops when the neck is still much thicker. Because anchoring is weak in aqueous gibbsite, we do not expect it to have a large effect on the breakup, which is supported by the fact that the pending droplet is prolate instead of oblate, the shape that would provide optimal anchoring for the majority of the particles at the interface. The neck and prolate drop shape in fact resemble more the shape observed in yield-stress fluids [199]. Although nematic phases in general do not exhibit a yield stress, remember that we are dealing here with a highly

concentrated suspension. The observed buckling distortions in the nematic phase also indicate that the system might indeed exhibit a yield stress.

We should probably also consider the role of anisotropic viscosity, as the viscosity of the nematic phase strongly depends on the flow geometry [57, 200]. However, if we take into account the symmetry of the uniform director field inside the drop compared to the shape of the drop, we find that the symmetry axis of the director field points in the horizontal direction, whereas for the droplet shape the symmetry axis is along the vertical axis. This suggests that the anisotropy of the viscosity plays a negligible role, at least for the observed elongated drop shape. This is supported by Zhou and coworkers [195], who reported only quantitative effects of the viscous anisotropy.

The formed drop has a droplet width and length of about 60 and 100 μm respectively, which is of the order of the capillary length, L_c (see Table 8.1), defined as $L_c = \sqrt{\gamma/g\Delta\rho}$, with g the gravitational acceleration.

Snap-off position – The first breakup appears to always take place at the top of the thread. Literature reports for viscous breakup usually breakup near the end of the thread (end-pinching), except in the case of very high viscosity, where the thread tends to break at random positions [178, 201]. When thermal noise determines the breakup process, the breakup position is also random [182, 184]. It is therefore remarkable that the thread in this case, where the final stage of breakup seems to be influenced by thermal noise, tends to break at the upper end of the neck.

Satellite drops – We observe one or two satellite drops of about 1-3 μm in diameter, comparable to the minimal neck thickness just before breakup. This might be attributed to the influence of thermal roughness, because theory predicts many satellite drops for viscous drops, against only a few if thermal noise drives the breakup [178, 182].

Neck thickness – In order to analyse the breakup process quantitatively, we measured the minimum neck thickness as a function of time for one breakup event. Figure 8.3 depicts the results in a linear (8.3(a)) and logarithmic (8.3(b)) representation.

According to Zhou, Yue and Feng, liquid crystalline threads, at least with a uniform director field, should break up as a Newtonian liquid, be it with a different critical wavelength and breakup time [195]. In Newtonian fluids, the minimum neck thickness h as a function of time obeys $h(t) \propto (t0 - t)^{\alpha}$, with $t0 - t$ the time to breakup and the exponent α depending on the nature of the breakup process [178]. If inertia is dominant, α has a value of 2/3. However, the viscous length L_η, which sets the hydrodynamic inertial regime and is defined as $\eta^2/\rho\gamma$ with η the viscosity of the nematic phase and ρ the mass density, is several orders of magnitude larger than the system size, which implies that inertia is completely negligible here. For viscous breakup a value for the exponent α of 1 has been reported [179]. Furthermore, if the viscosity of the outer fluid plays a significant role, α should also be 1 [202], but if thermal noise controls the

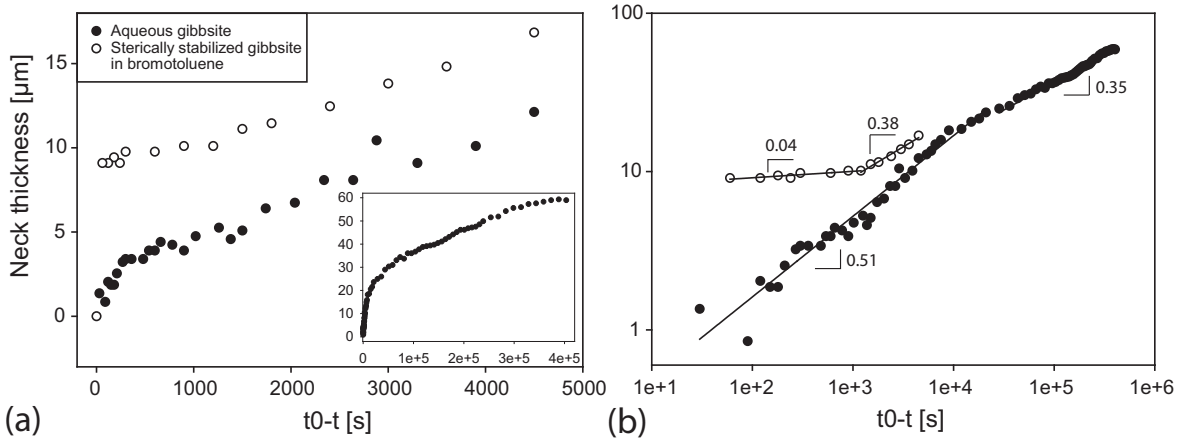

Figure 8.3. Minimal neck thickness as a function of the time to snap-off of both systems represented in a (a) linear plot (the inset shows the complete dataset of the breakup in aqueous gibbsite) and (b) logarithmic plot. Indicated are the fitted power-law exponents α (see also the main text).

breakup, α is expected to be 0.42 [183]. For the breakup of a *thermotropic* nematic thread (8CB), however, a significantly larger exponent of 1.5 has been measured [203].

When we fit our data with a power-law, we find for aqueous gibbsite an exponent α of 0.35 ($\pm$ 0.007) far away from breakup and 0.51 ($\pm$ 0.01) closer to breakup. Far away from breakup there is probably some restructuring of the nematic phase, because the defect that initially was located in the thinnest part of the neck moves upwards, away from the neck minimum, during 4 – 3 days before breakup (compare Figure 8.2 at 4.5 days and 6 hours before breakup). This may influence the value of α. The value $\alpha = 0.51$ close to breakup suggests that thermal fluctuations play a role here. Indeed, when the thread reaches a thickness of about 4 µm, the interface appears rough and the thread becomes slightly wavy.

8.3.2. Sterically stabilized gibbsite in bromotoluene

The value for K_1/w in sterically stabilized gibbsite dispersed in bromotoluene that we obtained in the previous chapters is much lower than that of aqueous gibbsite, namely 0.3 µm, which implies that at length scales larger than about 1 µm a non-uniform director field is energetically more favourable. More precisely, Goyal and Denn [194] predicted that if one assumes that the values of the splay, bend and saddle-splay elastic constants are equal ($K_1 = K_3 = K_{24}$, although that is not exactly true for plate-like particles [150]), a cylinder with radius R for values $wR/K_1 > 8.65$ would have an escaped radial (ER) director field. In this configuration the platelets are homeotropically aligned to the interface, forming a 2D radial director field with the director escaping along the 3rd dimension. The sterically system has a value for wR/K_1 of about 20

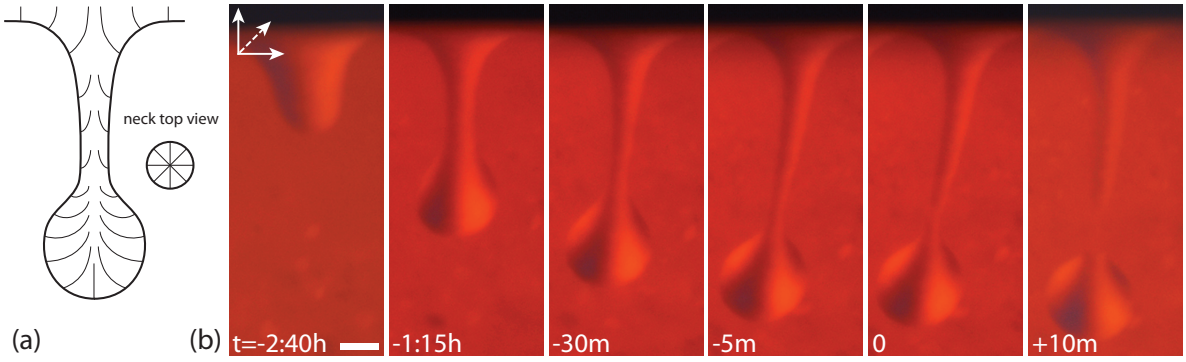

Figure 8.4. Droplet snap-off in sterically stabilized gibbsite in bromotoluene. (a) An escaped radial director field in the thinning neck and a distorted 3D radial field in the pending drop. (b) Time series of a droplet pinch off event. Time is set to zero at pinch-off. Solid arrows indicate the orientation of the polarizers and dashed arrow that of the retardation plate. The scale bar denotes 25 μm.

and indeed, when we deduce the director field from the polarized micrographs in Figures 8.1(c-d) and 8.4 we find in the neck this ER configuration, with the escape in the upward direction. The pending drop has a distorted 3D radial director field.

Neck and drop geometry – The thinning neck is asymmetric and the pending drop has a spherical shape, comparable to the shape reported for viscous breakup [178]. Even more striking is the resemblance of the drop shape and its birefringent pattern with the observations by Goyal and Denn [194], where simulations of the breakup of a nematic thread with an ER director field lead to exactly the same distorted radial director field in the drop. The formed drop has a diameter of 50-60 μm, which is of the order of the capillary length, L_c (see Table 8.1) and comparable to the drop size in aqueous gibbsite.

Snap-off position – In contrast to the aqueous gibbsite system, the neck in the sterically stabilized system breaks up near the droplet (end-pinching), in line with predictions for viscous breakup in isotropic fluids.

Satellite drops – Contrary to the observations for aqueous gibbsite, in the sterically stabilized system no satellite drops are observed at all. This may be related to the energy barrier that is involved in the breakup of a thread with an ER director field [194]. This energy barrier arises because the formation of a droplet requires the introduction of a point defect, which presumably suppresses drop formation. This effect is obviously absent in the case of a uniform director field.

Neck thickness – The neck thickness as a function of time is depicted in Figure 8.3 in a linear (8.3(a)) and logarithmic (8.3(b)) representation. From this figure it is immediately clear that the sterically stabilized system differs both quantitatively and qualitatively from the aqueous gibbsite system.

Far away from breakup the neck thins with a velocity comparable to that in aqueous gibbsite, but at a thickness of about 10 μm, the neck thinning slows down dramatically, and then the neck breaks suddenly. If we perform a power-law fit (which is somewhat questionable because the data comprises hardly two decades), we find an exponent α of 0.38 ($\pm$ 0.02) far away from breakup and $\alpha = 0.04$ ($\pm$ 0.008) close to breakup. To understand this extremely small value for the exponent α close to breakup, we consider what sort of mechanisms play a role in the breakup here. For the case of a thread with radial director field, Cheong and Rey distinguish two competing mechanisms [193]. The first is the surface tilting mechanism, where in the case of strong surface anchoring tilting of the surface leads to bend distortions in the thread. Frank elasticity in this case tends to stabilize the thread. The second effect is the so-called surface displacement mechanism, which is destabilizing in the case of a radial thread. However, when we calculate these two contributions for sterically stabilized gibbsite, we find that both effects contribute roughly equally, so we do not expect this to play a significant role.

Another important effect is the morphological change accompanying the breakup of the thread with ER director field, that we mentioned above [194]. At breakup, a point (or a small ring) defect has to be created in the separating droplet, which may form a considerable energy barrier and retard the breakup. Also, the neck thinning might be delayed because for a thinner thread the escaped radial configuration would become unfavourable, although at the thickness just before breakup, R = 4.5 μm, the value of wR/K_1 is still 14, well above the critical value 8.65 [194].

8.4. Breakup of elongated floating nematic drops

In the aqueous gibbsite samples we also observe relatively long nematic threads floating in the isotropic phase that break up in two or more droplets. Here, we study two of such breakup events. The first thread, depicted in Figure 8.5, is relatively short, with an initial length and width of about 190 and 55 μm respectively. The director field is again uniform and perpendicular to the long droplet axis. The thread breaks into two parts and its behavior is very similar to the case of the Rayleigh-Taylor instability in aqueous gibbsite discussed in the previous paragraph. The thinning neck has the same perfectly symmetric neck geometry, and two tiny satellite drops ($\sim$ 3 μm) form that coalesce in half an hour.

The second case, depicted in Figure 8.6 concerns a considerably longer thread, with at the start of the observations a length and a width of 330 and 50 μm respectively. Interestingly, from the retardation colours in Figure 8.6 it appears that the director field in this thread is uniform, but with a rotation of the director field halfway the thread, so that in the upper part the director field is more or less parallel to the thread, while in the lower part it is perpendicular. This implies that in the upper part of the thread the platelets exhibit planar anchoring, which is energetically unfavourable.

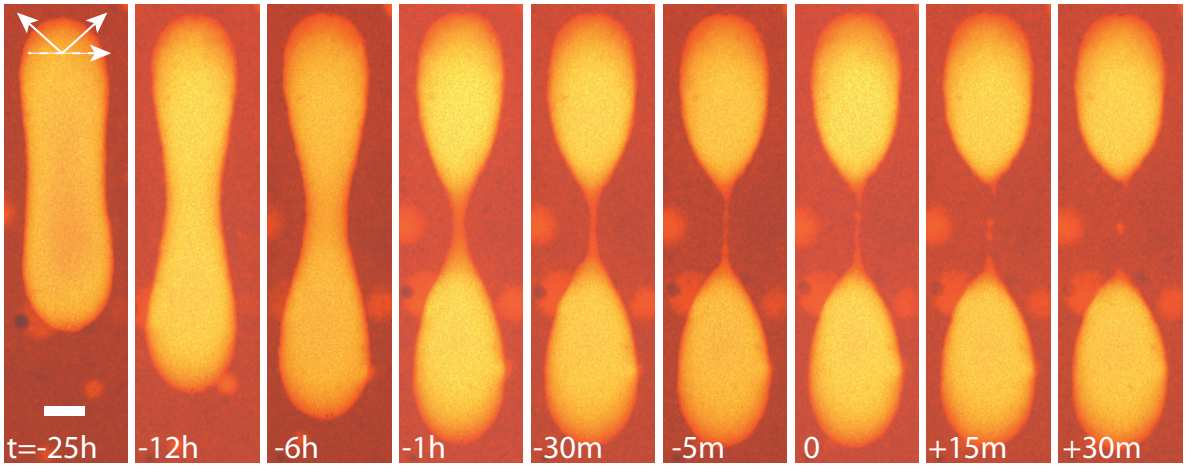

Figure 8.5. Time series of the breaukup of a floating nematic thread in aqueous gibbsite. Time is set to zero at breakup. Solid arrows indicate the orientation of the polarizers and dashed arrow that of the retardation plate. The scale bar denotes 25 μm.

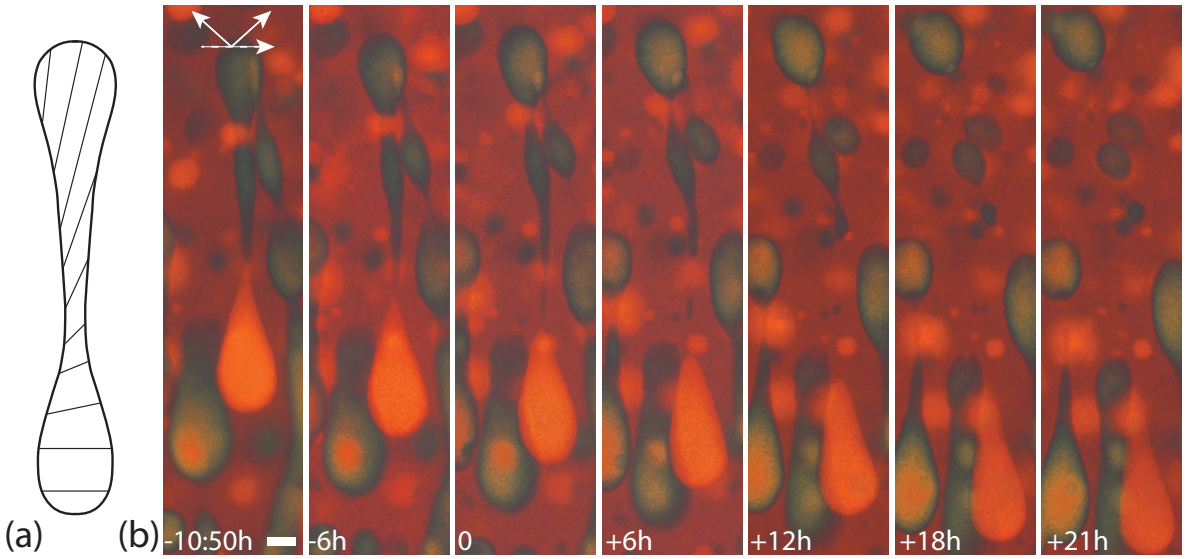

Figure 8.6. (a) Director field of a nematic thread floating in the isotropic phase. (b) The nematic thread breaks into droplets of various size. Time is set to zero at the first drop snap-off. Solid arrows indicate the orientation of the polarizers and dashed arrow that of the retardation plate. The scale bar denotes 25 μm.

This thread develops capillary instabilities over time and breaks up into several droplets. The first breakup is at the lower end, exactly at the point where the director field rotates from a vertical to a horizontal orientation. With this breakup, a large elongated drop with a length and width of 135 and 45 μm separates from the thread, together with a very thin filament that forms a tiny satellite drop of 2 μm.

Subsequently, the thread breaks at the other end, forms a drop of 50 μm, and leaves a middle part that then breaks into two smaller droplets of 28 and 17 μm. So, this thread breaks in an asymmetric way, leading to droplets of various sizes. Also, after breakup the droplets retract to a more or less spherical shape, apart from the lowest drop that remains highly elongated. The latter could be described to the orientation of the director field, except that a neighbouring droplet with a perpendicular orientation of the director field has the same elongated shape. Therefore, it is more likely that this particular shape is the consequence of shear forces during sedimentation.

8.5. Conclusion

We have studied the droplet snap-off of nematic liquid crystalline threads in suspensions of both charged gibbsite in water and sterically stabilized gibbsite in bromotoluene. Due to weak anchoring in aqueous gibbsite, the thinning neck has a uniform director field, while strong homeotropic anchoring in the case of sterically stabilized gibbsite leads to an escaped radial director field. This difference in director field configuration results in a considerably different breakup mechanism, both quantitatively and qualitatively. The uniform thread forms a drop with uniform director field, elongated in the z-direction, possibly due to a yield stress, whereas the neck thinning rate and satellite drop occurrence also show influence of thermal noise. On the other hand, in the sterically stabilized system the pending drop has a spherical shape with a distorted radial director field and no satellite drops form. Moreover, the neck thinning rate in this case decreases dramatically close to snap-off, probably due to an energy barrier related to the creation of a point defect in the separating drop.

Short free floating nematic threads in aqueous gibbsite break up in a similar way as droplets separate from pending Rayleigh-Taylor instabilities, while long nematic threads develop multiple capillary instabilities and subsequently break up in an asymmetric manner.

To conclude, although it is clear that the director field structure of a nematic thread significantly influences its breakup behaviour, these systems certainly need and deserve a more thorough analysis as well as theoretical work in order to be able to understand the exact breakup mechanisms.

Acknowledgements

Dirk Aarts is acknowledged for allowing us to use his IDL routine for the analysis of the image series of the breakup process. Emile Bakelaar is thanked for his IDL routine for edge detection. We thank David van der Beek for particle synthesis.

Part 4

Columnar phase and droplets

9

Observation of columnar liquid crystal droplets

Abstract

We present the first direct observation of droplets of the columnar phase in a suspension of gibbsite platelets. From polarized light microscopy and optical Bragg reflection measurements we find that these droplets consist of stacks of platelets in a hexagonal arrangement, forming a flat, disk-shaped droplet. We discuss how this structure might be related to the structure of the high concentration nematic phase and to the anisotropic isotropic-columnar interfacial tension.

9.1. Introduction

Suspensions of colloidal spheres, plates, and rods display crystalline and liquid crystalline phases with positional order in three dimensions (colloidal crystals) [204], two dimensions (columnar liquid crystals) [33] and one dimension (smectic liquid crystals) [10]. Direct observations of the nucleation and growth of colloidal crystals and smectic liquid crystalline phases have been reported [66, 205] and compared to the results of theory and simulation [67, 206]. These studies showed that while the nucleation of colloidal crystals of spheres involves roughly spherical 3D clusters, the nucleation of smectic phases in suspensions of rods proceeds via the formation of 2D lateral clusters of rods, which subsequently arrange in a 1D ordered structure.

The columnar liquid crystal phase, a two-dimensional hexagonal lattice of columns constituted of liquid-like stacks of particles, first predicted by computer simulations by Veerman and Frenkel to occur in suspensions of hard plate-like particles [30], was observed experimentally about 10 years ago [33, 34].

Here, we describe the first observation of columnar liquid crystal droplets, which result from nucleation in the nematic phase. We use a system of gibbsite platelets with a bimodal distribution of the platelet aspect ratio (diameter/thickness). This system displays an isotropic-nematic density inversion and subsequently at higher concentration a three phase coexistence with the isotropic phase located between the nematic top phase and the columnar bottom phase (Chapter 3). This arrangement of the phases allows observation of the columnar droplets in the non-birefringent isotropic middle phase, as they sediment from the nematic phase, where they originate in, to the columnar phase. From optical Bragg reflection measurements and polarized light microscopy we find that these droplets consist of stacks of platelets in a hexagonal arrangement, leading to a flat droplet.

9.2. Experimental

We used the gibbsite system described in Chapter 3, that is charge stabilized with aluminum chlorohydrate and dispersed in 10^{-2} M NaCl. The platelets have a well-defined hexagonal shape, with an average diameter (that is: corner-to-corner distance) of 207 nm ($\pm$35%) and an average thickness of 8.2 nm ($\pm$ 46%), both with a unimodal distribution. However, the platelet aspect ratio (diameter/thickness) has a bimodal distribution, with a narrow peak of small aspect ratio (thick) platelets and a broader peak of large aspect ratio (thin) platelets (see Figure 3.1 for histograms of the particle size and aspect ratio distributions). The suspensions were concentrated via centrifugation and subsequent redispersion in 10^{-2} M NaCl. Samples were prepared in $0.2 \times 4 \times 40$ mm^3 VitroCom flat glass capillaries that were flame-sealed and glued to avoid evaporation of the solvent.

The system was studied with polarized light microscopy as described in Chapter 2. Optical Bragg reflections were observed with the polarized light microscope while the sample was illuminated with a white light source (model 190, Dolan Jenner).

9.3. Results and Discussion

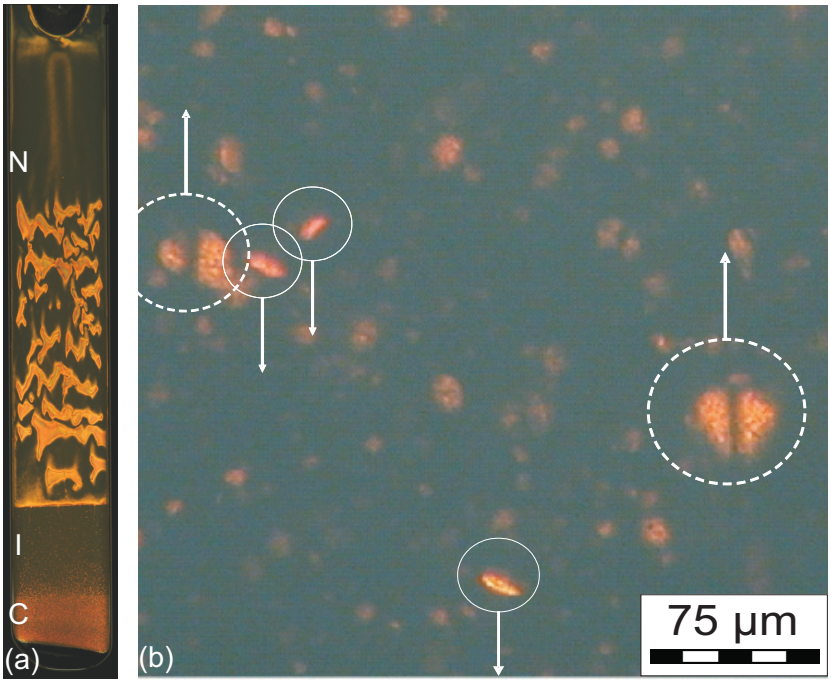

Figure 9.1. The isotropic phase between the nematic and columnar phase. (a) Suspension of gibbsite platelets with a bimodal distribution of the aspect ratio between crossed polarizers exhibiting a three phase coexistence with nematic (N) upper, isotropic (I) middle, and a columnar (C) bottom phase. (b) Polarized light microscopy image of the isotropic middle phase, which contains both rising nematic tactoids and sedimenting columnar droplets.

At a volume fraction of 30%, the system described above exhibits a three phase coexistence with a nematic upper phase, an isotropic middle phase and a columnar bottom phase, shown in Fig 2(a). In the isotropic middle phase two types of droplets can be observed, which are moving in opposite directions, as presented in Fig 9.1(b). The rising droplets originate from the columnar phase and move through the isotropic phase toward the nematic phase with which they coalesce. They have a spherical or ellipsoidal shape and can be identified as the well-known nematic droplets, or tactoids (Chapter 4).

Furthermore, we observe sedimenting droplets that originate in the nematic phase and settle through the isotropic phase toward the columnar phase. They appear as elongated droplets with a typical thickness ranging from 1.5 to 10 µm and a length

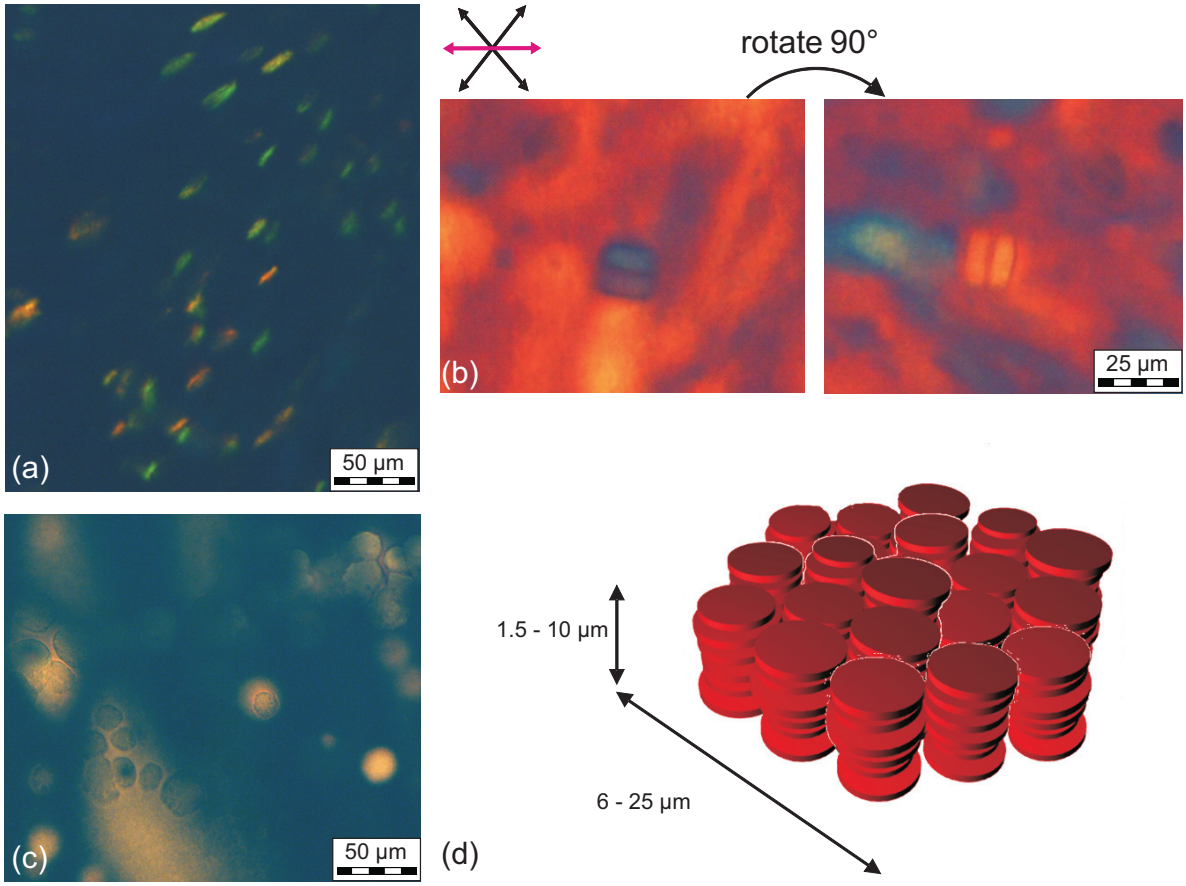

Figure 9.2. Columnar liquid crystal droplets. (a) Columnar droplets show iridescence in reflected light, with colors ranging from green to orange. (b) Two parallel columnar droplets viewed through the polarized light microscope with a full wave retardation plate ($\lambda = 530$ nm), in order to determine the orientation of the platelets (see the text for an explanation of the colors). Arrows indicate the orientation of the polarizers (black) and the slow axis of the retardation plate (purple). (c) Columnar droplets appear dark and with two long axes when located on top of a birefringent (nematic) background. (d) Schematic illustration of the structure of the columnar droplets (not to scale). The disk-like droplets consist of stacks of columns on a 2D hexagonal lattice.

ranging from 6 to 25 µm, and are strongly birefringent. If observed in reflected light, the droplets exhibit angle dependent iridescence with colors ranging from green to orange (see Figure 9.2(a)), which indicates that there is periodic ordering of the platelets. The observed Bragg colors correspond to an hexagonal columnar phase with a lattice spacing of about 250 nm. The droplets show only one iridescent color for a given angle, indicating that they consist of a single domain columnar phase.

By means of a full wave retardation plate the orientation of the platelets inside the droplet could be determined. Recall that in the case of aqueous gibbsite the birefringence is negative, which implies that if the particles have their director perpendicular to the slow axis of the retardation plate, the optical path difference adds, while in the perpendicular orientation it subtracts (Chapter 2). As shown in Figure 9.2(b), if the retardation plate is parallel to the long axis of the droplet, the droplet appears blue, which corresponds to an addition of the optical path difference, whereas in the perpendicular case it is red, meaning that the optical path difference is subtracted. So the particles must be oriented with their director along the short axis of the droplet. Although the columnar droplets appear elongated at first sight, careful examination with polarized light microscopy reveals that they have two long axes. Figure 9.2(c) shows columnar droplets lying flat in the focal plane, which appear dark when they are located on top of a birefringent (nematic) background. In this orientation they do not display birefringence, independent of the orientation of the polarizers.

Based on the above described observations, we conclude that the columnar droplets consist of a disk-like structure containing a single domain of hexagonally arranged columns of platelets, as illustrated in Figure 9.2(d). In this arrangement the platelets have their director perpendicular to the long side of the droplet, as was deduced from the retardation colors. With such a structure we can understand why the droplets appear as elongated in one direction, both in polarization microscopy and observations of iridescence. The columnar phase of platelets shows birefringence only when the director has a component in the focal plane and is not parallel to the polarization direction of the polarizers. If viewed from the flat side, the director is perpendicular to the focal plane, and the droplets will be practically invisible in polarized light microscopy. Likewise, for Bragg reflections to occur, light needs to enter perpendicular to the column direction, i.e., the short side of the disk shaped droplet, which again allows observation only from the edge side of the droplet.

One could argue that shear forces during sedimentation could influence the droplet shape, as flow might erode the different faces of the droplet at a different rate. However, this seems unlikely because the same elongated shape can also be observed in the nematic phase before the droplets start to sediment. Furthermore, the large polydispersity of this particular gibbsite system could have an effect on the droplet properties. However, for the experiments presented here, the polydispersity is of great advantage because it offers the opportunity to observe the columnar droplets in the non-birefringent isotropic phase, through which they sediment on their way to the columnar phase. Also, it has been shown in Chapter 3 both in experiment and by theory that there is fractionation in the system, as the lower aspect ratio (thicker) platelets accumulate in the isotropic phase, while the higher aspect ratio (thinner) platelets prefer the nematic phase. In addition there might be a fractionation effect in the columnar phase, because

the platelets have to fit in the columns. This implies that the platelets contained in the columnar droplets are probably less polydisperse than in the parent suspension.

It is interesting to compare the present results to observations on the nucleation of the smectic phase in suspensions of rod-like particles [66]. Maeda and Maeda observed that this started with the formation of laterally growing clusters. Then, as the number of clusters increased, multiple layering of the clusters occurred, resulting in a 1D ordered structure (smectic liquid crystal). Similar phenomena were observed by Dogic and Fraden in the isotropic-smectic phase transition in a colloidal rod-polymer mixture [44, 207]. The physical origin of this nucleation mechanism was studied by computer simulations [67,68]. Schilling and Frenkel showed that the growth of a cluster is inhibited because the rods tend to align perpendicular to the formed layer, resulting in lateral growth only.

Extending this idea naively to the case of platelets, one would expect the particles to align with the director perpendicular to the plane of a cluster, which would mean that lateral growth is the least favorable growth direction. This would result in clusters that are elongated in the direction of the columns. However, we observe the opposite: the droplets have their largest dimension in the lateral direction. This might suggest that not the individual platelets are the building units of the columnar droplets, but rather short stacks of platelets that might exist in the nematic phase. Indeed, replacing the rods in the Schilling-Frenkel-model [67] by stacks of platelets leads to lateral growth, as illustrated in Figure 9.3.

The presence of such stacks, while somewhat speculative here, was established in other gibbsite suspensions from small angle x-ray scattering [208]. In a gibbsite system with similar platelet size (225 nm compared to 207 nm for the platelets used here), it was found that at an ionic strength of 10^{-2} M, a columnar nematic phase was formed at concentrations above 450 g/L, while the system studied here is at 727 g/L. Furthermore, in computer simulations of thin charged platelets a stable columnar nematic phase was recently found at high pressures [209].

The explanation above for the observed flat droplet shape is in essence a kinetic one. We now consider whether the shape can be explained in terms of an equilibrium Wulff construction [210]. According to Wulff, the length of a vector drawn normal to a crystal face will be proportional to its interfacial energy [128]. This implies that the interfacial tensions $\gamma_{\parallel}$ and $\gamma_{\perp}$ for the director oriented parallel and perpendicular to the interface are related as:

$$\frac{\gamma_{\parallel}}{h_{\parallel}} = \frac{\gamma_{\perp}}{h_{\perp}} \tag{9.1}$$

with $h_{\parallel}$ and $h_{\perp}$ the distances from the droplet center to the respective interface. Using this equation and the observed droplet aspect ratio we obtain a value of 3 to 5 for the ratio of $\gamma_{\parallel}/\gamma_{\perp}$ for the isotropic-columnar interface.

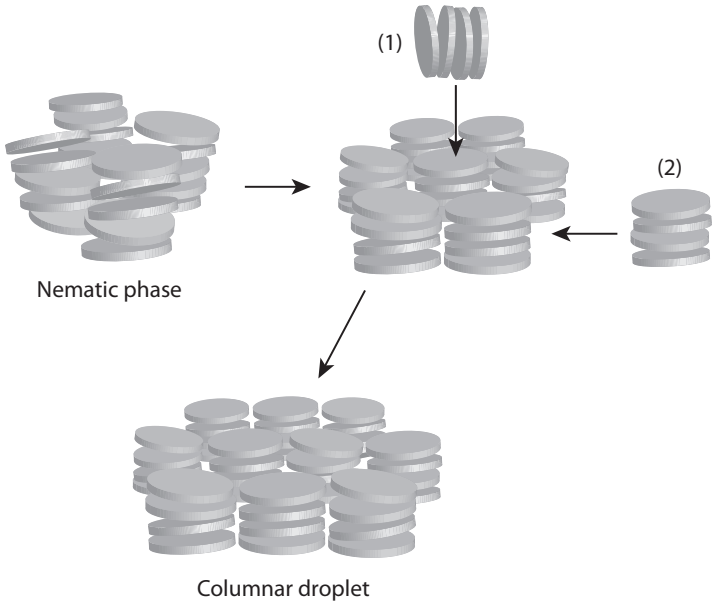

Figure 9.3. Schematic illustration of the suggested nucleation/growth pathway of the experimentally observed columnar liquid crystal droplets. Short stacks of particles present in the nematic phase tend to align parallel to the droplet surface (stack (1) and (2)). However, only stacks parallel to the side of the droplet (stack (2)) contribute to the growth of the droplet, which results in lateral growth.

For comparison, we can determine the ratio of $\gamma_\perp/\gamma_\parallel$ for the *isotropic-nematic* interface from the value for the dimensionless anchoring strength $\omega \equiv w/\gamma$ that we obtained in Chapter 4. We take the Rapini-Papoular type form for the anisotropic surface tension σ that we used in Chapter 4:

$$\sigma = \gamma + w \sin^2 \theta \tag{9.2}$$

with γ the bare surface tension, w the anchoring strength, and θ the angle between the surface normal and the director field at the surface [139]. This implies that the interfacial tension for the director perpendicular and parallel to the interface normal are related as:

$$\left.\begin{aligned} \gamma_\perp &= \gamma + w \\ \gamma_\parallel &= \gamma \end{aligned}\right\} \quad \frac{\gamma_\perp}{\gamma_\parallel} = 1 + \frac{w}{\gamma} = 1 + \omega \tag{9.3}$$

Using $\omega = 0.6$ from Chapter 4 we then obtain $\frac{\gamma_\perp}{\gamma_\parallel} = 1.6$, which is considerably smaller than the value we find here for the isotropic-columnar interface.

9.4. Conclusion

Ordered phases in suspensions of colloidal particles with different shapes are fascinating as they are direct physical manifestations of the great variety and subtlety of

entropy driven structures. The observations presented here, together with earlier work on the formation of colloidal crystals and smectic liquid crystals, demonstrates that shape is also a decisive factor in the nucleation pathways of these structures. To obtain further insight into the formation and structure of the remarkable columnar liquid crystal droplets described here and the possible relation to the nucleation of the columnar phase, is a challenge for both theory and simulation.

Acknowledgements

David van der Beek is thanked for particle synthesis.

10

Devitrification of the glassy state in suspensions of gibbsite platelets

Abstract

Colloidal suspensions of charged gibbsite platelets at salt concentrations of 10^{-2} M and below and with a sufficiently high particle concentration form a kinetically arrested, glassy state. We study the evolution of this glassy state over an extended period of time. After months to years, we observe small, iridescent grains of the hexagonal columnar phase. The connections between this devitrification phenomenon and the structure of the glassy state are discussed.

10.1. Introduction

In his classical (1905) paper on Brownian motion Einstein [211] clearly recognized that colloidal particles in a suspension obey the same thermo-statistics as atoms in assemblies. Hence, the thermodynamic properties of an assembly of colloids are formally the same as those of an assembly of atoms with an inter-atomic potential of the same form [212]. Conceptually, the simplest interaction between particles is that in a model system consisting of hard spheres, which experience an infinitely repulsive force when they touch, but no forces otherwise. Originally, this was proposed as a mathematically simple model of atomic liquids [213]. Over the last decades its benefit as a basic model for complex liquids has been demonstrated [212].

Although hard-sphere interacting atoms do not exist, good approximations to hard sphere-interacting colloids do [204, 214]. The equilibrium phase behaviour of systems of hard spheres was established many years ago by computer simulations [215, 216]. Up to a volume fraction $\phi = 0.494$ the equilibrium state is a fluid, while for $\phi > 0.545$ the equilibrium state is a crystal. For $0.494 < \phi < 0.545$, the fluid and crystal states coexist. This phase behaviour has indeed been observed in concentrated suspensions of nearly hard-sphere-interacting colloids [204,214]. Moreover, Pusey and Van Megen [204] observed that in disordered suspensions with volume fractions above 0.58, particles become so tightly trapped, or 'caged', by their neighbours that they are unable to move far enough to nucleate crystals. Instead, long-lived amorphous states called 'colloidal glasses' are obtained (for a recent review see [217]).

In 1999 Fabbian et al [218] and Bergenholtz and Fuchs [219] considered the effect of the addition of short-ranged attraction to the hard-sphere repulsion between particles. They predicted a new scenario of transitions with a pocket of liquid and crystal states enclosed by a repulsive glass and an attractive glass. This remarkable prediction has been verified experimentally, using colloidal particles with a tunable depletion attraction induced by the addition of non-adsorbing polymer molecules [220–222]. Remarkably, a phase diagram with the sol-region enclosed by two different kinetically arrested states turned out to be typical, not only for spherical colloids, but also for anisometric colloids. In particular, in suspensions of natural and synthetic smectite clays a very similar situation is observed experimentally [38, 223–225] and has been discussed theoretically [226]. Here, the balance between attractive and repulsive interactions is tuned by variation of the ionic strength. In these suspensions an attractive gel is observed at salt concentrations above $10^{-3} - 10^{-2}$ M and a glass [1] is observed at $10^{-4} - 10^{-5}$ M, while an enclosed region of sol states is found. Michot et al [38] observed isotropic-nematic phase equilibria in the sol-region.

[1] This state is also commonly referred to as repulsive gel [223]. We will refer to it as a glass following [226] since the kinetic arrest originates from caging effects.

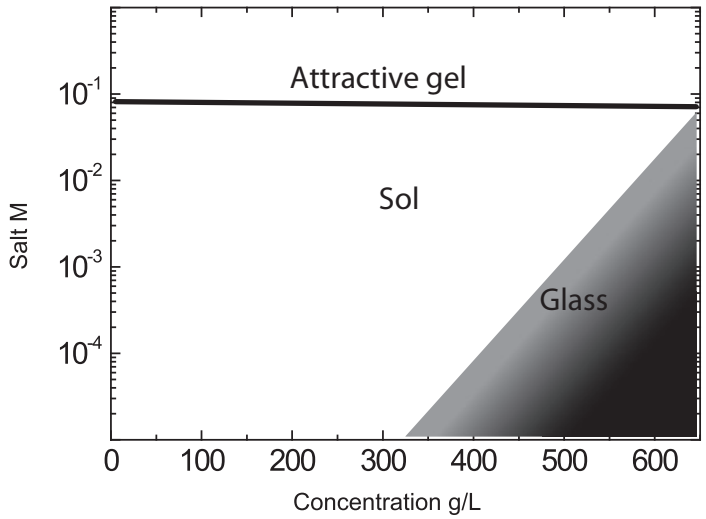

Figure 10.1. Schematic sol-gel/glass diagram of charged colloidal gibbsite platelets in water.

Recently, we have observed that suspensions of charged colloidal gibbsite platelets - which may be considered as model clay particles - display similar sol-gel/glass behaviour [227, 228], see also the schematic phase diagram in Figure 10.1. Birefringence and iridescence show that in the sol state both nematic and hexagonal columnar liquid crystal phases are formed. Upon decrease of the salt concentration and/or increase of the gibbsite concentration the nematic phase gradually transforms from the discotic nematic (N_D) into the columnar nematic (N_C) with strong side-to-side inter-particle correlations [208]. Subsequently, this N_C phase shows a transition to the hexagonal columnar phase, although at high particle concentration this phase transition is pre-empted by the formation of a kinetically arrested state. Small angle x-ray scattering (SAXS) experiments show that the structural features of this arrested state are similar to those of the N_C phase.

Here, we focus on the ageing of this kinetically arrested state of gibbsite suspensions just beyond the sol-gel transition, as schematically illustrated in Figure 10.1. Over a period of months to years small hexagonal columnar crystallites appear in the system.[2]

10.2. Experimental details

For this work we used the gibbsite system described in Chapter 3, dispersed in a 10^{-2} M NaCl solution. With centrifugation and subsequent redispersion samples were prepared with concentrations of 850 and 1050 g/L.

Naked eye observations in reflected light and between crossed polarizers were performed as described in Chapter 3 and the samples were photographed with a Nikon

[2]The devitrification phenomena in described in this chapter are discussed in a broader context in [229].

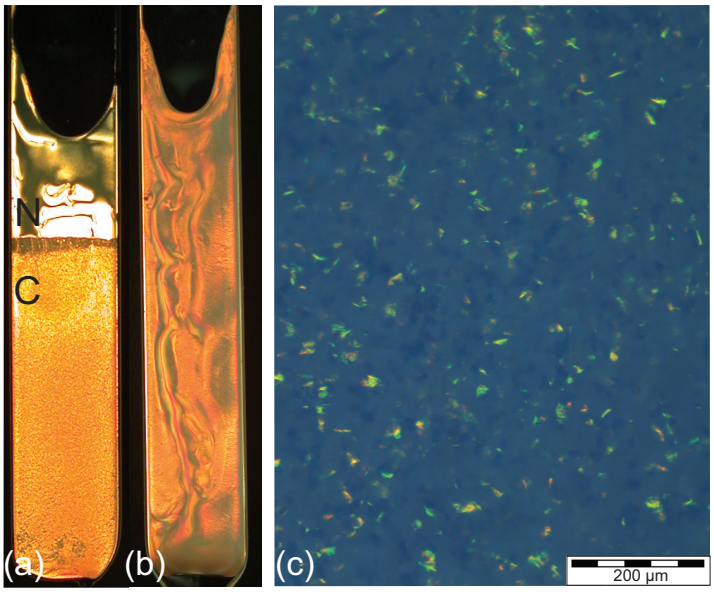

Figure 10.2. Gibbsite dispersions observed between crossed polarizers, at (a) 850 g/L with nematic-hexagonal columnar phase coexistence and (b) at 1050 g/L in the glassy state, both with 10^{-2} M NaCl. (c) Micrograph of the hexagonal columnar phase in (a) under white light illumination.

Coolpix 995 digital camera. Polarized light microscopy was performed as described in Chapter 2.

10.3. Results

The studied gibbsite system exhibits remarkable phase behaviour, due to the bimodal distribution of the aspect ratio of the platelets. This includes an isotropic-nematic density inversion and a nematic-isotropic-columnar phase equilibrium, that is described in detail in Chapter 3.

At very high particle concentration, we observe a transition from a sol state, displaying liquid crystal phase transitions, to a kinetically arrested state. In Figure 10.2 we present two samples, one in the sol-region with a particle concentration of 850 g/L and one in the glassy state with a particle concentration of 1050 g/L. The sample in the sol-region displays coexistence of the nematic and the hexagonal columnar phase, as is evident from the birefringent patterns and optical iridescence.

The sample in the glassy state displays birefringent patterns that originate from the macroscopic orientational ordering caused by the shear forces during the filling of the capillary, but no iridescence. The birefringent patterns in the glassy sample persist over months (see Figures 10.3 (a) and (b)). Eventually, after more than one year, an interface appears in the top part of the sample which separates an upper layer, containing isotropic and nematic domains, from the lower part of the sample. The latter

Figure 10.3. Time evolution of the glassy gibbsite sample, as observed between crossed polarizers.

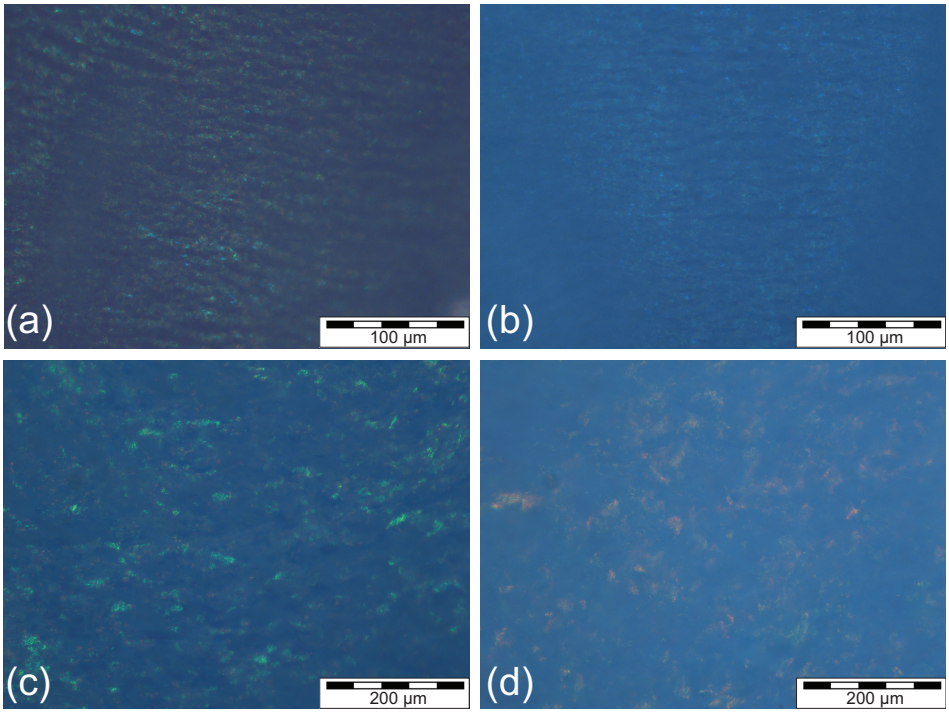

Figure 10.4. Micrographs of the glassy state under illumination with white light; (a) bottom part after 3 months; (b) bottom part, (c) middle part, and (d) top part of the sample after 17.5 months.

retained the original birefringence patterns, albeit slightly compressed. Apparently, the compression of the glassy phase under the influence of gravity lowers the particle concentration in the upper part of the sample to such a degree that it allows the formation of both isotropic and nematic domains.

After three months, optical iridescence was observed at various heights in the glassy sample, originating from grains with a size of about 2-5 μm (Figure 10.4 (a)), which is much smaller than the hexagonal columnar grain size in the phase separated sample in Figure 10.2. Moreover, the Bragg reflections in the glass are predominantly blue, rather than green-yellow-orange in the hexagonal columnar phase, indicating smaller inter-columnar distances.

After 17.5 months, the sizes and colours of the iridescent grains in the bottom part of the sample (Figure 10.4 (b)) are virtually unchanged (compare to Figure 10.4 (a)). Towards the top of the sample, the grain size increases (Figure 10.4 (c)) and at the same time a shift of the Bragg colour from predominantly blue via green to orange is observed, indicating an increase of the inter-columnar distance. Eventually, near the top of the sample, the iridescence resembles that of a hexagonal columnar phase (Figure 10.4 (d)).

10.4. Discussion and conclusions

The studied gibbsite system enters a kinetically arrested state upon an increase of the particle concentration. After an ageing period of months to years, this kinetically arrested state - while retaining its outside appearance - shows small iridescent grains, indicative of local transformation to the hexagonal columnar phase.

While we do observe the effect of the shear induced macroscopic orientational order, we have no indication that the degree of local columnar ordering, is affected by shear. The length scale of the shear-induced macroscopic orientational ordering pattern (being of the size of the system) is much larger than the size of the hexagonal columnar nuclei. Hence it seems unlikely that shear directly affects the devitrification.

It is conceivable that nucleation of these crystallites is facilitated by the local columnar order in the preceding arrested state [228]. Possibly, these short columns play a role comparable to that in the formation of the columnar droplets described in the previous chapter (Chapter 9).

It may be instructive to compare our results to devitrification phenomena observed in molecular glasses. In these systems an unusual acceleration of the crystal growth rate below the glass transition has been ascribed [230,231] to the slow beta mode [232], which is still active in the glassy state. Others ascribe it to the volume decrease upon ordering and the resulting creation of free volume near the interface between an ordered region and the surrounding glass region [233, 234]. The local transformation of the kinetically arrested columnar state to the hexagonal columnar phase is reminiscent of

the dynamical heterogeneities observed in colloidal hard sphere suspensions [235,236]. A possible link between structural order and dynamic heterogeneity has been emphasized by Tanaka [237, 238]. These papers suggest that even in a supercooled liquid and a glassy state some degree of structural order may develop. If this is the case, it may act as an initiator for devitrification. Something similar seems to occur in our suspensions of plate-like gibbsite colloids with the local columnar ordering playing the role of an initiator for devitrification. An alternative explanation may be that we are dealing with a nucleation phenomenon with a low nucleation barrier, which gives rise to many nuclei [239]. The low nucleation barrier may in turn be related to the columnar nature of the kinetically arrested state.

We want to conclude with a few comments on the relation between the glass state of a suspension of hard colloidal spheres and the glass state in a suspension of colloidal platelets. In the case of spheres, Frank [240] suggested, more than half a century ago, the existence of long-lived locally favoured structures, the geometry of which may prevent the system from relaxing to its equilibrium (crystal) state. Recently, Royall [241] provided direct experimental evidence of such a local structural mechanism for dynamical arrest. From this perspective, the hard-sphere fluid-to-crystal-transition may be considered as a locally favoured structure avoiding transition. In the case of platelets, computer simulations have shown that there is a strong tendency to form columns of platelets upon an increase of the volume fraction [30]. As the volume fraction is increased, these columns grow in length. The columns themselves are orientationally disordered and hence there is an appreciable interaction between different columns. It has been suggested, on the basis of small angle x-ray and neutron scattering on synthetic (Laponite [224]) and natural smectite (Montmorillonite [38, 225]) clays, and theoretical [226] considerations, that this interaction among the columns becomes so severe that it leads to a kinetically arrested glass phase. In our system of gibbsite platelets the particles are sufficiently monodisperse that the columns try to order in such a way that the packing problems are minimized. This then leads to a N_C phase, and upon a further increase of the volume fraction to the hexagonal columnar phase. Clearly then, the locally favoured structures in the case of platelets do not, as such, prevent the formation of liquid crystal phases. However, above a limiting concentration the columns may become kinetically arrested, leading to a glassy state. The eventual observation of small crystallites in this case appears to be enabled, rather than obstructed, by locally favoured structures. This is the opposite of the behaviour observed in the canonical hard-sphere model. In the case of platelets, the key structural element involved in the arrest transition is a stack of platelets, rather than an individual platelet. Such stacks are already present in the columnar nematic state, as well as in the arrested state itself. It may be that such (flexible) stacks can locally pack better in the arrested state than in the hexagonal columnar phase.

Acknowledgements

Maurice Mourad and Jeroen van Duijneveldt are thanked for helpful discussions.

Bibliography

[1] D. H. Everett. *Basic principles of colloid science*. Royal Society of Chemistry, London, 1988.

[2] W. B. Russel, D. A. Saville, and W. R. Schowalter. *Colloidal dispersions*. Cambridge University Press, New York, 1999.

[3] P. G. de Gennes and J. Prost. *The Physics of Liquid Crystals*. Oxford University Press, New York, 1995.

[4] S. Chandrasekhar. *Liquid Crystals*. Cambridge University Press, Cambridge, 1992.

[5] H. Zocher. Ueber freiwillige strukturbildung in solen. *Z. Anorg. Allg. Chem.*, 147:91, 1925.

[6] F. C. Bawden, N. W. Pirie, J. D. Bernal, and I. Fankuchen. Liquid crystalline substances from virus-infected plants. *Nature*, 138:1051, 1936.

[7] L. Onsager. The effect of shape on the interaction of colloidal particles. *Ann. NY Acad. Sci.*, 51:627–659, 1949.

[8] J. Vieillard-Baron. *J. Chem. Phys.*, 56:4729, 1972.

[9] D. Frenkel and B. M. Mulder. The hard ellipsoid-of-revolution fluid: I. Monte Carlo simulations. *Mol. Phys.*, 55:1171–1192, 1985.

[10] G. Oster. Two-phase formation in solutions of tobacco mosaic virus and the problem of long-range forces. *J. Gen. Physiol.*, 33:445–473, 1950.

[11] M. Hosino, H. Nakano, and H. Kimura. Effect of orientational fluctuaction on nematic-smectic A transition in the system of hard rod molecules. *J. Phys. Soc. Jap.*, 47:740–745, 1979.

[12] D. Frenkel, H. N. W. Lekkerkerker, and A. Stroobants. Thermodynamic stability of a smectic phase in a system of hard rods. *Nature*, 332:822–823, 1988.

[13] Y. Maeda and S. Hachisu. Structure of schiller layers in β-FeOOH sols: Observation by scanning electron microscope. *Colloids Surf.*, 7(4):357–360, 1983.

[14] P. A. Buining and H. N. W. Lekkerkerker. Isotropic-nematic phase separation of a dispersion of organophilic boehmite rods. *J. Phys. Chem.*, 97(44):11510–11516, 1993.

[15] B. J. Lemaire, P. Davidson, J. Ferré, J. P. Jamet, D. Petermann, P. Panine, I. Dozov, and J. P. Jolivet. Physical properties of aqueous suspensions of goethite (α-FeOOH) nanorods: Part I: In the isotropic phase. *Eur. Phys. J. E*, 13:291–308, 2004.

[16] B. J. Lemaire, P. Davidson, J. Ferré, J. P. Jamet, D. Petermann, P. Panine, I. Dozov, and J. P. Jolivet. Physical properties of aqueous suspensions of goethite (α-FeOOH) nanorods: Part II: In the nematic phase. *Eur. Phys. J. E*, 13:309–319, 2004.

[17] L.-S. Li, J. Walda, L. Manna, and A. P. Alivasatos. Semiconductor nanorod liquid crystals. *Nano Lett.*, 2:557–560, 2002.

[18] N. R. Jana, L. A. Gearheart, S. O. Obare, C. J. Johnson, K. J. Edler, S. Mann, and C. J. Murphy. Liquid crystalline assemblies of ordered gold nanorods. *J. Mater. Chem.*, 12:2909–2912, 2002.

[19] A. Kuijk, A. van Blaaderen, and A. Imhof. Synthesis of monodisperse, rod-like silica colloids with tunable aspect ratio. *Submitted*.

[20] P. Davidson, D. Petermann, and A. M. Levelut. The measurement of the nematic order parameter by x-ray scattering reconsidered. *J. Phys. II France*, 5:113–131, 1995.

[21] B. J. Lemaire, P. Davidson, J. Ferré, J. P. Jamet, P. Panine, I. Dozov, and J. P. Jolivet. Outstanding magnetic properties of nematic suspensions of goethite (α-feooh) nanorods. *Phys. Rev. Lett.*, 88:125507, 2002.

[22] W. J. Orts, L. Godbout, R. H. Marchessault, and J.-F. Revol. Enhanced ordering of liquid crystalline suspensions of cellulose microfibrils: a small angle neutron scattering study. *Macromolecules*, 31:5717–5725, 1998.

[23] H. Maeda. Atomic force microscopy studies for investigating the smectic structures of colloidal crystals of β-FeOOH. *Langmuir*, 12:1446–1452, 1996.

[24] O. Pelletier, P. Sotta, and P. Davidson. Deuterium nuclear magnetic resonance study of the nematic phase of vanadium pentoxide aqueous suspensions. *J. Phys. Chem. B*, 103:5427–5433, 1999.

[25] L.-S. Li, M. Marjanska, G. H. J. Park, A. Pines, and A. P. Alivasatos. Isotropic-liquid crystalline phase diagram of cdse nanorod solution. *J. Chem. Phys.*, 120:1149–1152, 2004.

[26] J. A. C. Veerman and D. Frenkel. Phase diagram of a system of hard spherocylinders by computer simluation. *Phys. Rev. A*, 41:3237–3244, 1990.

[27] S. C. McGrother, D. C. Williamson, and G. Jackson. A re-examination of the phase diagram of hard spherocylinders. *J. Chem. Phys.*, 104(17):6755–6771, 1996.

[28] P. Bolhuis and D. Frenkel. Tracing the phase boundaries of hard spherocylinders. *J. Chem. Phys.*, 106:666–687, 1997.

[29] I. Langmuir. The role of attractive and repulsive forces in the formation of tactoids, thixotropic gels, protein crystals and coacervates. *J. Chem. Phys.*, 6:873–896, 1938.

[30] J. A. C. Veerman and D. Frenkel. Phase behavior of disklike hard-core mesogens. *Phys. Rev. A*, 45(8):5632–5648, 1992.

[31] A. B. D. Brown, S. M. Clarke, and A. R. Rennie. Ordered phase of platelike particles in concentrated dispersions. *Langmuir*, 14(11):3129–3132, 1998.

[32] F. M. van der Kooij and H. N. W. Lekkerkerker. Formation of nematic liquid crystals in suspensions of hard colloidal platelets. *J. Phys. Chem. B*, 102(40):7829–7832, 1998.

[33] F. M. van der Kooij, K. Kassapidou, and H. N. W. Lekkerkerker. Liquid crystal phase transitions in suspensions of polydisperse plate-like particles. *Nature*, 406:868–871, 2000.

[34] D. van der Beek and H. N. W. Lekkerkerker. Liquid crystal phases of charged colloidal platelets. *Langmuir*, 20(20):8582–8586, 2004.

[35] J. O. Fossum, E. Gudding, D. D. M. Fonseca, Y. Meheust, E. DiMasi, T. Gog, and C. Venkataraman. Observations of orientational ordering in aqueous suspensions of a nano-layered silicate. *Energy*, 30(6):873–883, 2005.

[36] N. I. Ringdal, D. M. Fonseca, E. L. Hansen, H. Hemmen, and J. O. Fossum. Nematic textures in colloidal dispersions of na-fluorohectorite synthetic clay. *Phys. Rev. E*, 81:041702, 2010.

[37] J. Zhang, L. Luan, W. Zhu, S. Liu, and D. Sun. Phase behavior of aqueous suspensions of Mg_2Al Layered Double Hydroxide: the competition among nematic ordering, sedimentation, and gelation. *Langmuir*, 23(10):5331–5337, 2007.

[38] L. J. Michot, I. Bihannic, S. Maddi, S. S. Funari, C. Baravian, P. Levitz, and P. Davidson. Liquid-crystalline aqueous clay suspensions. *Proc. Nat. Acad. Sci.*, 103(44):16101–16104, 2006.

[39] E. Paineau, K. Antonova, C. Baravian, I. Bihannic, P. Davidson, I. Dozov, M. Impéror-Clerc, P. Levitz, A. Madsen, F. Menau, and L. J. Michot. Liquid-crystalline nematic phase in aqueous suspensions of a disk-shaped natural beidellite clay. *J. Phys. Chem. B*, 113:15858–15869, 2009.

[40] H. Zocher and K. Jacobsohn. Ueber freiwillige strukturbildung im vanadinpentoxydsol. *Koll.-Zeitschr.*, 41:220–222, 1927.

[41] K. Coper and H. Freundlich. The formation of tactoids in iron oxide sols. *Trans. Faraday Soc.*, 33:348–350, 1937.

[42] J. D. Bernal and I. Fankuchen. X-ray and crystallographic studies of plant virus preparations. *J. Gen. Physiology*, 25:111, 1941.

[43] H. Zocher and C. Török. Neuere beiträge zur kenntnis der taktosole. *Koll.-Zeitschr.*, 170(2):140–144, 1960.

[44] Z. Dogic and S. Fraden. Development of model colloidal liquid crystals and the kinetics of the isotropic-smectic transition. *Phil. Trans. R. Soc. Lond. A*, 359(1782):997–1014, 2001.

[45] Z. X. Zhang and J. S. van Duijneveldt. Isotropic-nematic phase transition of nonaqueous suspensions of natural clay rods. *J. Chem. Phys.*, 124:154910, 2006.

[46] P. W. Oakes, J. Viamontes, and J. X. Tang. Growth of tactoidal droplets during the first-order isotropic to nematic phase transition of f-actin. *Phys. Rev. E*, 75(6):061902, 2007.

[47] S. Chandrasekhar. Surface tension of liquid crystals. *Mol. Cryst. Liq. Cryst.*, 2:71–80, 1966.

[48] E. G. Virga. Drops of nematic liquid crystals. *Arch. Rationa Mech. Anal.*, 107:371–390, 1989.

[49] E. G. Virga. *Variational theories for liquid crystals*. Chapman & Hall, London, 1994.

[50] E. Dubois-Violette and O. Parodi. Emulsions nématiques. effets de champ magnétiques et effets piézoélectriques. *J. Physique Coll.*, 4:57–64, 1969.

[51] R. D. Williams. *Rutherford Appleton Laboratory Report No. RAL-85-028*, 1985 (unpublished).

[52] P. Prinsen and P. van der Schoot. Shape and director-field transformation of tactoids. *Phys. Rev. E*, 68(2):021701, 2003.

[53] P. Prinsen and P. van der Schoot. Continuous director-field transformation of nematic tactoids. *Eur. Phys. J. E*, 13(1):35–41, 2004.

[54] P. Prinsen and P. van der Schoot. Parity breaking in nematic tactoids. *J. Phys.: Condens. Matter*, 16(49):8835–8850, 2004.

[55] A. V. Kaznacheev, M. M. Bogdanov, and S. A. Taraskin. The nature of prolate shape of tactoids in lyotropic inorganic liquid crystals. *J. Exp. Theor. Phys.*, 95(1):57–63, 2002.

[56] A. V. Kaznacheev, M. M. Bogdanov, and A. S. Sonin. The influence of anchoring energy on the prolate shape of tactoids in lyotropic inorganic liquid crystals. *J. Exp. Theor. Phys.*, 97(6):1159–1167, 2003.

[57] P. G. de Gennes. *The Physics of Liquid Crystals*. Oxford University Press, 1974.

[58] Y. Trukhina, S. Jungblut, P. van der Schoot, and T. Schilling. Osmotic compression of droplets of hard rods: A computer simulation study. *J. Chem. Phys.*, 130(16):164513, 2009.

[59] N. Puech, E. Grelet, P. Poulin, C. Blanc, and P. Van der Schoot. Nematic droplets in aqueous dispersions of carbon nanotubes. *Phys. Rev. E*, 82:020702, 2010.

[60] P. S. Drzaic. *Liquid Crystal Dispersions*. World Scientific Publishing Co. Pte. Ltd., Singapore, 1995.

[61] J. H. Erdmann, S. Zumer, and J. W. Doane. Configuration transition in a nematic liquid crystal confined to a small spherical cavity. *Phys. Rev. Lett.*, 64:1907–1910, 1990.

[62] E. M Terentjev. Stability of liquid crystalline macroemulsions. *Europhys. Lett.*, 32(7):607–612, 1995.

[63] O. D. Lavrentovich. Topological defects in dispersed liquid crystals, or words and worlds around liquid crystal drops. *Liq. Cryst.*, 24(1):117–125, 1998.

[64] D. van der Beek, H. Reich, P. van der Schoot, M. Dijkstra, T. Schilling, R. Vink, M. Schmidt, R. van Roij, and H. N. W. Lekkerkerker. Isotropic-nematic interface and wetting in suspensions of colloidal platelets. *Phys. Rev. Lett.*, 97(8):087801, 2006.

[65] F. Bergaya, B. K. G. Theng, and G. Lagaly. *Handbook of clay science*. Elsevier, Amsterdam, 2006.

[66] H. Maeda and Y. Maeda. Liquid crystal formation in suspensions of hard rodlike colloidal particles: Direct observation of particle arrangement and self-ordering behavior. *Phys. Rev. Lett.*, 90(1):018303, 2003.

[67] T. Schilling and D. Frenkel. Self-poisoning of crystal nuclei in hard-rod liquids. *Phys. Rev. Lett.*, 92(8):085505, 2004.

[68] A. Patti and M. Dijkstra. Do multilayer crystals nucleate in suspensions of colloidal rods? *Phys. Rev. Lett.*, 102(12):128301, 2009.

[69] P. C. Robinson and S. Bradbury. *Qualitative Polarized-Light Microscopy*. Oxford University Press - Royal Microscopy Society, 1992.

[70] M. Wolman. Polarized light microscopy as a tool of diagnostic pathology. *J. Histochem. Cytochem.*, 23(1):21–50, 1975.

[71] V. Tuchin. *Tissue Optics, Light scattering methods and instruments for medical diagnosis*. SPIE, Bellingham, 2007.

[72] N. H. Hartshorne. *The microscopy of liquid crystals*. Microscope series. Microscope Publications Ltd., London, 1974.

[73] O. Wiener. *Abh. Schs. Ges. Akad. Wiss., Math.-Phys. Kl.*, 32:575, 1912.

[74] M. H. F. Wilkins, A. R. Stokes, W. E. Seeds, and G. Oster. Tobacco mosaic virus crystals and three-dimensional microscopic vision. *Nature*, 166:127–129, 1950.

[75] A. M. Wierenga, T. A. J. Lenstra, and A. P. Philipse. Aqueous dispersions of colloidal gibbsite platelets: synthesis, characterisation and intrinsic viscosity measurements. *Colloids Surf. A*, 134:359–371, 1998.

[76] Julien Hernandez. *Thèse de Doctorat de l'Université Pierre et Marie Curie*. PhD thesis, Université Pierre et Marie Curie, 1998.

[77] M. P. B. van Bruggen, M. Donker, H. N. W. Lekkerkerker, and T. L. Hughes. Anomalous stability of aqueous boehmite dispersions induced by hydrolyzed aluminium poly-cations. *Colloids Surf. A*, 150:115–128, 1999.

[78] L. Heux, G. Chauve, and C. Bonini. Nonflocculating and chiral-nematic self-ordering of cellulose microcrystals suspensions in nonpolar solvents. *Langmuir*, 16(21):8210–8212, 2000.

[79] M. C. D. Mourad, E. J. Devid, M. M. van Schooneveld, C. Vonk, and H. N. W. Lekkerkerker. Formation of nematic liquid crystals of sterically stabilized layered double hydroxide platelets. *J. Phys. Chem. B*, 112(33):10142–10152, 2008.

[80] M. Born and E. Wolf. *Principles of Optics, Electromagnetic Theory of Propagation, Interference and Diffraction of Light*. Cambridge University Press, 1998.

[81] J. F. Bowles, D. J. Vaughan, R. A. Howie, and J. Zussman. *Rock-Forming Minerals Volume 5A: Non-Silicates: Oxides, Hydroxides and Sulphides (2nd Edition)*. The Geological Society, London, 2011.

[82] S. Neveu-Prin, F. A. Tourinho, J.-C. Bacri, and R. Perzynski. Magnetic birefringence of cobalt ferrite ferrofluids. *Colloids Surf. A*, 80:1–10, 1993.

[83] W. L. Bragg and A. B. Pippard. The form birefringence of macromolecules. *Acta Cryst.*, 6:865–867, 1953.

[84] V. Twersky. Form and intrinsic birefringence. *J. Opt. Soc. Am.*, 65(3):239–245, 1975.

[85] D. van der Beek, A. V. Petukhov, P. Davidson, J. Ferre, J. P. Jamet, H. H. Wensink, G. J. Vroege, W. Bras, and H. N. W. Lekkerkerker. Magnetic-field-induced orientational order in the isotropic phase of hard colloidal platelets. *Phys. Rev. E*, 73(4):041402, 2006.

[86] J. A. Osborn. Demagnetizing factors of the general ellipsoid. *Phys. Rev.*, 67:351–357, 1945.

[87] D. van der Beek, P. Davidson, H. H. Wensink, G. J. Vroege, and H. N. W. Lekkerkerker. Influence of a magnetic field on the nematic phase of hard colloidal platelets. *Phys. Rev. E*, 77(3):031708, 2008.

[88] R. H. J. Otten and P. van der Schoot. Capillary rise of an isotropic-nematic fluid interface: Surface tension and anchoring versus elasticity. *Langmuir*, 25(4):2427–2436, 2009.

[89] J. V. Sanders and M. J. Murray. Ordered arrangements of spheres of two different sizes in opal. *Nature*, 275:201–203, 1978.

[90] J. V. Sanders. Close-packed structures of spheres of two different sizes. *Phil. Mag. A*, 42(6):705–740, 1980.

[91] S. Hachisu and S. Yoshimura. Optical demonstration of crystalline superstructures in binary mixtures of latex globules. *Nature*, 283:188–189, 1980.

[92] S. Yoshimura and S. Hachisu. Order formation in binary mixtures of monodisperse latices. *Prog. Colloid Polymer Sci.*, 68:59–70, 1983.

[93] P. Bartlett, R. H. Ottewill, and P. N. Pusey. Superlattice formation in binary-mixtures of hard-sphere colloids. *Phys. Rev. Lett.*, 68(25):3801–3804, 1992.

[94] N. Hunt, R. Jardine, and P. Bartlett. Superlattice formation in mixtures of hard-sphere colloids. *Phys. Rev. E*, 62(1):900–913, 2000.

[95] A. B. Schofield, P. N. Pusey, and P. Radcliffe. Stability of the binary colloidal crystals ab(2) and ab(13). *Phys. Rev. E*, 72(3):031407, 2005.

[96] K. Kajiwara, N. Donkai, Y. Fujiyoshi, and H. Inagaki. Lyotropic mesophase of imogolite. ii: Microscopic observation of imogolite mesophase. *Makromol. Chem.*, 187(12):2895–2907, 1986.

[97] T. Sato, N. Ikeda, T. Itou, and A. Teramoto. Phase-equilibrium in ternary solutions containing 2 semiflexible polymers with different lengths. *Polymer*, 30(2):311–316, 1989.

[98] G. J. Vroege and H. N. W. Lekkerkerker. Theory of the isotropic nematic nematic phase-separation for a solution of bidisperse rodlike particles. *J. Phys. Chem.*, 97(14):3601–3605, 1993.

[99] K. R. Purdy, S. Varga, A. Galindo, G. Jackson, and S. Fraden. Nematic phase transitions in mixtures of thin and thick colloidal rods. *Phys. Rev. Lett.*, 94(5):057801, 2005.

[100] S. Varga, A. Galindo, and G. Jackson. New types of phase behaviour in binary mixtures of hard rod-like particles. *Mol. Phys.*, 101:817–825, 2003.

[101] S. Y. Liu, J. Zhang, N. Wang, W. R. Liu, C. G. Zhang, and D. J. Sun. Liquid-crystalline phases of colloidal dispersions of layered double hydroxides. *Chem. Mater.*, 15(17):3240–3241, 2003.

[102] P. N. Pusey. The effect of polydispersity on the crystallization of hard spherical colloids. *J. Phys. (Paris)*, 48:709–712, 1987.

[103] M. A. Bates and D. Frenkel. Influence of polydispersity on the phase behavior of colloidal liquid crystals: A monte carlo simulation study. *J. Chem. Phys.*, 109(14):6193–6199, 1998.

[104] F. M. van der Kooij, D. van der Beek, and H. N. W. Lekkerkerker. Isotropic-nematic phase separation in suspensions of polydisperse colloidal platelets. *J. Phys. Chem. B*, 105(9):1696–1700, 2001.

[105] H. H. Wensink, G. J. Vroege, and H. N. W. Lekkerkerker. Isotropic-nematic density inversion in a binary mixture of thin and thick hard platelets. *J. Phys. Chem. B*, 105(43):10610–10618, 2001.

[106] M. Bier, L. Harnau, and S. Dietrich. Bulk and interfacial properties of binary hard-platelet fluids. *Phys. Rev. E*, 69:021506, 2004.

[107] H. H. Wensink. Equation of state of a dense columnar liquid crystal. *Phys. Rev. Lett.*, 93:157801, 2004.

[108] D. J. Lewis. The instability of liquid surfaces when accelerated in a direction perpendicular to their planes. ii. *Proc. Roy. Soc. A (London)*, 202(1068):81–96, 1950.

[109] D. G. Rowan, J.-P. Hansen, and E. Trizac. Screened electrostatic interactions between clay platelets. *Mol. Phys.*, 98:1369–1378, 2000.

[110] M. Bier, L. Harnau, and S. Dietrich. Free isotropic-nematic interfaces in fluids of charged platelike colloids. *J. Chem. Phys.*, 123:114906, 2005.

[111] L. Harnau and J.-P. Hansen. Colloid aggregation induced by oppositely charged polyions. *J. Chem. Phys.*, 116:9051, 2002.

[112] J. D. Parsons. Nematic ordering in a system of rods. *Phys. Rev. A*, 19:1225, 1979.

[113] S. D. Lee. A numerical investigation of nematic ordering based on a simple hard-rod model. *J. Chem. Phys.*, 87:4972, 1987.

[114] S. D. Lee. The onsager-type theory for nematic ordering of finite-length hard ellipsoids. *J. Chem. Phys.*, 89:7036, 1988.

[115] A. Malijevsky, G. Jackson, and S. Varga. Many-fluid onsager density functional theories for orientational ordering in mixtures of anisotropic hard-body fluids. *J. Chem. Phys.*, 129(14):144504, 2008.

[116] T. Odijk and H. N. W. Lekkerkerker. Theory of the isotropic-liquid crystal phase separation for a solution of bidisperse rodlike macromolecules. *J. Phys. Chem.*, 89:2090–2096, 1985.

[117] T. Odijk. *Liq. Cryst.*, 1:553, 1986.

[118] G. J. Vroege and H. N. W. Lekkerkerker. Phase transitions in lyotropic colloidal and polymer liquid crystals. *Rep. Prog. Phys.*, 55:1241–1309, 1992.

[119] J. E. Lennard-Jones and A. F. Devonshire. Critical phenomena in gases. *Proc. Roy. Soc. A (London)*, 163:53–70, 1937.

[120] J. G. Kirkwood. Critique of the free volume theory of the liquid state. *J. Chem. Phys.*, 18:380, 1950.

[121] A. Kilian. Computer-simulations of nematic droplets. *Liq. Cryst.*, 14(4):1189–1198, 1993.

[122] E. Penzenstadler and H. R. Trebin. Fine structure of point defects and soliton decay in nematic liquid crystals. *J. Phys. France*, 50(9):1027–1040, 1989.

[123] S. Mkaddem and E. C. Gartland. Fine structure of defects in radial nematic droplets. *Phys. Rev. E*, 62(5):6694–6705, 2000.

[124] A. Cuetos and M. Dijkstra. Kinetic pathways for the isotropic-nematic phase transition in a system of colloidal hard rods: A simulation study. *Phys. Rev. Lett.*, 98(9):095701, 2007.

[125] W. Huang and G. F. Tuthill. Structure and shape of nematic liquid-crystal microdroplets. *Phys. Rev. E*, 49(1):570–574, 1994.

[126] J. K. Gupta, S. Sivakumar, F. Caruso, and N. L. Abbott. Size-dependent ordering of liquid crystals observed in polymeric capsules with micrometer and smaller diameter. *Angew. Chem. Int. Ed.*, 48(9):1652–1655, 2009.

[127] Sonke Haseloh, Paul van der Schoot, and Rudolf Zentel. Control of mesogen configuration in colloids of liquid crystalline polymers. *Soft Matter*, 6(17):4112–4119, 2010.

[128] G. Wulff. *Z. Kristallogr.*, 34:449, 1901.

[129] P. Prinsen. *Master thesis*. Eindhoven University of Technology, 2003.

[130] S. Zumer and J. W. Doane. Light scattering from a small nematic droplet. *Phys. Rev. A*, 34(4):3373–3386, 1986.

[131] C. Chiccoli, P. Pasini, and F. Semeria. A computer simulation of nematic droplets with radial boundary conditions. *Phys. Lett. A*, 150(5,6,7):311–314, 1990.

[132] A. Stroobants and H. N. W. Lekkerkerker. Effect of electrostatic interaction on the liquid crystal phase transition in solutions of rodlike polyelectrolytes. *Macromolecules*, 19:2232–2238, 1986.

[133] H. N. W. Lekkerkerker and G. J. Vroege. Lyotropic colloidal and macromolecular liquid crystals. *Phil. Trans. R. Soc. Lond. A*, 344:419–440, 1993.

[134] Interactive data language, ITT visual information solutions (http://www.ittvis.com/).

[135] F. M. Alzahrani and T. Chen. A real-time edge detector: Algorithm and vlsi architecture. *Real-time Imaging*, 3(5):363–378, OCT 1997.

[136] S. C. Zhang and Z. Q. Liu. A robust, real-time ellipse detector. *Pattern Recogn.*, 38(2):273–287, FEB 2005.

[137] L. Li, Z. Feng, and K. He. A randomized algorithm for detecting multiple ellipses based on least square approach. *Opto-Electron. Rev.*, 13(1):61–67, 2005.

[138] iTEM, Olympus Soft Imaging Solutions GMBH, (http://soft-imaging.net/).

[139] A. Rapini and M. J. Papoular. *J. Phys. (Paris)*, Colloq. 30:C4–54, 1969.

[140] A. Pimpinelli and J. Villain. *Physics of crystal growth*. Cambridge University Press, 1998.

[141] G. E. Volovik and O. D. Lavrentovich. Topological dynamics of defects: boojums in nematic drops. *Sov. Phys. JETP*, 58:1159–1166, 1983.

[142] A. Fernandez-Nieves, D. R. Link, M. Marquez, and D. A. Weitz. Topological changes in bipolar nematic droplets under flow. *Phys. Rev. Lett.*, 98(8):087801, 2007.

[143] H. A. Stone. Dynamics of drop deformation and breakup in viscous fluids. *Annu. Rev. Fluid Mech.*, 26:65–102, 1994.

[144] E. M. Terentjev. Disclination loops, standing alone and around solid particles, in nematic liquid crystals. *Phys. Rev. E*, 51:1330–1337, 1995.

[145] M. Kleman and O. D. Lavrentovich. *Soft matter physics: an introduction*. Springer, New York, 2003.

[146] V. Frederiks and V. Zolina. *Trans. Faraday Soc.*, 29:919, 1933.

[147] R. B. Meyer, F. Lonberg, V. Taratuta, S. Fraden, S. D. Lee, and A. J. Hurd. Measurements of the anisotropic viscous and elastic properties of lyotropic polymer nematics. *Faraday Discuss. Chem. Soc.*, 79:125–132, 1985.

[148] F. C. Frank. *Discuss. Faraday Soc.*, 25:19, 1958.

[149] M. A. Osipov and S. Hess. The elastic-constants of nematic and nematic discotic liquid-crystals with perfect local orientational order. *Mol. Phys.*, 78(5):1191–1201, 1993.

[150] P. A. O'Brien, M. P. Allen, D. L. Cheung, M. Dennison, and A. Masters. Elastic constants of hard thin platelets by monte carlo simulation and virial expansion. *Phys. Rev. E*, 78:051705, 2008.

[151] P. Oswald and P. Pieranski. *Les cristaux liquides*, volume 1. Gordon and Breach Science Publishers, Paris, 2000.

[152] S. Kralj and S. Zumer. Freedericksz transitions in supra-μm nematic droplets. *Phys. Rev. A*, 45(4):2461–2470, 1992.

[153] H. Zocher and K. Jacobsohn. Ueber taktosole. *Kolloidchem. Beih.*, 28(3-5):167–206, 1929.

[154] E. Berggren, C. Zannoni, C. Chiccoli, P. Pasini, and F. Semeria. Monte-carlo study of the molecular-organization in model nematic droplets - field effects. *Chem. Phys. Lett.*, 197(3):224–230, 1992.

[155] R. H. J. Otten and P. van der Schoot. *to be published*, 2010.

[156] R. B. Zasadzinski, J. Meyer. Molecular imaging of tobacco mosaic-virus lyotropic nematic phases. *Phys. Rev. Lett.*, 56(6):636–638, 1986.

[157] W. Song, I. A. Kinloch, and A. H. Windle. Nematic liquid crystallinity of multiwall carbon nanotubes. *Science*, 302(5649):1363, 2003.

[158] O. Reynolds. *Chem. News.*, 44:211, 1881.

[159] J. J. Thomson and H. F. Newall. *Proc. R. Soc. Lond.*, 39:417, 1885.

[160] G. V. Jeffreys and G. A. Davies. *Recent advances in liquid-liquid extraction*. Pergamon Press, Oxford, 1971.

[161] S. Hartland. *Trans. Instn Chem. Engrs*, 45:T97–101, 1967.

[162] A. H. Brown and C. Hanson. Drop coalescence in liquid-liquid systems. *Nature*, 214:76–77, 1967.

[163] B. K. Chi and L. G. Leal. A theoretical study of the motion of a viscous drop toward a fluid interface at low reynolds number. *J. Fluid Mech.*, 201:123–146, 1989.

[164] D. G. A. L. Aarts and H. N. W. Lekkerkerker. Droplet coalescence: drainage, film rupture and neck growth in ultralow interfacial tension systems. *J. Fluid Mech.*, 606:275–294, 2008.

[165] S. T. Thoroddsen, K. Takehara, and T. G. Etoh. The coalescence speed of a pendant and a sessile drop. *J. Fluid Mech.*, 527:85–114, 2005.

[166] X. Chen, S. Mandre, and J. J. Feng. Partial coalescence between a drop and a liquid-liquid interface. *Phys. Fluids*, 18:051705, 2006.

[167] Z. Mohamed-Kassim and E. K. Longmire. Drop coalescence through a liquid/liquid interface. *Phys. Fluids*, 16(7):2170–2181, 2004.

[168] W. Yao, H. J. Maris, and G. M. Seidel. Coalescence of viscous liquid drops. *Phys. Rev. E*, 71:016309, 2005.

[169] P. Poulin and D. A. Weitz. Inverted and multiple nematic emulsions. *Phys. Rev. E*, 57(1):626–637, 1998.

[170] S. Hartland. The approach of a rigid sphere to a deformable liquid/liquid interface. *J. Colloid Interface Sci.*, 26(4):383–394, 1968.

[171] A. F. Jones and S. D. R. Wilson. The film drainage problem in droplet coalescence. *J. Fluid Mech.*, 87:263–288, 1978.

[172] J. Eggers, J. R. Lister, and H. A. Stone. Coalescence of liquid drops. *J. Fluid Mech.*, 401:293–310, 1999.

[173] A. S. Geller, S. H. Lee, and L. G. Leal. *J. Fluid Mech.*, 169:27–69, 1996.

[174] J. W. J. de Folter, V. W. A. de Villeneuve, D. G. A. L. Aarts, and H. N. W. Lekkerkerker. Rigid sphere transport through a colloidal gas-liquid interface. *New J. Phys.*, 12:023013, 2010.

[175] A. V. Anilkumar, C. P. Lee, and T. G. Wang. Surface-tension-induced mixing following coalescence of initially stationary drops. *Phys. Fluids A*, 3(11):2587–2591, 1991.

[176] M. Manga and H. A. Stone. Low reynolds number motion of bubbles, drops and rigid spheres through fluid-fluid interfaces. *J. Fluid Mech.*, 287:279–298, 1995.

[177] M. Manga and H. A. Stone. Buoyancy-driven interactions between two deformable viscous drops. *J. Fluid Mech.*, 256:647–683, 1993.

[178] J. Eggers. Nonlinear dynamics and breakup of free-surface flows. *Rev. Mod. Phys.*, 69(3):865–929, 1997.

[179] J. Eggers and E. Villermaux. Physics of liquid jets. *Rep. Prog. Phys.*, 71:036601, 2008.

[180] M. Döring. Ink-jet printing. *Philips Tech. Rev.*, 40:192, 1982.

[181] D. J. Hayes, W. R. Cox, and M. E. Grove. *J. Electron. Manuf.*, 8:209, 1998.

[182] Michael Moseler and Uzi Landman. Formation, Stability, and Breakup of Nanojets. *Science*, 289(5482):1165–1169, 2000.

[183] Jens Eggers. Dynamics of liquid nanojets. *Phys. Rev. Lett.*, 89(8):084502, Aug 2002.

[184] Y. Hennequin, D. G. A. L. Aarts, J. H. van der Wiel, G. Wegdam, J. Eggers, H. N. W. Lekkerkerker, and Daniel Bonn. Drop formation by thermal fluctuations at an ultralow surface tension. *Phys. Rev. Lett.*, 97(24):244502, Dec 2006.

[185] D. G. A. L. Aarts, M. Schmidt, and H. N. W. Lekkerkerker. Direct visual observation of thermal capillary waves. *Science*, 304:847, 2004.

[186] P. P. Bhat, S. Appathurai, M. T. Harris, M. Pasquali, G. H. McKinley, and O. A. Basaran. Formation of beads-on-a-string structures during break-up of viscoelastic filaments. *Nat. Phys.*, 6:625–631, 2010.

[187] L. B. Smolka and A. Belmonte. Drop pinch-off and filament dynamics of wormlike micellar fluids. *J. Non-Newtonian Fluid Mech.*, 115:1–25, 2003.

[188] D. Dutta, H. Fruitwalai, A. Kohlii, and R. A. Weiss. *Polym. Eng. Sci.*, 27:684–691, 1990.

[189] A. G. C. Machiels, J. van Dam, A. Posthuma de Boer, and B. Norder. Stability of blends of thermotropic liquid crystalline polymers with thermoplastic polymers. *Polym. Eng. Sci.*, 37(9):1512–1525, 1997.

[190] J. Wu and P. T. Mather. Interfacial tension of a liquid crystalline polymer in an isotropic polymer matrix. *Macromolecules*, 38:7343–7351, 2005.

[191] S.-W. Lee and A. M. Belcher. Virus-based fabrication of micro- and nanofibers using electrospinning. *Nano Letters*, 4(3):387–390, 2004.

[192] B. D. Hamlington, B. Steinhaus, J. J. Feng, D. Link, M. J. Shelley, and A. Q. Shen. Liquid crystal droplet production in a microfluidic device. *Liq. Cryst.*, 34(7):861–870, 2007.

[193] A.-G. Cheong and A. D. Rey. Texture dependence of capillary instabilities in nematic liquid crystalline fibers. *Liq. Cryst.*, 31(9):1271–1284, 2004.

[194] M. A. Goyal, R. K. Denn. Surface-induced morphology and free-energy pathways in breakup of a nematic liquid crystalline cylinder. *Phys. Rev. E*, 78(2):021706, August 2008.

[195] C. Zhou, Y. Pengtao, and J. Feng. Dynamic simulation of capillary breakup of nematic fibers: molecular orientation and interfacial rupture. *J. Comput. Theor. Nanosci.*, 7:683–692, 2010.

[196] G. Meng and R. B. Meyer. Buckling transition of nematic gels in confined geometry. *ArXiv e-prints*, October 2009.

[197] D. G. A. L. Aarts. *The interface in demixed colloid-polymer systems; Wetting, waves and droplets.* PhD thesis, Utrecht University, 2005.

[198] F. M. van der Kooij, E. S. Boek, and A. P. Philipse. Rheology of dilute suspensions of hard platelike colloids. *J. Colloid Interface Sci.*, 235(2):344–349, 2001.

[199] G. German and V. Bertola. Formation of viscoplastic drops by capillary breakup. *Phys. Fluids*, 22:033101, 2010.

[200] R. G. Larson. *The structure and rheology of complex fluids.* Oxford University Press, Oxford, 1999.

[201] D. Henderson, H. Segur, L. B. Smolka, and M. Wadati. The motion of a falling liquid filament. *Phys. Fluids*, 12(3):550–565, 2000.

[202] I. Cohen, M. P. Brenner, J. Eggers, and S. R. Nagel. Two fluid snap-off problem: experiments and theory. *Phys. Rev. Lett.*, 83(6):1147–1150, 1999.

[203] J. R. Savage, M. Caggioni, P. T. Spicer, and I. Cohen. Partial universality: pinch-off dynamics in fluids with smectic liquid crystalline order. *Soft Matter*, 6:892–895, 2010.

[204] P. N. Pusey and W. van Megen. Phase behaviour of concentrated suspensions of nearly hard colloidal spheres. *Nature*, 320(6060):340–342, 1986.

[205] U. Gasser, E. R. Weeks, A. Schofield, P. N. Pusey, and D. A. Weitz. Real-space imaging of nucleation and growth in colloidal crystallization. *Science*, 292(5515):258–262, 2001.

[206] S. Auer and D. Frenkel. Prediction of absolute crystal-nucleation rate in hard-sphere colloids. *Nature*, 409(6823):1020–1023, 2001.

[207] Z. Dogic. Surface freezing and a two-step pathway of the isotropic-smectic phase transition in colloidal rods. *Phys. Rev. Lett.*, 91(16):165701, 2003.

[208] M. C. D. Mourad, D. V. Byelov, A. V. Petukhov, D. A. M. de Winter, A. J. Verkleij, and H. N. W. Lekkerkerker. Sol-gel transitions and liquid crystal phase transitions in concentrated aqueous suspensions of colloidal gibbsite platelets. *J. Phys. Chem. B*, 113(34):11604–11613, 2009.

[209] H. H. Wensink. private communication.

[210] R. F. Sekerka. Equilibrium and growth shapes of crystals: how do they differ and why should we care. *Cryst. Res. Technol.*, 40(4-5):291–306, 2005.

[211] A. Einstein. On the motion, required by the molecular-kinetic theory of heat, of particles suspended in a fluid at rest. *Ann. Phys.*, 17:549–560, 1905.

[212] P. N. Pusey. *Liquids, Freezing and Glass Transition, Les Houches Session 51, NATO Advanced Study Institute, Series B: Physics*. North-Holland, Amsterdam, 1991.

[213] J. P. Hansen and I. R. McDonald. *Theory of Simple Liquids*. Academic Press, London, 2006.

[214] C. G. Kruif, P. W. Rouw, J. W. Jansen, and A. Vrij. Hard sphere properties and crystalline packing of lyophilic silica colloids. *J. Physique*, 46:C3–295, 1985.

[215] B. J. Alder and T. A. Wainwright. Phase transition for a hard sphere system. *J. Chem. Phys.*, 27:1208–1209, 1957.

[216] W. G. Hoover and F. H. Ree. Melting transition and communal entropy for hard spheres. *J. Chem. Phys.*, 49(8):3609–3617, 1968.

[217] P. N. Pusey. Colloidal glasses. *J. Phys.: Condens. Matter*, 20(49):494202, 2008.

[218] L. Fabbian, W. Götze, F. Sciortino, P. Tartaglia, and F. Thiery. Ideal glass-glass transitions and logarithmic decay of correlations in a simple system. *Phys. Rev. E*, 59(2):R1347–R1350, 1999.

[219] J. Bergenholtz and M. Fuchs. Nonergodicity transitions in colloidal suspensions with attractive interactions. *Phys. Rev. E*, 59(5):5706–5715, 1999.

[220] T. Eckert and E. Bartsch. Re-entrant glass transition in a colloid-polymer mixture with depletion attractions. *Phys. Rev. Lett.*, 89(12):125701, 2002.

[221] K. N. Pham, A. M. Puertas, J. Bergenholtz, S. U. Egelhaaf, A. Moussaid, P. N. Pusey, A. B. Schofield, M. E. Cates, M. Fuchs, and W. C. K. Poon. Multiple glassy states in a simple model system. *Science*, 296(5565):104–106, 2002.

[222] F. Sciortino. Disordered materials - one liquid, two glasses. *Nat. Mater.*, 1(3):145–146, 2002.

[223] S. Abend and G. Lagaly. Sol-gel transitions of sodium montmorillonite dispersions. *Appl. Clay Science*, 16(3-4):201, 2000.

[224] P. Levitz, E. Lcolier, A. Mourchid, A. Delville, and S. Lyonnard. Liquid-solid transition of laponite suspensions at very low ionic strength: Long range electrostatic stabilisation of anisotropic colloids. *Europhys. Lett.*, 49:672–677, 2000.

[225] A. Shalkevich, A. Stradner, S. K. Bhat, F. Muller, and P. Schurtenberger. Cluster, glass, and gel formation and viscoelastic phase separation in aqueous clay suspensions. *Langmuir*, 23(7):3570–3580, 2007.

[226] H. Tanaka, J. Meunier, and D. Bonn. Nonergodic states of charged colloidal suspensions: Repulsive and attractive glasses and gels. *Phys. Rev. E*, 69(3):031404, 2004.

[227] M. C. D. Mourad, J. E. G. J. Wijnhoven, D. D. Van 'T Zand, D. Van der Beek, and H. N. W. Lekkerkerker. Gelation versus liquid crystal phase transitions in suspensions of plate-like particles. *Philosophical Transactions of the Royal Society a-Mathematical Physical and Engineering Sciences*, 364(1847):2807–2816, 2006.

[228] M. C. D. Mourad, D. V. Byelov, A. V. Petukhov, and H. N. W. Lekkerkerker. Structure of the repulsive gel/glass in suspensions of charged colloidal platelets. *J. Phys.: Condens. Matter*, 20(49):494201, 2008.

[229] M. C. D. Mourad, A. A. Verhoeff, D. V. Byelov, A. V. Petukhov, and H. N. W. Lekkerkerker. Devitrification of the glassy state in suspensions of charged platelets. *J. Phys.: Condens. Matter*, 21:474218, 2009.

[230] T. Hikima, M. Hanaya, and M. Oguni. Microscopic observation of a peculiar crystallization in the glass transition region and [beta]-process as potentially controlloing the growth rate in triphenylethylene. *J. Mol. Struct.*, 479:245–250, 1999.

[231] M. Hatase, M. Hanaya, and M. Oguni. Studies of homogeneou-nucleation-based crystal growth: significant role of phenyl ring in the structure formation. *J. Non-Cryst. Solids*, 333:129–136, 2004.

[232] W. Götze. *Aspects of structural glass transitions, Liquids, Freezing and Glass transition (Les Houches Session 51, NATO Advanced Study Institute, Series B: Physics)*. North-Holland, Amsterdam, 1991.

[233] T. Konishi and H. Tanaka. Possible origin of enhanced crystal growth in a glass. *Phys. Rev. B*, 76:220201, 2007.

[234] H. Tanaka. Possible resolution of the kauzmann paradox in supercooled liquids. *Phys. Rev. E*, 68:011505, 2003.

[235] W. K. Kegel and A. van Blaaderen. Direct observation of dynamical heterogeneities in colloidal hard-sphere suspensions. *Science*, 287(5451):290–293, 2000.

[236] E. R. Weeks, J. C. Crocker, A. C. Levitt, A. Schofield, and D. A. Weitz. Three-dimensional direct imaging of structural relaxation near the colloidal glass transition. *Science*, 287(5453):627–631, 2000.

[237] H. Tanaka. Two-order-parameter description of liquids. i. a general model of glass transition covering its strong to fragile limit. *J. Chem. Phys.*, 111:3163–3174, 1999.

[238] H. Tanaka. Two-order-parameter description of liquids. ii. criteria for vitrification and predictions of our model. *J. Chem. Phys.*, 111:3175–3182, 1999.

[239] F. G. Shi, H. Y. Tong, and J. D. Ayers. Free energy barrier to nucleation of amorphous-to-crystalline transformation selects the scale of microstructure of crystallized materials. *Appl. Phys. Lett.*, 67(3):350–352, 1995.

[240] F. C. Frank. Supercooling of liquids. *Proc. Roy. Soc. A (London)*, 215(1120):43–46, 1952.

[241] C. P. Royall, S. R. Williams, T. Ohtsuka, and H. Tanaka. Direct observation of a local structural mechanism for dynamic arrest. *Nat. Mater.*, 7(7):556–561, 2008.

Summary

This thesis deals with liquid crystalline phases and in particular liquid crystal drops in suspensions of colloidal gibbsite platelets.

In **Part 1** we give a brief review of birefringence and polarized light microscopy, applied to liquid crystalline phases in gibbsite suspensions (Chapter 2). This is illustrated by an investigation of the intrinsic and form birefringence of the nematic phase in gibbsite suspensions as a function of solvent refractive index, where we show that if the refractive index of the solvent is close to that of gibbsite, the intrinsic birefringence of the platelets dominates. On the other hand, if the refractive index is considerably different, form birefringence due to the anisometric particle shape prevails over the intrinsic birefringence. In Chapter 3 we study a gibbsite system that plays a central role throughout the thesis. The bimodal distribution of the platelet aspect ratio in this system leads to remarkable phase behaviour, including an isotropic-nematic density inversion and a three phase coexistence. Both can be attributed to fractionation with respect to the platelet aspect ratio, which we demonstrate experimentally and by calculating phase diagrams of mixtures of thick and thin plates.

In **Part 2** we focus on the static properties of nematic droplets, or tactoids. We start in Chapter 4 with an investigation of the shape and director field of these tactoids in polar and apolar solvent and show that small tactoids have an oblate shape and a uniform director field, whereas larger tactoids are spherical with a radial director field. From a detailed analysis of the tactoid properties as a function of size we obtain values for the ratio of the splay elastic constant K_1 and the anchoring strength w. Furthermore, our analysis provides data for the ratio of the anchoring strength w and the isotropic-nematic interfacial tension γ, which reveals that the sterically stabilized platelets in an apolar solvent exhibit strong anchoring ($w/\gamma > 1$), while aqueous gibbsite suspensions exhibit weak anchoring ($w/\gamma < 1$). This is followed by a study of the deformation of tactoids in an externally applied magnetic field. We observe significant deformations of the tactoids, among which a transformation from a radial director field with a point defect to a split-core defect. First with a simple model (Chapter 5), and subsequently with a more extensive model (Chapter 6) we do not only account for the observed tactoid shapes and director configurations, but are also able to determine the splay elastic constant K_1, the isotropic-nematic interfacial tension γ, and the surface anchoring strength w of the platelets. The values we find are in very good agreement

with the values obtained from the analysis of the tactoid properties described in Chapter 4.

Subsequently, in **Part 3** dynamic phenomena of tactoids are studied. In Chapter 7 we investigate the coalescence of tactoids with the isotropic-nematic interface and the coalescence of two tactoids. Broadly speaking, small tactoids (with uniform director field) behave like isotropic molecular fluids, while the behavior of larger tactoids (with radial director field) is remarkably similar to that of an immiscible drop passing through a liquid-liquid interface. The buoyancy driven coalescence of two tactoids is accompanied with large droplet deformations, and appears to proceed as in the case of isotropic fluids. In Chapter 8 we show that droplet pinch-off and breakup of a nematic thread are strongly influenced by the liquid crystalline order present in the thread. In the case of relatively weak anchoring and a large extrapolation length (i.e., the ratio of the elastic constant and the anchoring strength, K/w) the thinning neck has a uniform director field and the snap-off is determined by the viscous properties of the nematic phase and by thermal fluctuations. On the other hand, in the case of strong anchoring and a small extrapolation length, the thinning neck has an escaped radial director field and the snap-off is hampered for topological reasons.

To conclude, in **Part 4** we study the formation of the columnar phase, first by an investigation of droplets of the columnar phase (Chapter 9), followed by a study of the devitrification of the glassy state, where after an extended period of time (months to years) the columnar phase nucleates in a dynamically arrested gibbsite suspension (Chapter 10). We observe that in both cases a key-role is played by short stacks of platelets.

Samenvatting voor Iedereen

Vloeibare kristallen

Vloeibare kristallen zijn een gevestigd onderdeel van ons dagelijks leven. Vloeibaarkristalbeeldschermen (LCDs, Liquid Crystal Displays) worden toegepast in onder andere camera's, computers en telefoons. Een vloeibaar kristal heeft kristallijne eigenschappen, maar vloeit nog wel (in tegenstelling tot een echt kristal). De vloeibare kristallen in een beeldscherm zijn gebaseerd op grote staafvormige organische moleculen die allemaal dezelfde richting uitwijzen. Deze ordening van de moleculen heeft tot gevolg dat de brekingsindex van het materiaal afhankelijk is van de invalrichting van het licht. Dit wordt dubbelbreking genoemd en leidt ertoe dat de polarisatierichting van het licht draait. De ordening en oriëntatie van de moleculen is te beïnvloeden met een elektrische spanning, een eigenschap die in beeldschermen gebruikt wordt om beeldelementen (pixels) aan en uit te zetten.

Minder bekend is dat ook oplossingen van staafvormige virusdeeltjes of kleiplaatjes, vanwege hun afmeting aangeduid als colloïdale deeltjes, spontaan geordende fasen kunnen vormen. Bij een lage concentratie van deze deeltjes in een oplosmiddel hebben de deeltjes veel ruimte ter beschikking en nemen ze willekeurige oriëntaties aan. Echter, als de concentratie deeltjes verhoogd wordt, zullen deze vanaf een kritische concentratie zich spontaan ordenen door dezelfde richting uit te wijzen. Op deze manier komt er voor de deeltjes weer meer bewegingsruimte vrij. We noemen deze geordende toestand de nematische fase en de richting waarin de deeltjes opgelijnd zijn de director.

In dit proefschrift bestuderen we vloeibare kristallen en met name druppels van vloeibare kristallen die zich vormen in oplossingen van plaatvormige deeltjes van het mineraal gibbsiet, dat bestaat uit aluminiumhydroxide (γ-$Al(OH)_3$). Dit materiaal is een belangrijke component van het erts bauxiet, de grondstof voor de aluminiumproductie. De gibbsietdeeltjes waar wij mee werken, maken we op gecontroleerde wijze vanuit organische aluminiumverbindingen. Daarna worden de deeltjes nabehandeld zodat ze extra lading aan het oppervlak krijgen waardoor ze goed stabiel zijn en niet samenklonteren in een zoutoplossing. De plaatjes kunnen ook bedekt worden met een polymeerlaagje, waardoor ze stabiel zijn in een apolair oplosmiddel, zoals tolueen.

Vanwege de eerder genoemde interactie van vloeibare kristallen met licht, is polarisatiemicroscopie een van de meest geschikte technieken om ze mee te bestuderen. In de polarisatiemicroscoop bevindt het monster zich tussen twee polarisatiefilters, die alleen licht doorlaten met één bepaalde polarisatierichting. Deze filters zijn gekruist

ten opzichte van elkaar, waardoor er in principe geen licht wordt doorgelaten. Echter, als zich tussen deze filters een dubbelbrekend materiaal bevindt, zoals een nematische fase, draait de polarisatie van het licht en wordt de fase zichtbaar. Hoe groot de draaiing van de polarisatierichting van het licht is, hangt onder andere af van de golflengte (kleur) van het licht en de mate van orde in het vloeibare kristal. Dit heeft prachtige kleureffecten tot gevolg. Met behulp van een speciaal filter kunnen we ook de richting bepalen van de deeltjes die het vloeibare kristal vormen.

Nematische druppels: vorm en structuur

Vloeistofdruppels, in het bijzonder waterdruppels, zijn een vertrouwde verschijning in ons dagelijks leven. Zowel in de vorm van regen als condensdruppeltjes in de badkamer. En wie heeft er nooit met verwondering de parelende dauwdruppels in een spinnenweb bekeken? Ook wetenschappers worden al eeuwenlang geboeid door de eigenschappen van druppels, en hoe deze met elkaar samenvloeien of juist opbreken. Met name die laatste twee fenomenen begrijpen we eigenlijk nog maar ten dele.

Het hoofdthema van dit proefschrift is het bestuderen van druppels bestaande uit vloeibaar kristal. In deel 2 richten we ons op druppels van de nematische fase. Deze druppels, ook wel tactoïden genoemd, zijn interessant vanwege hun bijzondere eigenschappen: ze kunnen verschillende vormen aannemen en bezitten een kenmerkende interne structuur. In combinatie met de dubbelbrekende eigenschap van het vloeibare kristal levert dat bijzonder fraaie microscopiebeelden op. Zie bijvoorbeeld Figuur 1 en 2. Niet minder belangrijk is dat we door de druppels te bestuderen, belangrijke eigenschappen van het vloeibare kristal kunnen bepalen.

Druppels van een gewone vloeistof, zoals water, zijn rond als gevolg van de grensvlakspanning. Het is voor een druppel gunstig om een zo klein mogelijk grensvlak te hebben en dat resulteert in een bolvorm. De eigenschappen van een vloeibaar kristallijne druppel worden ook bepaald door de grensvlakspanning. Maar nu is de grensvlakspanning afhankelijk van de oriëntatie van het vloeibare kristal ten opzichte van het grensvlak, ook wel verankering genoemd. De mate waarin de grensvlakspanning afhankelijk is van de verankering wordt aangegeven met de verankeringsterkte. In het geval van plaatvormige deeltjes is de grensvlakspanning het laagst als de plaatjes plat op het grensvlak liggen. Hiernaast speelt de structuur van het vloeibare kristal, oftewel het directorveld, in de druppel een belangrijke rol. Een vervorming van een uniform directorveld kost energie. Deze eigenschap van het vloeibare kristal noemen we elasticiteit, en de energietoename wordt bepaald door elastische constanten.

In een vloeibaar kristallijne druppel zijn de grensvlakspanning en de elasticiteit in competitie met elkaar. Een ongedeformeerd, uniform directorveld is het meest gunstig, maar heeft tot gevolg dat een groot deel van de deeltjes ongunstig ten opzichte van het grensvlak staan. Omgekeerd, als de deeltjes perfect verankerd zijn aan het grensvlak,

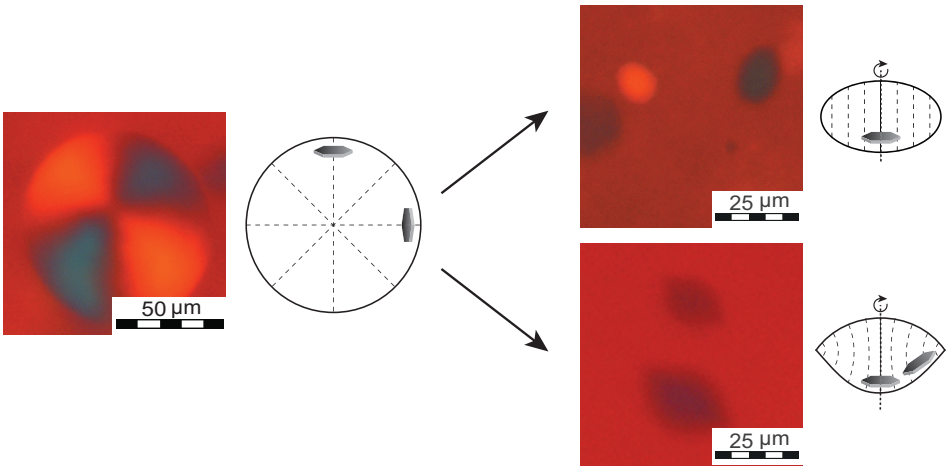

FIGUUR 1. Tactoïden zoals waargenomen m.b.v. de polarisatiemicroscoop met daarnaast een schematische tekening van het daarvan afgeleide directorveld. Grote tactoïden (links) zijn bolvormig en hebben een radieel director veld, terwijl kleine tactoïden (rechts) lensvormig zijn met een uniform directorveld. Het directorveld van de tactoïd rechts onderin is nog niet helemaal uniform.

moet het directorveld vervormen en dat kost elastische energie. Deze competitie leidt tot een rijke verscheidenheid aan druppelvormen en -structuren, waarvan er een aantal worden getoond in Figuur 1. In dit proefschrift laten we zien dat deze rijke verscheidenheid op basis van de hierboven beschreven competitie te begrijpen is. In het geval van grote druppels wint de verankering aan het grensvlak het van de elasticiteit. Dit leidt tot ronde druppels met een radieel directorveld en een puntdefect (egeldefect) in het centrum. Voor kleine druppels is het juist de elasticiteit die wint en dit leidt tot druppels met een uniform directorveld en een lensvorm. Afhankelijk van de verhouding tussen de verankeringsterkte en de grensvlakspanning heeft deze een afgeronde of een scherpe rand. De overgang van een radieel naar een uniform directorveld vindt plaats via een aantal tussenvormen die moeilijker te begrijpen zijn, maar met behulp van verschillende elastische constanten verklaard kunnen worden. Op basis van deze inzichten kunnen we door een gedetailleerde analyse van de tactoïdeigenschappen als functie van grootte, waarden bepalen voor de verhouding van de relevante elastische constante en de verankeringsterkte en de verhouding van de verankeringsterkte en de grensvlakspanning.

De gibbsietplaatjes die we in dit proefschrift bestuderen, reageren ook op de aanwezigheid van een magneetveld. De deeltjes gaan bij voorkeur met de korte as loodrecht op de veldrichting staan, wat vooral grote gevolgen heeft voor de tactoïden met een radieel directorveld. Als alle plaatjes hun voorkeursrichting in het magneetveld zouden aannemen, zou de verankering van een aanzienlijk deel van de plaatjes ongunstig zijn. De druppel blijkt een compromis te vinden waarbij het directorveld zodanig vervormt

dat zoveel mogelijk deeltjes de juiste verankering hebben en tegelijkertijd zoveel mogelijk deeltjes een gunstige oriëntatie ten opzichte van het magneetveld. Hierbij wordt het puntdefect uitgerekt tot een speciaal lijndefect, ook wel gespleten-kerndefect genoemd. Bij nog hogere veldsterkten wordt de druppel daarnaast ook uitgerekt in de richting van het magneetveld.

Ook hier hebben we een theoretisch model ontwikkeld om de waargenomen tactoïdvormen als functie van druppelgrootte en de magneetveldsterkte te kunnen verklaren. Daar waar we voor de analyse van de tactoïdeigenschappen verhoudingen van de elastische constante en de verankeringsterkte en van de verankeringsterkte en de grensvlakspanning vonden, zijn we nu in staat deze waarden onafhankelijk te bepalen uit de experimenten.

Samenvloeiende en opbrekende nematische druppels

In deel 3 van dit proefschrift bestuderen we de samenvloeiïng en het opbreken van tactoïden en nematische slierten. Het blijkt dat de grootte en interne structuur van de druppels een belangrijke rol speelt voor het verloop van deze processen. Opvallend is dat daar waar in het geval van waterdruppels het opbreken en samenvloeien slechts een fractie van een seconde duurt, het hier minuten tot zelfs uren kost. Daarom zijn we in staat deze processen op relatief eenvoudige wijze in groot detail te bestuderen.

We bekijken allereerst hoe tactoïden samenvloeien met een reeds gevormde nematische fase. De tactoïden ontstaan als druppels in de ongeordende (isotrope) fase en dalen of stijgen dan naar de nematische fase waarmee ze vervolgens samenvloeien. Bij kleine druppels blijkt het samenvloeien vooral bepaald te worden door de vloei-eigenschappen (viscositeit) van de isotrope fase. Als de druppel het grensvlak met de nematische fase dicht is genaderd, blijft ertussen een heel dun laagje isotrope fase over dat steeds langzamer dunner wordt. Uiteindelijk breekt het filmpje, waarna de druppel daadwerkelijk samenvloeit met de nematische fase. Dit fenomeen kunnen we ook waarnemen in het dagelijks leven tijdens het koffiezetten, wanneer koffiedruppels soms een paar seconden op het grensvlak blijven liggen. In het geval van vloeibaar kristallijne druppels duurt het wel tot twee uur voordat het filmpje dun genoeg is dat het kan breken, wat te verklaren is door de grote stroperigheid van de isotrope fase.

Grote druppels gedragen zich heel anders. Ze bewegen sneller naar het grensvlak toe, en in tegenstelling tot de kleine druppels vertragen ze nauwelijks als ze dichtbij het grensvlak komen. Ze breken door het grensvlak heen en rekken uit in de voortbewegingsrichting, en behouden daarbij voor een groot deel het oorspronkelijke directorveld. Dit lijkt heel erg op het gedrag van een onmengbare druppel of luchtbel die het grensvlak van twee vloeistoffen passeert. Waarschijnlijk zorgt de interne structuur van de druppel ervoor dat het lijkt alsof hij onmengbaar is met de nematische fase. Vervolgens

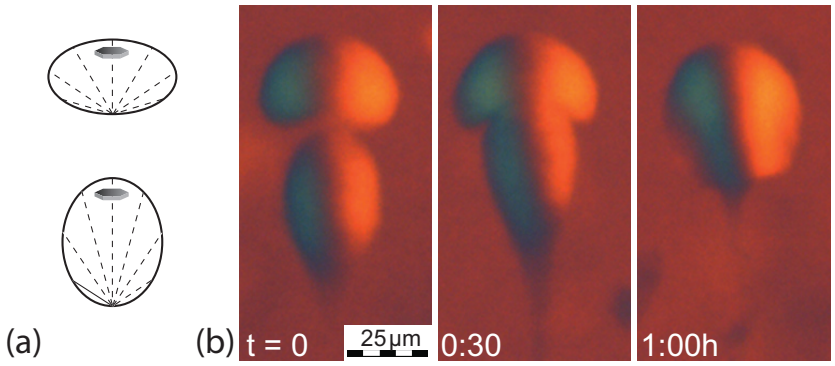

FIGUUR 2. Twee tactoïden die achter elkaar aan omhoog bewegen en onder flinke vervorming met elkaar samenvloeien. Links een schematische tekening van de tactoïden en rechts een tijdserie waargenomen met de polarisatiemicroscoop.

breekt de druppel in twee delen, één in de nematische fase en één aan het grensvlak, die uiteindelijk allebei samenvloeien met de nematische fase.

Een ander interessant fenomeen is druppels die achter elkaar aan bewegen. Als de achterste druppel groter is dan de eerste, zal hij de eerste inhalen en ermee samenvloeien. We zien dat dit gepaard gaat met grote vervormingen van de druppels. De voorste druppel wordt afgeplat, terwijl de achterste druppel juist uitrekt. Deze vervormingen zijn te verklaren vanuit de stromingsvelden die beide druppels opwekken. We zien dan ook dat hoe sneller de druppels bewegen, hoe groter de vervormingen worden.

Tot slot bekijken we in dit deel van het proefschrift hoe nematische slierten en druppels opbreken. Op de kaft van het proefschrift staat hiervan een voorbeeld afgebeeld. Ook in dit geval blijkt de interne structuur van de sliert of druppel van grote invloed. Als de druppel een uniform director veld heeft, verloopt het afbreken vergelijkbaar met het afbreken van een heel erg stroperige vloeistof. Het dunner worden van het nekje dat de druppels verbindt, gaat steeds sneller totdat de druppel uiteindelijk breekt. In het geval van een (vervormd) radieel directorveld daarentegen, versnelt het dunner worden eerst, maar als een bepaalde dikte is bereikt, komt het dunner worden bijna tot stilstand, waarna de druppel er alsnog vanaf breekt. Dit is waarschijnlijk te verklaren uit het feit dat als de druppel afbreekt er een defect gevormd moet worden in de druppel die loslaat.

COLUMNAIRE FASE EN DRUPPELS

We hebben gezien dat oplossingen van plaatvormige deeltjes vanaf een bepaalde concentratie een geordende, nematische fase vormen. Als we de concentratie deeltjes in oplossing nog verder verhogen, neemt de orde toe en vormt zich de columnaire fase.

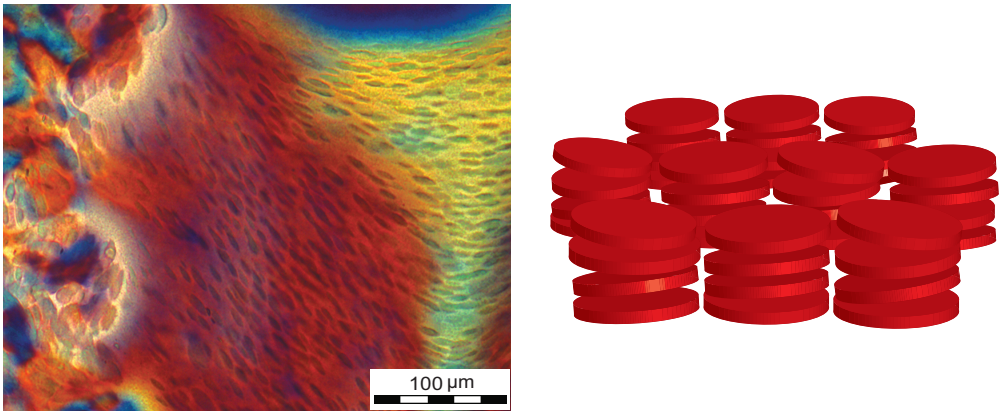

Figuur 3. Links: Een polarisatiemicroscopiebeeld van een zee van columnaire druppels tegen de achtergrond van een nematische fase. Rechts: Schematische tekening (niet op schaal) van een columnaire druppel, opgebouwd uit korte stapeltjes van plaatjes die hexagonaal geordend zijn.

Hierin hebben de deeltjes niet alleen orde qua oriëntatie, maar is ook hun positie gedeeltelijk geordend. De deeltjes vormen stapeltjes die op hun beurt in een hexagonaal patroon geordend zijn. In het laatste deel van dit proefschrift bestuderen we druppels van de columnaire fase, waarvan een microscopiebeeld wordt getoond in Figuur 3. Deze druppels blijken een heel platte vorm te hebben. Uit een nauwkeurige analyse van de microscoopbeelden kunnen we afleiden dat ze opgebouwd zijn uit relatief korte stapeltjes van plaatjes die hexagonaal gerangschikt zijn, zoals schematisch weergegeven in Figuur 3. Waarschijnlijk heeft deze vorm zijn oorsprong te danken aan stapeltjes van plaatjes die zich ook al bevinden in de hoog geconcentreerde nematische fase waarin de druppels ontstaan.

Als we de deeltjesconcentratie nog verder verhogen, komen de deeltjes in een glastoestand terecht, waarin ze geen bewegingsvrijheid meer hebben. Echter, het blijkt dat er na lange tijd toch kleine gebiedjes met columnaire fase gevormd worden in deze glastoestand. Waarschijnlijk spelen dezelfde korte stapeltjes plaatjes hierin ook een belangrijke rol.

Dankwoord

Aan het einde van dit proefschrift wil ik graag van de gelegenheid gebruik maken om een aantal mensen te bedanken die een belangrijke bijdrage aan dit proefschrift geleverd hebben.

Allereerst wil ik Henk Lekkerkerker bedanken voor zijn dagelijkse begeleiding. Ik heb veel te danken aan uw scherpe inzicht en fenomenale kennis van de literatuur. Ook uw warme belangstelling voor de persoonlijke (thuis)situatie heeft me altijd erg goed gedaan.

Mijn tweede promotor, Paul van der Schoot, ben ik ook veel dank verschuldigd. Door jouw inbreng kreeg ik de mogelijkheid om theorie en experiment te combineren, waarbij het resultaat significant meer was dan de som van de twee. Het vele rekenwerk van Ronald Otten was hierbij natuurlijk onmisbaar. Bedankt voor de fijne samenwerking.

Een soortgelijke combinatie van theorie en experiment kwam tot stand dankzij de samenwerking met Rik Wensink en George Jackson. Thanks very much for the pleasant collaboration and your hospitality during my visit.

Ik heb ook het voorrecht gehad diverse studenten te mogen begeleiden. Jos van Rijssel, Chris Evers, Manish Kalika, Rogier Brand en Emile Bakelaar bedankt voor jullie inzet en enthousiasme. Een deel van jullie werk is terug te vinden in dit proefschrift en/of heeft geleid tot mooie publicaties. Mark Vis, bedankt voor de vele AFM-metingen die je tijdens je student-assistentschap hebt gedaan.

Dominique Thies-Weesie, Chantal Vonk, Kanvaly Lacina, Bonny Kuipers, Emile Bakelaar en Marina uit de Bulten-Weerensteijn, wil ik bedanken voor alle ondersteuning op het lab en met de Utrechtse bureaucratie. Bonny, in het bijzonder dank voor je hulp met de polarisatiemicroscopie-opstelling in de elektromagneet. Hans Meeldijk wil ik bedanken voor zijn hulp met de TEM.

Mijn kamergenoten door de jaren heen, Stefano Sacanna, Maurice Mourad, Laura Rossi, Julius de Folter en Jos van Rijssel, wil ik bedanken voor alle gezelligheid, hulp en discussies. Maurice, van jou heb ik ook veel geleerd op het lab en over gibbsiet.

Esther van den Pol, bedankt voor de prettige samenwerking op het lab, maar ook voor de gezelligheid tijdens de vele conferenties die we samen bezochten. Onze minivakantie op Sicilië (inclusief het beklimmen van de Etna) zal ik ook niet snel vergeten! Volkert de Villeneuve wil ik bedanken voor de fijne samenwerking, die resulteerde in een mooi artikel. Bob Luigjes verdient een speciale vermelding vanwege de vele keren dat hij me van koffie heeft voorzien, vooral toen er tijdens de laatste maanden soms tot laat

doorgewerkt moest worden. Wie ook niet onvermeld mag blijven, is David van der Beek, die bij zijn vertrek een pot met gibbsiet achterliet waar ik veel interessante experimenten mee heb kunnen doen.

Verder wil ik alle andere leden van het Van 't Hoff lab bedanken, die er met elkaar voor zorgen dat het er zo prettig werken is. Bedankt ook voor alle gezelschap en afleiding tijdens koffiepauzes, conferenties, scholen, uitjes, schaatstochten, etc. Ook de leden van de Soft Condensed Matter groep bedankt voor jullie gezelligheid tijdens conferenties.

Gerdien, het was fijn om promotie-ervaringen met je te kunnen uitwisselen, maar ook bedankt voor je vriendschap en de afleiding tijdens onze vele dagjes uit. Erg leuk dat je mijn paranimf wilt zijn. Dorenda, bedankt voor je vriendschap, die, hoewel soms op een wat lager pitje, onlangs een gedenkwaardig jubileum beleefde (wat we echt nog moeten vieren!).

Pa en ma, Johan, Lydia en Annemarie, bedankt voor jullie onvoorwaardelijke steun en stimulans door de jaren heen.

Maar bovenal ben ik dank verschuldigd aan de Heere, Die mij het verstand en de kracht gaf om dit alles te kunnen doen.

Soli Deo Gloria

List of publications

This thesis is based on the following publications:

- A. A. Verhoeff, R. P. Brand, and H. N. W. Lekkerkerker, Tuning the birefringence of the nematic phase in suspensions of colloidal gibbsite platelets, submitted. (Chapter 2)
- A. A. Verhoeff, H. H. Wensink, M. Vis, G. Jackson and H. N. W. Lekkerkerker, *Liquid crystal phase transitions in systems of colloidal platelets with bimodal shape distribution*, J. Phys. Chem. B **113** (2009), 13476 - 13484. (Chapter 3)
- A. A. Verhoeff, I. A. Bakelaar, R. H. J. Otten, P. van der Schoot, and H. N. W. Lekkerkerker, *Tactoids of plate-like particles: size, shape and director-field*, in press, Langmuir, DOI: 10.1021/la104128m. (Chapter 4)
- A. A. Verhoeff, R. H. J. Otten, P. van der Schoot, and H. N. W. Lekkerkerker, *Shape and director field deformation of tactoids of plate-like colloids in a magnetic field*, J. Phys. Chem. B. **113** (2009), 3704. (Chapter 5)
- A. A. Verhoeff, R. H. J. Otten, P. van der Schoot, and H. N. W. Lekkerkerker, *Tactoids of plate-like particles in a magnetic field*, accepted for publication in J. Chem. Phys. (Chapter 6)
- M. C. D. Mourad, A. A. Verhoeff, D. V. Byelov, A. V. Petukhov and H. N. W. Lekkerkerker, *Devitrification of the glassy state in suspensions of charged platelets*, J. Phys.: Condens. Matter **21** (2009), 474218. (Chapter 10)

Other papers by the author:

- A. A. Verhoeff, J. van Rijssel, V. W. A. de Villeneuve, and H. N. W. Lekkerkerker, *Orientation dependent Stokes drag in a colloidal liquid crystal*, Soft Matter **4** (2008), 1602.
- A. A. Verhoeff, M. L. Kistler, A. Bhatt, J. Pigga, J. Groenewold, M. Klokkenburg, S. Veen, S. Roy, T. Liu, and W. K. Kegel, *Charge regulation as a stabilization mechanism for shell-like assemblies of polyoxometalates*, Phys. Rev. Lett. **99** (2007), 066104.

Manuscripts in preparation:

- A. A. Verhoeff and H. N. W. Lekkerkerker, *Coalescence of tactoids with the isotropic-nematic interface.* (Chapter 7)
- A. A. Verhoeff and H. N. W. Lekkerkerker, *Buoyancy-driven coalescence of two tactoids.* (Chapter 7)

- A. A. Verhoeff and H. N. W. Lekkerkerker, *Droplet snap-off and breakup of nematic threads.* (Chapter 8)
- A. A. Verhoeff and H. N. W. Lekkerkerker, *First direct observation of columnar liquid crystal droplets.* (Chapter 9)

Curriculum Vitae

Lia Verhoeff was born on the 17^{th} of May, 1983 in Utrecht, The Netherlands. After she graduated in 2001 from the Driestar College in Gouda, she studied Chemistry at Utrecht University from 2001 until 2006. In 2004 she performed a bachelor research project at the group of Condensed Matter and Interfaces on the stability of CdTe quantum dots (with Floris van Driel and Daniel Vanmaekelbergh). In the same year she graduated with distinction as a Bachelor of Science with a minor in Musicology. From 2004-2006 she performed her master research at the Van 't Hoff Laboratory for Physical and Colloid Chemistry with Willem Kegel on the self-assembly of polyoxometalates into hollow superstructures, which was awarded the Unilever Research Prijs 2006. Also as part of the Master Chemistry and Physics, she performed a research project on the interactions between eye lens proteins at Fribourg University, Switzerland (with Peter Schurtenberger, Anna Stradner, and Gabriela Savin). In 2006 she graduated with distinction as a Master of Science at Utrecht University. In the same year she started her PhD research at the Van 't Hoff Laboratory under supervision of Henk Lekkerkerker and Paul van der Schoot.